TESIS DE LA UNIVERSIDAD DE ZARAGOZA

2024 357

Iván Marín Miana

Functional nanoarchitectures based on liquid crystal phases: ionic pillararenes and chiral columnar organizations. Materials for ionic conductivity and molecular segregation

Director/es
Barberá Gracia, Joaquín Manuel
Serrano Ostáriz, José Luis

ISSN 2254-7606

Prensas de la Universidad Universidad Zaragoza

Universidad de Zaragoza
Servicio de Publicaciones

ISSN 2254-7606

Universidad Zaragoza
1542

Tesis Doctoral

FUNCTIONAL NANOARCHITECTURES BASED ON LIQUID CRYSTAL PHASES: IONIC PILLARARENES AND CHIRAL COLUMNAR ORGANIZATIONS. MATERIALS FOR IONIC CONDUCTIVITY AND MOLECULAR SEGREGATION

Autor

Iván Marín Miana

Director/es

Barberá Gracia, Joaquín Manuel
Serrano Ostáriz, José Luis

UNIVERSIDAD DE ZARAGOZA
Escuela de Doctorado

Programa de Doctorado en Química Orgánica

2024

Universidad Zaragoza
1542

Tesis Doctoral

Functional nanoarchitectures based on liquid crystal phases: ionic pillararenes and chiral columnar organizations. Materials for ionic conductivity and molecular segregation

Autor

Iván Marín Miana

Director/es

José Luis Serrano Ostáriz

Joaquín Barberá Gracia

Universidad de Zaragoza

Facultad de Ciencias / Química Orgánica

2024

Functional nanoarchitectures based on liquid crystal phases: ionic pillararenes and chiral columnar organizations. Materials for ionic conductivity and molecular segregation

Iván Marín Miana

Memoria presentada en la Universidad de Zaragoza para optar al Grado de Doctor

Departamento de Química Orgánica

Facultad de Ciencias-INMA

Universidad de Zaragoza-CSIC

Zaragoza, Abril 2024

This work was supported by the MINECO FEDER funds (PGC2018-097583-B-I00 and PID2021-122882NB-I00 Projects) and Gobierno de Aragón-FSE (E47_23R-research group). The use of the SAI (Universidad de Zaragoza) and CEQMA (Universidad de Zaragoza-CSIC) services is also acknowledged.

El Dr. JOSÉ LUIS SERRANO OSTÁRIZ, Catedrático de la Universidad de Zaragoza y el Dr. JOAQUÍN BARBERÁ GRACIA, Catedrático de la Universidad de Zaragoza, pertenecientes al Instituto de Nanociencia y Materiales de Aragón y al Departamento de Química Orgánica de la Universidad de Zaragoza

HACEN CONSTAR

Que el trabajo original titulado "Functional nanoarchitectures based on liquid crystal phases: ionic pillararenes and chiral columnar organizations. Materials for ionic conductivity and molecular segregation" ha sido realizado por D. IVÁN MARÍN MIANA bajo nuestra supervisión en el Departamento de Química Orgánica de la Universidad de Zaragoza y reúne las condiciones para su presentación como tesis doctoral.

En Zaragoza, a 8 de Abril de 2024

Fdo. José Luis Serrano Ostáriz

Fdo. Joaquín Barberá Gracia

Acronyms List

1D One-Dimensional

2D Two-Dimensional

3D Three-Dimensional

AC Alternating current

AcOEt Ethyl acetate

AFM Atomic force microscopy

AIE Aggregation-induced emission

CD Circular dichroism

Col_{ob} Oblique columnar mesophase

Col_r Rectangular columnar mesophase

CPL Circular polarized light

c Stacking distance in columnar mesophases

Cr Crystal

DC Dark conglomerate

DCC N,N'-Dicyclohexylcarbodiimide

DCM Dichloromethane

DIAD Diisopropyl azodicarboxylate

DMF *N,N*-Dimethylformamide

DMSO Dimethylsulfoxide

DPTS 4-(dimethylamino)pyridinium 4-toluenesulfonate

DSC Differential scanning calorimetry

Ea Activation energy

EIS Electrochemical impedance spectroscopy

ESI	Electrospray ionization
eV	Electron-volt
I	Isotropic liquid
FTIR	Fourier transform infrared Spectroscopy
HMBC	Heteronuclear multiple bond correlation
HNF	Helical nanofilament
HPLC	High-performance liquid chromatography
HRMS	High-resolution mass spectrometry
HSQC	Heteronuclear single quantum coherence spectroscopy
ITO	Indium tin oxide
LC	Liquid crystal
MALDI	Matrix-assisted laser desorption/ionization
MS	Mass spectrometry
MWCO	Molecular weight cut-off
N	Nematic mesophase
$\mathbf{N_D}$	Discotic nematic mesophase
$\mathbf{N_g}$	Nematic glass mesophase
NR	Nile red
NMR	Nuclear magnetic resonance
NOESY	Nuclear overhauser effect spectroscopy
PAMAM	Poly(amidoamine)
PEI	Polyethylenimine
PPI	Poly(propylene imine)
PPM	Part per million

POM	Polarized optical microscopy
RT	Room temperature
SAED	Selected area electron diffraction
SAXS	Small-angle X-ray scattering
SEM	Scanning electron microscopy
TEG	Triethylene glicol
TEM	Transmission electron microscopy
TGA	Thermogravimetry
THF	Tetrahydrofuran
TFA	Trifluoroacetic acid
TMS	Trimethylsilane
TOF	Time of flight
UV	Ultraviolet
Vis	Visible
WAXS	Wide-angle x-ray scattering
XPS	X-ray photoelectron spectroscopy
XRD	X-ray diffraction

Chapter 1

Introduction

"Science is always worth it, because its discoveries, sooner or later, are always applied." Severo Ochoa

Liquid crystals (LCs) are a unique state of matter discovered in 1888 that exists between the solid and isotropic liquid phase and is called mesophase. These materials combine the anisotropy of the solids and the mobility of the liquids turning in potential materials for many applications such as sensors,[1] organic electronics,[2] nanoporous films…[3] (**Figure 1.1**) Due to the high mobility of the molecules, these materials are extremely sensible to external stimuli like light, pH, electric and magnetic fields, heat, etc.[4,5]

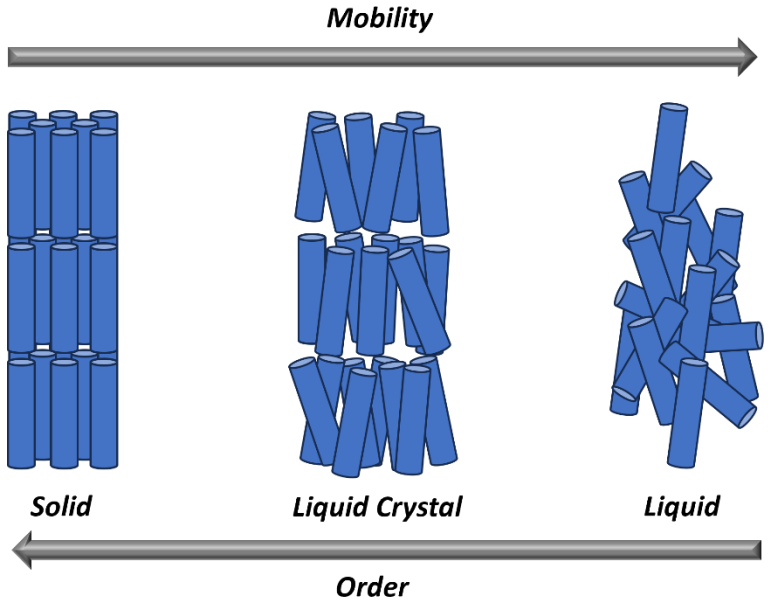

Figure 1.1. *Schematic representation of the states of matter and their order/mobility.*

Attending to their classification, liquid crystals (LCs) are categorized into two classes: thermotropic and lyotropic. This organization is distinguished by the mechanism that drives their self-organization. Thermotropic liquid crystals manifest mesophases in pure compounds within a specific temperature range. In contrast, lyotropic LCs are prepared using amphiphilic compounds and solvents, where both concentration and temperature play a key role.

Thermotropic LCs are further classified into various types (nematic, columnar, smectic, etc.). The resulting mesophase is influenced by the structural shape of the molecules. For instance, rod-like[6] compounds exhibit nematic and smectic mesophases. Disc-like[7] molecules typically self-organize into columnar mesophases or nematic phases, while bent-

core[8] compounds mainly display smectic and columnar mesophases (**Figure 1.2**).

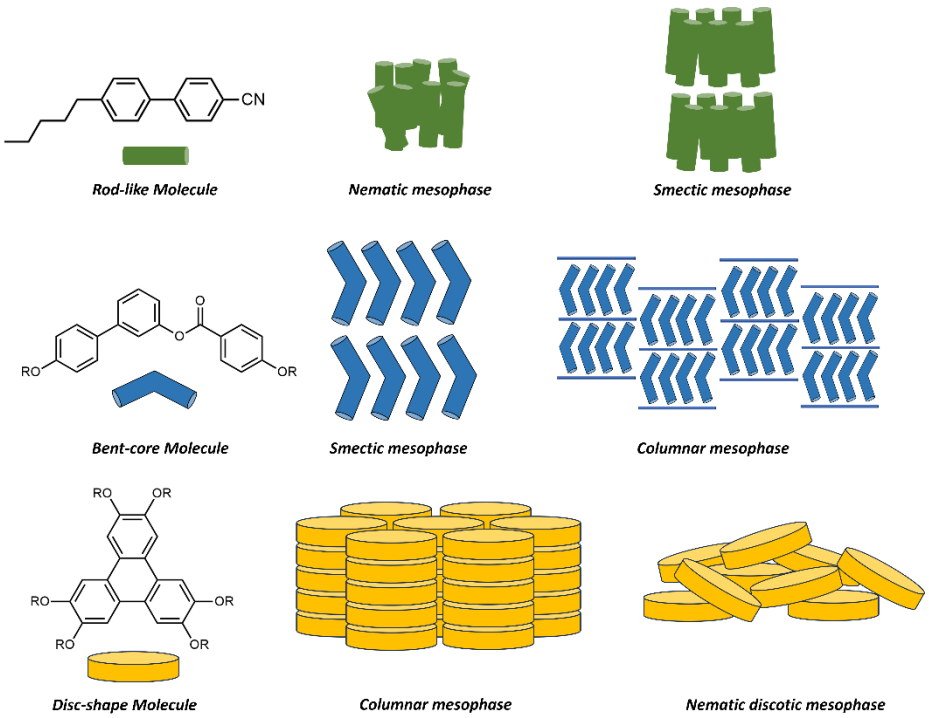

Figure 1.2. *Some of the thermotropic LC mesophases and their common molecular shape.*

Over the last decades, LCs have experienced a great development in the fields of nanotechnology and nanoscience. Beyond the LC displays which have revolutionized the telecommunication world, there are many daily applications where LCs are employed in areas like material science,[9,10] biomedical science,[11,12] technology…[13,14] Their multiple stimuli response, their mechanical properties and their easy alignment and orientation are some of the causes for their expansion.

These advances have required the development of more sophisticated materials. In this context, it has been necessary to create materials that go beyond single molecules. Supramolecular LCs provide new routes to different phases, maximizing the intermolecular interactions and minimizing free space.

In the last decades supramolecular chemistry has transformed the science of materials, developing complex systems through basic interactions of single molecules. Some of the interactions that induce

the self-assembly are hydrogen-bonds, electrostatic forces, halogen bonds, van der Waals forces or π–π interactions. These non-covalent bonds are reversible and very sensitive to external stimuli .

One of the most explored approaches in the supramolecular LCs field are hydrogen bonds. This interaction is dynamic, directional and highly selective, and furthermore dependent of temperature, solvents and concentration. These characteristics allow to control the strength and the H-bonded supramolecular system in future applications. Hydrogen bonds are prepared through a donor molecule with an acid hydrogen atom available to interact with an acceptor moiety with nonbonding electron lone pairs. This approach has been employed in a wide variety of chemical systems, for instance, in side-chain and main-chain H-bonded supramolecular LC polymers.[15,16] Other common structures are assembled through carboxylic acids and aromatic rings containing nitrogen groups[17,18] (**Figure 1.3**).

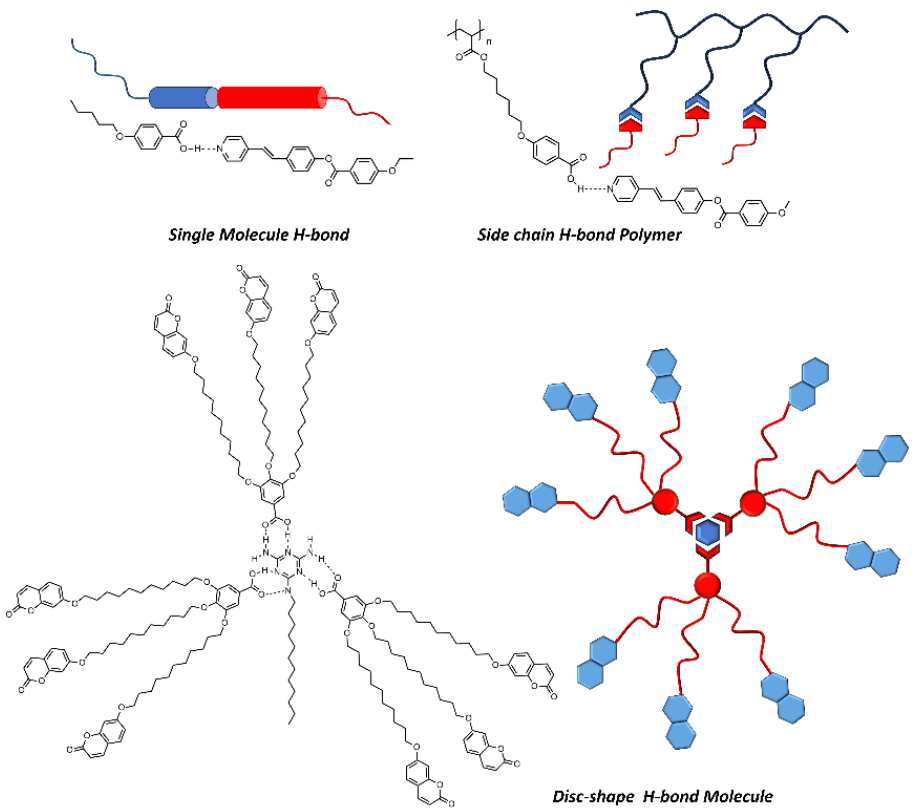

Figure 1.3. *Examples of H-bonded supramolecular liquid crystals.*

Another kind of supramolecular system deeply studied in the "*Liquid Crystals and Polymers Group*" are ionic dendrimers by electrostatic interactions. Dendrimers are monodisperse macromolecular systems, which present a radial 3D structure and contains several branching points in their periphery. The chemical structure consists of a central nucleus with repeating units radially attached to the core. Each layer of the macromolecule is called generation and each subunit joined to the core is called dendron. The periphery of the dendrimer contains a large number of terminal groups that are suitable for further functionalization, adjusting the global properties of the macromolecule (**Figure 1.4**).

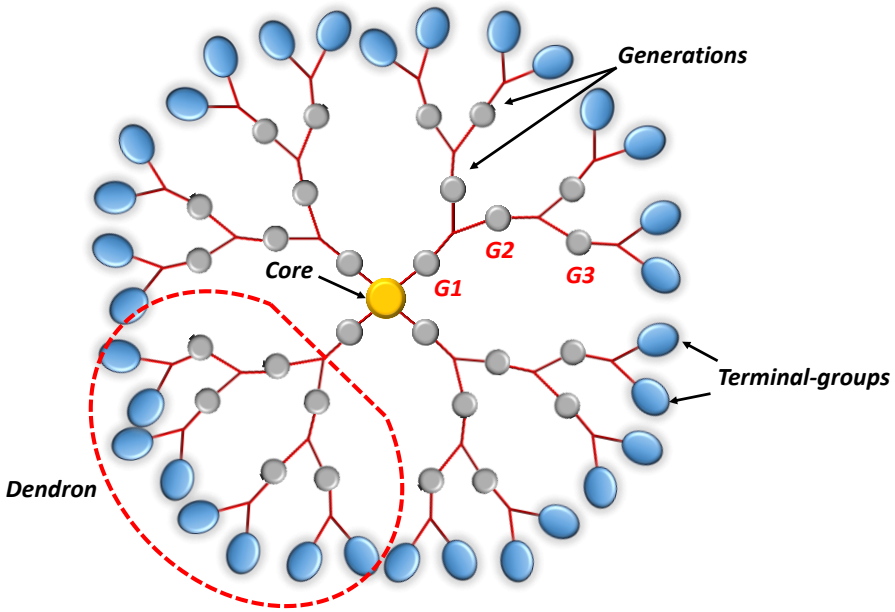

Figure 1.4. Structural details of a dendrimer.

The preparation of liquid crystals based on dendrimers as building blocks has provided the creation of multifunctional LCs and led to the formation of unique mesophases. Their hyperbranched structure allows the functionalization with useful moieties, resulting in a high density of functional groups that enhances their activity and the LC properties.

These interesting macromolecules can be achieved through two different routes, giving rise to covalent or ionic dendrimers. Covalent LC dendrimers are typically synthesized by attaching mesogenic moieties

to the terminal groups of a dendrimer or by incorporating mesogenic units as repeating blocks within the dendritic structure. On the other hand, ionic LC dendrimers are prepared through electrostatic interactions allowing an easy and fast functionalization of the end-groups.[19,20] To obtain the ionic pairs it is necessary to introduce in the dendrimer and mesogenic units functional groups prone to easily acquire a positive or negative charge (**Figure 1.5**).

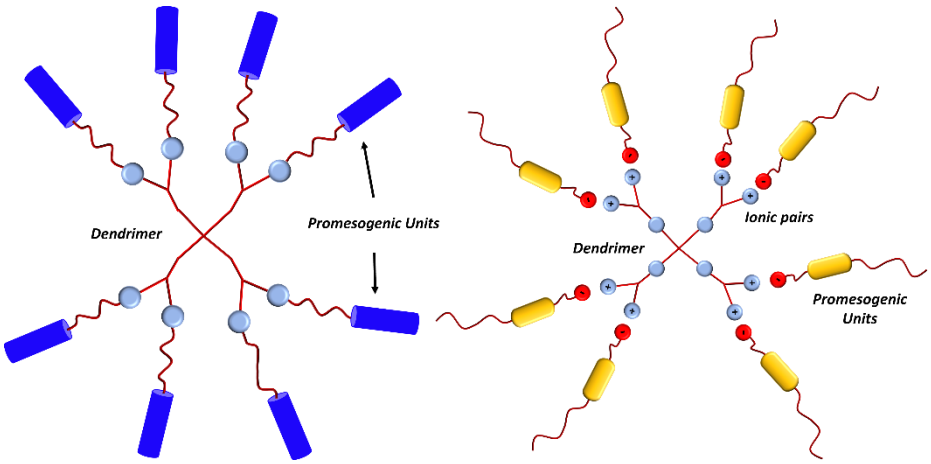

Figure 1.5. *Covalent (left) and ionic (right) liquid crystal dendrimers.*

The "*Liquid Crystals and Polymers Group*" has extended the knowledge of ionic LC dendrimers using PPI and PAMAM dendrimers. These materials are commercial and contain amines in their periphery allowing their functionalization with acids through a proton-transfer reaction. Moreover, the relationship between the generation of the dendrimer and the kind of mesophase was demonstrated, stablishing that higher generations could not accommodate the increasing number of acids in a parallel arrangement, turning from smectic mesophases into columnar LCs.[21,22] Similarly, when more alkyl chains were added to the acids (from mono- to tri-substituted) the mesophase changed from smectic to columnar.[23] These studies confirmed a cylindrical arrangement model for low generations, where the flexible dendrimer is located in the central region of the cylinder with the ionic pairs in both sides and the alkyl chains organized in a preferred direction, resulting in a cylinder. However, for higher generations and polysubstituted acids,

the huge number of alkyl chains cannot be accommodated in a cylinder and the chains are folded into a disc resulting in columnar mesophases. This scaffold produces a marked segregation between the different parts of the dendrimers: the hydrophilic ionic pairs (ammonium/carboxylate) and the aliphatic alkyl chains, yielding ionic liquid crystals without the requirement of any promesogenic unit.[24,25]
Further studies looked into the thermal stability of the ionic dendrimers, substituting the perhydrogenated chains for perfluorinated analogues.[26,27] Fluorinated derivatives are bulkier, possess more rigidity and lower interaction between neighboring chains (van der Waals forces) increasing the thermal stability of the ionic LCs in comparison with their hydrogenated analogues.[28]
Multiple research groups have studied the functionalization of PAMAM and PPI dendrimers with complex moieties such as photoactive,[29] fluorescent[30] or bent-shaped[31] units. These materials have demonstrated applicability in different fields such as ion conductive materials,[32] luminescent materials[33] or preparation of nanostructures.[34]

In this doctoral thesis we set up as main objective the use of supramolecular chemistry for the development of new functional materials in the fields of proton conduction, nanoporous materials and the preparation of nanostructures.

In **Chapter 2** we describe the use of a pillar[5]arene derivative for the preparation of ionic liquid crystals. The pillar[5]arene plays the role of PAMAM or PPI in ionic LC dendrimers and its functionalization with different acids and dendrons leads to the formation of LCs. This method provides materials with potential application in **proton conduction**. Moreover, the introduction of coumarin moieties in the different acids allows the fixation of the structure through irradiation with light, via coumarin dimerization, obtaining a mechanically and thermally stable polymer. The ionic pathways followed in the pillar[5]arene´s functionalization provides an amphiphilic character to these materials, which enables the preparation of a wide variety of **nanostructures** in

water. Some of the structures show ability to encapsulate drugs and release them in a controlled way.

Chapter 3 reports the functionalization of the same pillar[5]arene prepared in **Chapter 2** with bent-core acids. In this case several bent-core aromatic acids with different functional groups (ester, biphenyl and azobenzene) are employed in the preparation of ionic bent-core pillar[5]arenes. Similarly to **Chapter 2**, these materials show good **proton mobility** because of the ionic pathways followed in the pillar[5]arene functionalization. Moreover, the presence of azobenzene units turn them into photoresponsive materials owing to its *cis*/*trans* isomerization. The ionic materials self-organize in water obtaining fibers, ribbons, nanotubes… The structural modifications of the bent-core units (functional group, length of the linker between the carboxyl group and the bent-core structure…) provide a detailed analysis of the relationship between the chemical structure and the morphology of the aggregates.

Chapters 4 and **5** detail the synthesis of multiple disc-shaped molecules by hydrogen bond between acid dendrons and amine-containing templates. These molecules self-organize in columnar liquid crystals with application in **nanoporous materials**. The acid dendrons incorporate azobenzene units, which, upon irradiation with circular polarized light, generate a tunable chirality in the material. The photopolymerization of coumarins (**Chapter 4**) and methacrylates (**Chapter 5**) provides nanoporous polymeric materials with a controlled pore size. These chiral membranes show a highly selective adsorption by size for different dyes by controlling the pore size with different template molecules. Furthermore, the tunable chirality generated in the materials allows to control the selective adsorption of different enantiomers and the separation of racemic mixtures.

References

[1] M. Khan, S. Liu, L. Qi, C. Ma, S. Munir, L Yu and Q. Hu, Liquid crystal-based sensors for the detection of biomarkers at the aqueous/LC interface, *Trac trends in analytical chemistry*, 2021, **144**, 116434-116448.

[2] H. Iino and J.-i. Hanna, Liquid crystalline organic semiconductors for organic transistor applications, *Polymer Journal*, 2017, **49**, 23–30.

[3] K. Salikolimi, A. A. Sudhakar and Y. Ishida, Functional Ionic Liquid Crystals, *Langmuir*, 2020, **36**, 11702−11731.

[4] Z. Li and Y. Yin, Stimuli-Responsive Optical Nanomaterials, *Adv. Mater.*, 2019, **31**, 1807061-1807094.

[5] L. Hu, Y. Wan, Q. Zhang and M. J. Serpe, Harnessing the Power of Stimuli-Responsive Polymers for Actuation, *Adv. Funct. Mater*., 2020, **30**, 1903471-1903487.

[6] R. J. Mandle, S. J. Cowling and J. W. Goodby, A nematic to nematic transformation exhibited by a rod-like liquid crystal, *Phys. Chem. Chem. Phys*., 2017, **19**, 11429-11435.

[7] S. Kumar, Self-organization of disc-like molecules: chemical aspects, *Chem. Soc. Rev*., 2006, **35**, 83–109.

[8] R. A. Reddy and C. Tschierske, Bent-core liquid crystals: polar order, superstructural chirality and spontaneous desymmetrisation in soft matter systems, *J. Mater. Chem.*, 2006, **16**, 907–961.

[9] M. Pilz da Cunha, S. Ambergen, M. G. Debije,E. F. G. A. Homburg, J. M. J. den Toonder and A. P. H. J. Schenning, A Soft Transporter Robot Fueled by Light, *Adv.Sci*., 2020, **7**, 1902842-1902849.

[10] D. J. Broer, C. M. Bastiaansen, M. G. Debije and A. P. H. J. Schenning, Functional organic materials based on polymerized liquid-crystal monomers: Supramolecular hydrogen-bonded systems, *Angew. Chem. Int. Ed*., 2012, **51**, 7102–7109.

[11] H. Zeng, O. M. Wani, P. Wasylczyk, R. Kaczmarek and A. Priimagi, Self-Regulating Iris Based on Light-Actuated Liquid Crystal Elastomer, *Adv. Mater*., 2017, **29**, 1701814-1701821.

[12] H. Zeng, O. M. Wani, P. Wasylczyk and A. Priimagi, Light-Driven, Caterpillar-Inspired Miniature Inching Robot, *Macromol. Rapid Commun*., 2018, **29**, 1700224-1700230.

[13] T. Kato, N. Mizoshita and K. Kishimoto, Functional liquid-crystalline assemblies: Self-organized soft materials. *Angew. Chem. Int. Ed*., 2006, **45**, 38–68.

[14] T. J. White and D. J. Broer, Programmable and adaptive mechanics with liquid crystal polymer networks and elastomers, *Nature Materials*, 2015, **14**, 1087-1098.

[15] T. Kato, H. Kihara, U. Kumar, T. Uryu and J. M. J. Fréchet, A Liquid-Crystalline Polymer Network Built by Molecular Self-Assembly through Intermolecular Hydrogen Bonding, *Angew. Chem. Int. Ed*., 1994, **33**, 1644–1645.

[16] T. Kato, O. Ihata, S. Ujiie, M. Tokita, and J. Watanabe Self-Assembly of Liquid-Crystalline Polyamide Complexes through the Formation of Double Hydrogen Bonds between a 2,6-Bis(amino)pyridine Moiety and Benzoic Acids, *Macromolecules,* 1998, **31**, 11, 3551–3555.

[17] H. Kihara, T. Kato, T. Uryu and J. M. J. Fréchet, Supramolecular Liquid-Crystalline Networks Built by Self-Assembly of Multifunctional Hydrogen-Bonding Molecules, *Chem. Mater*., 1996, **8**, 961-968.

[18] A. Martínez-Felipe and C. T. Imrie, The role of hydrogen bonding in the phase behaviour of supramolecular liquid crystal dimers, *Journal of Molecular Structure*, 2015, **1100**, 429-437.

[19] A. Concellón and V. Iguarbe, in Supramolecular Assemblies Based on Electrostatic Interactions, ed. M. A. Aboudzadeh, A. Frontera, Springer International Publishing, Cham, 2022, p. 85.

[20] A. G. Cook, U. Baumeister, C. Tschierske, Supramolecular dendrimers: unusual mesophases of ionic liquid crystals derived from protonation of DAB dendrimers with facial amphiphilic carboxylic acids, *J. Mater. Chem.*, 2005, **15**, 1708–1721.

[21] S. Hernández-Ainsa, J. Barberá, M. Marcos and J. L. Serrano, Influence of the Poly(propylene imine) Generation in the LC Properties of Ionic Codendrimers Bearing Fluorinated and Perhydrogenated Chains, *Journal of Polymer Science Part A: Polymer Chemistry*, 2011, **49**, 278-285.

[22] S. Hernandez-Ainsa, E. Fedeli, J. Barberá, M. Marcos, T, Sierra and J. L. Serrano, Self-assembly modulation in ionic PAMAM derivatives, *Soft Matter*, 2014, **10**, 281-289.

[23] M. Marcos, R. Martín-Rapún, A. Omenat, J. Barberá and J. L. Serrano, Ionic liquid crystal dendrimers with mono-, di- and trisubstituted benzoic acids, *Chem. Mater*., 2006, **18**, 5, 1206–1212.

[24] S. Hernández-Ainsa, M. Marcos and J. L. Serrano, in Hand-book of Liquid Crystals, ed. J. W. Goodby, P. J. Collings, T. Kato, C. Tschierske, H. Gleeson and P. Raynes, Wiley-VCH Verlag GmbH & Co. KGaA, 2014, vol. 7, p. 2.

[25] M. Marcos, R. Martín- Rapún, A. Omenat and J. L. Serrano, Highly congested liquid crystal structures: dendrimers, dendrons, dendronized and hyperbranched polymers, *Chem. Soc. Rev*., 2007, **36**, 1889–1901.

[26] R. Martín-Rapún, M. Marcos, A. Omenat, J. L. Serrano, E. T. de Givenchy and F. Guittard , Liquid crystalline semifluorinated ionic dendrimers*, Liq Cryst.*, 2007, **34**, 3, 395–400.

[27] S. Hernández-Ainsa, J. Barberá, M. Marcos and J. L. Serrano, Effect of the phobic segregation between fluorinated and perhydrogenated chains on the supramolecular organization in ionic aromatic dendrimers, *Chem. Mater.,* 2010, **22**, 16, 4762–4768.

[28] S. Hernández-Ainsa, M. Marcos, J. Barberá and J. L. Serrano, Philic and Phobic Segregation in Liquid-Crystal Ionic Dendrimers: An Enthalpy–Entropy Competition, *Angew. Chem*., 2010, **122**, 2034 –2038.

[29] M. Marcos, R. Alcalá, J. Barberá, P. Romero, C. Sánchez and J. L. Serrano, Photosensitive Ionic Nematic Liquid Crystalline Complexes Based on Dendrimers and Hyperbranched Polymers and a Cyanoazobenzene Carboxylic Acid, *Chem. Mater.,* 2008, **20**, 16, 5209–5217.

[30] S. Hernández-Ainsa, J. Barberá, M. Marcos and J. L. Serrano, Liquid Crystalline Ionic Dendrimers Containing Luminescent Oxadiazole Moieties, *Macromolecules*, 2012, **45**, 1006−1015.

[31] M. Cano, A. Sánchez-Ferrer, J. L. Serrano, N. Gimeno and M. B. Ros, Supramolecular architectures from bent-core dendritic molecules. *Angew. Chem. Int. Ed*., 2014, **53**, 13449–13453.

[32] A. Concellón, T. Liang, A. P. H. J. Schenning, J. L. Serrano, P. Romero and M. Marcos, Proton-conductive materials formed by coumarin photocrosslinked ionic liquid crystal dendrimers, *J. Mater. Chem. C*, 2018, **6**, 1000-1007.

[33] P.K. S. Antharjanam, M. Jaseer, K.N. Ragi, E. Prasad, Intrinsic luminescence properties of ionic liquid crystals based on PAMAM and PPI dendrimers, *Journal of Photochemistry and Photobiology A: Chemistry*, 2009, **203**, 50–55.

[34] S. Hernández-Ainsa, J. Barberá, M. Marcos and J.L. Serrano, Nanoobjects coming from mesomorphic ionic PAMAM dendrimers, *Soft Matter*, 2011, **7**, 2560-2568.

Chapter 2

Ionic pillar[5]arene derivatives: proton-conductive liquid crystals and formation of nanostructures with encapsulation properties

---

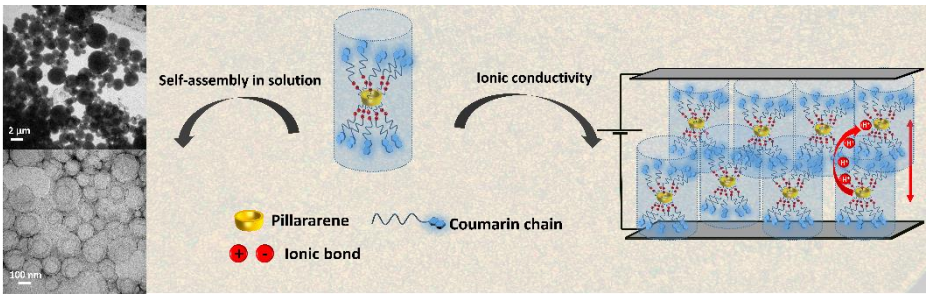

This Chapter is based on the published article: I. Marín, R. I. Merino, J. Barberá, A. Concellón and J. L. Serrano, Ionic self-assembly of pillar[5]arenes: proton-conductive liquid crystals and aqueous nanoobjects with encapsulation properties*, Mater. Adv.*, 2023, **4**, 5564–5572. DOI: 10.1039/d3ma00698k

"Never too high never too low"

Ricky Rubio

2.1 Introduction

Pillar[n]arenes[1] are a novel class of macrocycles composed by 1,4-dialkoxybenzenes connected by methylene groups in *para*-position, giving them a symmetrical structure. This unique symmetry sets them apart from other well-known basket-shaped structures like calixarenes and cyclodextrins. Another notable feature of their structure is their cavity, which enables them to capture electron-deficient molecules or cations. The presence of multiple aromatic rings creates an electron rich environment within the cavity, playing a crucial role in several applications such as host-guest systems,[2,3] supramolecular polymers,[4] fluorescence switches,[5] etc.

Furthermore, pillar[n]arenes possess an interesting characteristic: the methylene bridges allow the rotation of the phenolic units, generating a dynamic system.[6] This rotation leads to the formation of chiral planarity (**Figure 2.1**). However, it has been demonstrated[7] that incorporating bulky substituents to the aromatic rings inhibits rotation due to the limited size of the cavity.

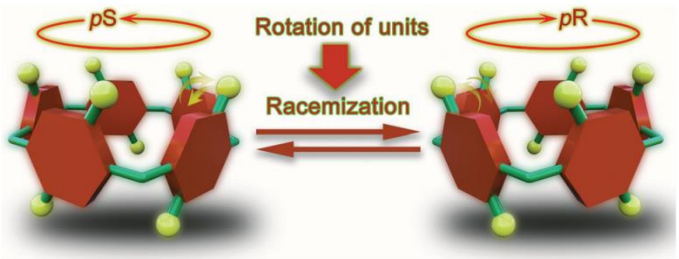

Figure 2.1. *Planar chirality of pillar[5]arene and their racemization (adapted from reference 6).*

Since their discovery in 2008 by *prof. Ogoshi,*[1] pillar[n]arenes have found utility in numerous applications. One of the most recent applications involves their role in the preparation of circularly polarized luminescence switches.[8] In a study conducted by *Yang et al.* a chiral [3]rotaxane was developed, wherein the chirality was originated from a pillar[n]arene (**Figure 2.2**). Notably, the chiral luminescent signal could be modulated based on the distance between the pillar[n]arene and the aggregation-induced emission-active unit, in this case 9,10-

distyrylanthracene (DSA). This investigation demonstrated that by inhibiting the rotation of the phenolic units, the pillar[n]arene could induce and transfer chirality to a supramolecular system.

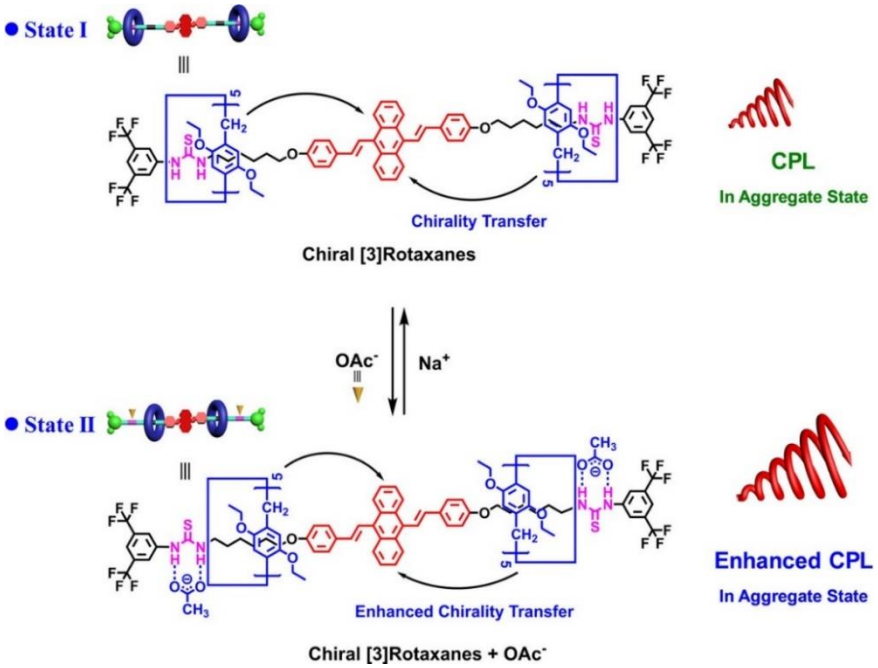

Figure 2.2. *Circularly polarized luminescence switch based on pillar[n]arene (adapted from reference 8).*

In another project *Wang et al.*[9] synthesized an ionic pillar[5]arene with carboxylic acids in the periphery of the structure. The exchange of the acid proton with different cations (Li^+, Na^+, K^+, Rb^+, Cs^+, NH_4^+) revealed an influence in the fluorescence of the compound. They found that big cations braked the rotation of the hydroquinone units enhancing the fluorescence, whereas small cations allowed the rotation reducing the fluorescence (**Figure 2.3**).

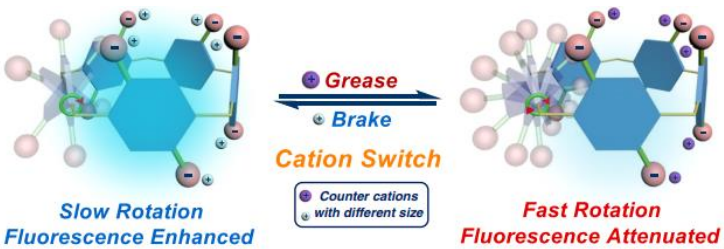

Figure 2.3. *Representation of the cation influence in pillar[n]arene fluorescence (adapted from reference 9).*

The applications of the system are wide, such as fluorescence switches for sensing, molecular devices and smart materials, for example, as anti-counterfeiting ink. In the cited article, *Wang and co-workers* showed the process of writing (with a fluorescent compound), revealing (with light) and erasing (with a solution of the cation which favors the rotation).

Despite the multiple functionalization and applications[10,11] above considered, one area that has received less attention is the formation of ionic pairs (ammonium-carboxylate) within pillar[n]arene chains. This represents a straightforward and rapid method to incorporate diverse functional groups into the pillar[n]arene structure. Such an approach could broaden the scope of research, while takes advantage of the exceptional properties of pillar[n]arenes (symmetry, planar chirality, electron rich cavity…). Functionalizing pillar[n]arenes with promesogenic units opens a new avenue for the development of a unique class of ionic liquid crystals. These materials have the potential to find applications in various fields, including ionic conductivity, the formation of chiral aggregates, drug delivery systems and host-guest interactions. By combining the distinct properties of pillar[n]arenes and promesogenic units, these novel materials can offer enhanced functionality and contribute to advance in multiple domains.

Liquid crystal (LC) pillar[n]arene-based macrocycles are a prominent class of LCs wherein the shape-persistent cavity and the rich host-guest properties of the macrocyclic unit in an ordered environment enable a plethora of opportunities in the design of functional materials.[12,13] Several macrocycles have been employed for the preparation of LCs, including calixarenes, cycloaramides oligopeptides or cyclic phenylacetylenes, among others.[14,15,16,17,18]
For example, Yuan *et al.* reported a family of alkyl-substituted cycloaramides (**Figure 2.4**) which exhibited different kinds of mesophases (lamellar, discotic nematic, columnar…).[15] These cycloaramides were capable of encapsulating small molecules in their cavity, producing a change in the mesophase. This work demonstrated

that host-guest interactions in liquid crystal macrocycles are a promising strategy to manipulate the mesophases.

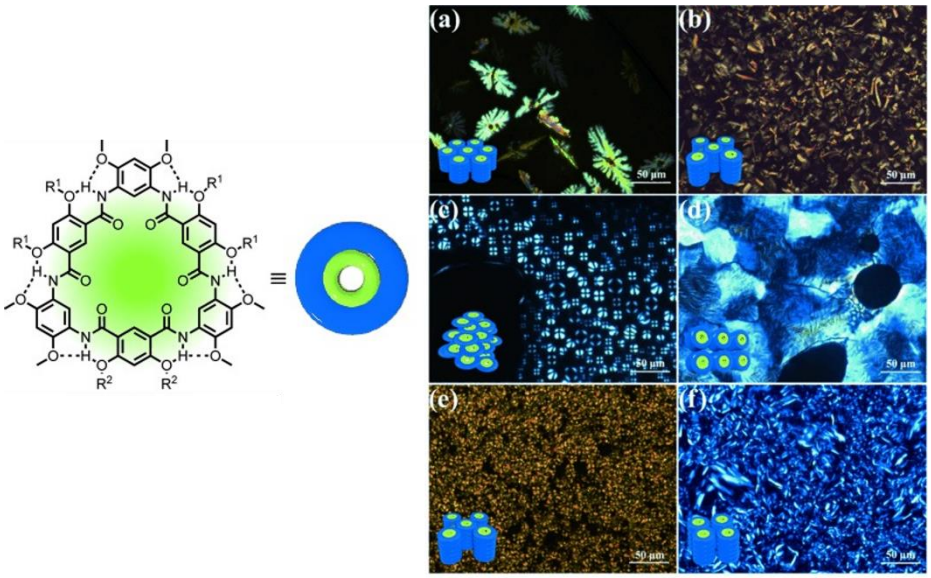

Figure 2.4. *Schematic representation of an alkyl-substituted cycloaramide and different POM textures of liquid crystal cycloaramide derivatives (adapted from reference 15).*

Nonetheless, the use of pillar[n]arene derivatives has been less often considered, despite their promising properties in metal-ion separations,[19] drug delivery,[20] surface modifications,[21] or the preparation of supramolecular polymers.[22]

Wang and co-workers described some of the first examples of nanocarriers based on pillar[n]arenes; these amphiphilic complexes self-organized in micelles and vesicles.[20] Nanocarriers showed good biocompatibility in cytotoxicity studies and response to pH and light; moreover, when they were charged with anticancer drugs their activity was comparable to that of the free drug (**Figure 2.5**).

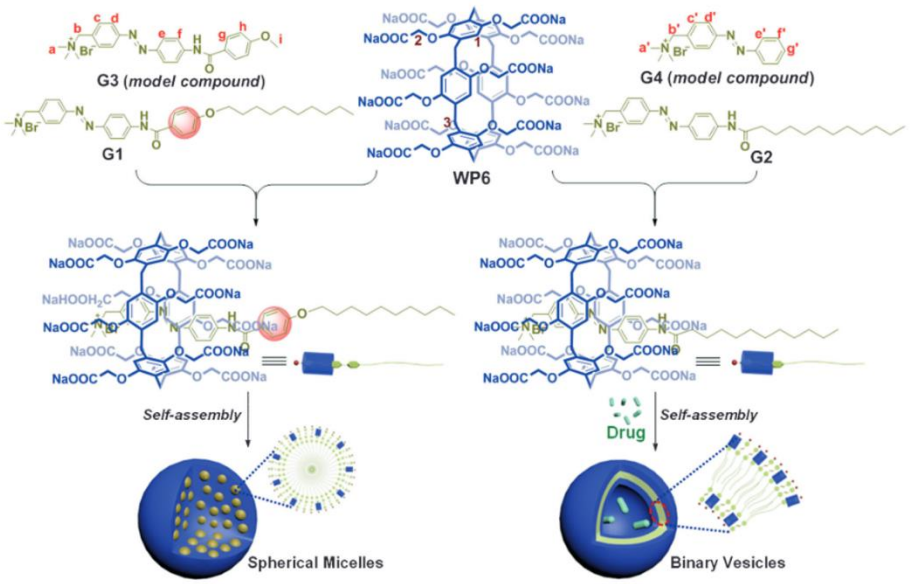

Figure 2.5. *Ionic pillar[5]arenes and their self-assembled nanostructures (adapted from reference 20).*

LC pillar[n]arenes are usually synthesized by the functionalization of a central macrocyclic scaffold with promesogenic units, resulting in lamellar and columnar LC organizations.[23,24] Additionally, pillar[n]arene macrocycles have been decorated with azobenzene or coumarin moieties to yield LCs that showed photoactive and/or fluorescent properties.[24,25,26,27] The introduction of such complex, function-bearing units into pillar[n]arenes requires the use of extremely efficient reactions, such as "click" chemistry. Recently our group has explored the introduction of coumarins by click chemistry (**Figure 2.6**) that lead to the formation of polymeric films through their photodimerization reaction with light of 325 nm.[24] The obtained polymeric films set the basis for the development of new aligned films with stable pore cavities.

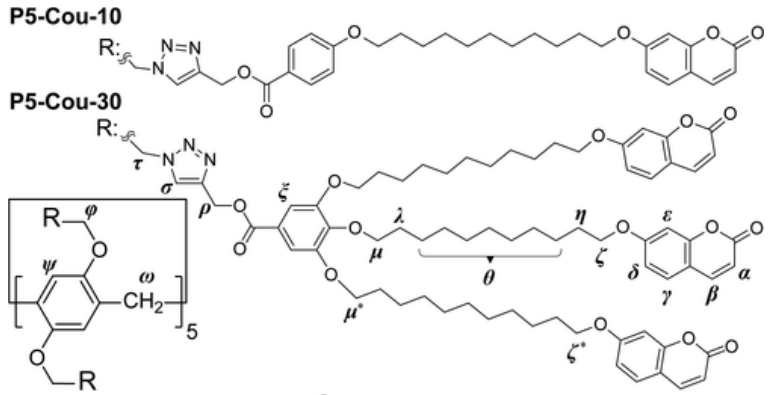

Figure 2.6. *Chemical structures of coumarin-substituted pillar[5]arenes (adapted from reference 24).*

Ogoshi *et al.* reported chiral responsive pillar[5]arenes introducing azobenzenes with chiral chains by a click reaction (**Figure 2.7**). These materials tend to homeotropic alignment caused by azobenzenes, which provokes an amplification of the chiral signal. However, once they are irradiated with UV light, azobenzenes isomerize losing the alignment and reducing the chiral signal.[27]

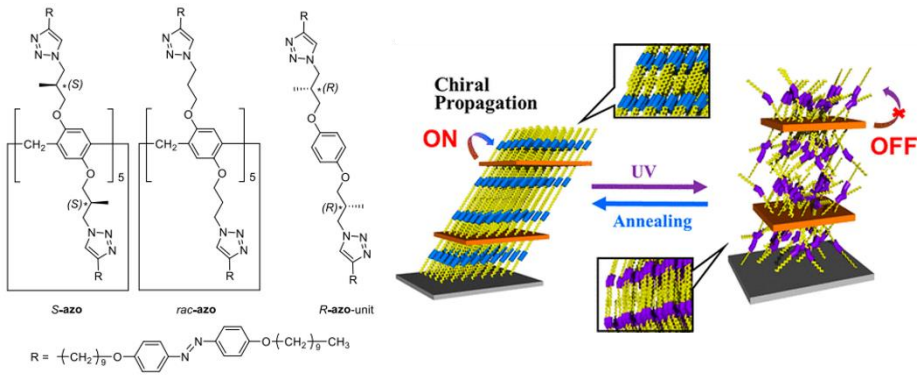

Figure 2.7. *Chemical structures of chiral pillar[5]arenes and schematic representation of stimuli- responsive mesophase (adapted from reference 27).*

However, to avoid the time-consuming synthesis associated with the preparation of these covalent systems, we envisioned that a very interesting approach may consist of using supramolecular interactions to functionalize pillar[n]arene macrocycles. Among the diverse non-covalent interactions that hold molecular building blocks together, electrostatic interactions have recently shown high potential to create LCs with promising properties as ion-conductors or drug delivery

systems.[28,29,30] In these ionic materials, the presence of charged sites within the molecular structure results in a cooperative assembly process that leads to self-organized nanostructures both in solution and in solid state. The most representative example are ionic dendrimers that are capable of self-organizing in the solid state to produce LC behavior even without being functionalized with any promesogenic unit.[31,32] Ionic interactions are essential in this self-assembly process as the segregation between polar and non-polar parts is the driving force for the formation of the LC phases.

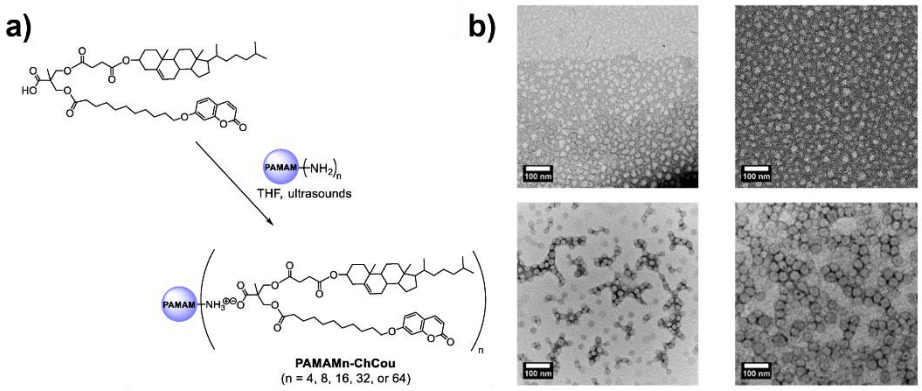

Figure 2.8. *a) Ionic derivatives from PAMAM b) TEM images of the different self-assemblies in water (adapted from reference 33).*

Similarly, the introduction of charged sites within a dendritic polymer modifies its amphiphilic character and results in a microphase separation in solution that leads to the formation of several self-assembled nanostructures as spherical or cylindrical micelles, vesicles, nanotubes, etc. (**Figure 2.8**)[33,34,35]

2.2 Objectives

In this chapter, we plan to examine for the first time the use of ionic non-covalent interactions to functionalize a pillar[5]arene macrocycle. This approach could result in a new family of ionic pillar[5]arene derivatives with unprecedented functional properties. In particular, we propose the synthesis of ionic complexes between the terminal amino groups of a pillar[5]arene and several carboxylic acids. The acids selected for this study comprise two aliphatic acids, two benzoic acids substituted at the 4-position and two at the 3,4,5-positions with alkyl chains with and without terminal coumarins. These changes in the chemical structure of the acids will allow us to analyze the influence of the chemical structure in future applications. The introduction of coumarin units into the chemical structure of ionic complexes is expected to exhibit light-sensitive properties due to their ability to undergo photoinduced [2+2] cycloaddition.

In the pure state, the ionic complexes are expected to self-organize into LC phases with good proton-conductive properties; the ionic segregated areas (formed by the positively and negatively charged groups) are the continuous ionic pathways necessary for proton transport. Additionally, in the case of the complexes bearing coumarin units the LC phases will be crosslinked to lock the LC arrangement and consequently fabricate mechanical stable proton-conductive materials. Besides, the formation of ionic pairs should lead to a hierarchical self-assembly process in solution, in which the charged sites promote additional self-assembly that ultimately could result in the formation of a wide variety of nanostructured materials in aqueous medium. Moreover, in this case the introduction of the coumarin units could allow to obtain photo-responsive nanocarriers that could be used to induce light-release of guest molecules.

Considering these hypotheses, we propose the synthesis and characterization of a new family of ionic complexes based on pillar[5]arenes as main objective. To achieve the abovementioned considerations, we set the following secondary objectives:

1. Synthesis and characterization of a pillar[5]arene that contains terminal amino groups in the side chains.
2. Synthesis and characterization of five aliphatic and benzoic acids with and without coumarin terminal moieties that will be used as counterions in the formation of ionic complexes.
3. Preparation and characterization (structural and thermal) of six ionic complexes formed between the terminal amine-functionalized pillar[5]arene and a commercial undecanoic acid, as well as the five synthesized acids.
4. Study of the proton-conductive properties of the six ionic complexes and the three crosslinked structures obtained with the coumarin derivatives. Investigation of the structure-activity relationship in these materials.
5. Preparation of nanostructured materials in aqueous solution using the co-solvent method.
6. Study of the encapsulation and light-induced release of fluorescent molecules in the photosensitive nanocarriers that contain coumarin units.

2.3 Results and discussion

2.3.1 Synthesis and characterization of ionic pillar[5]arenes

To facilitate the nomenclature of the ionic complexes prepared in this chapter, the compounds have been assigned the acronyms that appear in **Figure 2.9**. The ionic complexes are named by combining the acronyms of the pillar[5]arene and of the acids employed in their synthesis.

The synthetic procedures and the structural characterization of the carboxylic acids (**$AcBzC_{11}$, Acd_1C_{11}, $AcC_{11}Cou$, $AcBzC_{11}Cou$ and $Acd_1C_{11}Cou$**) and pillar[5]arene **P5N10** are described in the experimental part. The acid **AcC_{11}** was employed without any purification from commercial sources. These procedures were carried out following synthetic methods previously described.[36,37,38,39] All ionic compounds were prepared by the same methodology (**Figure 2.9**): a THF solution of the corresponding acid was slowly added to a THF solution of pillar[5]arene **P5N10** in a 10:1 stoichiometry to completely functionalize all the amine groups of **P5N10**. The mixture was ultrasonicated for 5 min, then THF was slowly evaporated at room temperature, and the sample was dried under vacuum at 40°C until the weight remained stable. Formation of the complexes between **P5N10** and the different acids was confirmed by infrared spectroscopy (FT-IR) and nuclear magnetic resonance (NMR).

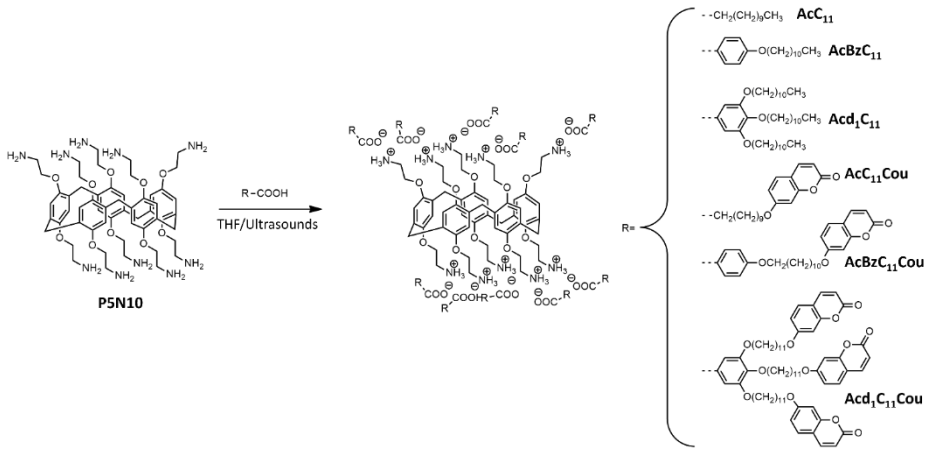

Figure 2.9. *Scheme of the preparation of the six ionic complexes studied.*

As an example, the FT-IR spectra of **Acd$_1$C$_{11}$Cou, Acd$_1$C$_{11}$Cou-P5N10** and **P5N10** are shown in **Figure 2.10** (all FT-IR spectra are collected in section **2.6.2 Appendix**). In the C=O region, **Acd$_1$C$_{11}$Cou** showed two stretching bands at 1733 and 1676 cm^{-1} that correspond to the ester groups of the coumarin moieties and to the dimeric form of the carboxylic acid, respectively. However, in the FT-IR spectrum of **Acd$_1$C$_{11}$Cou-P5N10**, the dimeric band of the acid was replaced by two bands at 1555 and 1369 cm^{-1} due to asymmetric and symmetric stretching vibrations of the newly formed carboxylate groups, thereby indicating the formation of the ionic complex.

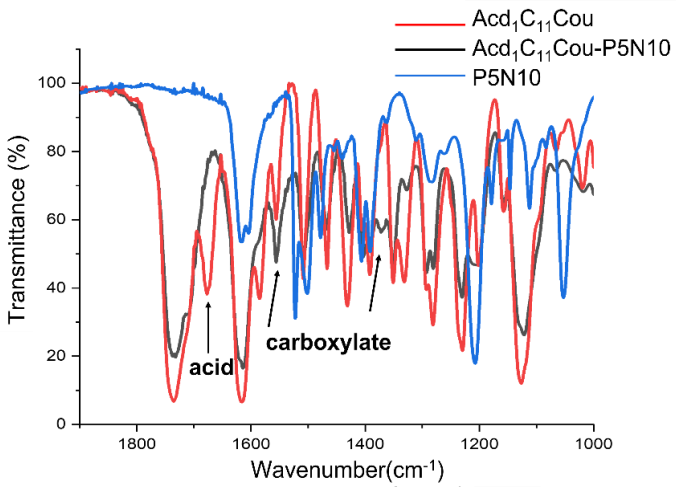

Figure 2.10. *FT-IR spectra (C=O st. region).*

The NMR spectra of the ionic complexes also confirmed the formation of the ionic salts (see section **2.6.1 Appendix**). As an example, **Figure 2.11** displays the ^{1}H-NMR spectra of **AcBzC$_{11}$Cou**, **P5N10** and **AcBzC$_{11}$Cou-P5N10**, in which the broad signal at 12.53 ppm of the carboxylic acid proton of **AcBzC$_{11}$Cou** disappeared in the spectrum of the ionic complex **AcBzC$_{11}$Cou-P5N10**. Moreover, the protons H_a and H_b of the methylene groups of **P5N10** shifted from 3.81/2.91 to 3.91/3.30 ppm, respectively.

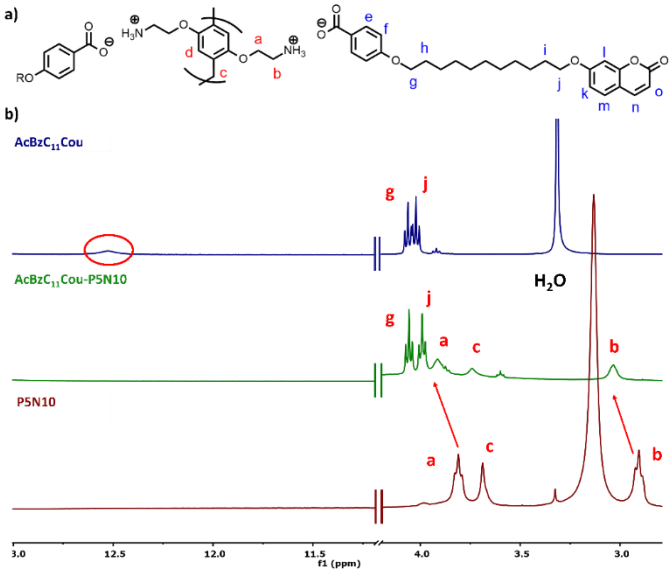

*Figure 2.11. a) Schematic representation of **AcBzC$_{11}$Cou-P5N10,** b) Comparative ^{1}H-NMR (DMSO-d$_6$, 298K, 400 MHz) spectra of **AcBzC$_{11}$Cou-P5N10, AcBzC$_{11}$Cou** and **P5N10.***

The ^{13}C-NMR spectra also confirmed the ionic salt formation. For instance, the carboxylic carbon signal shifted from 167.00 to 167.94 ppm due to the formation of the carboxylate **(Figure 2.12)**. The aromatic carbon "*C$_e$*" next to the carboxyl group shifted from 131.33 to 131.13 ppm, also evidencing the ionic complex formation (**Figure 2.12**).

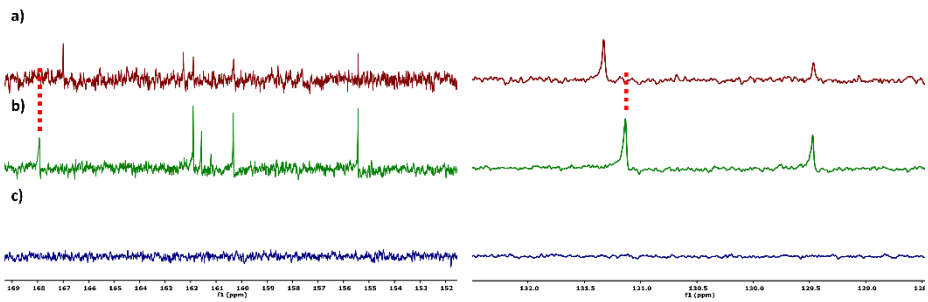

*Figure 2.12. ^{13}C-NMR (DMSO-d$_6$, 298K, 100 MHz) comparison (selected regions of the spectra) of a) **AcBzC$_{11}$Cou**, b) **AcBzC$_{11}$Cou-P5N10** and c) **P5N10.***

^{1}H-^{1}H NOESY experiments (**Figure 2.13**) were recorded to fully confirm the formation of the ionic salts. NOESY experiments are widely used in supramolecular chemistry as they provide information about the spatial relationships (distance) in the molecules.[40] In this case, meaningful correlations were observed

between the signal H_b of **P5N10** and the signal H_g of **AcBzC$_{11}$Cou**, thereby indicating their proximity in the space because of the ionic bond formation.

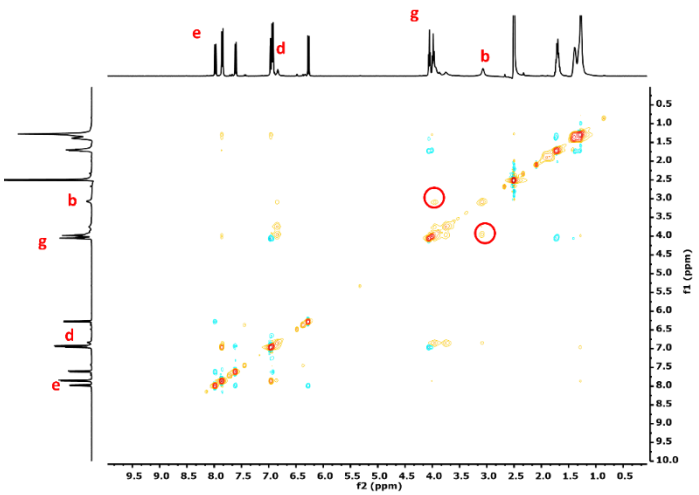

Figure 2.13. ^{1}H-^{1}H NOESY (DMSO-d_6, 298K) spectrum of **AcBzC$_{11}$Cou-P5N10.**

2.3.2 Liquid crystalline properties

Thermal stability is required for melt processing and was studied by thermogravimetric analysis (TGA). All ionic complexes showed good thermal stability with 2% weight loss temperatures ($T_{2\%}$) above the isotropization temperatures (**Table 2.1**).

The thermal and liquid crystal properties were studied by polarized-light optical microscopy (POM), differential scanning calorimetry (DSC), and X-ray diffraction (XRD), and the results are summarized in **Table 2.1**. The ionic complexes **AcC$_{11}$-P5N10** and **AcC$_{11}$Cou-P5N10,** that contain acids in which the carboxyl group is bonded to an aliphatic chain, are crystalline materials that melt to give an isotropic liquid phase. On the other hand, the introduction of benzoic acids into **P5N10** via ionic interactions yielded ionic complexes that showed stable enantiotropic liquid crystal phases over a wide temperature range (**Figure 2.14a**). Ionic complexes containing acids with coumarin units (i.e., **AcBzC$_{11}$Cou-P5N10** and **Acd$_1$C$_{11}$Cou-P5N10**) exhibited lower isotropization temperatures than those of ionic complexes containing acids with undecyl alkyl

chains without terminal coumarin moieties which is traduced in an entropy increase (i.e., **AcBzC$_{11}$-P5N10** and **Acd$_1$C$_{11}$-P5N10**). While highly birefringent textures were observed by POM for **AcBzC$_{11}$-P5N10** and **Acd$_1$C$_{11}$-P5N10**, **AcBzC$_{11}$Cou-P5N10** and **Acd$_1$C$_{11}$Cou-P5N10** showed spontaneous tendency to homeotropic alignment and the mesophase was properly observed via POM on applying mechanical stress to the samples (**Figure 2.14b**). This spontaneous homeotropic alignment is induced by the terminal coumarin units, which are known to produce such phenomenon in other liquid crystals containing coumarins.[38]

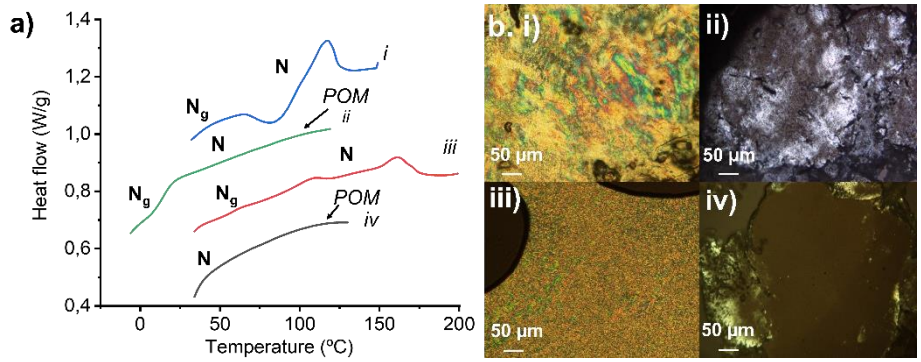

Figure 2.14. *a) DSC curves in the second heating of i)* ***AcBzC$_{11}$Cou-P5N10*** *ii)* ***Acd$_1$C$_{11}$Cou-P5N10****, iii)* ***AcBzC$_{11}$-P5N10*** *and iv)* ***Acd$_1$C$_{11}$-P5N10*** *b) POM textures at room temperature in the cooling process of i)* ***AcBzC$_{11}$Cou-P5N10****, ii)* ***Acd$_1$C$_{11}$Cou-P5N10****, iii)* ***AcBzC$_{11}$-P5N10*** *and iv)* ***Acd$_1$C$_{11}$-P5N10****.*

Table 2.1. *Thermal properties of ionic compounds.*

Compound	$T_{2\%}$ (°C)[a]	Thermal Transitions[b]
AcC$_{11}$-P5N10	166	*Cr* 142 *I*
AcBzC$_{11}$-P5N10	200	N_g 108 *N* 161 *I*
Acd$_1$C$_{11}$-P5N10	224	*N* 120[c] *I*
AcC$_{11}$Cou-P5N10	135	*Cr* 97 *I*
AcBzC$_{11}$Cou-P5N10	135	N_g 44 *N* 116 *I*

Acd$_1$C$_{11}$Cou-P5N10	226	N_g 25 *N* 69 *I*

[a] Temperature at which 2% of mass loss is detected in the TGA curve.
[b] DSC data of the 2nd heating scan at a rate of 10°C/min. Ng: glassy nematic phase, N: nematic phase, Cr: crystal, I: isotropic liquid.
[c] POM data.

The assignment of the mesophase was achieved by XRD (**Figure 2.15**). The XRD patterns showed diffuse scattering in the low-angle region, whereas a broad diffuse scattering maximum was observed in the high-angle region that is related to the lateral interactions of the hydrocarbon chains. The absence of Bragg reflections and the presence of only diffuse scattering indicate that there is no periodical order, and thus such XRD patterns are consistent with nematic mesophases that have only orientational order. An increase in the number of alkyl substituents in the molecule (from 10 to 30) reduces the transition temperatures (i.e., both T_g and $T_{N\text{-}I}$; compare **AcBzC$_{11}$-P5N10** to **Acd$_1$C$_{11}$-P5N10**, and **AcBzC$_{11}$Cou-P5N10** to **Acd$_1$C$_{11}$Cou-P5N10**), but does not significantly alter the degree of order of the nematic mesophase.

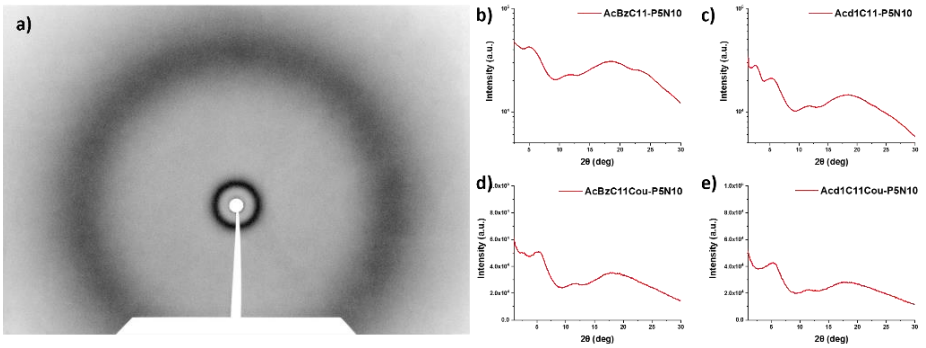

Figure 2.15. *a) 2D XRD of* ***AcBzC$_{11}$Cou-P5N10*** *and* ***b-e****) 1D XRD patterns of the ionic compounds.*

2.3.3 Proton conduction properties

Ionic liquid crystals are promising materials for ion conduction. The presence of ten charged groups in our ionic LC pillar[5]arenes make them ideal materials for proton transport. To measure the proton conduction properties, we used electrochemical impedance

spectroscopy (EIS) in samples that consisted of thin films sandwiched between two ITO-coated electrodes using silicon spacers of 25 µm. In this technique a voltage is applied to the cell and the sinusoidal response is measured in a range of frequencies. The typical response to this stimulus is called Nyquist plot and after some mathematical transformation we can obtain the conductivity value at that temperature. Thin films of the samples were prepared by pressing the ionic material between two ITO-coated electrodes above the isotropization temperature. Then, the cell was slowly cooled down to room temperature to obtain samples with a uniform homeotropic alignment over large areas. This alignment process is quite relevant since in anisotropic materials, such as LCs, the measured proton conductivity depends on the macroscopic degree of order and the orientation of the LC phase with respect to the electrodes (**Figure 2.16**).

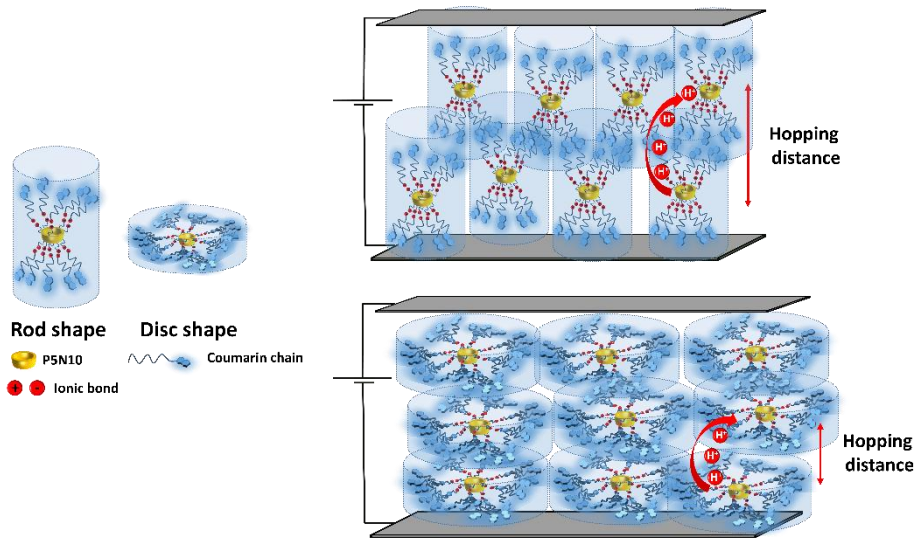

Figure 2.16. *Schematic representation of rod and disc shaped molecules containing coumarins aligned between the ITO-coated electrodes.*

Examples of EIS data (in the form of Nyquist plots) are given in section **2.6.5 Appendix**, **Figure 2.39**. **Acd$_1$C$_{11}$Cou-P5N10** and **Acd$_1$C$_{11}$-P5N10** show a slightly depressed arc corresponding to the electrical response of the compound (conductivity and electrical permittivity), without relevant polarization contribution at the electron conducting electrodes at low frequencies. This is a strong

hint that these compounds show electronic conduction, which dominates their electrical response. For the other compounds, **AcC$_{11}$-P5N10**, **AcBzC$_{11}$-P5N10**, **AcC$_{11}$Cou-P5N10** and **AcBzC$_{11}$Cou-P5N10**, the Nyquist plots show a spike towards low frequencies, that is at the high values of Z_{real}, with fast increase in the absolute value of Z_{im}. This corresponds to polarization of the electrodes, typical of ion blocking electron conducting electrodes (such as ITO) on a mainly ionic conducting material. The dominant charge conduction carriers in those samples would be ions. Since diffusible ions other than protons are not present in the ionic LC pillar[5]arenes, the observed EIS responses were related to proton conduction, which was calculated from the EIS responses and the cell constant. The conductivity was calculated from the value of Z_{real} at the minimum between the spike and the depressed semicircle or from the Z_{real} at low frequencies, as corresponds to each material, and the cell constant. The conductivity of these materials as a function of the temperature is shown in **Figure 2.17a**. At low temperatures **Acd$_1$C$_{11}$Cou-P5N10** and **Acd$_1$C$_{11}$-P5N10** showed the highest conductivity values, very slightly dependent on temperature and apparently dominated by electronic carriers. In contrast, **AcC$_{11}$Cou-P5N10** and **AcC$_{11}$-P5N10** showed comparable conductivity values to **Acd$_1$C$_{11}$Cou-P5N10** and **Acd$_1$C$_{11}$-P5N10** at high temperatures, probably because their crystalline structure favors higher order in these compounds than in nematic mesophases. **AcC$_{11}$-P5N10** and **AcBzC$_{11}$-P5N10** and their counterparts with coumarin moieties show temperature-dependent ionic conductivity that can be ascribed to proton conductivity, with relatively large activation energies from 0.8 eV to 1.4 eV in the measured temperature range. The proton conductivity is higher for **AcC$_{11}$-P5N10** than for **AcBzC$_{11}$-P5N10** and is smaller in the compounds with coumarin units with respect to the compounds without them. Conformational differences in the LC mesophases must be behind the differences in conductivity and activation energies. Smaller molecules such as **AcC$_{11}$-P5N10**

with crystalline order would favor proton diffusion through shorter effective hopping distances.

The conformational arrangement of the mesophases is expected to contribute strongly to the conductivity. The mobile protons are located at the COO^-/NH_3^+ ionic bonds, around the pillar[5]ene macrocycle. Rod-shaped ionic pillar[5]arenes (i.e., **AcC$_{11}$Cou-P5N10** and **AcC$_{11}$-P5N10**), which possess a crystal-ordered phase, show the highest ionic conductivity in the series. **AcBzC$_{11}$Cou-P5N10** and **AcBzC$_{11}$-P5N10**, in which each benzoic ring has one substituent (10 alkyl chains per pillar[5]arene macrocycle) also show an elongated shape (rod shape), with a nematic phase, less ordered than a crystalline one. Their proton conductivity is lower than the ones without the benzoic ring. In **Acd$_1$C$_{11}$Cou-P5N10** and **Acd$_1$C$_{11}$-P5N10**, the presence of three substituents in each benzoic ring produces a total of 30 alkyl chains per pillar[5]arene macrocycle, probably resulting in a flatter conformation (disc shape) (**Figure 2.16**). Such an ordering should make the proton hopping easier as long as the distance between molecules (and the ionic bond regions) are kept short. The presence of 30 alkyl chains per pillar[5]arene macrocycle might however be increasing the hopping distance. Nevertheless, as the measured conductivity in these materials is dominated by the electronic carriers, a change in the electronic charge distribution must have been produced.

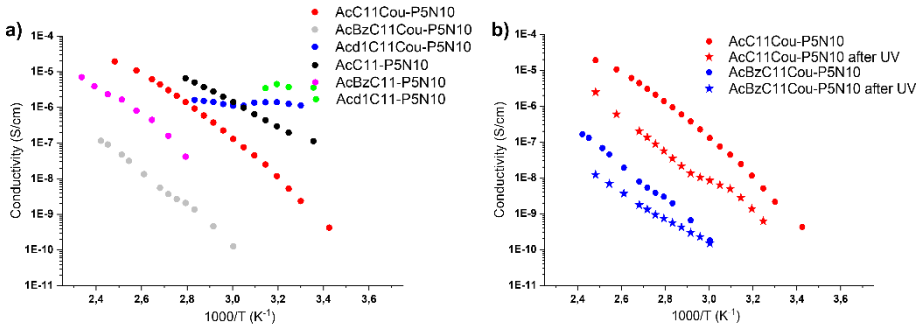

Figure 2.17. *a) Conductivity variation with temperature, measured by EIS, of a) all ionic compounds b)* ***AcC$_{11}$Cou-P5N10*** *and* ***AcBzC$_{11}$Cou-P5N10*** *before and after irradiation with 325 nm light.*

Coumarin compounds undergo a well-known photoinduced [2+2] cycloaddition (so-called photodimerization) to form stable cyclobutene dimers when they are exposed to light of the appropriate wavelength (λ> 300 nm) (**Figure 2.19a**). This photodimerization was previously exploited as a crosslinking reaction to fabricate mechanical stable membrane materials with a locked LC organization[41] (**Figure 2.18**).

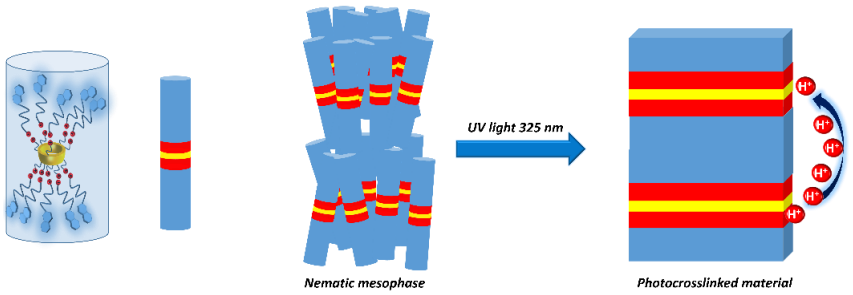

Figure 2.18. *Schematic representation of the nematic mesophase fixation and proton mobility in the crosslinked material.*

As a representative example, in **Figure 2.19b**, the effect of crosslinking of **Acd$_1$C$_{11}$Cou-P5N10** in film of 25 µm on its UV spectrum is shown. Upon irradiation with 325 nm light, the intensity of the π–π* band of coumarin showed a remarkable decrease, and this is consistent with photodimerization of coumarin units that produces a crosslinked polymer network that retains the morphology of the LC phase. It is apparent that after crosslinking the conductivity values decreased approximately one order of magnitude due to a decrease in the mobility of the ion-transporting moieties (**Figure 2.17b**). Such ion conductivity decrease is similar to those observed in previously reported polymerizable LCs.[42] Nonetheless, a more dramatic reduction in proton conductivity was observed in **Acd$_1$C$_{11}$Cou-P5N10**, for which no EIS response was observed, suggesting a lack of ion transport in photocrosslinked **Acd$_1$C$_{11}$Cou-P5N10**. This fact can be explained by a total lack of mobility of the ion-transporting moieties (ionic pairs) due to the large number of peripheral photocrosslinkable units (coumarins).

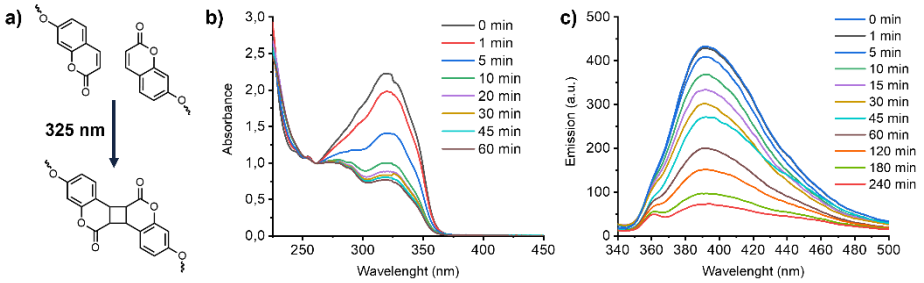

***Figure 2.19**. a) Photodimerization reaction of coumarins followed by UV absorption in film (b) and fluorescence in aqueous nanoassemblies (c) in compound **Acd$_1$C$_{11}$Cou-P5N10**.*

2.3.4 Self-assembly in aqueous solution

Amphiphilic molecules self-assemble in water to yield a variety of well-defined nano-assemblies, such as spherical and tubular micelles or vesicles.[43,44] Formation of these self-assemblies is driven by hydrophobic-hydrophilic interactions, through which the hydrophobic parts of the molecule locate inside the nano-assembly to minimize their interaction with water, while the hydrophilic segments locate in contact with water to stabilize the nano-assembly. Pillar[n]arene derivatives were previously employed to prepare nanoparticles in aqueous solution, wherein the amphiphilic character was obtained by host-guest interactions between an ionic pillar[n]arene and a guest molecule.[45,46,47] In our case, the introduction of charged sites in the pillar[5]arene scaffold via ionic functionalization with carboxylic acids has already modified the amphiphilic character of these macrocycles, which leads to pillar[5]arene-containing materials with intrinsic amphiphilicity, simplifying the preparation of the nano-assemblies. The self-assemblies were prepared by the co-solvent method. Briefly, water was slowly added over a THF solution of the ionic compound (2 mg/mL) while monitoring the turbidity of the solution. An increase in turbidity indicated that self-assembly process had started. When turbidity kept a stable value, the sample was dialyzed against water to remove the THF, obtaining stable aqueous solutions of self-assemblies (for more details, see **Experimental part, section 2.5.3**).

The morphology of the self-assemblies was studied by transmission electron microscopy (TEM) (**Figure 2.20**). For these studies 10 µL of the

solution were deposited over copper grids coated by graphite and they were dyed with uranyl acetate to obtain a better contrast. **AcC$_{11}$-P5N10** generated solid nanospheres of around 200 nm (**Figure 2.20a**). The introduction of terminal coumarin units in complex **AcC$_{11}$Cou-P5N10** produced a significant variation of the size of the nanospheres, whereas the formation of vesicles was also detected (**Figure 2.20b**). On the other hand, the ionic complexes derived from benzoic acids produced two clear different morphologies. **AcBzC$_{11}$-P5N10** showed solid ring-shaped structures with a thickness of around 90-120 nm (**Figure 2.20c**), whereas **AcC$_{11}$BzCou-P5N10** produced large tubular nanoaggregates (more than 1 µm in length) incorporating some small vesicles in the walls of the nanotubes (**Figure 2.20d**). In the case of gallic acid derivatives, **Acd$_1$C$_{11}$-P5N10** self-assembled in solid coral-type structures (**Figure 2.20e**), whereas **Acd$_1$C$_{11}$Cou-P5N10** that incorporates terminal coumarin moieties exclusively formed large vesicles (> 500 nm) (**Figure 2.20f**).

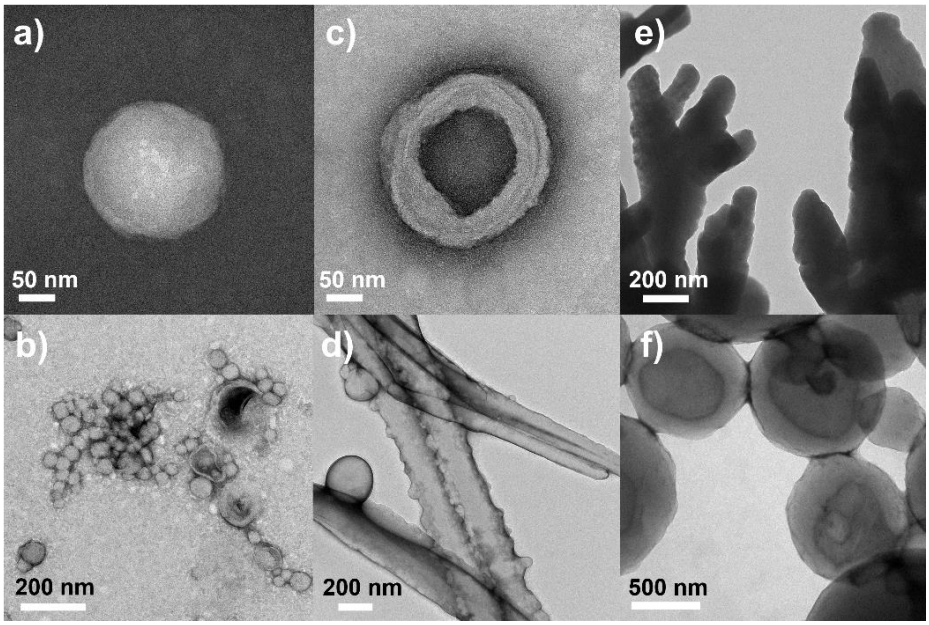

Figure 2.20. *TEM micrographs of a) nanospheres obtained from* ***AcC$_{11}$-P5N10****, b) vesicles from* ***AcC$_{11}$Cou-P5N10*** *c) ring-shaped structures from* ***AcBzC$_{11}$-P5N10*** *d) tubular structures from* ***AcBzC$_{11}$Cou-P5N10*** *e) coral shaped structures from* ***Acd$_1$C$_{11}$-P5N10*** *and f) vesicles from* ***Acd$_1$C$_{11}$Cou-P5N10****.*

As can be deduced from the TEM studies, ionic complexes that incorporate terminal alkyl chains (**AcC$_{11}$-P5N10**, **AcBzC$_{11}$-P5N10**, and **Acd$_1$C$_{11}$-P5N10**) tend to self-assemble into solid nanostructures, whereas the formation of hollow nanostructures (e.g., vesicles or nanotubes) seems to be unfavorable. However, ionic complexes containing terminal coumarin units (**AcC$_{11}$Cou-P5N10, AcBzC$_{11}$Cou-P5N10,** and **Acd$_1$C$_{11}$Cou-P5N10**) led to the formation of bilayer-based nano-assemblies, such as vesicles or nanotubes. The presence of terminal coumarin groups may increase the lateral π-π intermolecular interactions, favoring the formation of stable bilayers that curve to generate vesicles (**AcC$_{11}$Cou-P5N10** and **Acd$_1$C$_{11}$Cou-P5N10**), or that bend to form tubular structures (**AcBzC$_{11}$Cou-P5N10**).

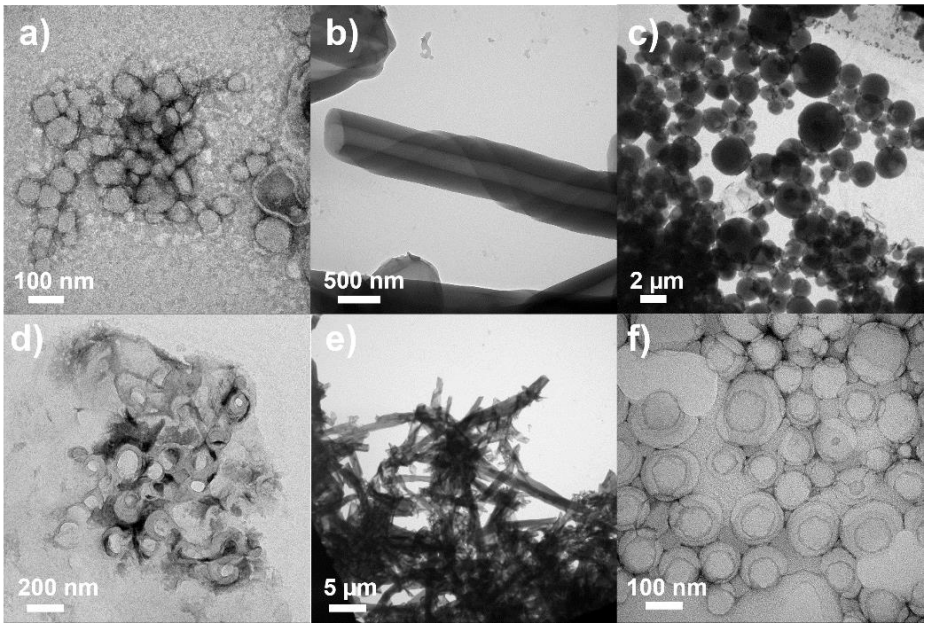

Figure 2.21. *TEM micrographs of the nanostructures before (top) and after (bottom) photodimerization: a) d)* ***AcC$_{11}$Cou-P5N10****, b) e)* ***AcBzC$_{11}$Cou-P5N10*** *and c) f)* ***Acd$_1$C$_{11}$Cou-P5N10****.*

Additionally, the coumarin photodimerization process may provide both types of light-responsive nanocarriers with a simple method to produce cross-linked self-assemblies with enhanced robustness and stability.[48,49] Therefore, we irradiated the corresponding aqueous solutions of the self-assemblies with 325 nm light for one hour. The photodimerization process was monitored by measuring the emission

of the solutions. Irradiation with 325 nm light resulted in a gradual decrease in the intensity of the coumarin emission band at ca. 400 nm (**Figure 2.19c**). This photodimerization gave different morphology responses for each nano-assembly based on coumarin-containing ionic complexes (**Figure 2.21**). Both **AcC$_{11}$Cou-P5N10** and **AcBzC$_{11}$Cou-P5N10** collapsed, obtaining broken micelles with a non-defined structure (**Figure 2.21a-d**) or a solid precipitate (**Figure 2.21b-e**), respectively. Nonetheless, **Acd$_1$C$_{11}$Cou-P5N10** yielded stable vesicles after light irradiation, but a significant size reduction was observed in comparison to the vesicles obtained before irradiation (**Figure 2.21c-f**).

2.3.5 Encapsulation and light-induced release of fluorescence probes

These pillar[5]arene-based nano-assemblies may have potential as drug delivery systems, and thus we studied their ability to encapsulate hydrophobic drugs. In order to test the potential of these self-assemblies as light-responsive nanocarriers, we studied the encapsulation and subsequent release of a fluorescent probe in two ionic complexes containing the photoactive coumarin unit. We selected Nile Red (NR) as a model hydrophobic drug that in a hydrophobic environment presents a fluorescence emission band at 620 nm, but its emission is quenched in hydrophilic environments.[50]

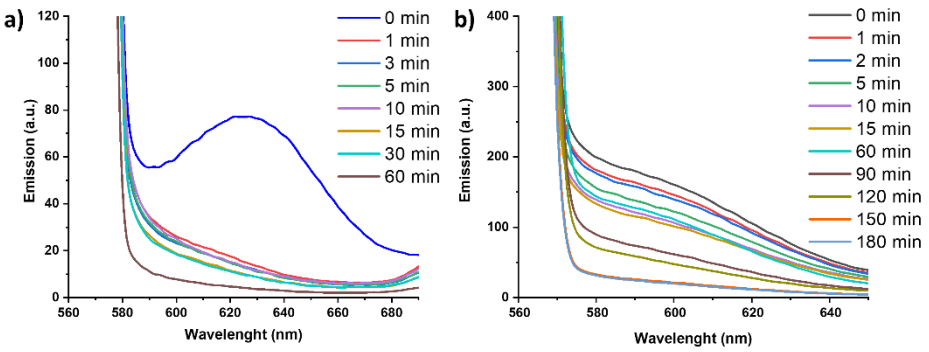

Figure 2.22. *Release of Nile Red upon irradiation in a)* ***AcC$_{11}$Cou-P5N10*** *and b)* ***Acd$_1$C$_{11}$Cou-P5N10****.*

AcC$_{11}$Cou-P5N10 and **Acd$_1$C$_{11}$Cou-P5N10** (2mg/ml) self-assemblies were loaded with NR by stirring overnight the aqueous solutions of the

self-assemblies together with NR ($1.0x10^{-6}$M) (diffusion method). Encapsulation of NR was confirmed by measuring the emission of the NR-loaded self-assemblies, which showed a strong emission band from 560 to 700 nm ($\lambda_{excitation}$ = 550 nm). Such strong NR emission indicates that NR is in a hydrophobic environment since it is encapsulated by the self-assemblies. Upon light irradiation, an abrupt decrease in the initial NR emission was observed in **AcC_{11}Cou-P5N10** due to a migration of NR to a non-hydrophobic environment (**Figure 2.22**). This fact can be explained by a complete release of NR from the self-assemblies to the aqueous media. In contrast, **Acd$_1$C$_{11}$Cou-P5N10** showed a gradual decrease of NR emission, suggesting a more controlled light-induced release of the encapsulated molecules.

2.4 Conclusions

In conclusion, we have developed an easy and reliable method to functionalize pillar[n]arene macrocycles through ionic interactions. This approach leads to new ionic materials with promising properties as ion-conductors or drug delivery systems. In the bulk, the ionic pillar[5]arenes self-organize into liquid crystal phases with good proton conductivity properties. Due to the newly amphiphilic character generated by the ionic moieties, these ionic pillar[5]arenes also self-assemble in water resulting in several nanostructures (e.g., spherical or cylindrical micelles, vesicles, solid nanospheres, or nanotubes) that can encapsulate Nile Red, as a model hydrophobic drug. Additionally, the introduction of coumarin units in the chemical structure of some of our ionic pillar[5]arene leads to nanostructured materials with photo-responsive properties. Specifically, we demonstrate that coumarin photodimerization can be employed to fabricate mechanical stable proton-conductive liquid crystal materials, as well as to obtain photo-responsive nanocarriers with light-induced release of encapsulated molecules.

2.5 Experimental part

2.5.1 Characterization techniques

All reagents were purchased from Aldrich and used without further purification. Anhydrous CH_2Cl_2 and THF were purchased from Scharlab and dried by using a solvent purification system.

^{1}H-NMR and **^{13}C-NMR** spectra were acquired on a Bruker AV400 spectrometer. The experiments were performed at room temperature in different deuterated solvents ($CDCl_3$ CD_2Cl_2 or DMSO-d_6). Chemical shifts are given in ppm relative to TMS and the solvent residual peak was used as the internal standard.

Infrared spectra were recorded on a Bruker Vertex 70 FT-IR spectrometer. The samples were prepared on KBr pellets with a concentration of the product of 1-2% (w/w).

MALDI-TOF mass spectrometry was performed on an Autoflex Bruker mass spectrometer with a dithranol matrix. Positive and negative ion electrospray ionization high resolution (**ESI HRMS**) was performed on a Bruker Q-TOF-MS in a positive or negative ESI mode.

Mesogenic behavior was investigated by **polarized-light optical microscopy** (POM) using an Olympus BH-2 polarizing microscope fitted with a Linkam THMS600 hot stage.

Thermogravimetric analysis (TGA) was performed using a Q5000IR from TA instruments at a heating rate of 10 ºC min^{-1} under a nitrogen atmosphere.

Thermal transitions were determined by **differential scanning calorimetry** (DSC) using a DSC Q2000 from TA instruments with powdered samples (2−5 mg) sealed in aluminum pans. Glass transition temperatures (Tg) were determined at the half height of the baseline

jump, and first order transition temperatures were read at the maximum of the corresponding peak.

UV-Vis absorption spectra were recorded on an ATI-Unicam UV4-200 spectrophotometer. Fluorescence measurements were performed using a Perkin-Elmer LS 50B fluorescence spectrophotometer.

X-ray diffraction measurements were carried out using an XRD-PANanalytical Empyrean diffractometer equipped with platform Scatter X78. Samples were heated until isotropization temperature between two kapton films and then were allowed to cold down until room temperature. Photographic patterns were recorded with a Pinhole camera (Anton Paar) operating with a point-focused Ni-filtered Cu-Kα beam. Samples were contained in Lindemann glass capillaries (0.9 or 0.7 mm diameter) and, when necessary, a variable-temperature attachment was used to heat the sample. The patterns were collected on flat photographic film perpendicular to the X-ray beam.

Electrochemical impedance spectroscopy was recorded with a SI1260 Frequency Response Analyser from Schlumberger Instruments in the frequency range from 1 Hz to 1 MHz, with an AC applied voltage 50 mV amplitude. The sample with ITO coated glass slides and spacers was placed inside a variable temperature hotstage equipped with a temperature controller (Linkam TMS94). The conductivities were studied as a function of temperature between 30°C and isotrope temperature at 5°C intervals. For the preparation of the cells, the appropriate amount of the ionic dendrimer was placed onto an ITO electrode that was sandwiched with another ITO electrode controlling the thickness by using glass spacers (25 µm). The cell was heated up to a few degrees above the melting point of the liquid crystal and the cell was pressed to obtain the thin film. The impedance spectrum was analysed using Nyquist plots, imaginary (Z'') versus real (Z') components, see figures S2.6.17. The resistance (R_b) was estimated from the intersection of the real axis (Z') and the high frequency semicircle of the impedance spectrum. Alternatively, R_b was taken from

the Z' value at the minimum between the high frequency semicircle and low frequency spike. The conductivities σ ($S \cdot cm^{-1}$) were calculated with the formula: $\sigma = d / (R_b \cdot A)$), where d (cm) is the thickness of the film, A (cm^2) is the area of the film and R_b (Ω) is the resistance of the sample. After the preparation of the cell, a random orientation of the mesophase was observed between electrodes. Nematic samples were mechanically sheared within the cell (in order to obtain an alignment of the molecules) at isotropic temperature and then slowly cool down to room temperature (0.05 $^{o}C \cdot min^{-1}$).

Photocrosslinking of coumarin units (photodimerization) was carried out by exposing the aligned LC films of 25 µm of thickness to 325 nm LED light (ThorsLab) for 60 min with a UV power of 8 mW/cm^2.

Transmission Electron Microscopy (TEM) analysis was performed using a FEI Tecnai T20 microscope (FEI Company, Waltham, MA, USA) operating at 200 kV. TEM samples were prepared adding 10 µL of each self-assembly dispersion at an approximately 1.0 mg mL^{-1} concentration on a continuous carbon film-copper grid, and the excess was removed by capillarity using filter paper. Then, the grids were stained with uranyl acetate (1% aqueous solution), removing the excess again by capillarity using filter paper.

2.5.2 Synthetic procedures

2.5.2.1 Synthesis of $AcBzC_{11}$ (2)

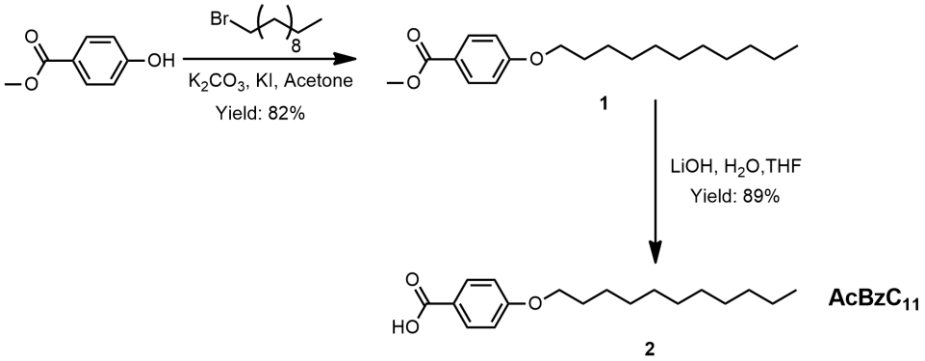

Scheme 2.1. Synthesis of $AcBzC_{11}$.

Synthesis of **methyl 4-(undecyloxy)benzoate (1):** A mixture of 1-bromoundecane (8.71 g, 39.43 mmol), methyl 4-hydroxybenzoate (3.00 g, 19.71 mmol), potassium carbonate (8.15 g, 59.13 mmol) and a spatula tip of potassium iodide were dissolved in acetone (100 ml), stirred and heated under reflux overnight. The salts were filtered off and washed with acetone; then the solvent was evaporated, and the crude product was precipitated in methanol, obtaining 4.74 g. Yield: 82%.

^{1}H-NMR ($CDCl_3$, 298K, 400 MHz, δ, ppm): 7.98 (d, J=12 Hz, 2H), 6.90 (d, J=12 Hz, 2H), 4.00 (t, J=6.56 Hz, 2H), 3.88 (s, 3H), 1.79 (q, J=8 Hz 2H), 1.61 ppm (m, 2H), 1.32 (m, 16H), 0.88 (t, J=7 Hz, 3H).

^{13}C-NMR ($CDCl_3$, 298K, 100 MHz, δ, ppm): 167.07, 163.12, 131.71, 122.48, 114.22, 68.37, 51.96, 32.04, 29.70, 29.51, 29.46, 29.27, 26.13, 22.82, 14.25.

Synthesis of **4-(undecyloxy)benzoic acid (2):** Over a solution of methyl 4-(undecyloxy)benzoate **(1)** (2.00 g, 6.81 mmol) in THF (50 ml) was added a solution of LiOH (0.82 g, 34.08 mmol) in water (20 ml). The mixture was stirred at reflux for 14 hours and after that time the crude was precipitated over HCl/H_2O. The solid obtained was filtered and recrystalized in EtOH, obtaining 1.70 g with an 89% of yield.

^{1}H-NMR ($CDCl_3$, 298K, 400 MHz, δ, ppm): 8.04 (d, J=8.96 Hz, 2H), 6.93 (d, J=8.96 Hz, 2H), 4.00 (t, J=6.56 Hz, 2H), 1.81 (q, J=7.96 Hz 2H), 1.61 ppm (m, 2H), 1.30 (m, 16H), 0.88 (t, J=7 Hz, 3H).

^{13}C-NMR ($CDCl_3$, 298K, 100 MHz, δ, ppm): 172.12, 163.86, 132.49, 121.52, 114.34, 68.44, 32.04, 29.70, 29.50, 29.46, 29.24, 26.13, 14.26.

FT-IR (KBr, ν, cm^{-1}): 3450 (OH), 2916 (=C-H), 2842 (C-H), 1685 (C=O), 1663 (C=O), 1607 (C=C), 1258 (C-O).

MS/ESI$^+$ (CH_2Cl_2,): found 300.38 [M+Na^+] calculated with sodium 300.36 (277.38+22.98).

*2.5.2.2 Synthesis of **Acd_1C_{11}** (4)*

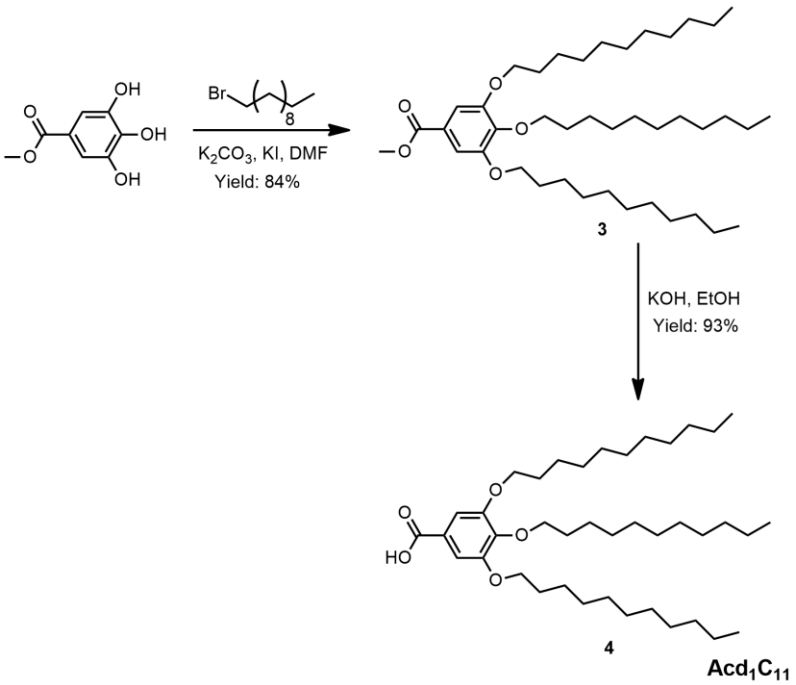

***Scheme 2.2.** Synthesis of **Acd_1C_{11}**.*

Synthesis of **methyl 3,4,5-tris(undecyloxy)benzoate (3):** A mixture of methyl gallate (1.50 g, 8.15 mmol), potassium carbonate (6.10 g, 43.60 mmol) and a spatula tip of potassium iodide were dissolved in DMF (75 ml), stirred and heated to 110°C; then 1-bromoundecane (5.88, 25 mmol) was slowly added. The reaction was stirred at 110°C overnight.

The mixture was cooled down to room temperature, poured into water and extracted with hexane/ethyl acetate (1:1). The organic phases were washed with water, sodium hydroxide 10% (aq.), brine and dried over magnesium sulphate. The solvent was removed under reduced pressure and the crude product was recrystallized in ethanol. Yield: 84%

^{1}H-NMR ($CDCl_3$, 298K, 400 MHz, δ, ppm): 7.25 (s, 2H), 4.01 (m, 6H), 3.89 (s, 3H), 1.76 (m, 6H), 1.50-1.20 (m, 48H), 0.88 (t, J=7 Hz, 9H).

^{13}C-NMR ($CDCl_3$, 298K, 100 MHz, δ, ppm): 167.11, 152.97, 124.80, 108.15, 73.64, 69.33, 52.25, 32.09, 32.07, 30.48, 29.88, 29.82, 29.78, 29.74, 29.72, 29.54, 29.50, 29.46, 26.23, 26.21, 22.84, 14.26.

Synthesis of **3,4,5-tris(undecyloxy)benzoic acid (4):** Over a solution of methyl 3,4,5-tris(undecyloxy)benzoate **(3)** (1.85 g, 2.68 mmol) in ethanol an aqueous solution of potassium hydroxide was added (0.75 g, 2 ml). The reaction was stirred under reflux overnight, and after that the crude product was precipitated over an aqueous solution of HCl pH=2, filtered and recrystallized in ethanol. Yield: 93%

^{1}H-NMR ($CDCl_3$, 298K, 400 MHz, δ, ppm): 7.22 (s, 2H), 3.98 (t, J=6.56 Hz, 2H), 3.94 (t, J=6.36 Hz, 4H), 1.76 (m, 6H), 1.50-1.20 (m, 42H), 0.88 (t, J=7 Hz, 9H).

^{13}C-NMR ($CDCl_3$, 298K, 100 MHz, δ, ppm): 171.71, 152.79, 142.19, 108.26, 73.60, 69.17, 32.10, 30.55, 29.94, 29.92, 29.87, 29.81, 29.70, 29.56, 26.35, 26.27, 22.86, 14.26.

FT-IR (KBr, ν, cm^{-1}): 3230 (OH), 2923 (=C-H), 2862 (C-H), 1736 (C=O), 1685 (C=O), 1617 (C=C), 1236 (C-O).

MS/ESI^{+} (CH_2Cl_2,): found 713.54 [M+K^{+}] calculated with potassium 714.08 (674.99+39.09).

2.5.2.3 Synthesis of ***AcC$_{11}$Cou (6)***

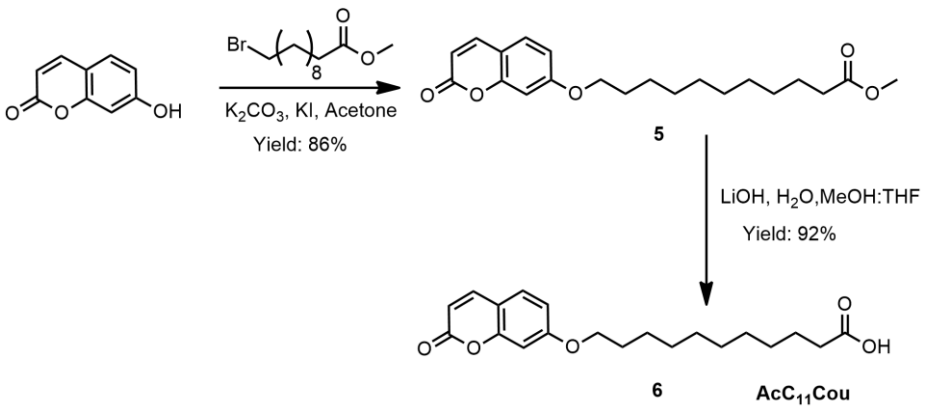

Scheme 2.3. *Synthesis of* ***AcC$_{11}$Cou****.*

Synthesis of **methyl 11-((2-oxo-2H-chromen-7-yl)oxy)undecanoate (5):** A mixture of umbelliferone (1.5 g, 9.25 mmol), methyl 11-bromoundecanoate (2.8 g, 10.15 mmol), potassium carbonate (2.5 g, 18.50 mmol) and a spatula tip of potassium iodide were dissolved in acetone (100 ml), stirred and heated under reflux overnight. The salts were filtered off and washed with acetone; then the solvent was evaporated and the crude product was purified by flash column chromatography on silica gel using hexane 8:2 ethyl acetate. Yield: 86%.

^{1}H-NMR ($CDCl_3$, 298K, 400 MHz, δ, ppm): 7.63 (d, J=9.44 Hz, 1H), 7.35 (d, J=8.6 Hz, 1H), 6.81 (m, 2H), 6.23 (d, J=9.44 Hz, 1H), 4.00 (t, J=6.52 Hz, 2H), 3.66 (s, 3H), 2.30(t, J=7.60 Hz, 2H), 1.80 (m, 2H), 1.61 ppm (m, 2H), 1.34 (m, 12H).

^{13}C-NMR ($CDCl_3$, 298K, 100 MHz, δ, ppm): 174.45, 162.59, 161.42, 156.09, 143.57, 128.82, 113.14, 113.07, 112.51, 101.48, 68.80, 51.58, 34.24, 29.58, 29.47, 29.43, 29.35, 29.26, 29.11, 26.08, 25.08.

Synthesis of **11-((2-oxo-2H-chromen-7-yl)oxy)undecanoic acid (6):** An aqueous solution of litium hydroxide (1.25 g, 50 mL) was added to a solution of compound **5** (2.00 g, 5.78 mmol) in THF-methanol 1:1 (100 mL). The mixture was stirred at reflux overnight and then the reaction was neutralized with HCl until acid pH. The white

precipitate was filtered off and purified by recrystallization in ethanol. Yield 92%.

^{1}H-NMR (DMSO-d_6, 298K, 400 MHz, δ, ppm): 11.96 (s, 1H), 7.98 (d, J=9.44 Hz, 1H), 7.61 (d, J=8.6 Hz, 1H), 6.94 (m, 2H), 6.27 (d, J=9.44 Hz, 1H), 4.06 (t, J=6.52 Hz, 2H), 2.18 (t, J=7.36Hz, 2H), 1.72 (m, 2H), 1.44 ppm (m, 4H), 1.25 (m, 10H).

^{13}C-NMR (DMSO-d_6, 298K, 100 MHz, δ, ppm): 174.46, 161.89, 160.29, 155.38, 149.42, 144.32, 129.45, 112.70, 112.35, 112.21, 101.11, 68.27, 33.64, 28.89, 28.81, 28.69, 28.66, 28.52, 28.40, 25.38, 24.47.

FT-IR (KBr, ν, cm^{-1}): 3406 (OH), 2920 (=C-H), 2846 (C-H), 1714 (C=O), 1666 (C=O), 1602 (C=C), 1292 (C-O).

MS/ESI^{+} (CH_2Cl_2,): found 369.16 [M+Na^{+}] calculated with sodium 369.40 (346.42+22.98).

*2.5.2.4 Synthesis of **AcBzC$_{11}$Cou (9)***

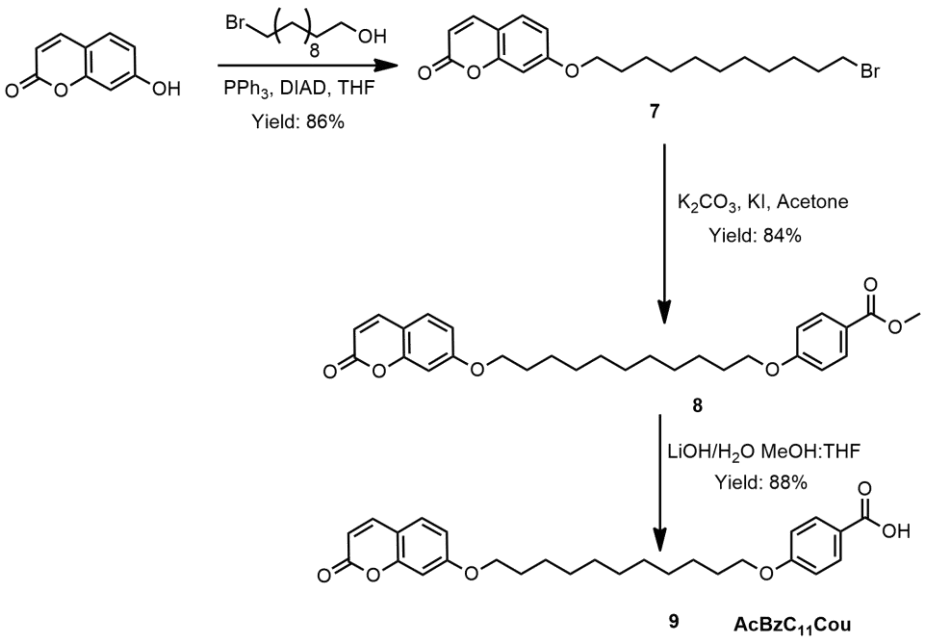

***Scheme 2.4.** Synthesis of **AcBzC$_{11}$Cou**.*

Synthesis of **7-(11-bromoundecyloxy)-2H-chromen-2-one (7):** Umbelliferone (8.00 g, 49.34 mmol), 11-bromoundecan-1-ol (12.39 g, 49.34 mmol) and triphenylphosphine (12.94 g, 49.34 mmol) were dissolved in anhydrous THF (450 ml). The reaction flask was cooled in an ice bath and flushed with argon, and then DIAD (9.98 g, 49.34 mmol) was added dropwise. The mixture was stirred at room temperature overnight under an argon atmosphere. The white precipitate was filtered off. The solvent was evaporated and the crude product was recrystallized in ethanol. Yield 86%.

^{1}H-NMR ($CDCl_3$, 298K, 400 MHz, δ, ppm): 7.63 (d, J=9.45 Hz, 1H), 7.36 (d, J=8.49Hz, 2H), 6.82 (m, 2H), 6.24 (d, J=9.48Hz, 1H), 4.00 (t, J=6.54 Hz, 2H), 3.40 (t, J=6.84Hz, 2H), 1.80 (m, 4H), 1.47 ppm (m, 4H), 1.29 (m, 10H).

^{13}C-NMR ($CDCl_3$, 298K, 100 MHz, δ, ppm): 162.55, 161.40, 156.06, 143.57, 128.82, 113.11, 113.04, 112.49, 101.44, 68.77, 34.19, 32.94, 29.59, 29.55, 29.42, 29.08, 28.87, 28.28, 26.06.

Synthesis of **methyl 4-(11-((2-oxo-2H-chromen-7-yl)oxy)undecyloxy)benzoate (8):** A mixture of methyl-4-hydroxybenzoate (0.46 g, 3.04 mmol), potassium carbonate (0.85 g, 6.15 mmol) and a spatula tip of KI were dissolved in acetone (50 ml) and heated at reflux. After one hour compound **7** (1.20 g, 3.04 mmol) was added to the solution and stirred at reflux overnight; then the reaction was allowed to cool down and the solids were filtered off and washed with acetone. The crude was evaporated and purified by flash column chromatography using DCM 6:4 hexane as eluent. Yield: 84%.

^{1}H-NMR ($CDCl_3$, 298K, 400 MHz, δ, ppm): 7.97 (d, J=8.94 Hz, 2H), 7.62 (d, J=9.48 Hz, 1H), 7.35 (d, J=8.43Hz, 2H), 6.89 (d, J=8.94 Hz, 2H), 6.82 (m, 2H), 6.24 (d, J=9.48Hz, 1H), 4.00 (td, J=6.48, 1.5 Hz, 4H), 3.88 (s, 3H), 1.80 (m, 4H), 1.46 ppm (m, 4H), 1.32 (m, 10H).

^{13}C-NMR ($CDCl_3$, 298K, 100 MHz, δ, ppm): 168.69, 167.06, 163.09, 162.58, 161.43, 143.58, 131.71, 128.83, 122.48, 114.20, 113.15, 113.08,

112.51, 101.47, 68.80, 68.33, 51.98, 29.65, 29.62, 29.48, 29.46, 29.26, 29.11, 26.13, 26.09.

Synthesis of **4-((11-((2-oxo-2H-chromen-7-yl)oxy)undecyl)oxy)benzoic acid(9):**

An aqueous solution of litium hydroxide (0.35 g, 20 mL) was added to a solution of compound **8** (0.60 g, 1.28 mmol) in THF-methanol 1:1 (20 mL). The mixture was stirred at reflux overnight and then the reaction was neutralized with HCl until acid pH. The white precipitate was filtered off and purified by recrystallization in ethanol. Yield 88%.

^{1}H-NMR ($CDCl_3$, 298K, 400 MHz, δ, ppm): 8.04 (d, J=8.82 Hz, 2H), 7.63 (d, J=9.48 Hz, 1H), 7.36 (d, J=8.49Hz, 2H), 6.93 (d, J=8.82 Hz, 2H), 6.82 (m, 2H), 6.24 (d, J=9.48Hz, 1H), 4.00 (m, 4H), 1.80 (m, 4H), 1.47 ppm (m, 4H), 1.33 (m, 10H).

^{13}C-NMR (DMSO-d_6, 298K, 100 MHz, δ, ppm): 167.00, 162.28, 161.89, 160.31, 155.43, 144.34, 131.32, 129.46, 122.77, 114.19, 112.71, 112.36, 112.22, 101.11, 68.27, 67.74, 28.94, 28.89, 28.72, 28.69, 28.51, 28.41, 25.42, 25.40.

FT-IR (KBr, v, cm^{-1}): 3415 (OH), 2923 (=C-H), 2853 (C-H), 1732 (C=O), 1712 (C=O), 1678 (C=O), 1604 (C=C), 1242 (C-O).

MS/ESI$^+$ (CH_2Cl_2,): found 475.20 [M+Na^+] calculated with sodium 475.51 (452.53+22.98).

2.5.2.5 Synthesis of ***Acd$_1$C$_{11}$Cou (11)***

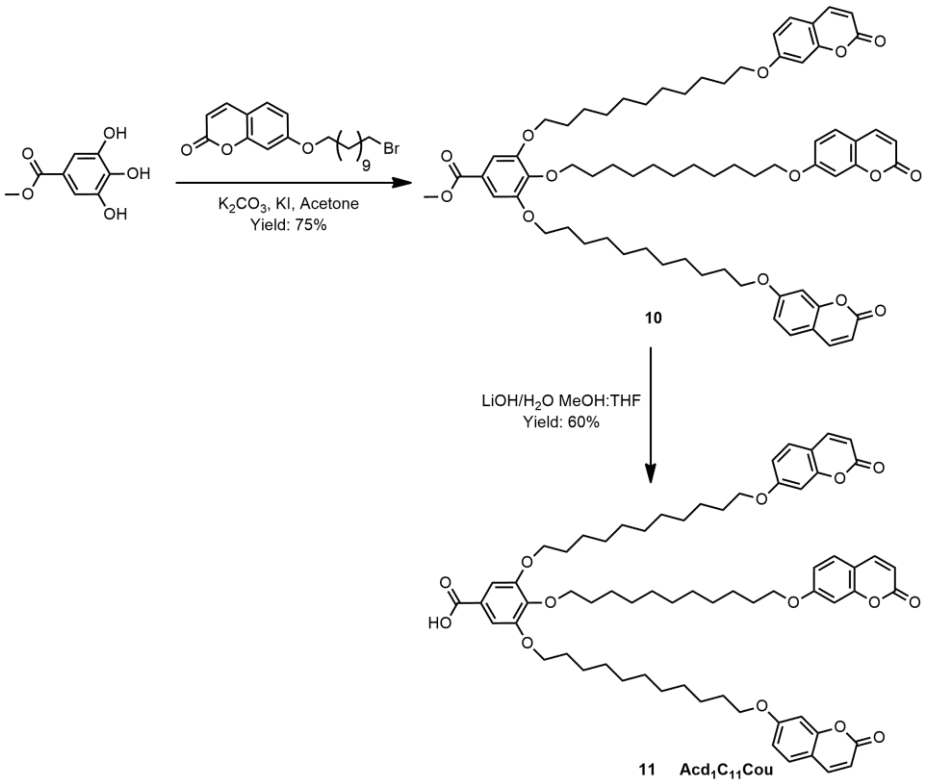

Scheme 2.5. *Synthesis of* ***Acd$_1$C$_{11}$Cou****.*

Synthesis of **methyl 3,4,5-bis(11-((2-oxo-2H-chromen-7-yl)oxy)undecyloxy)benzoate (10):** A mixture of compound **7** (8.00 g, 20.30 mmol), methyl gallate (1.13 g, 6.15 mmol), potassium carbonate (8.50 g, 61.5mmol), a spatula tip of potassium iodide and acetone (200 mL) was stirred and heated under reflux overnight. The reaction mixture was allowed to cool down to RT and the solids were filtered off and washed with acetone. The solvent was evaporated and the crude product was purified by flash column chromatography on silica gel using DCM as eluent and gradually changing the composition of the eluent to DCM/ethyl acetate (8:2). Yield: 75%.

^{1}H-NMR ($CDCl_3$, 298K, 400 MHz, δ, ppm): 7.65 (d, J=9.6Hz, 3H), 7.37 (d, J=9.4Hz, 3H), 7.28 (s, 2H), 6.81 (m, 6H), 6.26 (d, J=9.6Hz, 3H), 4.01 (m, 12H), 3.85 (s, 3H), 1.82 (m, 12H), 1.49 (m, 42H).

^{13}C-NMR ($CDCl_3$, 298K, 100 MHz, δ, ppm): 167.22, 162.99, 161.44, 156.33, 153.41, 143.94, 142.67, 129.33, 125.36, 133.37, 133.27, 112.96, 108.17, 101.73, 73.94, 69.65, 69.30, 52.49, 30.89, 30.25, 30.17, 30.15, 30.12, 29.96, 29.94, 29.92, 29.89, 29.58, 29.56, 26.64, 26.52, 26.49.

Synthesis of **$Acd_1C_{11}Cou$ (11):** An aqueous solution of litium hydroxide (0.53 g, 50 mL) was added to a solution of compound **10** (3.60 g, 3.18 mmol) in THF-methanol 1:1 (100 mL). The mixture was stirred at room temperature during four hours and then the reaction was neutralized with concentrated hydrochloric acid until pH 2. The organic solvents were evaporated under reduced pressure and the resulting aqueous phase was extracted with DCM. The combined organic phases were washed with brine and dried over anhydrous magnesium sulphate. The solution was filtered and the solvent was removed under reduced pressure. The product was purified by flash chromatography on silica gel using DCM 9:1 AcOEt obtaining 2.3 g of product with a 60% of yield.

^{1}H-NMR (CD_2Cl_2, 298K, 400 MHz, δ, ppm): 7.65 (d, J= 9.6 Hz, 3H), 7.38 (d, J=8.4Hz, 3H), 7.30 (s, 2H), 6.81 (m, 6H), 6.20 (d, J=9.6 Hz, 3H), 4.01 (m, 12H), 1.79 (m, 12H), 1.46 (m, 42H).

^{13}C-NMR (CD_2Cl_2, 298K, 100 MHz, δ, ppm): 170.98, 162.55, 161.46, 161.43, 156.03, 152.97, 143.60, 143.19, 128.83, 123.79, 113.13, 113.03, 112.50, 108.69, 101.45, 101.42, 73.65, 69.31, 68.80, 30.47, 29.82, 29.70, 29.66, 29.49, 29.41, 29.19, 29.14, 26.10.

FT-IR (KBr, ν, cm^{-1}): 3242 (OH), 2921 (=C-H), 2927 (C-H), 1740 (C=O), 1680 (C=O), 1617, 1511 (C=C), 1233 (C-O).

MS (MALDI$^+$, dithranol, m/z): found 1113.4 [M^+] calculated 1113.4.

*2.5.2.6 Synthesis of **P5N10 (15)***

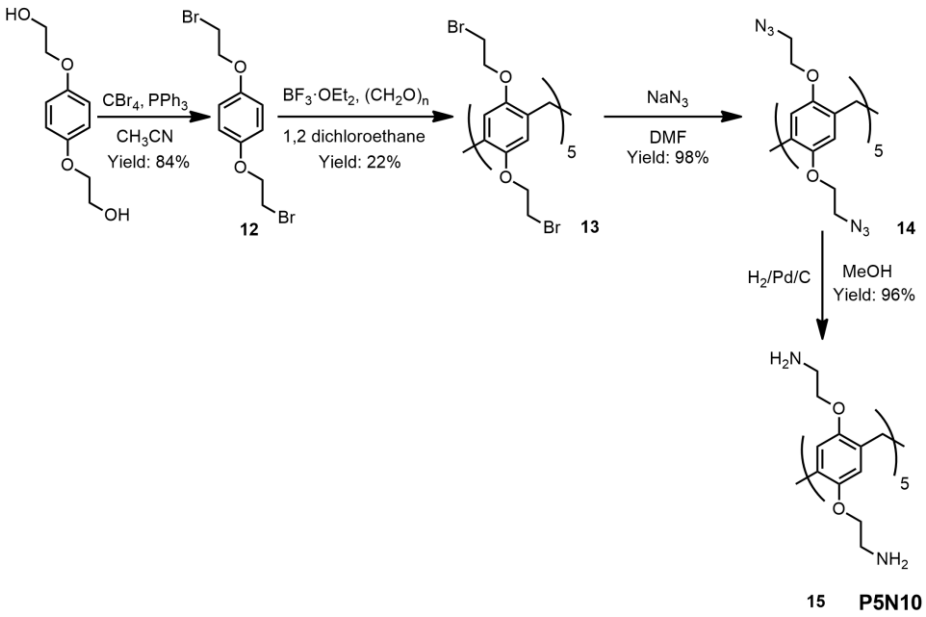

***Scheme 2.6.** Synthetic route of pillar[5]arene **P5N10**.*

Synthesis of **1,4-bis(2-bromoethoxy)benzene (12):** In a two-neck flask of 250 ml a solution of 1,4-bis(2-hydroxyethoxy)benzene (3.00 g, 15.13 mmol) was prepared in 100 ml of acetonitrile at 0°C. Then PPh_3 (9.00 g, 34.08 mmol) was added under stirring and then carbon tetrabromide (11.5 g, 34.08 mmol) was slowly added. The mixture was stirred at room temperature during 24 hours. After this time water was added and the precipitate obtained was filtered and washed with a methanol 1:1 water mixture. To purify the product, it was recrystallized in methanol, obtaining 4.10 g of a white solid with a yield of 84%.

^{1}H-NMR ($CDCl_3$, 298K, 400 MHz, δ, ppm): 6.86 (s, 4H), 4.24 (t, J=6.4 Hz, 4H), 3.61 (t, J=6.4 Hz, 4H).

^{13}C-NMR ($CDCl_3$, 298K, 100 MHz, δ, ppm): 152.94, 116.20, 66.82, 29.40.

Synthesis of **P5Br10 (13):** In a two-neck flask of 250 ml a solution of 1,4-bis(2-bromoethoxy)benzene **(12)** (3.00 g, 9.26 mmol) was prepared in 150 ml of 1,2-dichloroethane under argon atmosphere. Paraformaldehyde (0.278 g, 9.26 mmol) was added and finally $BF_3{\cdot}OEt_2$

(1.30 g, 9.26 mmol) was added dropwise. The resulting mixture was stirred during 3 hours at room temperature. After that time the solution was filtered and concentrated to vacuum; the solid obtained was dissolved in 100 ml of dichloromethane and washed with water (2x100 ml) and brine (1x100ml), and finally it was dried over $MgSO_4$. Then, the solvent was removed under vacuum and the residue was purified by silica-gel flash column chromatography in a mix of DCM 2:1 hexane, obtaining 2.83 g of a white solid with a yield of 22%.

^{1}H-NMR ($CDCl_3$, 298K, 400 MHz, δ, ppm): 6.91 (s, 10H), 4.23 (t, J=7.6 Hz, 20H), 3.85 (s, 10H), 3.63 (t, J=7.6 Hz, 20H).

^{13}C-NMR ($CDCl_3$, 298K, 100 MHz, δ, ppm): 149.80, 119.21, 116.22, 69.12, 30.80, 29.55.

FT-IR (KBr, ν, cm^{-1}): 2938 (=C-H), 2910 (C-H), 1508 (C=C), 1204 (C-O).

MS (MALDI$^+$, dithranol, m/z): found 1679.9 [M-H$^+$] calculated 1680.10.

Synthesis of **P5N$_3$ (14):** Over a solution of **P5Br10 (13)** (0.50 g, 0.2976 mmol) in anhydrous DMF (20 ml) was added NaN_3 (0.232 g, 3.5712 mmol) under argon atmosphere. After stirring at 100^{o}C overnight, the mixture was cooled to room temperature and then poured into water (150 ml). After that it was extracted with diethyl ether (3x150 ml), dried with $MgSO_4$, filtered and finally concentrated, obtaining 350 mg of a white solid with a yield of 98%.

^{1}H-NMR ($CDCl_3$, 298K, 400 MHz, δ, ppm): 6.85 (s, 10H), 4.02 (t, J=4.8 Hz, 20H), 3.84 (s, 10H), 3.56 (t, J=4.8 Hz, 20H).

^{13}C-NMR ($CDCl_3$, 298K, 100 MHz, δ, ppm): 149.08, 128.08, 114.88, 66.65, 50.12, 49.35, 28.81.

FT-IR (KBr, ν, cm^{-1}): 2932 (=C-H), 2870 (C-H), 2103 (N=N=N), 1502 (C=C), 1205 (C-O).

MS (MALDI$^+$, dithranol, m/z): found 1324.28 [M+Na$^+$] calculated with sodium 1324.24 (1301.26+22.98).

Synthesis of **P5N10 (15):** A suspension of **$P5N_3$ (14)** (0.39 g, 0.29 mmol) in methanol (15 ml) was prepared in a two-neck flask; then 3 cycles of vacuum-argon were carried out and 75 mg of Pd/C were added under argon atmosphere. Finally, three cycles of vacuum-hydrogen were realized and the mixed was stirred under argon atmosphere during a weekend at 30°C. The resulting mixture was filtered over celite, washed with methanol and concentrated under reduced pressure. The solid was purified by recrystallization from chloroform to produce 0.29 g of product with a yield of 96%.

^{1}H-NMR (MeOD, 298K, 400 MHz, δ, ppm): 6.76 (s, 10H), 3.82 (m, 30H), 2.94 (t, J=5.6 Hz, 20H).

^{13}C-NMR (MeOD, 298K, 400 MHz, δ, ppm): 151.40, 130.34, 115.29, 71.59, 42.19, 29.08.

FT-IR (KBr, ν, cm^{-1}): 3368 (NH_2), 2949 (=C-H), 2926 (C-H), 1502 (C=C), 1210 (C-O).

MS (MALDI$^+$, dithranol, m/z): found 1041.5 [M-H$^+$] calculated 1042.5.

2.5.2.7 *Synthesis of ionic pillar[5]arenes*

Ionic dendrimers were prepared following the previously described methodology.[42] A solution of the corresponding acid in dry tetrahydrofuran was added to a solution of the pillar[5]arene **P5N10**, in approximately 1:1 (primary amine groups: carboxyl groups) stoichiometry. The mixture was ultrasonicated for 5 min, and then it was slowly evaporated at room temperature and dried in vacuum at 40°C until the weight remained constant.

AcC_{11}-P5N10

^{1}H-NMR ($CDCl_3$, 298K, 400 MHz, δ, ppm): 6.80 (s, 10H), 5.87 (s, 40H), 4.11 (m, 20H), 3.70 (s, 10H), 3.20 (m, 20H), 2.23 (t, J=10 Hz, 20H), 1.57 (q, J=8.52 Hz, 20H), 1.24 (m, 130H), 0.87 (t, J=9.2 Hz, 30H).

^{13}C-NMR ($CDCl_3$, 298K, 100 MHz, δ, ppm): 180.38, 150.19, 129.55, 116.53, 67.62, 39.65, 36.83, 32.08, 29.83, 29.53, 26.13, 22.84, 14.25.

FT-IR (KBr, ν, cm^{-1}): 3423 (-NH_3^+), 2949 (=C-H), 2925 (C-H), 1652 (C=O), 1636 (Ar), 1558 (COO^-asym), 1406 (COO^-sym), 1217 (C-O).

AcBzC_{11}-P5N10

^{1}H-NMR ($CDCl_3$, 298K, 400 MHz, δ, ppm): 7.91 (d, J=8.08 Hz, 20H), 6.82 (s, 10H), 6.72 (d, J=8.08Hz, 20H), 5.07 (s, 30H), 3.85 (m, 20H), 3.09 (s, 30H), 1.73 (m, 20H), 1.30 (m, 160H), 0.88 (t, J=7.04 Hz, 30H).

^{13}C-NMR ($CDCl_3$, 298K, 100 MHz, δ, ppm): 172.78, 162.05, 150.41, 131.61, 129.55, 126.66, 115.52, 113.83, 68.16, 39.48, 32.06, 29.76, 29.64, 29.49, 29.41, 26.21, 22.83, 14.26.

FT-IR (KBr, ν, cm^{-1}): 3440 (-NH_3^+), 2918 (=C-H), 2852 (C-H), 1689 (C=O), 1607 (Ar), 1539 (COO^-asym), 1380 (COO^-sym), 1205 (C-O).

Acd$_1$$C_{11}$-P5N10

^{1}H-NMR ($CDCl_3$, 298K, 400 MHz, δ, ppm): 7.25 (s, 20H), 6.84 (s, 10H), 3.97 (m, 60H), 3.70 (m, 80H), 1.73 (hex, J=6.96 Hz, 60H), 1.43 (hex, J=6.96Hz, 60H), 1.25 (m, 420H) 0.87 (t, J=6.92 Hz, 90H).

^{13}C-NMR (DMSO- d_6, 298K, 100 MHz, δ, ppm): 167.25, 140.64, 107.78, 73.14, 68.73, 31.88, 30.41, 29.72, 29.29, 26.41, 22.54.

FT-IR (KBr, ν, cm^{-1}): 3327 (-NH_3^+), 2940 (=C-H), 2848 (C-H), 1712 (C=O), 1620 (Ar), 1512 (COO^-asym), 1434 (COO^-sym), 1296 (C-O).

AcC_{11}Cou-P5N10

^{1}H-NMR (DMSO-d_6, 298K, 400 MHz, δ, ppm): 7.98 (d, J=9.48 Hz, 10H), 7.61 (d, J=8.6Hz, 10H), 6.95 (m, 20H), 6.82 (s, 10H), 6.28 (d, J=9.48 Hz, 10H), 4.06 (t, J=6.51 Hz, 20H), 3.75 (m, 30H), 2.95 (s, 10H), 2.17 (t, J=7.32 Hz, 20H), 1.73 (m, 20H), 1.33 (m, 140H).

^{13}C-NMR (DMSO- d_6, 298K, 100 MHz, δ, ppm): 174.55, 161.90, 160.33, 155.43, 150.94, 144.37, 134.59, 129.48, 116.66, 112.74, 112.37, 112.23, 101.12, 68.29, 59.96, 41.26, 33.73, 28.94, 28.86, 28.74, 28.70, 28.57, 28.43, 25.42, 24.33.

FT-IR (KBr, ν, cm^{-1}): 3134 (-NH_3^+), 2925 (=C-H), 2851 (C-H), 1724 (C=O), 1617 (Ar), 1519 (COO^-asym), 1426 (COO^-sym), 1207 (C-O).

AcBzC_{11}Cou-P5N10

^{1}H-NMR ($CDCl_3$, 298K, 400 MHz, δ, ppm): 7.97 (d, J=9.48 Hz, 10H), 7.85 (d, J=8.76 Hz, 20H), 7.60 (d, J=8.6Hz, 10H), 6.94 (m, 40H), 6.83 (s, 10H), 6.27 (d, J=9.48 Hz, 10H), 4.06 (t, J=6.48 Hz, 20H), 3.99 (t, J=6.48 Hz, 20H), 3.91 (s, 20H), 3.74 (s, 10H), 3.03 (s, 20H), 1.72 (m, 40H), 1.33 (m, 140H).

^{13}C-NMR (DMSO- d_6, 298K, 100 MHz, δ, ppm): 167.51, 161.90, 161.86, 160.32, 155.43, 151.17, 144.35, 131.21, 131.14, 129.47, 124.23, 113.98, 113.88, 112.72, 112.36, 112.23, 101.11, 71.25, 68.27, 67.67, 43.40, 30.70, 28.95, 28.90, 28.73, 28.69, 28.55, 28.41, 25.44, 25.40.

FT-IR (KBr, ν, cm^{-1}): 3437 (-NH_3^+), 2927 (=C-H), 2852 (C-H), 1731 (C=O), 1610 (Ar), 1558 (COO^-asym), 1387 (COO^-sym), 1206 (C-O).

Acd$_1$$C_{11}$Cou-P5N10

^{1}H-NMR ($CDCl_3$, 298K, 400 MHz, δ, ppm): 7.60 (d, J=9.48 Hz, 30H), 7.33 (d, J=8.6 Hz, 30H), 7.27 (s, 10H), 6.77 (m, 60H), 6.21 (d, J=9.44 Hz, 30H), 3.97 (m, 120H), 1.77 (m, 120H), 1.43 (m, 120H), 1.29 (m, 340H).

^{13}C-NMR ($CDCl_3$, 298K, 100 MHz, δ, ppm): 170.53, 162.48, 161.33, 143.18, 143.54, 128.67, 112.83, 112.79, 112.23, 108.50, 101.11, 73.51, 68.68, 29.82, 29.60, 29.49, 29.31, 29.21, 26.12, 26.04.

FT-IR (KBr, ν, cm^{-1}): 3442 (-NH_3^+), 2923 (=C-H), 2848 (C-H), 1736 (C=O), 1617 (Ar), 1555 (COO^-asym), 1369 (COO^-sym), 1273 (C-O).

2.5.3 General Procedure for the preparation of the aggregates

For the preparation of the self-assemblies, a solution of 2 mg/mL of the amphiphilic ionic pillar[5]arene in THF was prepared, and Milli-Q water was gradually added while self-assembly was followed by measuring the turbidity in UV. When a critical water content was reached, a sudden increase in turbidity happened, indicating that the self-assembling process took place. Once turbidity reached an almost constant value, the mixture was dialyzed against water to remove the organic solvent using a Spectra/Por dialysis membrane (MWCO 1000) for 3 days. Water suspensions of the aggregates with a concentration around 2 mg/mL were obtained.

2.5.4 Nile Red encapsulation

119 µL of a solution of Nile Red in DCM (5×10^{-6} M) was added into flasks and then the solvent evaporated. Afterwards, a water suspension of nanoparticles of concentration 2.0 mg/mL was added to each flask. The vesicles suspensions were prepared by diluting the former 2 mg/mL nanoparticle suspension. In each flask a final concentration of 1.0×10^{-6} M of Nile Red was reached. These solutions were stirred overnight to reach equilibrium before fluorescence was measured. The emission spectra of Nile Red were registered from 560 to 700 nm while exciting at 550 nm.

2.6 Appendix

2.6.1 NMR Spectra

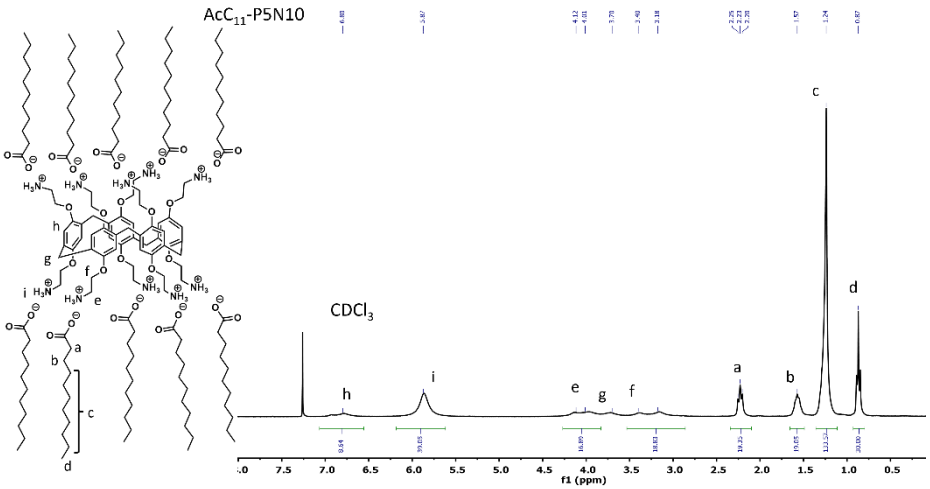

Figure 2.23. *^{1}H-NMR spectrum of **AcC_{11}-P5N10**, $CDCl_3$, 298K, 400 MHz.*

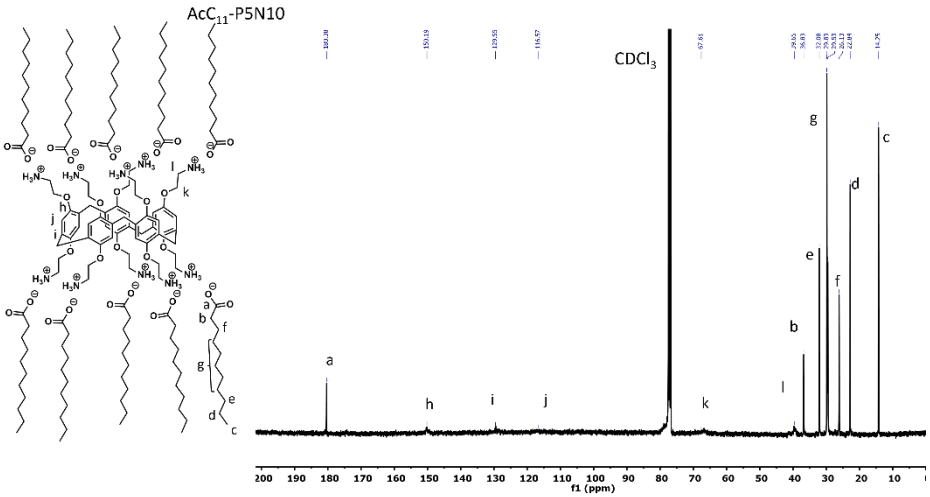

Figure 2.24. *^{13}C-NMR spectrum of **AcC_{11}-P5N10**, $CDCl_3$, 298K, 100 MHz.*

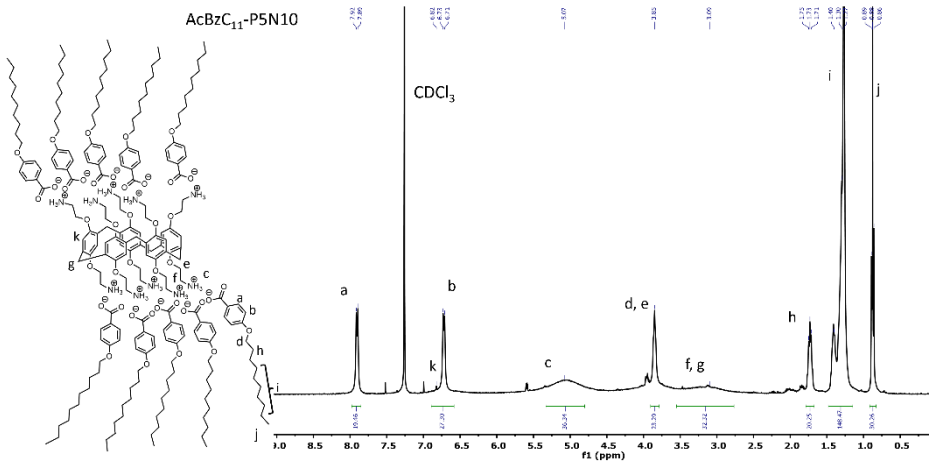

Figure 2.25. *^{1}H-NMR spectrum of **AcBzC$_{11}$-P5N10**, CDCl$_3$, 298K, 400 MHz.*

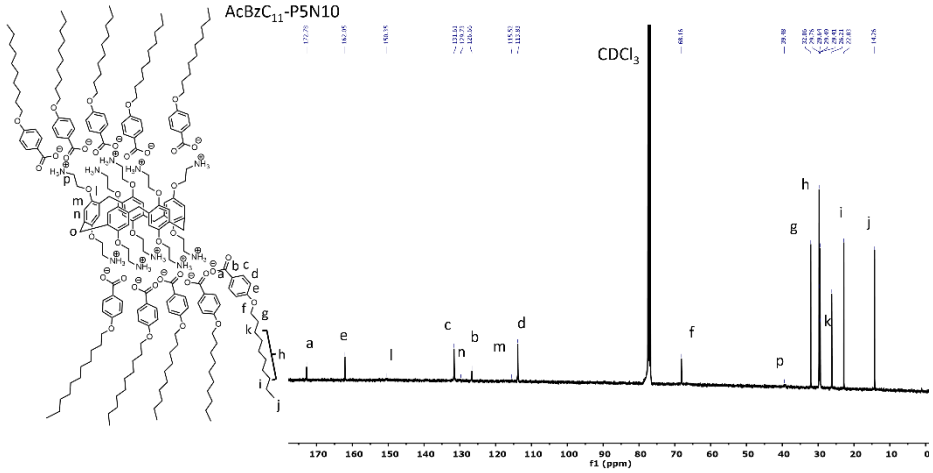

Figure 2.26. *^{13}C-NMR spectrum of **AcBzC$_{11}$-P5N10**, CDCl$_3$, 298K, 100 MHz.*

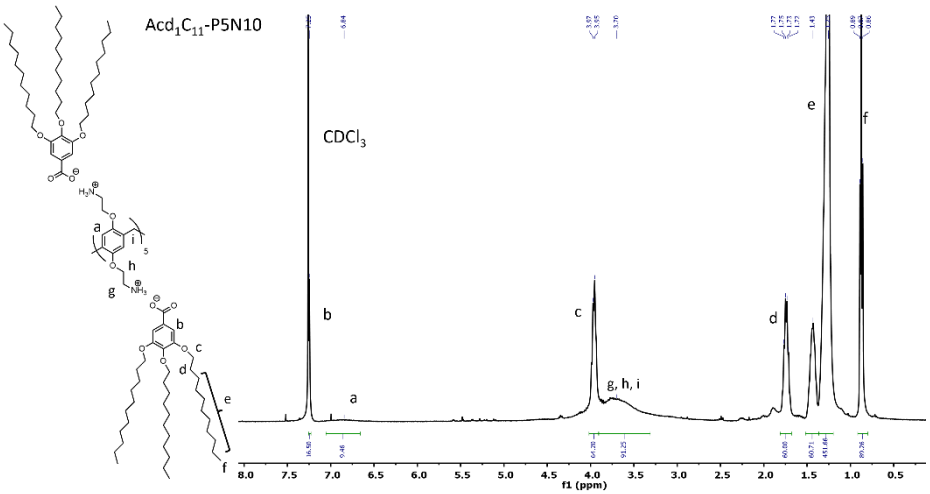

Figure 2.27. *^{1}H-NMR spectrum **Acd_1C_{11}-P5N10**, $CDCl_3$, 298K, 400 MHz.*

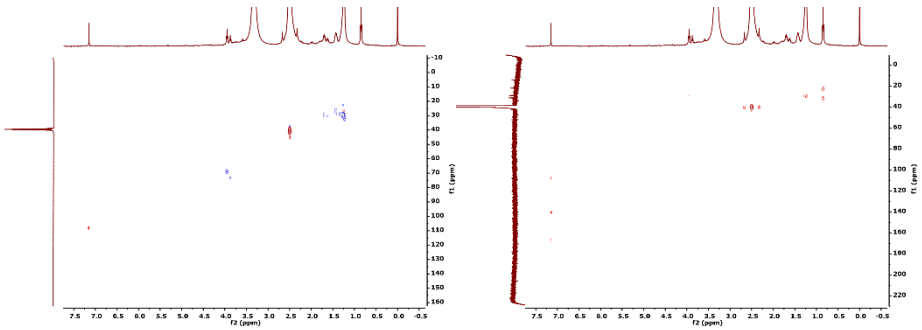

Figure 2.28. *HSQC and HMBC spectra of **Acd_1C_{11}-P5N10**, $CDCl_3$, 298K.*

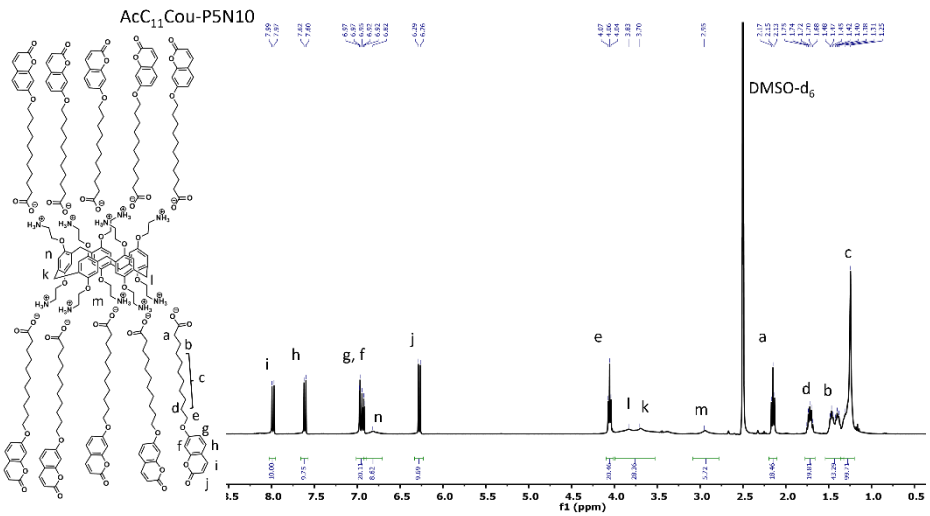

Figure 2.29. *^{1}H-NMR spectrum of **AcC$_{11}$Cou-P5N10**, DMSO-d$_6$, 298K, 400 MHz.*

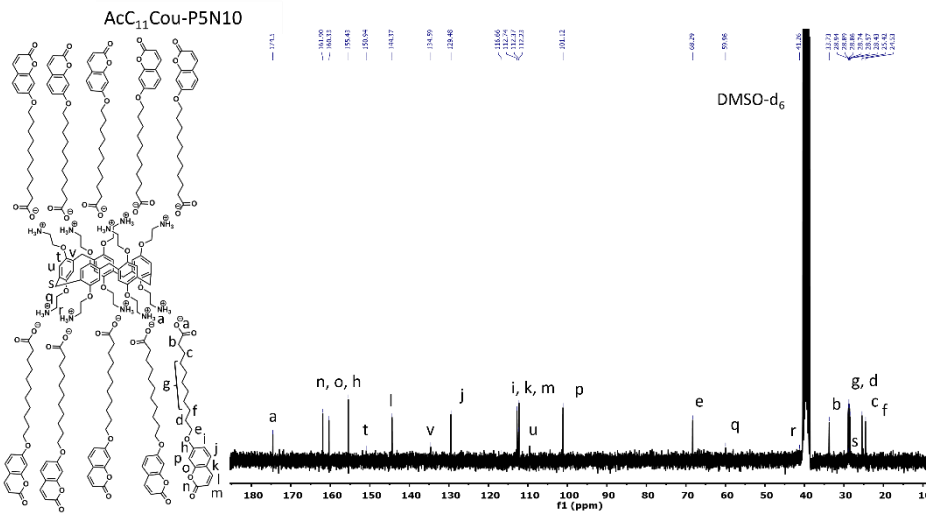

Figure 2.30. *^{13}C-NMR spectrum of **AcC$_{11}$Cou-P5N10**, DMSO-d$_6$, 298K, 100 MHz.*

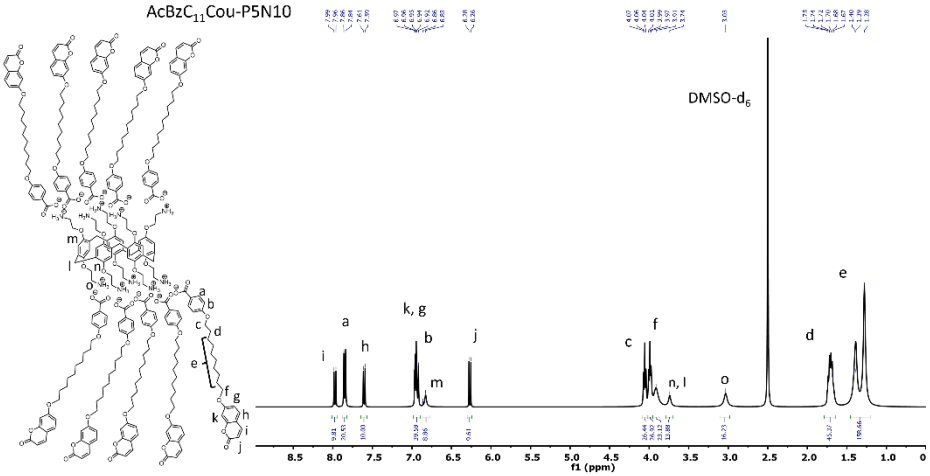

Figure 2.31. *^{1}H-NMR spectrum of **AcBzC$_{11}$Cou-P5N10**, DMSO-d$_6$, 298K, 400 MHz.*

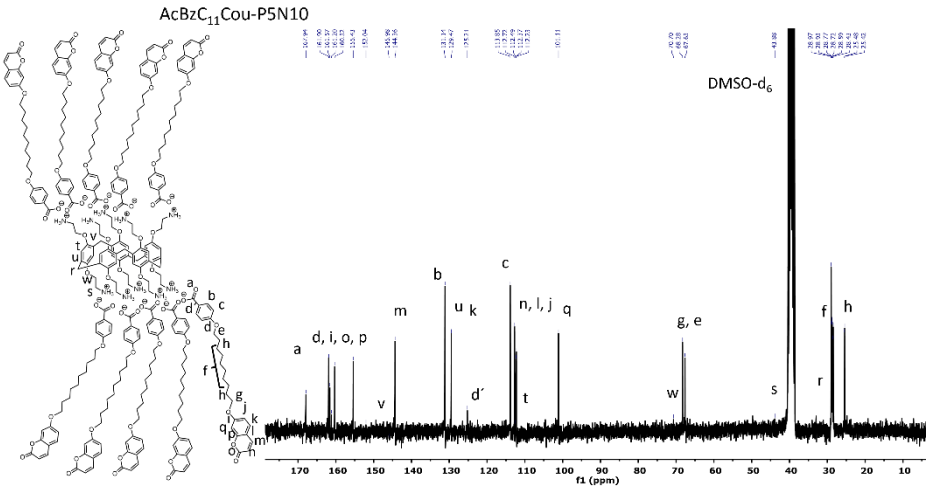

Figure 2.32. *^{13}C-NMR spectrum of **AcBzC$_{11}$Cou-P5N10**, DMSO-d$_6$, 298K, 100 MHz.*

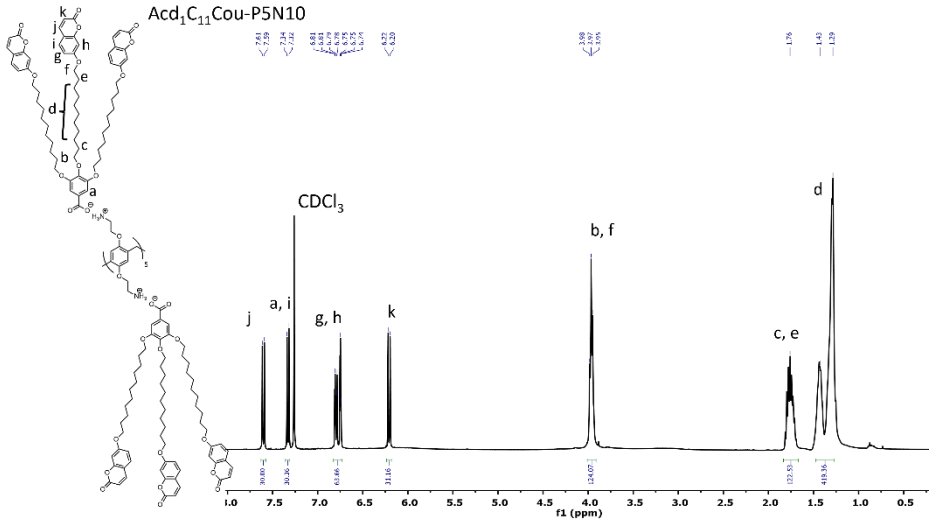

Figure 2.33. *^{1}H-NMR spectrum of **Acd$_1$C$_{11}$Cou-P5N10**, $CDCl_3$, 298K, 400 MHz.*

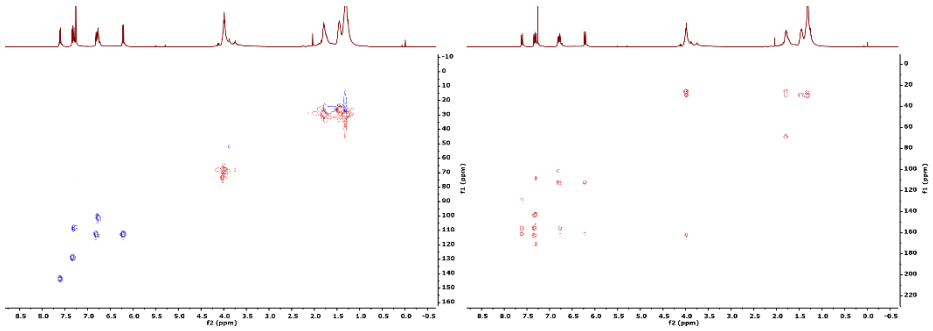

Figure 2.34. *HSQC and HMBC spectra of **Acd$_1$C$_{11}$Cou-P5N10**, $CDCl_3$, 298K.*

2.6.2 FT-IR spectra

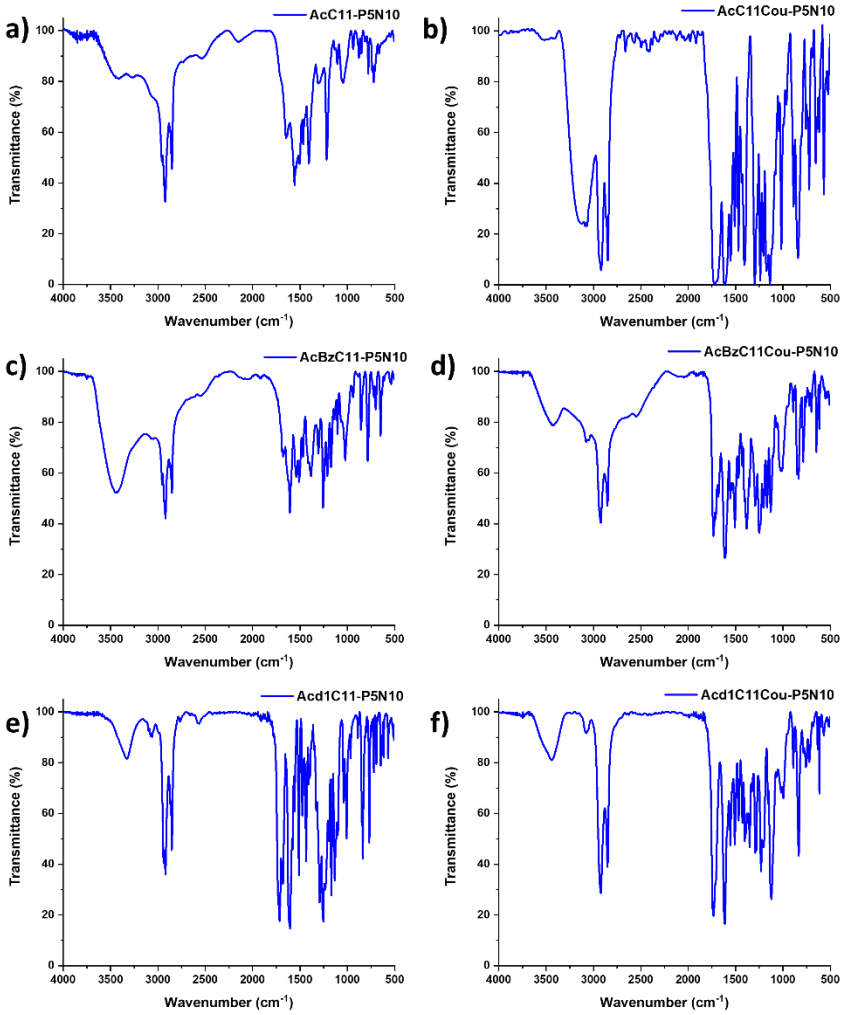

Figure 2.35. *FT-IR spectra in KBr of: a)* ***AcC$_{11}$-P5N10****, b)* ***AcC$_{11}$Cou-P5N10****, c)* ***AcBzC$_{11}$-P5N10****, d)* ***AcBzC$_{11}$Cou-P5N10****, e)* ***Acd$_1$C$_{11}$-P5N10*** *and f)* ***Acd$_1$C$_{11}$Cou-P5N10****.*

2.6.3 DSC thermograms

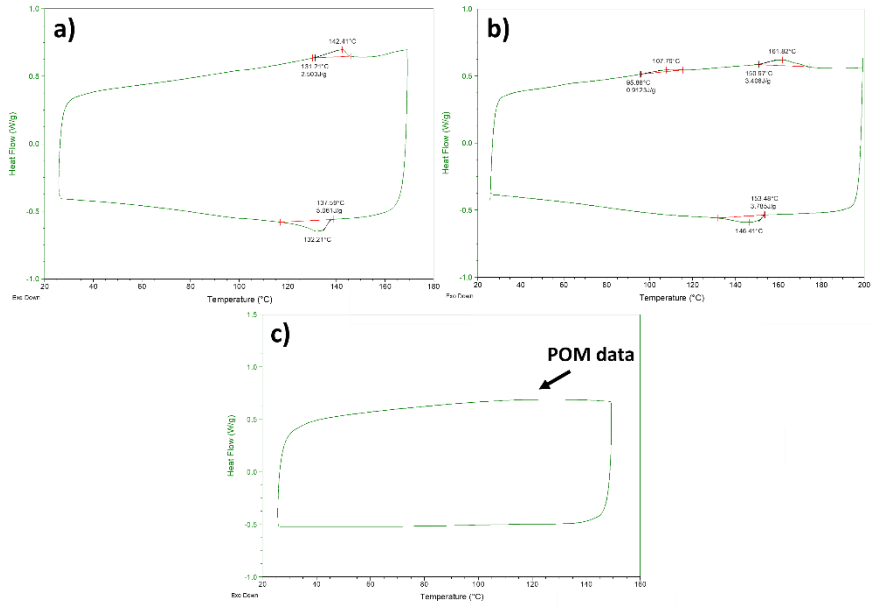

*Figure 2.36. Second heating-cooling cycle at 10°C/min of a) **AcC$_{11}$-P5N10**, b) **AcBzC$_{11}$-P5N10** and c) **Acd$_1$C$_{11}$-P5N10**.*

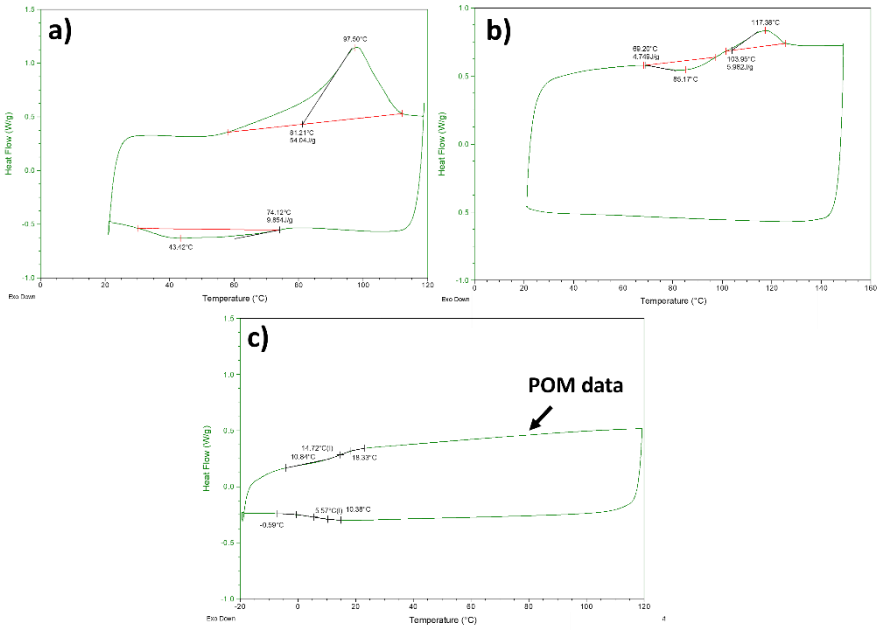

*Figure 2.37. Second heating-cooling cycle at 10°C/min of a) **AcC$_{11}$Cou-P5N10**, b) **AcBzC$_{11}$Cou-P5N10** and c) **Acd$_1$C$_{11}$Cou-P5N10**.*

2.6.4 X-ray diffractograms

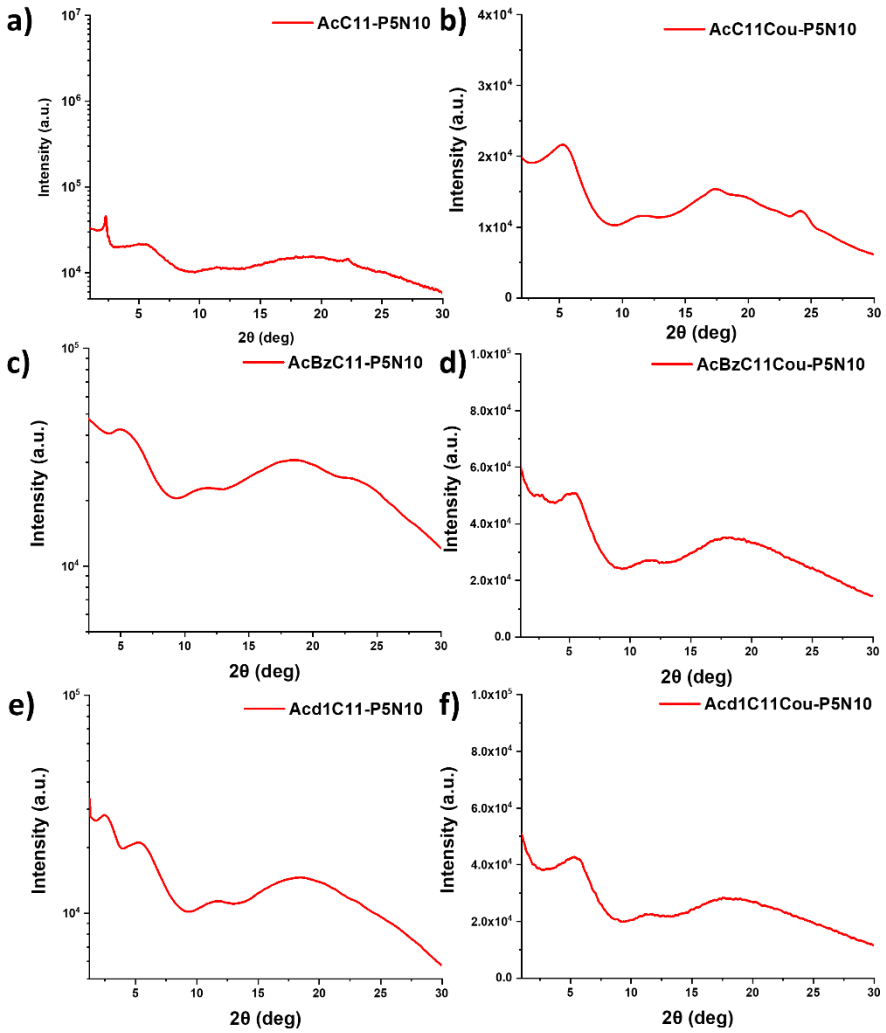

Figure 2.38. *X-Ray diffractograms at room temperature of: a)* ***AcC$_{11}$-P5N10****, b)* ***AcC$_{11}$Cou-P5N10****, c)* ***AcBzC$_{11}$-P5N10****, d)* ***AcBzC$_{11}$Cou-P5N10****, e)* ***Acd$_1$C$_{11}$-P5N10*** *and f)* ***Acd$_1$C$_{11}$Cou-P5N10****.*

2.6.5 Nyquist plots

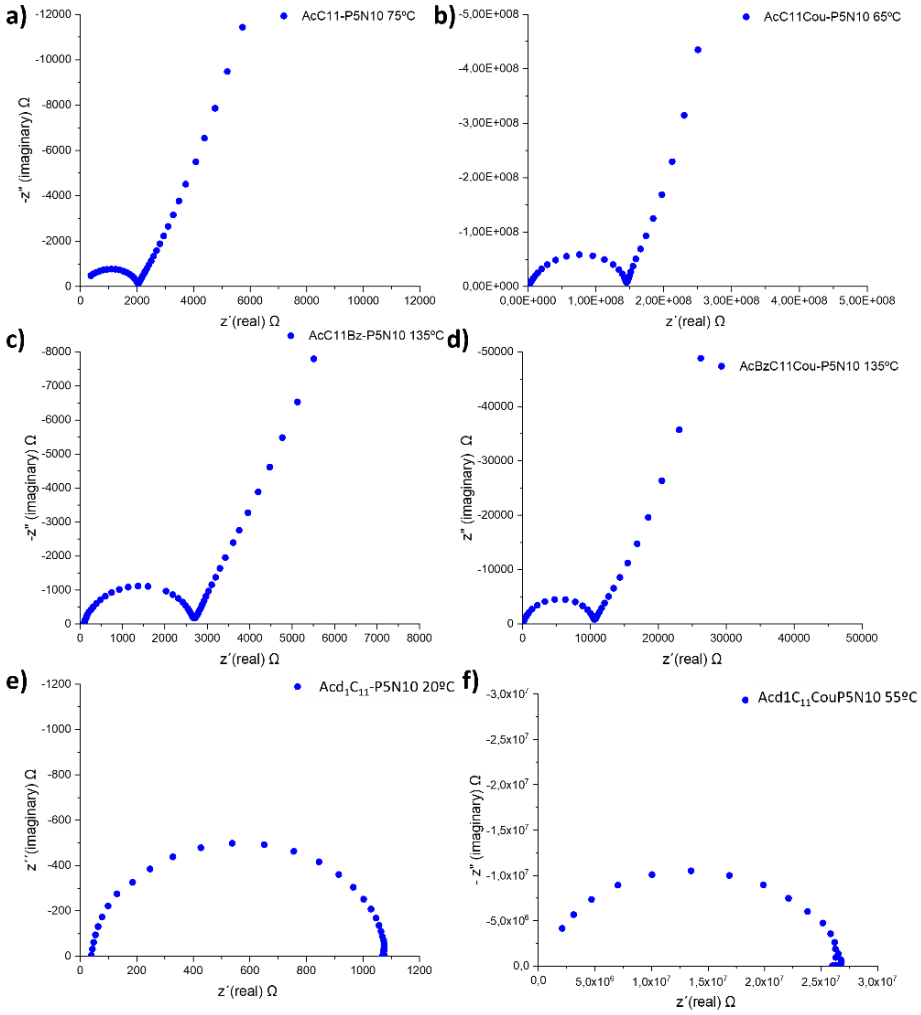

Figure 2.39. *Nyquist plots of a)* ***AcC$_{11}$-P5N10*** *at 75ºC, b)* ***AcC$_{11}$Cou-P5N10*** *at 65ºC, c)* ***AcBzC$_{11}$-P5N10*** *at 135ºC, d)* ***AcBzC$_{11}$Cou-P5N10*** *at 135ºC e)* ***Acd$_1$C$_{11}$-P5N10*** *at 20ºC and f)* ***Acd$_1$C$_{11}$Cou-P5N10*** *at 55ºC.*

2.7 References

[1] T. Ogoshi, S. Kanai, S. Fujinami, T-aki. Yamagishi and Y. Nakamoto, para-Bridged Symmetrical Pillar[5]arenes: Their Lewis Acid Catalyzed Synthesis and Host–Guest Property, *J. Am. Chem. Soc.,* 2008*,* **130***,* 5022–5023.

[2] N. L. Strutt, R. S. Forgan, J. M. Spruell, Y. Y. Botros and J.F. Stoddart, Monofunctionalized Pillar[5]arene as a Host for Alkanediamines, *J. Am. Chem. Soc.,* 2011*,* **133**, 5668–5671.

[3] Y. Sun, F. Zhang, J. Quan, F. Zhu, W. Hong, J. Ma, H. Pang, Y. Sun, D. Tian and H. Li, A biomimetic chiral-driven ionic gate constructed by pillar[6]arene-based host–guest systems, *Nat. Commun.,* 2018, **9**, 2617-2624.

[4] B. Hua, C. Zhang, W. Zhou, L. Shao, Z. Wang, L. Wang, H. Zhu and F. Huang, Pillar[5]arene-Based Solid-State Supramolecular Polymers with Suppressed Aggregation-Caused Quenching Effects and Two Photon Excited Emission, *J. Am. Chem. Soc.,* 2020*,* **142**, 16557−16561.

[5] H. Zhu, Q. Li, W. Zhu and F. Huang, Pillararenes as Versatile Building Blocks for Fluorescent Materials, *Acc. Mater. Res*., 2022, **3**, 658−668.

[6] J-F. Chen, J-D. Ding and T-B. Wei, Pillararenes: fascinating planar chiral macrocyclic arenes, *Chem. Commun***.**, 2021, **57**, 9029-9039.

[7] T. Ogoshi, K. Masaki, R. Shiga, K. Kitajima, and T-aki. Yamagishi, Planar-Chiral Macrocyclic Host Pillar[5]arene: No Rotation of Units and Isolation of Enantiomers by Introducing Bulky Substituents, *Org. Lett*., 2011, **13**, 5*,* 1264–1266.

[8] W-J. Li, Q. Gu, X-Q. Wang, D-Y. Zhang, Y-T. Wang, X. He, W. Wang and H-B. Yang, AIE-Active Chiral [3]Rotaxanes with Switchable Circularly Polarized Luminescence, *Angew. Chem. Int. Ed.,* 2021, **60**, 9507 – 9515.

[9] H. Zheng, L. Fu, R. Wang, J. Jiao, Y. Song, C. Shi, Y. Chen, J. Jiang, C. Lin, J. Ma and L. Wang*,* Cation controlled rotation in anionic pillar[5]arenes and its application for fluorescence switch, *Nat. Commun*., 2023, **14**, 590-598.

[10] X. Wu, J. Yang, J. Xing, Y. Lyu, R. Zou, X. Wang, J. Yao, D. Zhang, D. Qi, G. Shao, A. Wu and J. Li, Using host–guest interactions at the interface of quantum dots to load drug molecules for biocompatible, safe, and effective chemo-photodynamic therapy against cancer, *J. Mater. Chem. B,* 2023, **11**, 4855–4864.

[11] Z. Jia, R. Tang, X. Yuan, H. Zhu, J. Guo, Y. Chen, Y. Yang, B. Liang, S. Lu, D. Cao and J. Liu, Multifunctional Supramolecular Vesicles as Zn2+-Triggered Microglial Modulator Alleviates Alzheimer's Disease, *Small,* 2023, **19**, 2302176-2302187.

[12] S. Pan, M. Ni, B. Mu, Q. Li, X-Y. Hu, C. Lin, D. Chen and L. Wang, Well-Defined Pillararene-Based Azobenzene Liquid Crystalline Photoresponsive Materials and Their Thin Films with Photomodulated Surfaces, *Adv. Funct. Mater.*, 2015, **25**, 3571-3580.

[13] S. Fa, M. Mizobata, S. Nagano, K. Suetsugu, T. Kakuta, T-a. Yamagishi and T. Ogoshi, Reversible "On/Off" Chiral Amplification of Pillar[5]arene Assemblies by Dual External Stimuli, *ACS Nano,* 2021, **15**, 10, 16794-16801.

[14] V. S. Sharma, V. K. Vishwakarma, P. S. Shrivastav, A. A. Sudhakar, A. S. Sharma and P. A. Shah, Calixarene Functionalized Supramolecular Liquid Crystals and Their Diverse Applications, *ACS Omega,* 2022, **7**, 45752-45796.

[15] X. Li, B. Li, L. Chen, J. Hu, C. Wen, Q. Zheng, L. Wu, H. Zeng, B. Gong and L. Yuan, Liquid-crystalline mesogens based on cyclo[6]aramides: distinctive phase transitions in response to macrocyclic host-guest interactions, *Angew. Chem. Int. Ed.,* 2015, **54**, 11147-11152.

[16] S-i. Kawano, M. Kato, S. Soumiya, M. Nakaya, J. Onoe and K. Tanaka, Columnar Liquid Crystals from a Giant Macrocycle Mesogen, *Angew. Chem. Int. Ed.*, 2018, **57**, 167-171.

[17] W.-Q. Ding, H. Liu, S.-Y. Qin, Y. Jiang, X. Lei and A-Q, Zhang, A Lyotropic Liquid Crystal from a Flexible Oligopeptide Amphiphile in Dimethyl Sulfoxide, *ACS Appl. Bio Mater.,* 2020, **3**, 12, 8989–8996.

[18] J. Zhang, D. J. Pesak, J. L. Ludwick and J. S. Moore, Geometrically-Controlled and Site-Specifically-Functionalized Phenylacetylene Macrocycles, *J. Am. Chem. Soc.*, 1994, **116**, 4227-4239.

[19] L. Chen, Y. Cai, W. Feng and L. Yuan, Pillararenes as macrocyclic hosts: a rising star in metal ion separation, *Chem. Commun*., 2019, **55**, 7883-7898.

[20] X-Y. Hu, K. Jia, Y. Cao, Y. Li, S. Qin, F. Zhou, C. Lin, D. Zang and L. Wang, Dual Photo- and pH-Responsive Supramolecular Nanocarriers Based on Water-

Soluble Pillar[6]arene and Different Azobenzene Derivatives for Intracellular Anticancer Drug Delivery, *Chem. Eur. J*., 2015, **21**, 1208-1220.

[21] R. Wang, Y. Sun, F. Zhang, M. Song, D. Tian and H. Li, Temperature-Sensitive Artificial Channels through Pillar[5]arene-based Host–Guest Interactions, *Angew. Chem. Int. Ed.,* 2017, **56**, 5294-5298.

[22] T. Ogoshi, T. Kakuta and T-A. Yamagishi, Applications of Pillar[n]arene-Based Supramolecular Assemblies, *Angew. Chem. Int. Ed*., 2019, **58**, 2197-2206.

[23] I. Nierengarten, S. Guerra, J-F. Nierengarten and R. Deschenaux, Building liquid crystals from the 5-fold symmetrical pillar[5]arene core, *Chem. Commun*., 2012, **48**, 8072-8074.

[24] A. Concellón, P. Romero, M. Marcos, J. Barberá, C. Sánchez-Somolinos, M. Mizobata, T. Ogoshi, J.L. Serrano and J. Del Barrio, Coumarin Containing Pillar[5]arenes as Multifuctional Liquid Crystal Macrocycles, *J. Org. Chem*., 2020, **85**, 8944-8951.

[25] I. Nierengarten, S. Guerra, M. Holler, L. Karmazin-Brelot, J. Barberá, R. Deschenaux and J-F. Nierengarten, Macrocyclic Effects in the Mesomorphic Properties of Liquid-Crystalline Pillar[5]- and Pillar[6]arenes, *Eur. J. Org. Chem*., 2013, **18**, 3675-3684.

[26] I. Nierengarten, S. Guerra, H. B. Aziza, M. Holler, R. Abidi, J. Barberá, R. Deschenaux and J-F. Nierengarten, Piling Up Pillar[5]arenes To Self-Assemble Nanotubes, *Chem. Eur. J.,* 2016, **22**, 6185-6189.

[27] S. Fa, M. Mizobata, S. Nagano, K. Suetsugu, T. Kakuta, T-A. Yamagishi and T. Ogoshi, Reversible "On/Off" Chiral Amplification of Pillar[5]arene Assemblies by Dual External Stimuli, *ACS Nano,* 2021, **15**, 16794-16801.

[28] C. F. J. Faul, M. Antonietti, Ionic Self-Assembly: Facile Synthesis of Supramolecular Materials, *Adv. Mater*., 2003, **15**, 673-683.

[29] C. F. J. Faul, Ionic Self-Assembly for Functional Hierarchical Nanostructured Materials, *Acc. Chem. Res*., 2014, **47**, 3428-3438.

[30] A. Concellón, V. Iguarbe, in Supramolecular Assemblies Based on Electrostatic Interactions, ed. M. A. Aboudzadeh, A. Frontera, Springer International Publishing: Cham, 2022, p. 85-118.

[31] S. Hernández-Ainsa, M. Marcos and J. L. Serrano, in *Handbook of Liquid Crystals*, ed. J. W. Goodby, P. J. Collings, T. Kato, C. Tschierske, H. Gleeson and P. Raynes, Wiley-VCH Verlag GmbH & Co. KGaA, 2014, vol. **7**, p. 259-300.

[32] M. Marcos, R. Martín- Rapún, A. Omenat and J. L. Serrano, Highly congested liquid crystal structures: dendrimers, dendrons, dendronized and hyperbranched polymers, *Chem. Soc. Rev*., 2007, **36**, 1889-1901.

[33] A. Concellón, M. San Anselmo, S. Hernández-Ainsa, P. Romero, M. Marcos and J. L. Serrano, Micellar Nanocarriers from Dendritic Macromolecules Containing Fluorescent Coumarin Moieties, *Polymers,* 2020, **12**, 2872-2883.

[34] M. Cano, A. Sánchez-Ferrer, J. L. Serrano, N. Gimeno and B. Ros, Supramolecular Architectures from Bent-Core Dendritic Molecules, *Angew. Chem. Int. Ed*., 2014, **53**, 13449-13453.

[35] S. Hernández-Ainsa, J. Barberá, M. Marcos and J. L. Serrano, Nanoobjects Coming From Mesomorphic PAMAM Ionic derivatives, *Soft Matter,* 2011, **7**, 2560-2568.

[36] C. Mertesdorf, H. Ringsdorf, Self-organization of substituted azacrowns based on their discoid and amphiphilic nature, *Liq. Cryst*., 1989, **5**, 1757-1772.

[37] C. Lin, H. Ringsdorf, M. Ebert, R. Kleppinger, J. H. Wendorff, Structural variations of liquid crystalline polymers with phasmidic-type mesogens, *Liq. Cryst.,* 1989, **5**, 1841-1847.

[38] A. Concellón, M. Marcos, P. Romero, J. L. Serrano, R. Termine and A. Golemme, Not Only Columns: High Hole Mobility in a Discotic Nematic Mesophase Formed by Metal-Containing Porphyrin-Core Dendrimers, *Angew. Chem. Int. Ed.,* 2017, **129**, 1279-1283.

[39] Y. Sun, F. Zhang, J. Quan, F. Zhu, W. Hong, J. Ma, H. Pang, Y. Sun, D. Tian and H. Li, A biomimetic chiral-driven ionic gate constructed by pillar[6]arene-based host–guest systems, *Nat Commun.,* 2018, **9**, 2617-2624.

[40] A. Pérez, D. de Saá, A. Ballesteros, J. L. Serrano, T. Sierra and P. Romero, NMR Spectroscopic Study of the Self-Aggregation of 3-Hexen-1,5-diyne Derivatives, *Chem. Eur. J.,* 2013, **19**, 10271-10279.

[41] A. Concellón, A. P. H. J. Schenning, P. Romero, M. Marcos and J. L. Serrano, Size-Selective Adsorption in Nanoporous Polymers from Coumarin Photo-Cross-Linked Columnar Liquid Crystals, *Macromolecules,* 2018, **51**, 2349−2358.

[42] A. Concellón, T. Liang, A. P. H. J. Schenning, J. L. Serrano, P. Romero and M. Marcos, Proton-conductive materials formed by coumarin photocrosslinked ionic liquid crystal dendrimers, *J. Matter. Chem. C,* 2018, **6**, 1000–1007.

[43] H. Cabral, K. Miyata, K. Osada and K. Kataoka, Block Copolymer Micelles in Nanomedicine Applications, C*hem. Rev*., 2018, **118**, 6844-6892.

[44] M. Abad, M. Nardi, L. Oriol, M. Piñol and E. Blasco, Aqueous seeded RAFT polymerization for the preparation of self-assemblies containing nucleobase analogues, *Polym. Chem.,* 2023, **14**, 71-80.

[45] L. Rui, L. Liu, Y. Wang, Y. Gao and W. Zhang, Orthogonal Approach to Construct Cell-Like Vesicles via Pillar[5]arene-Based Amphiphilic Supramolecular Polymers, *ACS Macro Lett*., 2016, **5**, 112-117.

[46] L. Shao, B. Hua, J. Yang and G. Yu, Pillar[7]arene-based host–guest complex in water: dual-responsiveness and application in controllable self-assembly, *RSC Adv.,* 2016, **6**, 60029-60033.

[47] G. Yu, W. Yu, Z. Mao, C. Gao and F. Huang, A pillararene-based ternary drug-delivery system with photocontrolled anticancer drug release, *Small*, 2015, **11**, 919-925.

[48] D. Wang, T. Zhang, B. Wu, C. Ye, Z. Wei, Z. Cao and G. Wang, Reversibly Photoswitchable Dual-Color Fluorescence and Controlled Release Properties of Polymeric Nanoparticles, *Macromolecules,* 2019, **52**, 7130-7136.

[49] Y. C. Gong, X. Y. Xiong, X. J. Ge, Z. L. Li and Y. P. Li, Effect of the Folate Ligand Density on the Targeting Property of Folated-Conjugated Polymeric Nanoparticles, *Macromol. Biosci*., 2019, **19**, 1800348-1800359.

[50] A. Concellón, E. Blasco, A. Martínez-Felipe, J. C. Martínez, I. Šics, T. A. Ezquerra, A. Nogales, M. Piñol, L. Oriol, Light-Responsive Self-Assembled Materials by Supramolecular Post-Functionalization via Hydrogen Bonding of Amphiphilic Block Copolymers, *Macromolecules,* 2016, **49**, 7825-7836.

Chapter 3

Preparation of Ionic Bent-Core Pillar[5]arenes for Proton Conduction and Self-Assembly Nanostructures

---

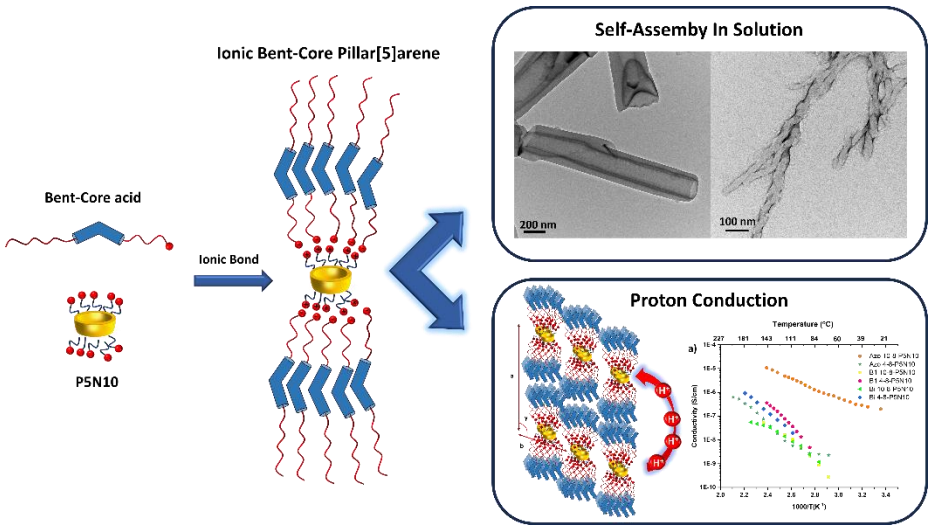

"I signed a contract with myself, I´m doing it"

Kobe Bryant

3.1 Introduction

3.1.1 Bent-core liquid crystals

Bent-core liquid crystals, also known as banana-shaped[1] liquid crystals, are a unique class of materials that exhibit fascinating properties and unique mesophases. Their bend shape sets them apart from conventional rod-shaped or discotic liquid crystals. Apart from the typical rigid bent-core structure, two more kind of molecules capable of generate bent-core mesophases have been described: hockey stick mesogens and dimers (**Figure 3.1**).

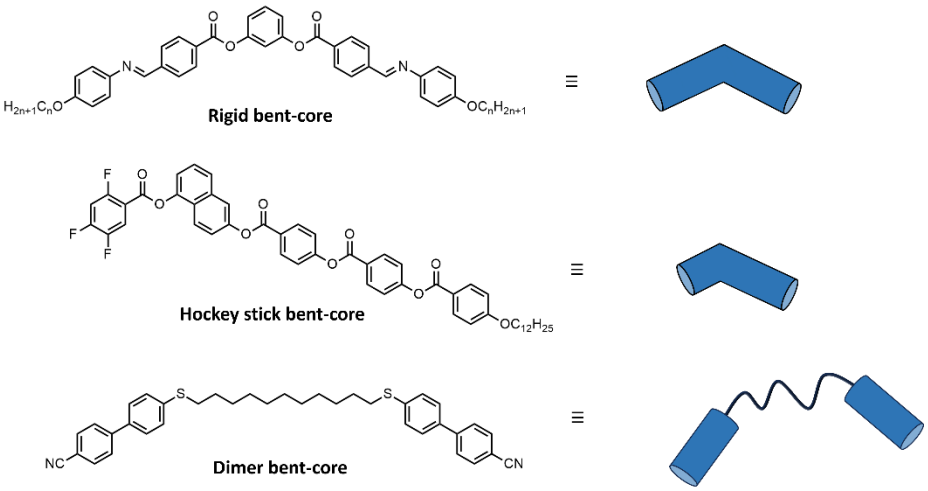

Figure 3.1. *Representation of the different types of bent-core mesogens.*

However, in most of the cases a rigid bent-core structure is employed, and in this molecular architecture a central nucleus supplies the angular shape. This curvature is provided by different rigid aromatic moieties such as 1,3-phenylene,[2] 3,4'-biphenylene[3] and 2,7-naphthalene;[4] these nuclei organize the lateral structures with an angle of around 120º. Furthermore, lateral chains incorporate aromatic rings joined by several functional groups such as azobenzene, biphenyl, imine, ester… The number of aromatic rings, the nature of functional groups and the terminal alkyl chains affect the kind of mesophase, the stacking of the bent-core molecules and the properties of the material.

One crucial aspect of the bent-core structure is the number of aromatic rings: typically, these molecules possess 5, 6 or 7 aromatic units constituting the rigid part of the molecule. Their presence not only affect the length and rigidity of each individual bent-core molecule, but the aromatic rings of neighboring molecules also interact by π-π stacking, modifying the properties and mesomorphic behavior. For example, the rotation of the single molecules is hindered by the stacking and the geometry of the structures, generating a polar phase (**Figure 3.2**). Moreover, if we consider the inclination of the molecules produced by the stacking, the result is a supramolecular chirality[5,6,7] in the mesophase and bulk material.[8]

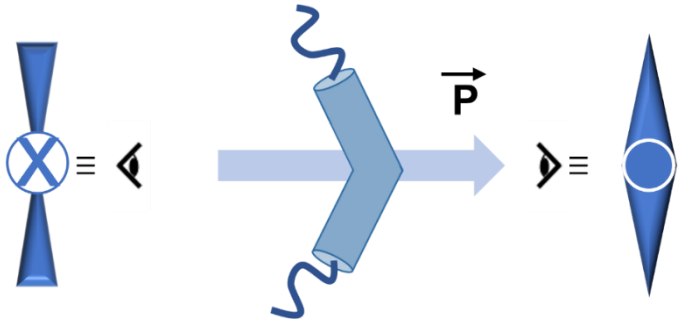

Figure 3.2. *Schematic representation of a bent-core molecule and its polarization vector.*

The above mentioned different functional groups in the lateral chains, have an impact in the properties and applications. For example, the kind of mesophase, its thermal range or the isotropization temperature are tuned by the bent-core structure and the terminal alkyl chains. But the application of the material is related with the functional group present in the structure: azobenzene,[9,10] cyanostilbene,[11] etc. Finally, terminal chains are essential in the stacking and microsegregation in the mesophase, affecting the molecular order in the material. Recently, this subject has been explored, substituting classical alkyl chains by fluorinated,[12] silyl[13] or oligo(ethyleneglycol)[14] chains, resulting in different mesophases and supramolecular assemblies. Lateral chains pave the way to introduce reactive groups in the bent-core structure. For example, recent works in the area have used photopolymerizable units (methacrylate,

acrylate or vinyl)[14,15] (**Figure 3.3**) or carboxylic acids capable to react with different dendrimers such as PPI,[16] PAMAM or PEI.[17]

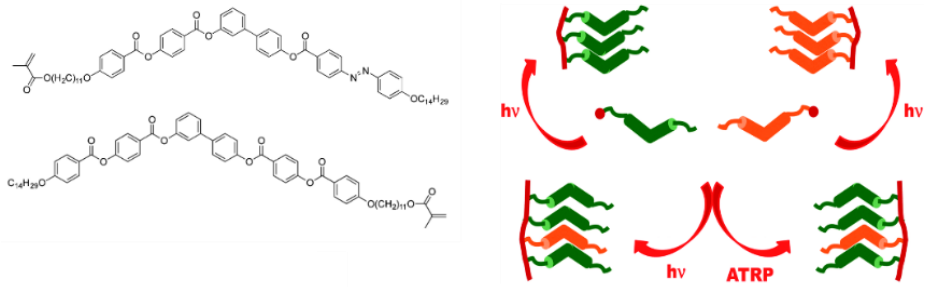

Figure 3.3. *Examples of photopolymerizable bent-core molecules and different kinds of polymers containing bent-cores (adapted from reference 3).*

The unique properties of bent-core molecules have enabled the discovery of novel classes of mesophases, which are associated with the polarity and inclination of the molecules within different layers.

The novel bent-core mesophases can be classified in several groups, among which polar mesophases stand out by their interesting properties: the most extensively studied mesophase to date is known as **SmCP**. In this mesophase, molecules are organized into layers, resembling the arrangement seen in the smectic A phase. However, in the **SmCP** phase, the molecules forming the layers are densely packed and tilted with respect to the normal layer. This strong packing produces a dipole in the layers that, added to the bent-shape of the molecules, generates a supramolecular chirality in each layer. However, these materials are composed of multiple layers, and the orientation of each layer determines the overall chirality of the material. As a result, the mutual orientation of consecutive layers gives rise to two distinct behaviors: ferroelectric and antiferroelectric. In the case of ferroelectric materials, the orientation of successive layers is the same, whereas in the case of antiferroelectric materials, the orientation alternates (**Figure 3.4**).

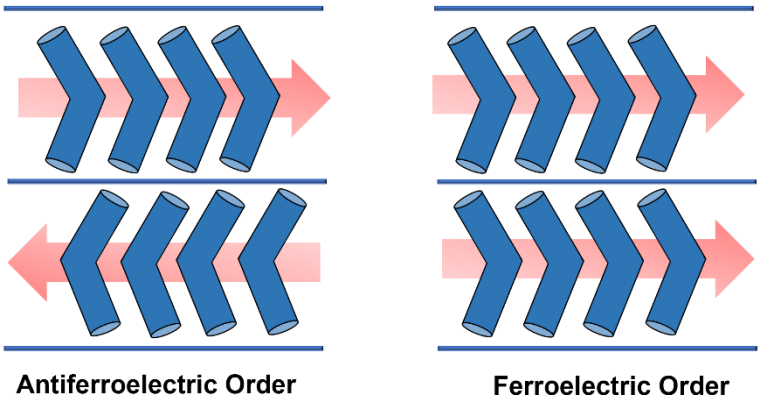

Figure 3.4. *Representation of the bent-core order between layers.*

Antiferroelectric materials offer greater stability compared to ferroelectrics due to their ability to generate a smaller excluded volume. However, in the field of nanotechnology, ferroelectric materials hold greater value. Considering these characteristics, a change in orientation or tilt will result in different layer chirality, influencing the specific type of mesophase: two polar (**SmC_SP_F** and **SmC_AP_F**) and two chiral mesophases (**SmC_SP_F** and **SmC_AP_A**), (where C_S means synclinic, C_A anticlinic, P_F ferroelectric and P_A antiferroelectric) **(Figure 3.5)**.[18]

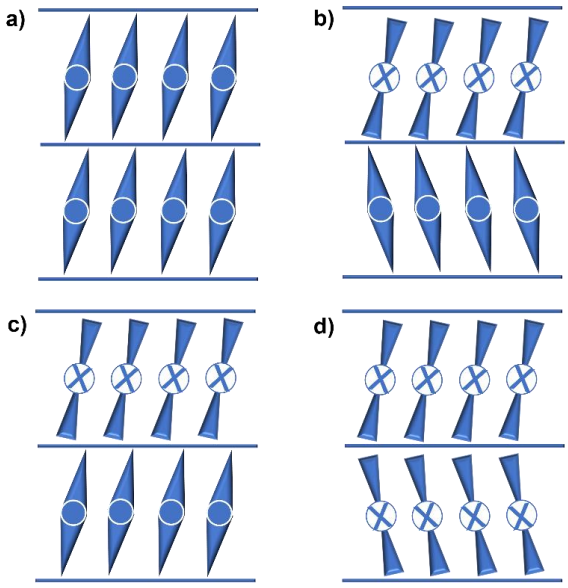

Figure 3.5. *Molecular order in the layers of the SmCP mesophase: a) Synclinic ferroelectric, b) anticlinic antiferroelectric, c) synclinic antiferroelectric and d) anticlinic ferroelectric.*

Ferro and antiferroelectric materials exhibit interconversion in presence of an external electric field and, in this process, molecules rotate inside the layers. The rotation could be produced around the long axis of the molecule (with an inversion of the chirality because of an inversion of the polarity) or with a rotation in the tilt cone, keeping the chirality. This tunable transition from anti to ferroelectric makes these materials a powerful tool in several applications.

One more outlined mesophase is the polar smectic A, **SmAP**. Its main characteristic is the stacking in layers, but, in contrast with **SmCP**, their molecules are not tilted in the layers.

Among the unique mesophases, the "**Dark conglomerate**" (**DC**) and the "**Helical nanofilaments**" (**HNFs**)[19] have attracted the attention of the science community because of their chirality. Regarding **Dark conglomerate**, its structure is similar to **SmCP** but, after a strong tension, the layers start to twist producing a 3D network with a sponge shape where the empty volume is filled with the smectic layers (**Figure 3.6**).[20] A periodicity between layers of 5-6 nm has been described in the sponge structure.[21] Some of its main characteristics are macroscopic chirality, low birefringence and response to electric fields.

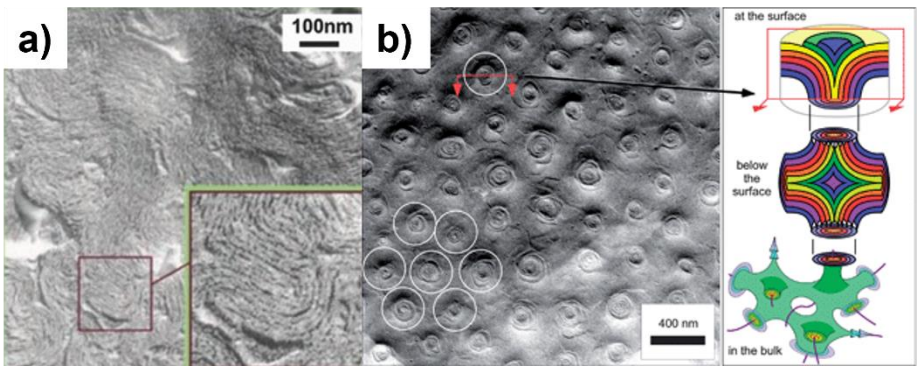

***Figure 3.6**. TEM images (a,b) and schematic representation (c) of DC mesophase (adapted from references 19 and 20).*

One of the most studied mesophases in the field of bent-core liquid crystals is **Helical nanofilaments**.[22] Its structure is close to **SmCP**; however, the layers are twisted helicoidally, this torsion being the

result of a strong stacking between bent-core molecules. In contrast with **DC**, these layers do not collapse into a 3D network, and the result is a unique helical chiral filament (**Figure 3.7**). The dimensions of the filaments (length, width and inter-layer distance) can be measured with different techniques such as XRD, TEM, SEM and AFM.[23]

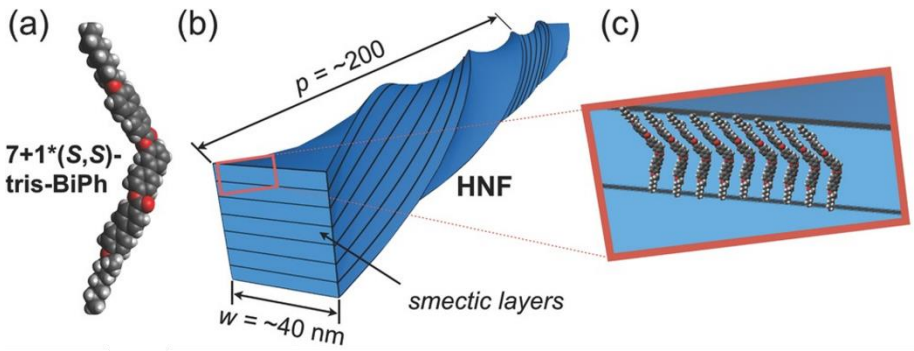

Figure 3.7. *Representation of the HNF mesophase and its dimensions (adapted from 21).*

The applications of **HNFs** have awakened the interest in different fields, for example in biological systems, where they can be employed to transfer the chirality through different scales by intermolecular forces and sergeant-soldier or majority-rule effects.[24,25]

Another intensively discussed topic is the use of **HNFs** for developing chiroptical materials with high luminescence.[26,27] A project developed by *prof. Hegmann* is based on the process of aggregation-induced emission (AIE) of circularly polarized luminescence.[27] In this case the aggregation process of the bent-core materials takes place in presence of a guest dye, producing a chiral HNF phase with the fluorescent dye in the interior of the layers and resulting in a chiral fluorescent signal (**Figure 3.8**).

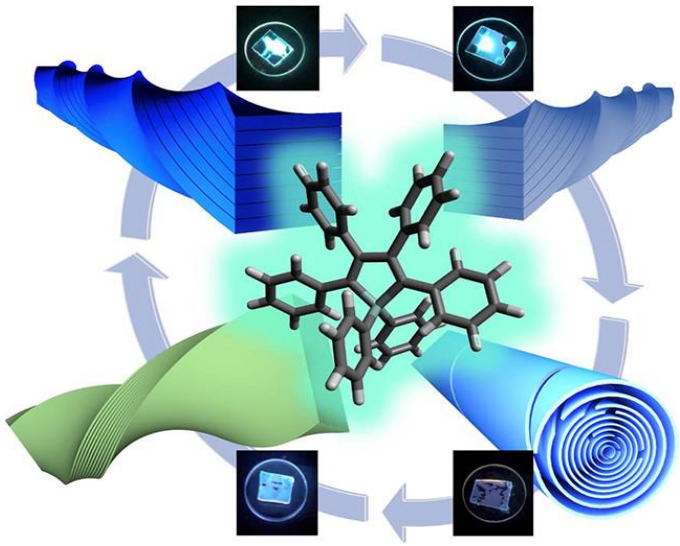

Figure 3.8. *Fluorescent helical nanofilaments (**HNFs**) obtained from reference 27.*

Finally, bent-core molecules may exhibit mesophases in which the lamellar order has failed. As it was mentioned before the macroscopic polar order is not favored by several repulsions, resulting in an unstable layer arrangement. Among the most studied lamellar failed mesophases are **modulated smectic mesophases** and **columnar mesophases (Figure 3.9)**. For the **modulated smectic mesophase (B7),** molecules are located in layers but suffering a progressive, changing inclination. This fact results in a reduction of the macroscopic polarity without any internal order. The **columnar mesophase,** also known as **B1,** is a lamellar mesophase but characterized by an ordered sequence of steps in the lamellar order, giving rise to columns in the perpendicular direction to the steps. Macroscopic steps are periodic and are favored by the interaction of terminal alkyl chains, producing an effective stacking between layers.

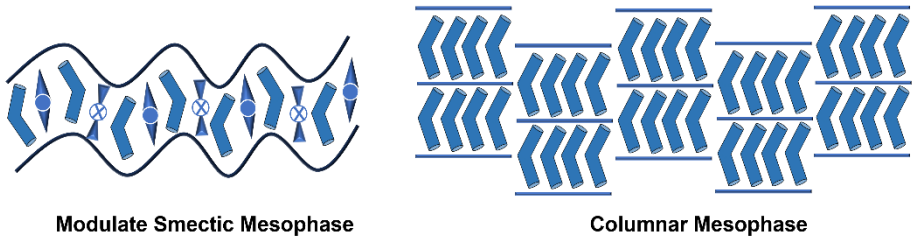

Figure 3.9. *Representation of modulated and columnar mesophases for bent-core molecules.*

3.1.2 Supramolecular bent-core liquid crystals

Bent-core molecules have demonstrated their applicability in several fields with extraordinary properties and very special mesophases that stand out from the classical liquid crystals. Recent investigations have focused their attention on the incorporation of bent-core structures in supramolecular systems. Some of the most studied approaches are the preparation of ionic bent-core supermolecules based on ionic dendrimers,[28,29] inclusion of salts in the bent-core structure[30] or synthesis of ionic bent-core derivatives.[31,32] These routes look for the combination of their most interesting properties: bent-core molecules mainly provide unique mesophases, stacked structures and a great versatility in their scaffold with all kinds of functional groups; the incorporation of a ionic structure imparts an amphiphilic character to the supermolecule, enabling the formation of chelate systems and offering applicability in a wide range of purposes, such as ionic conductivity,[33] solid electrolytes[34] or preparation of nanoaggregates.

As it was explained in ***Chapter 1*** **"Introduction",** dendrimers are hyperbranched macromolecules with a controlled structure, characterized by the repetition of specific chemical groups. They possess high molecular weight while remain monodisperse, making them highly interesting molecules for several applications. Different articles in the bibliography described the formation of ionic liquid crystals using commercially available dendrimers such as PPI or PEI, which facilitate the incorporation of acid derivatives due to their commercial availability and the presence of terminal amines in their structure. These amines can easily react with carboxylic acids in a proton transference reaction $-NH_3^+/COO^-$ giving rise to an ionic pair. The ionic reaction has been studied by several groups in the field of liquid crystals, resulting in a wide variety of structures,[35] mesophases and different applications of these materials.[36,37,38] However, the examples of ionic bent-core dendrimers is reduced.

The preparation of bent-core ionic macromolecules based on PPI and PEI has been extensively explored in the group of *Liquid Crystals and Polymers.*[28,29] *J. Vergara et al.*[17] published the firsts examples of ionic

bent-core liquid crystals, using PPI and PEI as dendritic cores **(Figure 3.10).** In this systematic work several parameters were studied (number of aromatic rings in the bent-core molecule, short and long terminal chains…). They found that all ionic compounds showed LC behavior (**Col$_r$** and **SmCP**), in contrast with the precursory bent-core acids, none of which showed it.

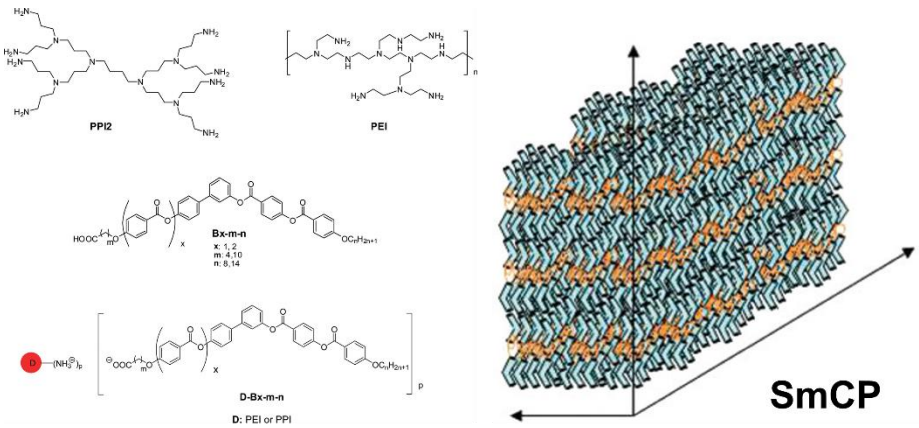

Figure 3.10. *Ionic bent core molecules with dendritic cores (left) and representation of their* ***SmCP*** *mesophase (right) adapted from reference 17.*

After that, *Cano et al.*[28] expanded the knowledge in the topic with the preparation of chiral bent-core molecules introducing chiral terminal chains in the structure. Furthermore, they demonstrated the aggregation of these molecules in water giving rise to different morphologies such as fibers, helical ribbons, spheres, etc. **(Figure 3.11)**. This discovery opened a stream of study because the bent-core structure alone did not aggregate. However, the presence of the ionic bonds allowed the formation of aggregates because of the amphiphilic character of the supermolecules.

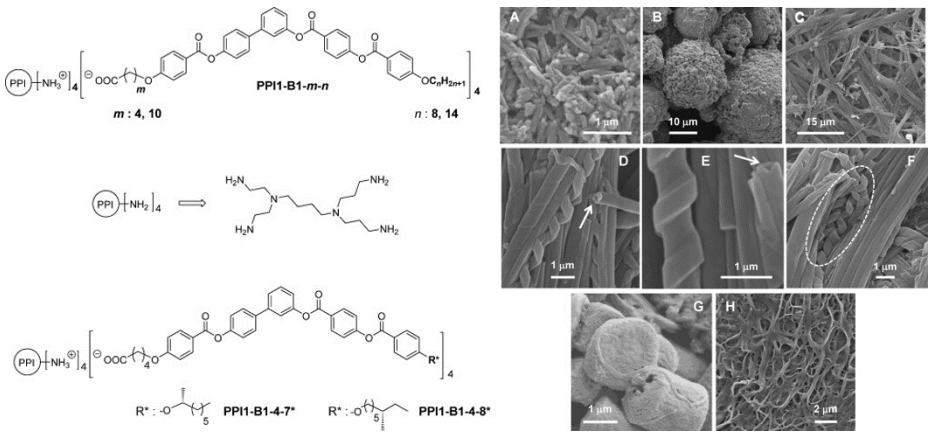

Figure 3.11. *Chiral ionic bent-core molecules with dendritic cores (left) and different morphologies obtained by SEM (right) adapted from reference 28.*

Subsequently, M. Castillo-Vallés developed several series of ionic bent-core liquid crystals during his PhD, employing two different strategies: one using PPI dendrimers and the other involving the functionalization of TEG terminal chains with lithium salts.[29,30,39] In one of these publications *M. Castillo-Vallés et al.*[30] demonstrated that the introduction of lithium salts stabilized the bent-core mesophases, as the precursors alone did not exhibit liquid crystal behavior. Furthermore, the combination of Li-TEG-BC as a supramolecular system has emerged in the field of organogels, owing to its amphiphilic character that has led to the formation of various 3D systems with distinct morphologies, such as fibers, tubes, and helical structures **(Figure 3.12).**

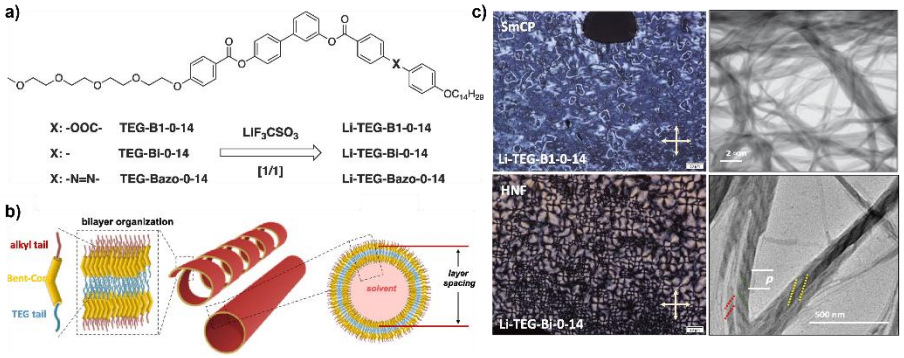

Figure 3.12. *a) TEG bent-core structures b) Schematic representation of the bilayer organization c) POM (left) and TEM (right) microphotographs of lithium derivatives (adapted from 30).*

In the light of the interesting results achieved by the ionic interactions in the BC liquid crystals field, another way to access that interesting ionic microsegregation capable of generating amphiphilic character in the supermolecules is the use of ionic heterocycles in the rigid structure of the bent-core molecule. Some reports in the bibliography have described imidazolium and pyridinium in the rigid structure.[31,32,40] *Ciastek-Iskrzycka et al.*[33] studied the use of imidazolium BC liquid crystals for ion conduction materials. They synthesized a series of paramagnetic stable radicals which exhibited smectic phases with weak antiferromagnetic interactions and conduction values between 10^{-5} and 10^{-8} S/cm (**Figure 3.13**).

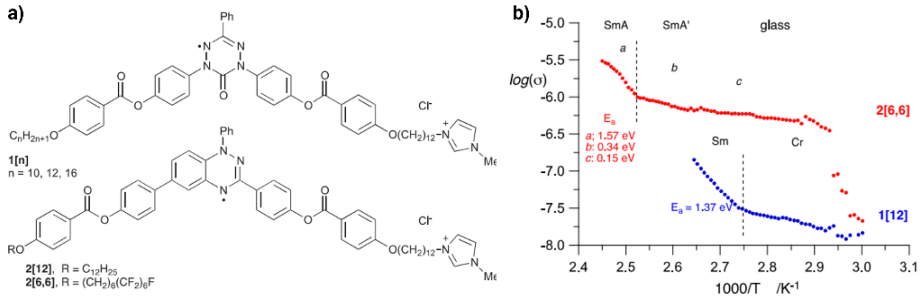

Figure 3.13. *a) Bent-core molecules containing imidazolium and stable radicals b) Variation in the ion conduction with temperature (from reference 33).*

3.2 Objectives

The main objective of this chapter is the preparation and the study of new ionic bent-core complexes combining a central core of pillar[5]arene functionalized with different bent-core acids. The segregation produced by the ionic pairs of the materials turned them in a very interesting tool in several applications including proton conduction, preparation of aggregates in water or optical response materials.

The pillar[5]arene will provide a rigid cylindrical shape that can run the formation of different nanoaggregates in solution and different mesophases in pure state. Its functionalization with amines allows the easy and fast formation of ionic bonds and turns these ionic pillar[5]arenes in potential materials for proton conduction **(Figure 3.14)**. Up to date, a few examples of liquid crystal pillar[n]arenes has been reported but none of them with ionic bent-core derivatives.

To achieve the general objective set, the following secondary objectives have been designed:

1. Synthesis and characterization of different bent-core carboxylic acids containing azobenzene, ester and biphenyl. In all three cases two bent-core molecules bearing two spacers (4 and 10 carbons) between the rigid structure of the bent-core and the carboxylic group have been prepared.
2. Synthesis and characterization of a pillar[5]arene containing amine terminal groups (**P5N10**). This compound was described in ***Chapter 2***.
3. Preparation, and structural and thermal characterization of the ionic materials.
4. Study of the proton conduction properties of the ionic materials.
5. Preparation of nanoaggregates in water using the co-solvent method.

The purpose of introducing different functional groups in the lateral bent-core arm is the study of their influence in the mesogenic properties, in their proton mobility and in the morphology of the aggregates in water. Moreover, the azobenzene, as photo-responsive unit, expands the possibilities: its isomerization with the appropriate wavelength can modulate the nanostructures obtained in solution. This isomerization turns the materials into switchable photo-responsive materials that also affect the proton conductive properties, as it has been reported previously.

The same comparison will be carried out with the length of the spacer. For instance, it has been demonstrated that short chains induce the formation of helical structures in a water solution. Once the mesophase and the aggregates are characterized, it will be possible to analyze the influence of the pillar[5]arene as a core, instead of the previously studied dendrimers, in the liquid crystal properties and the aggregates.

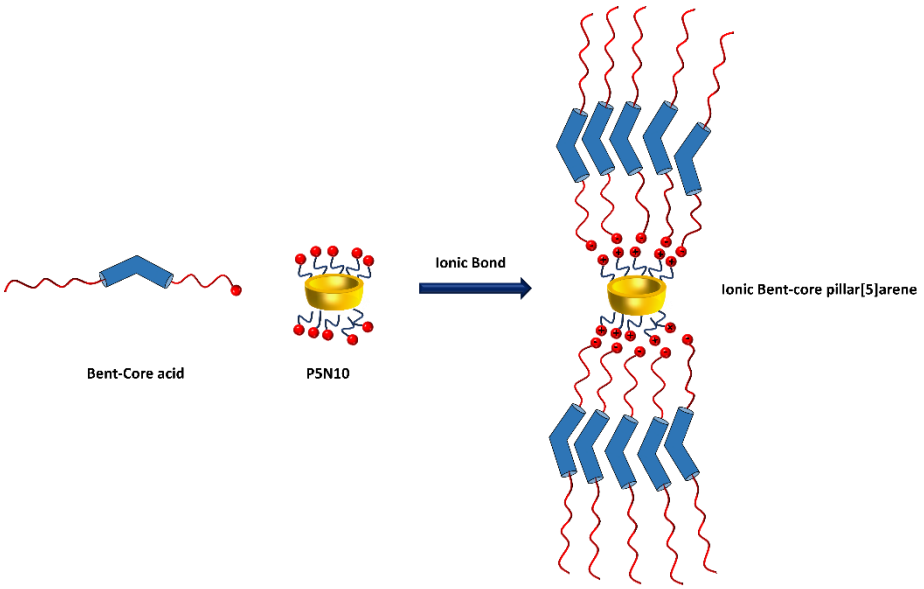

Figure 3.14. *Schematic representation of the ionic bent-core pillar[5]arene formation.*

3.3 Results and discussion

3.3.1 Synthesis and characterization of ionic bent-core pillar[n]arenes

The synthesis of the ionic bent-core pillar[5]arenes was carried out following procedures described in the literature.[29] The pillar[5]arene **P5N10** was addressed in ***Chapter 2***. Concerning the bent-core acids, they were prepared following a convergent synthesis using classical organic chemistry reactions such as Williamson etherification, Steglich esterification, hydrolysis, hydrogenation, etc. The synthetic procedure was considered in three different steps: 1) the preparation of three different acids containing an aromatic ester, biphenyl or azobenzene unit with an alkyl terminal chain of eight carbons. 2) Synthesis of two hydroxy-substituted biphenyl molecules with two different spacers (4 or 10 carbons) between the aromatic rings and the protected carboxyl group. This terminal acid was protected with two different groups: benzyl (for ester and biphenyl derivatives) or trimethylsilyl (for azobenzene derivatives) (**Figure 3.15**).

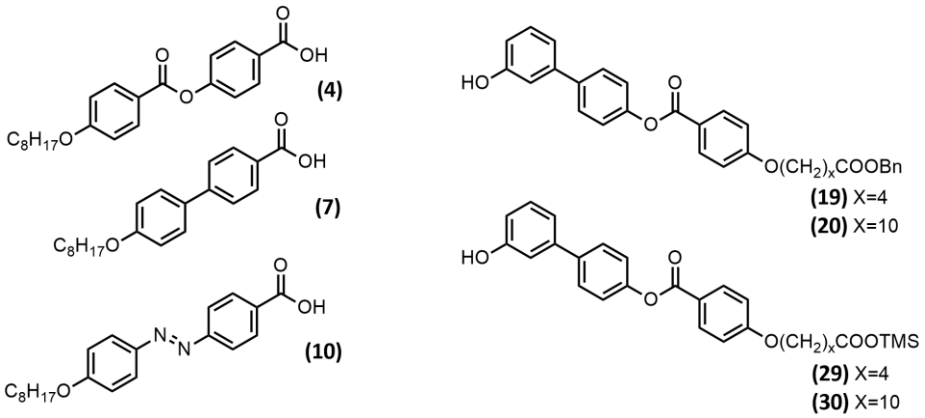

Figure 3.15. *Molecules used in the synthesis of the bent-core acids.*

3) The esterification reaction between the three acids and the two hydroxyl-substituted compounds and the corresponding deprotection (hydrogenation for ester and biphenyl bent-cores and an acid treatment with TFA for azobenzene derivatives). This procedure led to the preparation of six different acids, with a large and a short spacer for each family (ester, biphenyl or azobenzene) (**Figure 3.16**).

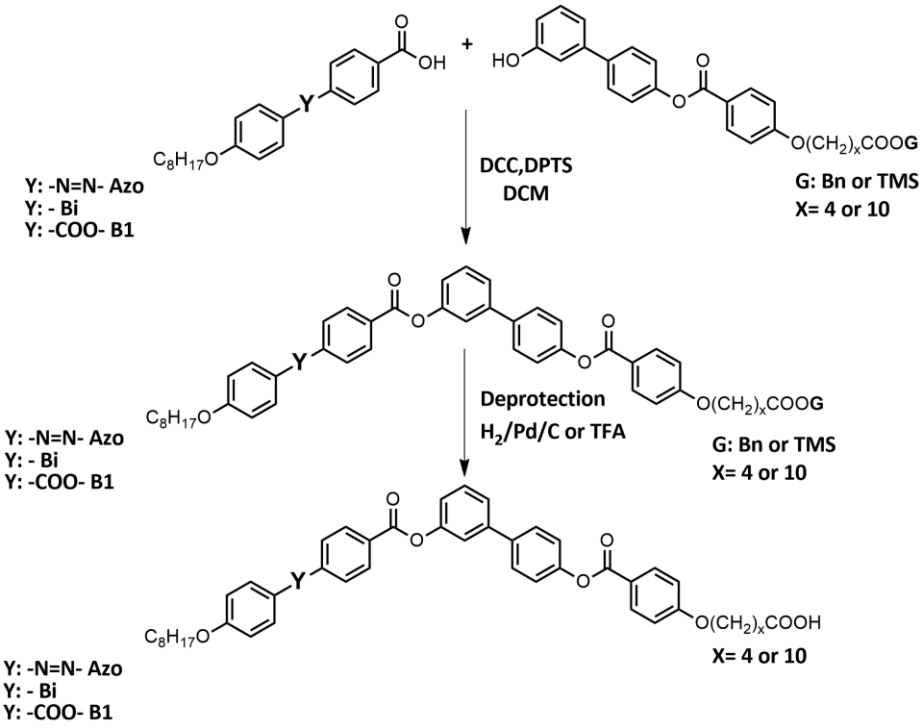

Figure 3.16. *General procedure for the synthesis of the bent-core compounds: esterification-deprotection.*

Once the bent-core acids and pillar[5]arene **P5N10** were characterized, the procedure to obtain ionic pillar[5]arenes was the typical for ionic dendrimers: a solution of the corresponding acid and a solution of **P5N10** in proportion 10:1 (both in THF) were mixed, ultrasonicated for 10 minutes and slowly evaporated at room temperature until the weight of the solid obtained remained stable. (**Figure 3.17**)

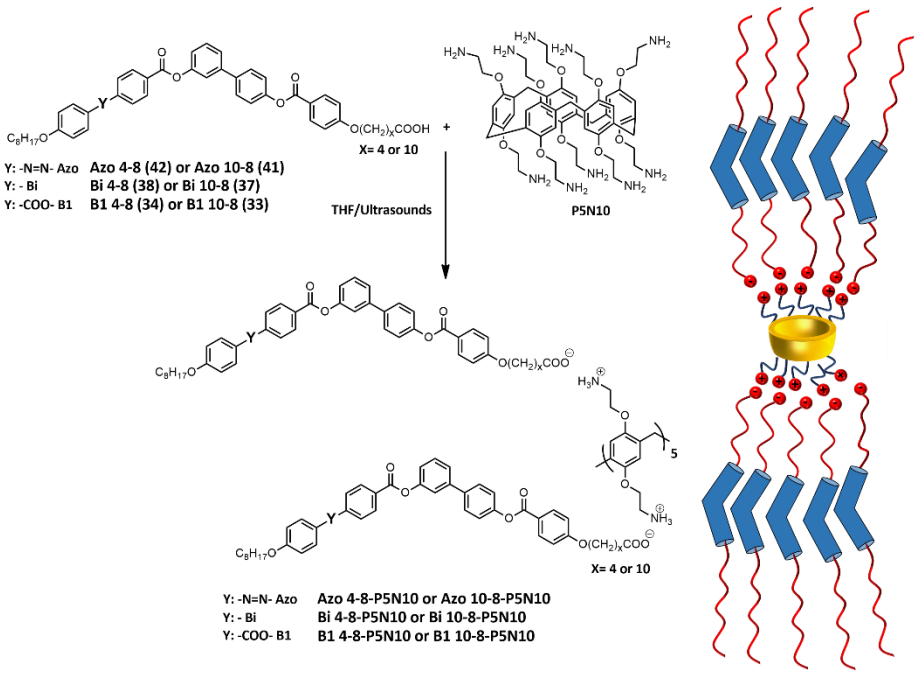

Figure 3.17. *Preparation of ionic bent-core pillar[5]arenes.*

The characterization of the ionic complexes was carried out with the classical techniques FT-IR, ^{1}H-NMR, ^{13}C-NMR (see **3.6 Appendix** section). As an example of the ionic salt formation, comparison of the FT-IR of **Azo 4-8-P5N10, P5N10 and Azo 4-8** is shown in **Figure 3.18:** the dimer stretching absorption of the amino groups in **P5N10** disappeared and a broad band appeared around 3429 cm^{-1} because of the ionic bond formation (**Figure 3.18a**). Attending to the carbonyl zone (**Figure 3.18b**), the acid **Azo 4-8** showed two bands from the dimeric (1697 cm^{-1}) and free (1734 cm^{-1}) forms of the carboxylic acid. However, in the ionic pillar[5]arene the dimeric band disappeared, and two new bands appeared because of the symmetric and asymmetric vibrations of carboxylate (1580 and 1314 cm^{-1}).

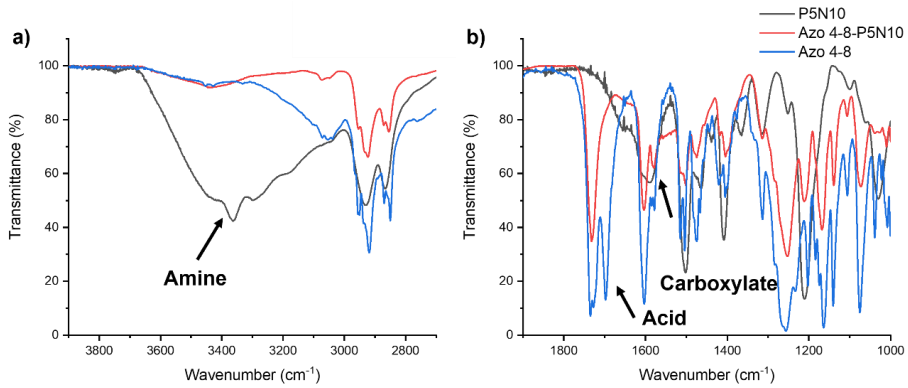

Figure 3.18. *Comparison of the FT-IR spectra of* ***P5N10*** *(black line),* ***Azo 4-8-P5N10*** *(red line) and* ***Azo 4-8*** *(blue line) in different regions.*

The ^{1}H-NMR experiments also confirmed the formation of the ionic bond; for instance, in **Figure 3.19** the spectra of **B1 4-8**, **P5N10** and **B1 4-8-P5N10** were compared. A broad band appeared at 5.75 ppm in the **B1 4-8-P5N10** ^{1}H-NMR spectrum because of the ammonium salt (-NH_3^+). Moreover, several shifts in the peaks were observed both in acids and **P5N10**. These changes were mainly located in protons next to the carbonyl and the amine: -C$\underline{H}_2$COO$^-$ (signal c) was shifted upfield from 2.48 to 2.36 ppm, -C$\underline{H}_2$NH$_3^+$ (signal a) downfield from 2.88 to 3.38 ppm and -OC$\underline{H}_2$CH$_2$NH$_3^+$ (signal d) from 3.80 to 3.96 ppm. The aromatic signals of the bent-core acid suffered small displacements due to the interaction between different bent-core units. One of the main characteristics of the bent-core structure is its stiffness, which produces a π-π interaction between the aromatic rings of different bent-core units. The influence of this interaction is evident in the ^{1}H-NMR spectra through observable shifts in the aromatic protons peaks.

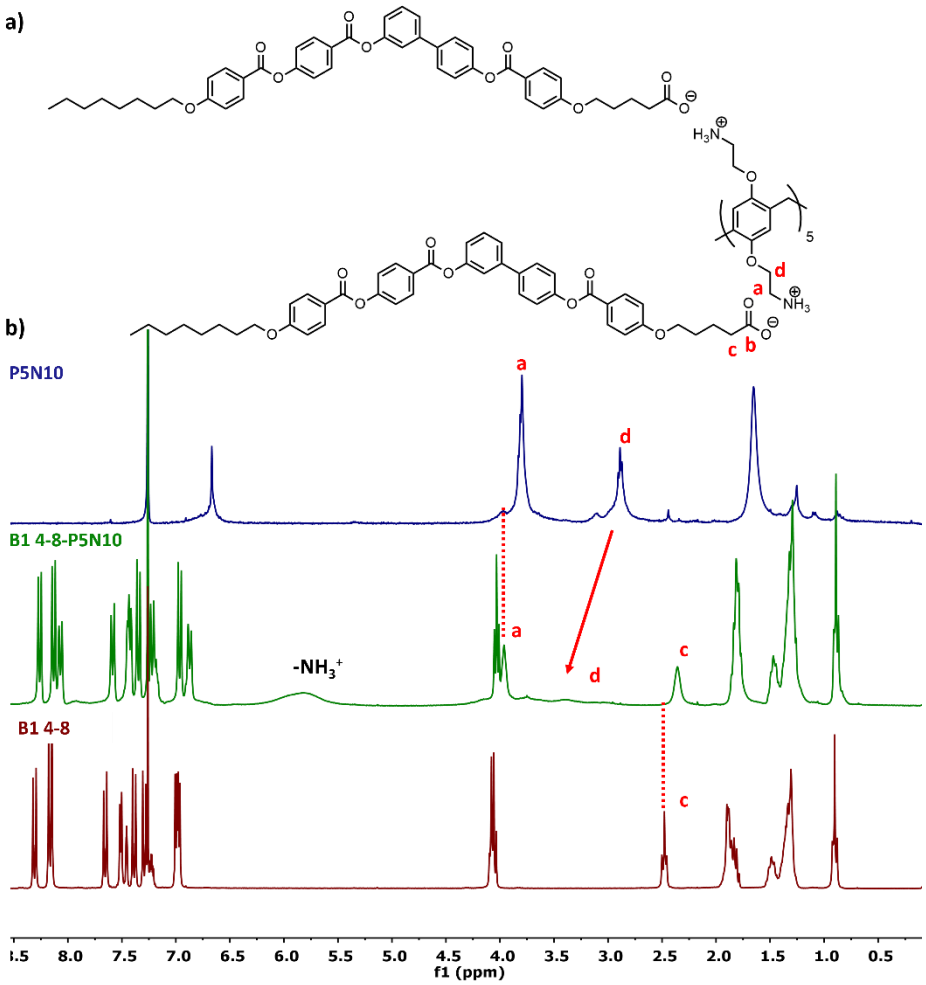

Figure 3.19. *a)* ***B1 4-8-P5N10*** *structure b) Comparison of the* ^{1}*H-NMR spectra (*$CDCl_3$*, 298K, 400 MHz) of* ***P5N10***, ***B1 4-8-P5N10*** *and* ***B1 4-8****.*

Regarding ^{13}C-NMR **(Figure 3.20)**, several shifts confirmed the formation of the ionic bond: the carbonyl group (signal a) suffered a shift from 178.80 to 179.60 ppm, and signals in the proximity to the ionic bond supports the formation of the ionic pillar[5]arene (see experimental section). The π-π interaction between bent-cores reflected before in ^{1}H-NMR spectra emerged too in the ^{13}C-NMR; for example, signals b and c of the central rigid core shifted upfield.

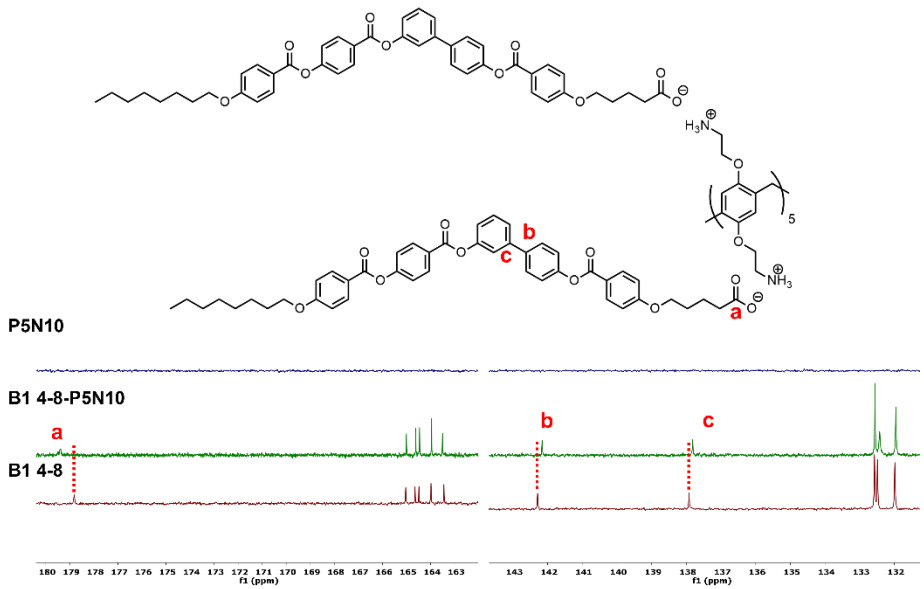

Figure 3.20. *Comparison of the ^{13}C-NMR ($CDCl_3$, 298K, 100 MHz) spectra of* ***B1 4-8***, ***B1 4-8-P5N10*** *and* ***P5N10****.*

3.3.2 Thermal characterization and mesogenic behavior

The thermal properties of the ionic complexes were studied with the standard techniques for liquid crystals: polarized optical microscopy (POM), thermogravimetry (TGA), differential scanning calorimetry (DSC) and X-ray diffraction (XRD) at variable temperature. These techniques are complementary, and their different experimental conditions (rate of heating/cooling or amount of sample) explain slight differences in the results. In all cases the compounds exhibited good stability as it was demonstrated by TGA, revealing decomposition temperatures higher than the isotropization temperature. The ionic complexes exhibited liquid crystal behavior over a wide temperature range, enabling their use as proton conductive materials. In contrast with the precursory acids that present crystalline structure, POM observations (**Figure 3.21**) revealed fluid and birefringent materials for **Azo** and **B1** complexes with classical textures of liquid crystals. However, **Bi** derivatives were less fluid and birefringent, suggesting a different kind of mesophase for these compounds. It is remarkable

that POM examination did not reveal any crystallization process in any of the compounds.

DSC experiments were carried out to determine phase transitions in the materials and their enthalpies (see **Appendix** section **3.6.3**), and these data are collected in **Table 3.1** (from second cycle out of three). However, some of the isotropization points were established by POM observations. All bent-core pillar[5]arenes presented liquid crystal behavior. For **B1** derivatives DSC curves displayed a glass transition, which means that the mesophase freezes on cooling until room temperature, observing crystallization with time. However, **Azo** and **Bi** compounds undergo a phase transition during the cooling process that can be assigned to crystallization.

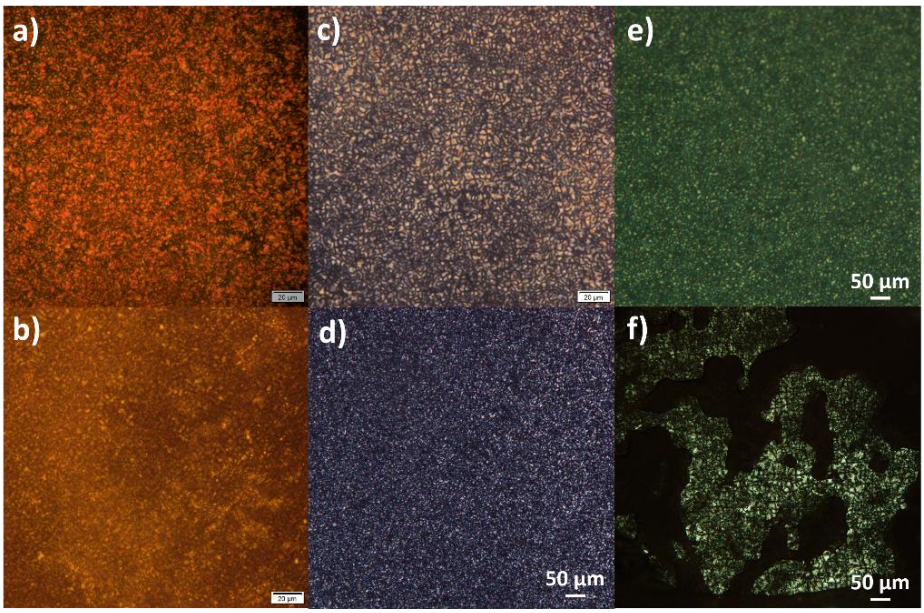

Figure 3.21. *POM textures in the cooling process of a)* ***Azo 4-8-P5N10*** *at 169ºC, b)* ***Azo 10-8-P5N10*** *at 125ºC, c)* ***B1 4-8-P5N10*** *at 85ºC, d)* ***B1 10-8-P5N10*** *at 130ºC, e)* ***Bi 4-8-P5N10*** *at 140ºC, f)* ***Bi 10-8-P5N10*** *at 110ºC.*

It is worth mentioning that POM observations and DSC curves were reproducible after several cycles, confirming that none of the ionic compounds suffered degradation after the isotropization point as happened in some of the ionic bent-core materials studied in the bibliography.

The specific kind of mesophase of each ionic bent-core pillar[5]arene was determined by XRD at variable temperatures. Each material was studied carefully at different temperatures depending on its phase transitions, isotropization temperature, etc. Overall, the materials were studied at room temperature before the first heating cycle, in the cooling cycle at several temperatures after reaching the isotropization point and finally at room temperature to examine the evolution of the XRD diffractogram throughout the heating-cooling cycle.

Table 3.1. *Thermal properties of the bent-core pillar[5]arenes.*

Compound	$T_{2\%}$[a](°C)	Phase transitions[b]
B1 4-8-P5N10	169	Cr 78 Col_{ob} 140 I*
B1 10-8-P5N10	221	Cr_1 118 Cr_2 126 Col_r 170 I*
Bi 4-8-P5N10	251	Cr 139 Col_r 170 I*
Bi 10-8-P5N10	190	Cr 104 Col_r 160 I*
Azo 4-8-P5N10	219	Cr 167 M 220 I
Azo 10-8-P5N10	194	Cr 120 Col_r 150 I

[a] *Temperature corresponding to a 2% weight loss.*

[b] *DSC data obtained on second heating at a rate of 10°C/min. Cr: crystal, Col_r: rectangular columnar, Col_{ob}: oblique columnar, I: isotropic liquid and M: indeterminate mesophase. *Data obtained from POM observations.*

For compound **B1 4-8-P5N10**, XRD diffractograms (**Figure 3.22**) displayed different reflections at low angle that were indexed in an oblique columnar mesophase at 110°C. The observed spacing allowed to obtain the cell parameters *a* and *b* (74.8 Å and 66.3 Å respectively) with an angle of 55.3° and a cell area of 4077.2 $Å^2$ at 110°C (**Table 3.2**). The broad band obtained at high angles corresponds to the diffuse halo characteristic of the mesophases caused by the alkyl chain interactions.

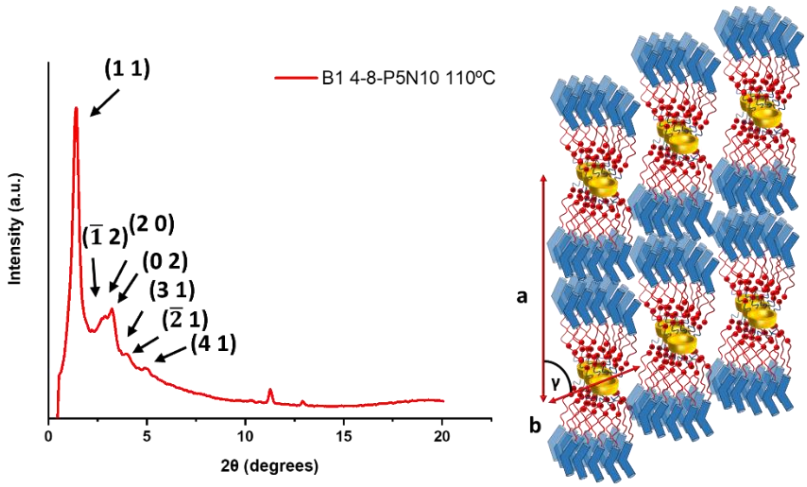

Figure 3.22. *XRD diffractogram of* ***B1 4-8-P5N10*** *at 110ºC and schematic representation of its oblique columnar mesophase.*

The long terminal chain ester derivative **B1 10-8-P5N10**, in contrast with the short chain analogue, showed six reflections at low angles that corresponds to a rectangular columnar mesophase with lattice parameters *a*=69.2 Å and *b*=83.3 Å and an area of 5764.4 Å^2 (**Table 3.2**). In this compound the XRD pattern (**Figure 3.23**) was taken at 170ºC. The diffractogram recorded at room temperature has not the features of a mesophase.

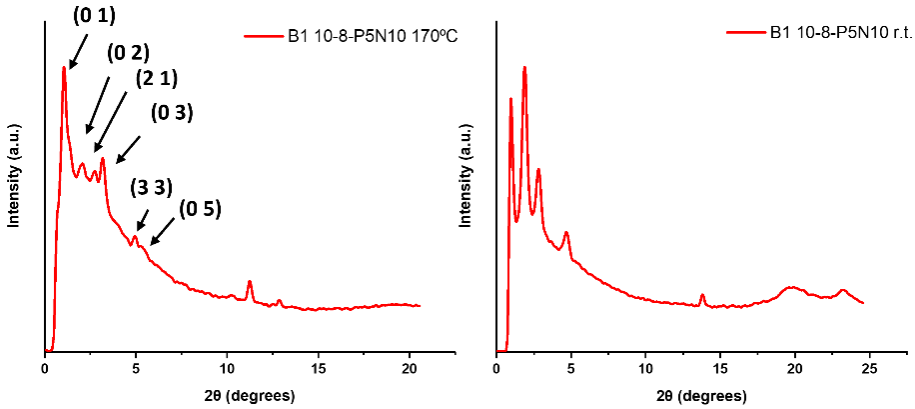

Figure 3.23. *XRD diffractograms of* ***B1 10-8-P5N10*** *at 170ºC and room temperature.*

Biphenyl pillar[5]arenes exhibited multiple reflections in the low angle region that can be indexed in a rectangular columnar mesophase, with

longer *a* parameter for the long chain compound, being 74.6 Å for **Bi 4-8-P5N10** and 110.8 Å for **Bi 10-8-P5N10 (Figure 3.24)**.

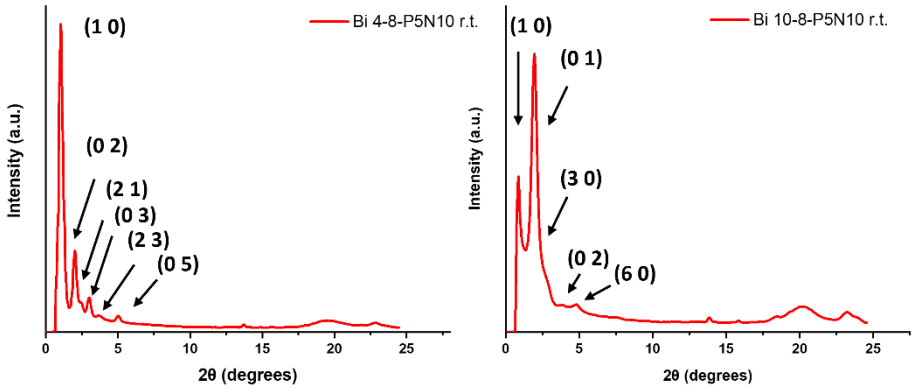

Figure 3.24. *XRD diffractograms of biphenyl derivatives.*

In the case of the Azo derivatives, they exhibited different behaviors. The short spacer **Azo 4-8-P5N10** tended to crystallize, as evident in its XRD patterns at several temperatures (90°C, 110°C, 130°C, etc.), displaying multiple reflections characteristic of a crystalline phase. However, the pattern recorded at 200°C is consistent with a mesophase and contains one main peak and a weak second-order reflection corresponding to a spacing of 55.6 Å; the lack of reflections does not allow to determine the specific mesophase. On the other hand, **Azo 10-8-P5N10** (**Figures 3.25** and **3.26**) exhibited a pattern of a rectangular columnar mesophase over a wide range of temperatures. This pattern was retained during cooling from isotropic liquid to room temperature, revealing a very slow crystallization process. The multiple reflections observed at low angles were indexed as a columnar mesophase with the following cell parameters: a = 91.6 Å, b = 90.0 Å, and A = 8244.0 $Å^2$

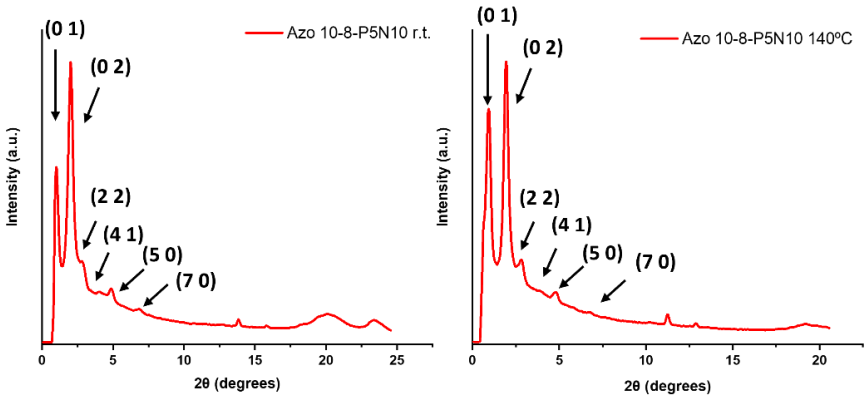

***Figure 3.25. Azo 10-8-P5N10** diffractograms at room temperature and at 140ºC.*

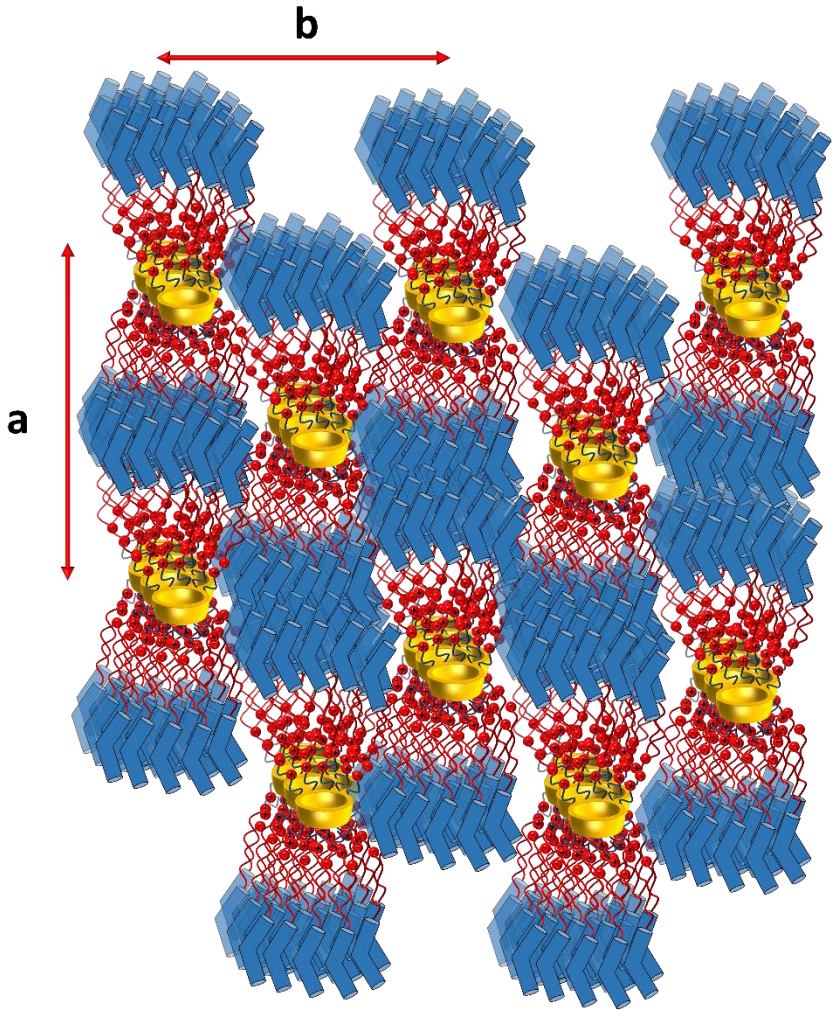

***Figure 3.26.** Schematic representation of the rectangular columnar mesophase of **Azo 10-8-P5N10**.*

Table 3.2. *Structural parameters of the bent-core pillar[5]arenes.*

Compound	Mesophase	d (Å)	Miller Index (hkl)	Structural Parameters[a]
B1 4-8-P5N10	Col_{ob} (110°C)	72.82 37.40 24.54 24.31 21.98 18.43 17.68	110 $\bar{1}10$ 200 020 310 $\bar{2}10$ 410	a=74.8 Å b=66.3 Å γ=55.3° A=4077.2 Å^2
B1 10-8-P5N10	Col_r (170°C)	83.30 41.65 31.95 27.76 17.74 16.66	010 020 210 030 330 050	a=69.2 Å b=83.3 Å A=5764.4 Å^2
Bi 4-8-P5N10	Col_r (140°C)	74.60 39.15 26.10 19.57 15.66	100 020 030 040 050	a=74.6 Å b=78.3 Å A=5841.2 Å^2
Bi 10-8-P5N10	Col_r (25°C)	110.80 46.71 39.93 23.35 18.46	100 010 300 020 600	a=110.8 Å b=46.7 Å A=5174.3 Å^2
Azo 4-8-P5N10	M (200°C)		100 200	a=55.6 Å

Azo 10-8-P5N10	Col_r (140ºC)	90.00 45.00 32.09 22.19 18.32 13.08 3.80	010 020 220 410 500 700	a=91.6 Å b=90.0 Å A=8244.0 Å^2

[a] *Area of the cell A=a*b for Col_r mesophase or A=a*b*sin(γ) for Col_{ob}.*

3.3.3 Proton conductivity studies

The ionic conductivity of the compounds was measured using the electrochemical impedance spectroscopy technique (EIS). The material was sandwiched between two ITO coated electrodes using spacers of 10 µm. Then, it was heated until isotropization temperature and allowed to cool down at 0.05ºC/min obtaining large, ordered domains. In these anisotropic materials a large order domain favors the mobility of protons between electrodes, obtaining better values of conductivity. In **Figure 3.27** we can see the typical curves obtained at each temperature for each compound. The point where the semicircle crosses the straight line is called "R" and is used to obtain the conductivity value. To obtain this value the following formula was applied:

$$\sigma = \frac{1}{R} * \frac{\alpha}{A}$$

Where α is the thickness (cm) of the cell, A (cm^2) is the area of the cell and σ is the conductivity of the cell (S/cm)

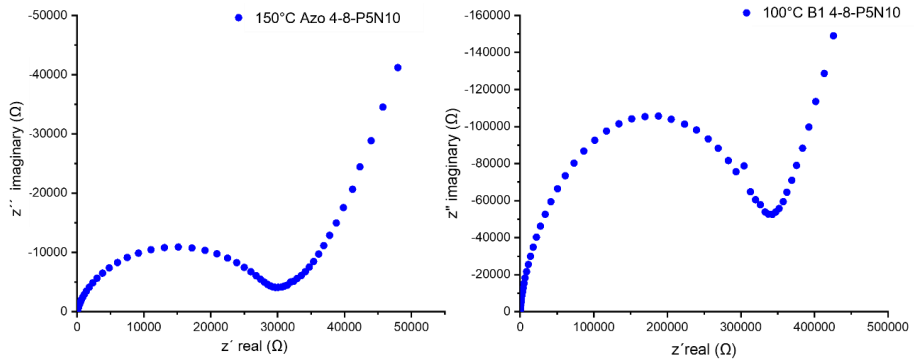

*Figure 3.27. Nyquist plots of **Azo 4-8-P5N10** at 150°C and **B1 4-8-P5N10** at 100°C.*

In **Figure 3.28a** the conductivity variation with temperature is represented for all ionic compounds, all of which exhibited proton conduction in a wide range of temperatures. We assign this conduction to proton conduction as the contribution of the charge transfer at the electrodes (sample – ITO) is very resistive (a spike towards low frequency in the Nyquist plots, **Figure 3.27**), a strong hint towards ionic conduction within the samples. Although they were studied from room temperature to the isotropization temperature of each material, only **Azo 10-8-P5N10** exhibited proton mobility at low temperatures. This well-ordered material is translated into proton mobility, observed from room temperature to the isotropic phase transition with an activation energy (Ea) of 1.30 eV. These values suggest that the material was highly ordered in the cell, leading to the best mobilities. Moreover, XRD patterns (**Figure 3.25**) revealed a material that retained the Col_r arrangement in the whole range of temperatures of cooling from isotropization point until room temperature but crystallizes after some time. For this reason, the material showed a good proton mobility in the whole range, despite showing a crystallization in DSC. However, in its homologue with a shorter spacer, **Azo 4-8-P5N10**, X-ray diffraction (XRD) experiments revealed a crystalline structure within a wide range of temperatures. The presence of a non-mesomorphic structure is reflected in the proton mobility values at low temperatures with similar activation energy (1.34 eV), resulting in less favorable outcomes compared to the azobenzene with a longer spacer.

Among the other functional groups investigated, **Bi** and **B1**, proton conduction was observed only after heating them above their respective transition temperatures. In the case of biphenyl derivatives, **Bi 4-8-P5N10** and **Bi 10-8-P5N10**, the compound with the shorter spacer exhibited higher conductivity values than its counterpart with the longer spacer, with activation energies (Ea) around 0.80 eV.
This disparity in the conductivity value indicates a better alignment of the mesophase in the compound with shorter spacer **Bi 4-8-P5N10**, enhancing the conductivity value.

For **B1 4-8-P5N10** and **B1 10-8-P5N10,** the behavior is the same as for the biphenyl compounds: a shorter spacer leads to better conductivity values with activation energies around 1.00-1.10 eV. Notably, these compounds exhibit different mesophases: Col_{ob} for **B1 4-8-P5N10** and Col_r for **B1 10-8-P5N10**. This divergence in mesophase suggests that the Col_{ob} mesophase offers dense packing within the cell, accommodating a higher number of ionic pairs in close proximity and, consequently, leading to enhanced conductivity values.

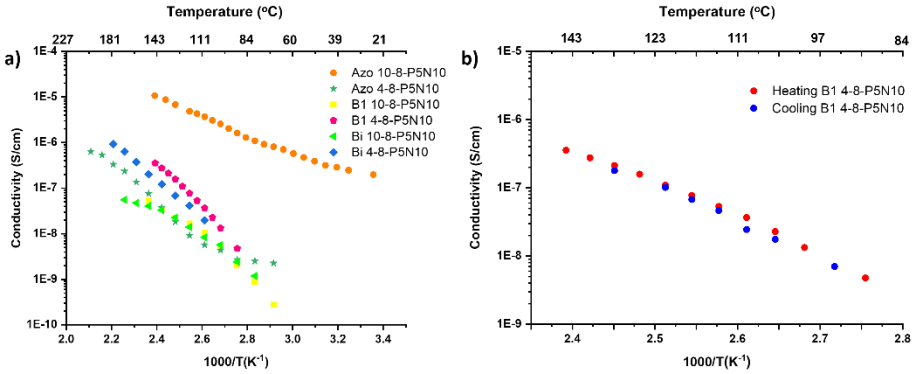

Figure 3.28. *a) Comparison of proton conductivity variation with temperature in all ionic compounds. b) Heating-cooling process in compound* ***B1 4-8-P5N10****.*

A fundamental consideration in these materials is their reproducibility and thermal stability during the heating-cooling measurement process. Some of the of ionic compounds (carboxylate-ammonium) described in the literature tend to suffer degradation at high temperatures or transformation of the ionic pairs into amide groups. This loss of ionic bonds results in a lower conductivity during the

cooling process. For this reason, all compounds were studied during the heating-cooling process and in **Figure 3.28b**, as an example, the complete cycle of **B1 4-8-P5N10** is shown. It is remarkable that the compound exhibited the same values at each temperature in both processes. This fact allows to affirm that this compound did not suffer any degradation after reaching the isotropization temperature. However, in some of the bent-core pillar[5]arenes studied the values obtained in the cooling cycle are slightly lower than in heating measures (see **Figure 3.58** in section **3.6 Appendix**). This difference is specially observed at lower temperatures and is attributed to charge carriers (H^+ or OH^-) caused by humidity in the first cycle of heating, but not related with degradation.

Exposure of the azobenzene cells (**Azo 10-8-P5N10** and **Azo 4-8-P5N10**) to UV light of 325 nm produced the photoisomerization of the azobenzene unit from *trans* to *cis*. This reversible process was observed by UV spectroscopy with a significant decrease in the intensity of the n–π* band and an increase in the intensity of the π-π* band at 500 nm (**Figure 3.29**). The isomerization reverts to the original state upon exposure to light or after some hours. Before coming back to the *trans* state, the proton conductivity of the compounds was measured again. Interestingly, in the irradiated cells the proton mobility disappeared even several hours after irradiation. The isomerization of the azobenzenes produced a disturbance in the planarity of the layers, removing the stacking between bent-core molecules that set up the column order. As a result, the long-distance order that benefits the proton mobility disappeared.

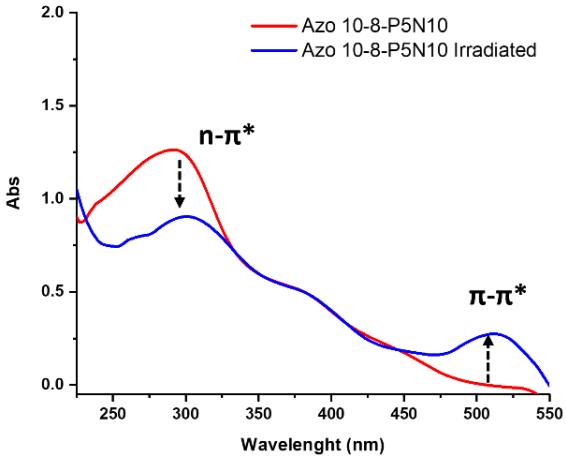

Figure 3.29. UV spectra of the non-irradiated and irradiated **Azo 10-8-P5N10** cell.

3.3.4 Aggregation studies

The next objective in this chapter is to study the aggregation of the ionic compounds in water. Bent-core structures are potential materials in the generation of supramolecular materials and chiral self-assemblies that have been studied in the last years in the Liquid Crystals and Polymers group.[39]

The preparation of nanostructures was carried out by the co-solvent method. This procedure is based on the addition of small aliquots (10 µL) of water over a solution of the ionic compound dissolved in THF (4 mg/ml) with smooth stirring. The self-assembly process was followed by turbidimetry recorded at a wavelength of 650 nm, after each addition of water (**Figure 3.30**). This value was chosen because the ionic compound does not absorb at this wavelength and the turbidity of the solution corresponds to the formation of nanostructures. This addition-measurement method was repeated until a sudden ascent in the turbidity value. At that point, the solution reached the critical aggregation concentration and after some additions the value barely changed. Then, the solution was dialyzed against water in a membrane of 1000 KDa for 2 days obtaining stable nanostructures dispersed in water.

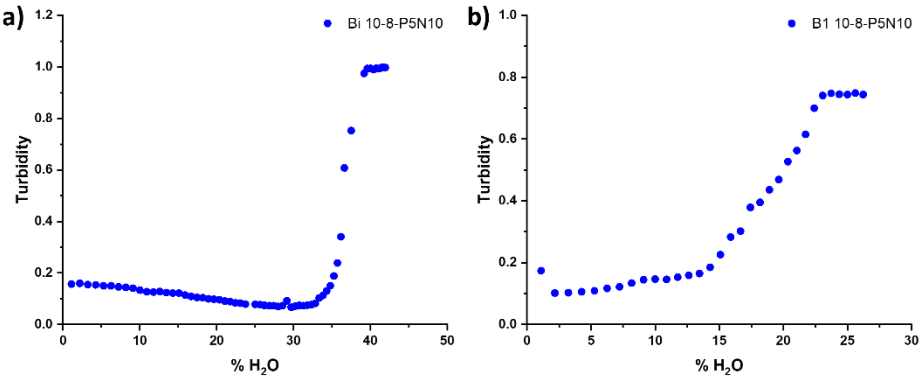

Figure 3.30. *Turbidity curves of* ***Bi 10-8-P5N10*** *(a) and* ***B1 10-8-P5N10*** *(b).*

The obtained nanostructures were studied by TEM. For these studies 10 µL of the solution were deposited over copper grids coated by graphite and they were dyed with uranyl acetate to obtain a better contrast. As it was mentioned in the objectives, one of the goals was to establish a relation between the functional group of the bent-core pillar[5]arene derivatives and the aggregates obtained in solution. First, Azo derivatives with long chain and with short chain were studied. It is worth mentioning that in both cases the TEM measurements were carried out on samples dialyzed and without dialyzing against water. Comparing dialyzed and non-dialyzed samples could yield insights into the self-assembly process in water or result in a more homogeneous sample. In the case of the long chain derivative, **Azo 10-8-P5N10**, the morphologies obtained were the same before and after dialyzing: helical fibers (**Figure 3.31**). The dimensions of the fibers were similar in both cases with 70-80 nm of pitch and with a width of the fiber around 25-30 nm. It is remarkable that in all images, these fibers did not evolve to gross ribbons, and they remained isolated without twisting over.

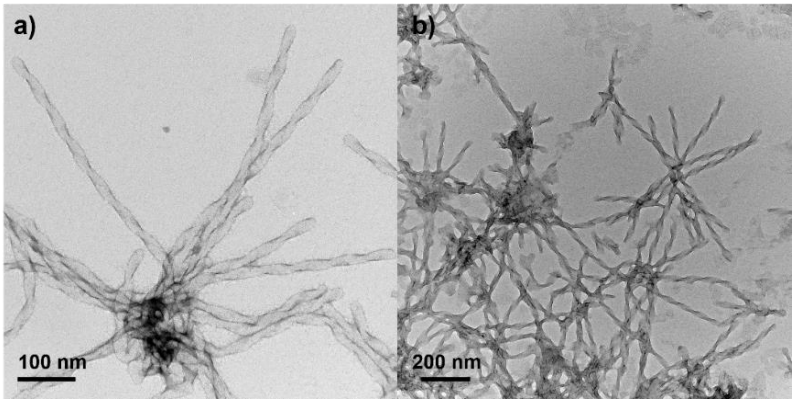

Figure 3.31. *TEM micrographs of* ***Azo 10-8-P5N10*** *dialyzed (a) non-dialyzed (b).*

In **Figure 3.32** TEM images of **Azo 4-8-P5N10** are shown. In this compound we can see an evolution of the aggregates during the dialysis process. For the sample without dialyzing (**Figure 3.32 a-b**), the morphology found were helical fibers; however, after dialyzing (**Figure 3.32 c-d**) the sample evolved to HNFs.

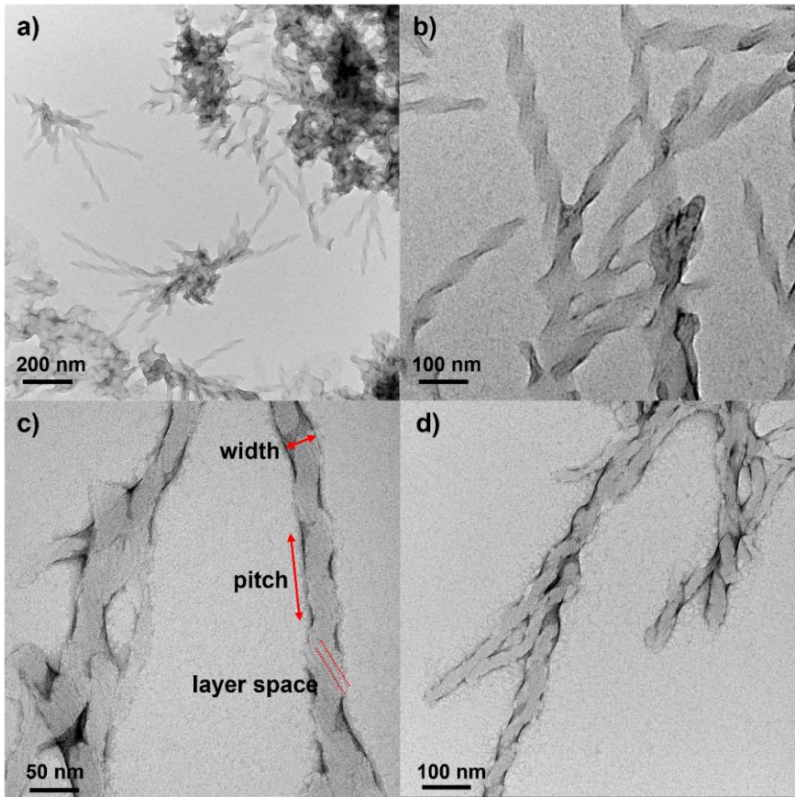

Figure 3.32. *TEM images of* ***Azo 4-8-P5N10*** *dialyzed (c-d) and non-dialyzed (a-b).*

The helical fibers appeared as twisted flat fibers with a pitch of 70-80 nm and a width of 25-30 nm, but the HNFs are self-assembled by a few fibers and therefore their dimensions are bigger: 80-90 nm of pitch and 30-40 nm of width. Moreover, the distance between layers (5 nm) could be measured since the outline of the different fibers came out as can be seen in **Figure 3.32c.**

The next functional group studied was biphenyl. Regarding aggregates of the long chain complex, **Bi 10-8-P5N10**, morphologies evolved from helical fibers to a "belt of fibers" during dialysis procedure. The fibers obtained without dialysis (**Figure 3.33a**) measured 62-72 nm of pitch and 32-34 nm of width. The dialyzed sample (**Figure 3.33b**) progressed from single fiber to a handful of them twisted over but did not stack to an HNF. The pitch of these belts (58-74 nm) was close to that of the previous sample, verifying that the fibers were not stacked. However, their width grew to 120-140 nm.

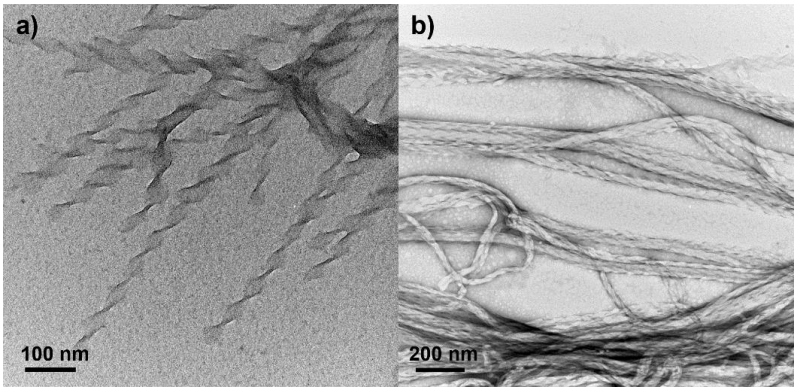

Figure 3.33. *TEM micrographs of* ***Bi 10-8-P5N10*** *before (a) and after dialyzing (b).*

For the short chain compound of biphenyl, **Bi 4-8-P5N10**, HNFs were obtained in both cases (dialyzed and without dialyzing) with a pitch of 60-67 nm and a width of 18-20 nm. The layer spacing between the different strata of the HNF was 5-6 nm (**Figure 3.34**).

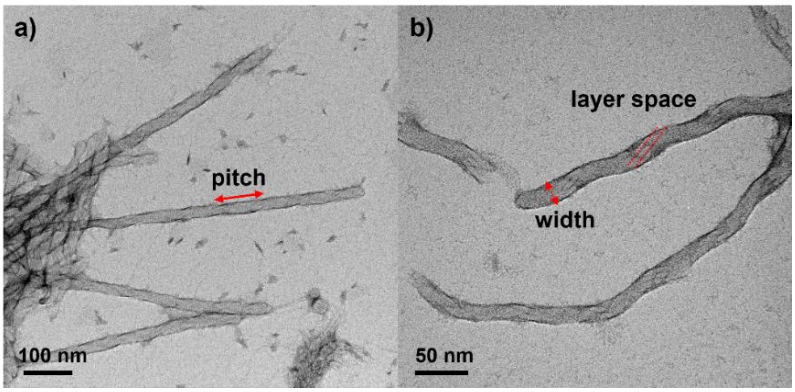

Figure 3.34. *TEM images of* ***Bi 4-8-P5N10*** *before (a) and after dialyzing (b).*

Finally, ester aggregates are shown in **Figure 3.35**. Both compounds **B1 10-8-P5N10 (a)** and **B1 4-8-P5N10 (b)** self-assembled in nanotubes and ribbons with a width of 225-250 nm for the sample without dialyzing. The length of the nanotubes was around 1 µm. The presence of ribbons suggested an evolution from fibers to ribbons and finally nanotubes during the dialysis process as has been described in the bibliography.[29]

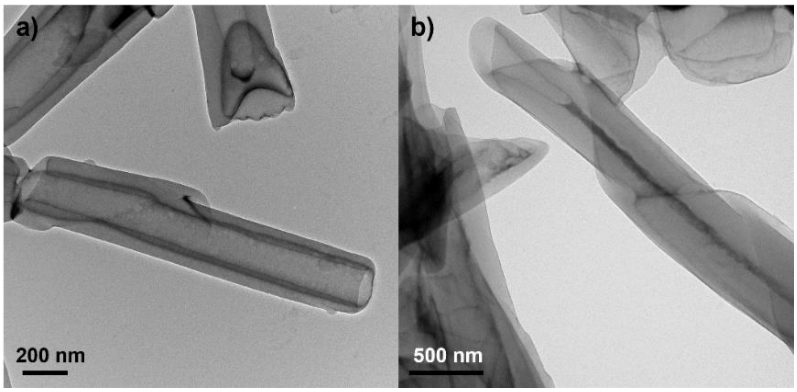

Figure 3.35. *TEM images of* ***B1 10-8-P5N10*** *(a) and* ***B1 4-8-P5N10*** *(b).*

For a further knowledge of the assembly process, different samples of **B1 10-8-P5N10** and **B1 4-8-P5N10** at lower percentage of water during the co-solvent method were prepared. These samples were analyzed by TEM after dialyzing and before dialyzing. In **Figure 3.36** it can be seen the evolution of the aggregates from fiber (a) to ribbon formed by several fibers (b). This ribbon finally evolved to the nanotubes described previously in **Figure 3.35**. These studies confirmed the

assembly mechanism explained in the bibliography[29] for similar ionic bent-core compounds: the ionic pairs of the pillar[5]arene were exposed to water once it was added during the co-solvent procedure and the hydrophobic bent-core portion stacked in layers. The force that produced the layers is the π-π stacking between different aromatic rings of the bent-cores. This interaction produces a conformational force which twists the layers and, as a consequence, the morphologies obtained changed from fibers to ribbons and nanotubes when the proportion of water was raised in the solution. Therefore, the diameter of the nanotubes is noticeably larger than that of ribbons or fibers because it is built by several ribbons.

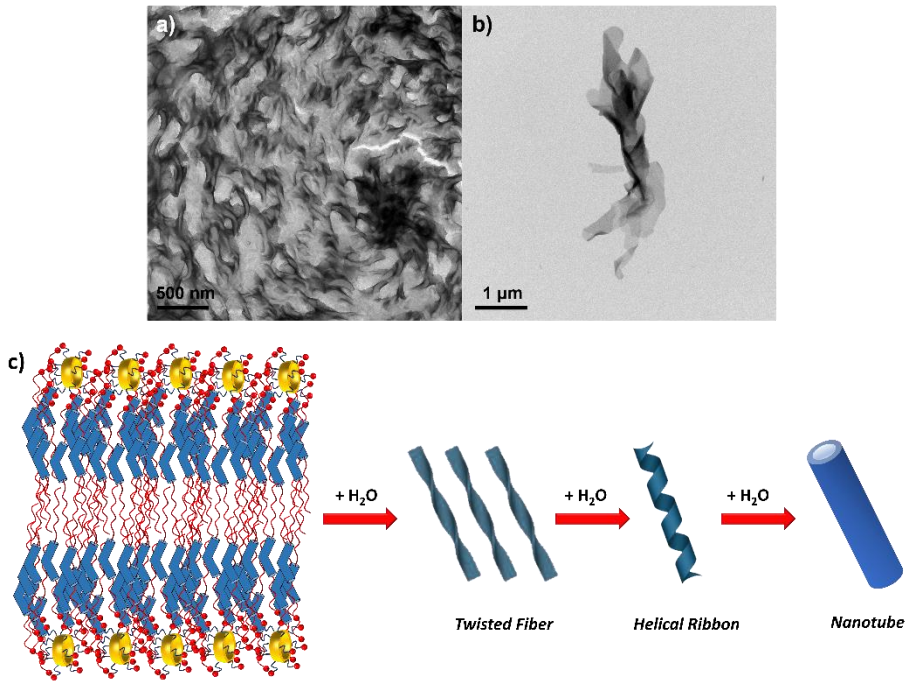

Figure 3.36. *Progression from fibers (a) to ribbons (b) followed by TEM c) Schematic representation of the process from the molecular assembly to the nanotubes.*

These results indicate a clear influence of several parameters: one is the length of the spacer between the hydrophobic core and the carboxyl group. The long spacer in Azo and Biphenyl derivatives resulted in the formation of systems without stacking: helical fibers and ribbons with similar dimensions. The short spacer produces a proximity between hydrophobic cores, which interact by π-π stacking.

This stacking caused the formation of HNFs with higher thickness and several layers whose layer spacing could be measured. In the case of the Ester derivatives, the length of the spacer did not show an influence in the morphology of the aggregates, probably caused for their facility to evolve until nanotubes. This fact is related with the second parameter: the modification in the hydrophobic nature of the bent-core structure. Azo, Biphenyl and Ester showed a diverse behavior in the self-assembly process which is revealed in different morphologies of aggregates for each compound. Ester aggregates were the only compounds to reach nanotube structures, which suggested a tendency to the stacking process that Azo and Biphenyl did not exhibit. Probably, the ester bond between the aromatic rings provides an adequate mobility to twist the fibers, but the interactions are strong enough to stack different layers. However, Azo and Biphenyl are more rigid, precluding the necessary twist to reach nanotubes. For Azo and Biphenyl, their morphologies were similar: fibers and ribbons for the long spacer and HNF for the short spacer. However, if we focus on the long spacer, we can see differences before and after dialyzing. **Bi 10-8-P5N10** evolved from isolated fibers to a bunch of interlaced fibers after dialysis, whereas **Azo 10-8-P5N10** did not evolve and remained as isolated fibers in both situations (before and after dialysis).

For better understanding of the self-assembly process, several ^{1}H-NMR studies were performed: compound **B1 4-8-P5N10** was dissolved in deuterated THF and the co-solvent method was carried out with deuterated water. After each addition of D_2O an NMR spectrum was performed (**Figure 3.37**). These studies confirmed that the aromatic rings stack when the water percentage increases, observing shifts upfield in the peaks of the aromatic rings.

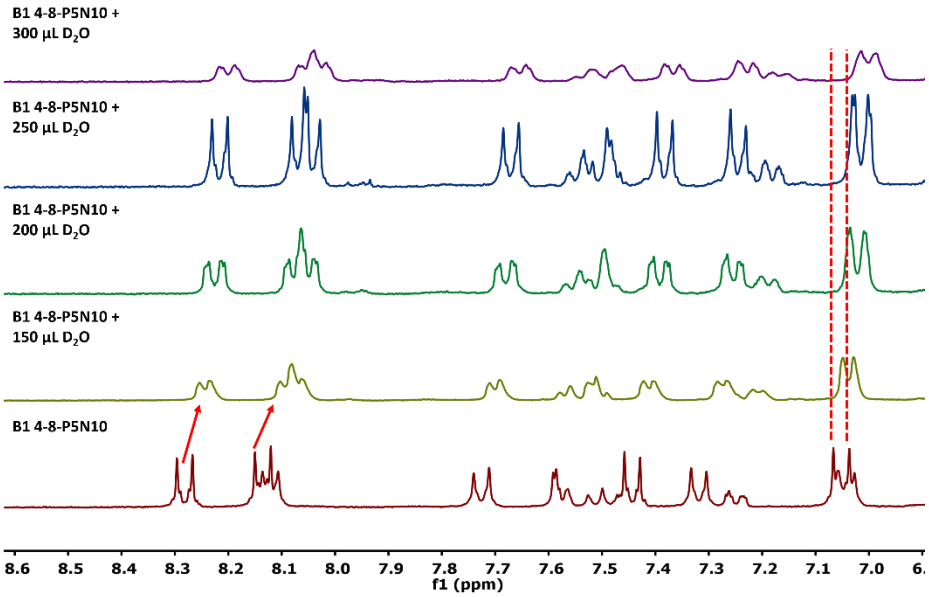

Figure 3.37. *Comparative ^{1}H-NMR (THF-d_8, 298K, 400 MHz) spectra of **B1 4-8-P5N10** after adding aliquots of D_2O.*

The image obtained by TEM showed in multiple cases (**Azo 4-8-P5N10, Bi 4-8-P5N10**…) a set of layers throughout the width of the HNFs caused by the stacking of multiple layers. In the compounds that did not evolve to multiple layers, the fibers obtained were the result of the assembling of multiple molecules, as it was described in the section of liquid crystal behavior. To estimate these distances, SAED diffraction of the aggregates was carried out (**Figure 3.38**), obtaining spacing distances of around 4-5 nm, which are in fair agreement with the distances described in the bibliography for these kinds of compounds and the measurements carried out by TEM. These diffractograms showed differences between layers (**Figure 3.38a**) and inside the fibers (**Figure 3.38b**) revealing shorter distances between molecules in the fibers than between layers in HNFs. Moreover, the absence of specific spots confirms that these structures are not crystalline and the liquid crystal arrangement remained inside the studied structures (fibers, ribbons, HNFs…).

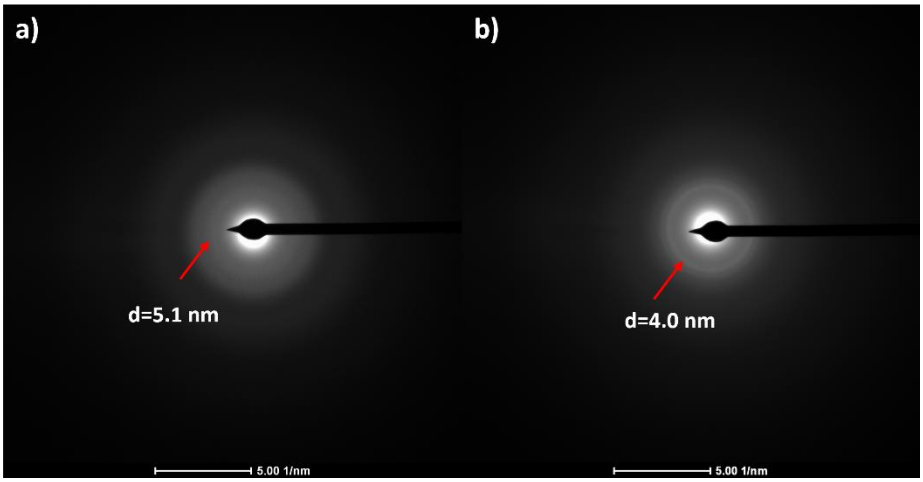

Figure 3.38. *SAED diffractograms of aggregates a)* ***Bi 4-8-P5N10*** *and b)* ***Azo 10-8-P5N10****.*

3.4 Conclusions

In this chapter six bent-core pillar[5]arenes complexes have been synthesized by ionic bond, by mixing a pillar[5]arene that contains 10 amino groups (**P5N10**) and different bent-core acids (Azo, Ester and Biphenyl derivatives with two different polymethylene spacers) in a proportion of 1:10. The ionic approach has empowered the materials for their application as proton conductance materials. Moreover, a relationship has been established between their liquid crystal structure and the proton mobility values, concluding that shorter spacers enhance the values. Additionally, the ionic pairs have led to the assembly of these materials in water resulting in a variety of morphologies that can be related with the chemical structure of the compounds, obtaining HNFs for shorter spacers and different kinds of fibers for longer spacers. To conclude, it has been demonstrated the formation of new ionic bent-core pillar[5]arenes with an easy and fast method, and these materials exhibit liquid crystal behavior and can potentially be employed in different fields.

3.5 Experimental part

3.5.1 Characterization techniques

All reagents were purchased from Aldrich and used without further purification. Anhydrous CH_2Cl_2 and THF were purchased from Scharlab and dried by using a solvent purification system.

^{1}H-NMR and **^{13}C-NMR** spectra were acquired on a Bruker AV400 spectrometer. The experiments were performed at room temperature in different deuterated solvents ($CDCl_3$ CD_2Cl_2 or DMSO-d_6). Chemical shifts are given in ppm relative to TMS and the solvent residual peak was used as the internal standard.

FT-IR were recorded on a Bruker Vertex 70 FT-IR spectrometer. The samples were prepared on KBr pellets with a concentration of the product of 1-2% (w/w).

MALDI-TOF mass spectrometry was performed on an Autoflex Bruker mass spectrometer with a dithranol matrix. Positive and negative ion electrospray ionization high resolution (**ESI HRMS**) was performed on a Bruker Q-TOF-MS in a positive or negative ESI mode.

Mesophases were investigated by **polarized-light optical microscopy** (POM) using an Olympus BH-2 polarizing microscope fitted with a Linkam THMS600 hot stage.

Thermogravimetric analysis (TGA) was performed using a Q5000IR from TA instruments at a heating rate of 10 ºC min^{-1} under a nitrogen atmosphere.

Thermal transitions were determined by **differential scanning calorimetry** (DSC) using a DSC Q2000 from TA instruments with powdered samples (2−5 mg) sealed in aluminum pans. Glass transition temperatures (Tg) were determined at the half height of the baseline jump, and first order transition temperatures were read at the maximum of the corresponding peak.

X-ray diffraction diagrams were recorded using a Stoe Stadivari goniometer equipped with a Genix3D microfocus generator (Xenocs) and a Dectris Pilatus 100K detector. Temperature control was achieved using a nitrogen-gas Cryostream controller (Oxford Cryosystems) allowing for a temperature control of about 0.1 ºC. Lindemann capillaries of diameter 0.6 mm were utilized. Monochromatic CuKα radiation (λ = 1.5418 Å) was used. The exposure time was 2 minutes.

UV-Vis absorption spectra were recorded on an ATI-Unicam UV4-200 spectrophotometer.

Electrochemical impedance spectroscopy was recorded with a Frequency Response Analyzer, Solarton SI1260A from AMETEK in the frequency range from 1 Hz to 1 MHz (amplitude of the applied voltage: 50 mV). The conductivities were studied as a function of temperature between 30°C and isotropization temperature at different intervals. For the preparation of the cells for ionic conductivities, the appropriate amount of the ionic dendrimer was placed onto an ITO electrode that was sandwiched with another ITO electrode controlling the thickness by using glass spacers (10-20 µm). The cell was heated up to a few degrees above the melting point of the liquid crystal and the cell was pressed to obtain the thin film. The impedance spectrum can be modeled as an equivalent circuit and divided into imaginary (Z'') and real (Z') components. The resistance (Rb) was estimated from the intersection of the real axis (Z') and the semicircle of the impedance spectrum. The proton conductivities σ ($S \cdot cm^{-1}$) were calculated with the formula: $\sigma = d / (Rb \cdot A)$), where d (cm) is the thickness of the film, A (cm^2) is the area of the film and Rb (Ω) is the resistance of the sample.

After the preparation of the cell, a random orientation of the mesophase was observed between electrodes. Samples were mechanically sheared within the cell (in order to obtain an alignment of the molecules) in the isotropic phase and then slowly cooled down to room temperature (0.05 ºC·min^{-1}).

Transmission Electron Microscopy (TEM) analysis was performed using a FEI Tecnai T20 microscope (FEI Company, Waltham, MA, USA) operating at 200 kV. TEM samples were prepared adding 10 µL of each self-assembly dispersion at an approximately 1.0 mg mL^{-1} concentration on a continuous carbon film-copper grid, and the excess was removed by capillarity using filter paper. Then, the grids were stained with uranyl acetate (1% aqueous solution), removing the excess again by capillarity using filter paper.

3.5.2 Synthetic procedures

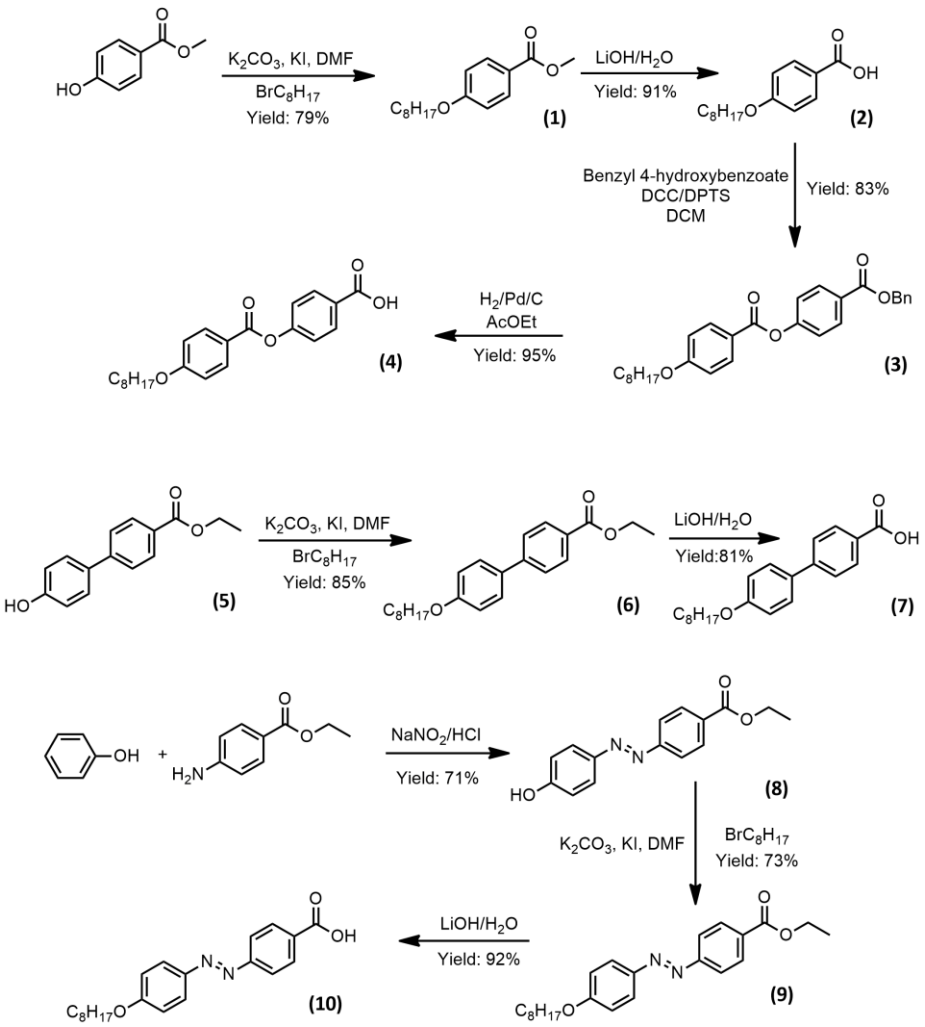

Scheme 3.1. *Synthetic route of functionalized acids.*

3.5.2.1 *Synthesis of* ***C_8B1COOH (4)***

Synthesis of **methyl 4-(octyloxy)benzoate (1):** Over a stirred solution of methyl 4-hydroxybenzoate (3.00 g, 19.7 mmol) in dimethylformamide (50 ml), potassium carbonate (8.15 g, 59.13), 1-bromooctane (8.71 g, 39.43 mmol) and potassium iodide (spatula tip) were added. The mixture was stirred under reflux overnight, cooled to room temperature and then filtered over celite. The solvent was removed, and the crude was precipitated in methanol, filtered and washed with cold methanol. Yield: 79%.

^{1}H-NMR ($CDCl_3$, 298K, 400 MHz, δ, ppm): 7.97 (d, J=8.9 Hz, 2H), 6.90 (d, J=8.9 Hz, 2H), 4.00 (q, J=6.6 Hz, 2H), 3.88 (s, 3H), 1.79 (q, J=8.0Hz, 2H), 1.51-1.21 (m, 10H), 0.88 (t, J=7.0 Hz, 3H)

^{13}C-NMR ($CDCl_3$, 298K, 100 MHz, δ, ppm): 167.07, 163.12, 131.71, 122.48, 114.22, 68.37, 51.95, 32.04, 29.70, 29.27, 29.46, 26.13, 22.82, 14.25.

Synthesis of **4-(octyloxy)benzoic acid (2):** over a solution of methyl 4-(octyloxy)benzoate **(1)** (2.00 g, 6.81 mmol) in THF (50 ml) was added a solution of lithium hydroxide (817 mg, 34.08 mmol) in water (10 ml). The mixture was stirred under reflux overnight and then precipitated in HCl/H_2O (pH=2) obtaining a white solid. The solid was filtered and recrystallized in ethanol. Yield: 91%.

^{1}H-NMR ($CDCl_3$, 298K, 400 MHz, δ, ppm): 8.04 (d, J=8.9 Hz, 2H), 6.93 (d, J=8.9 Hz, 2H), 4.02 (q, J=6.6 Hz, 2H), 1.81 (q, J=8.0Hz, 2H), 1.51-1.21 (m, 10H), 0.88 (t, J=7.0 Hz, 3H)

^{13}C-NMR ($CDCl_3$, 298K, 100 MHz, δ, ppm): 172.12, 163.86, 132.49, 121.52, 114.34, 68.44, 32.04, 29.70, 29.46, 29.24, 26.13, 22.84, 14.26.

Synthesis of **benzyl 4-(4-(octyloxy)benzoyloxy)benzoate (3):** In a flask were dissolved 4-(octyloxy)benzoic acid **(2)** (2.50 g, 9.98 mmol), benzyl 4-hydroxybenzoate (2.27 g, 9.98mmol) and DPTS (0.88 g, 3.02 mmol) in 10 ml of dry DCM under argon atmosphere at 0^{o}C. Over this solution was added DCC (2.66 g, 12.93 mmol). The mixture was stirred at room temperature 16 hours. After that time the crude was filtered over celite and the solvent was removed. The product was purified by flash column chromatography in an eluent mix of DCM 1:1 hexane. Yield: 83%.

^{1}H-NMR ($CDCl_3$, 298K, 400 MHz, δ, ppm): 8.16 (m, 2H), 8.13 (m, 2H), (7.40 m, 5H), 7.30 (m, 2H), 6.98 (m, 2H), 5.38 (s, 2H), 4.05 (t, J=6.8 Hz, 2H), 1.81 (m, 2H), 1.43-1.20 (m, 10H), 0.88 (t, J=7.2 Hz, 3H).

^{13}C-NMR (CDCl$_3$, 298K, 100 MHz, δ, ppm): 165.9, 164.5, 163.9, 155.1, 136.2, 132.5, 131.4, 128.8, 128.4, 128.3, 127.7, 122.0, 121.2, 114.5, 68.5, 66.9, 32.0, 29.7, 29.5, 29.2, 26.1, 22.8, 14.2.

Synthesis of **4-(4-(octyloxy)benzoyloxy)benzoic acid (4):** In a flask was prepared a solution of benzyl 4-(4-(octyloxy)benzoyl)oxy)benzoate **(3)** (1.50 g, 3.25 mmol) in ethyl acetate (50 ml). Three cycles of vacuum/argon were performed and then Pd/C was added (150 mg, 10% wt); after that another three cycles of vacuum/argon were performed, followed by three cycles of vacuum/hydrogen. The mixture was stirred under hydrogen atmosphere overnight. The crude was filtered over celite and the solvent was evaporated. The product was recrystallized in ethanol. Yield: 95%.

^{1}H-NMR (CDCl$_3$, 298K, 400 MHz, δ, ppm): 8.08 (m, 2H), 8.02 (m, 2H), 7.40 (m, 2H), 7.09 (m, 2H), 4.07 (t, J=6.8 Hz, 2H), 1.81 (m, 2H), 1.43-1.20 (m, 10H), 0.88 (t, J=7.2 Hz, 3H)

^{13}C-NMR (CDCl$_3$, 298K, 100 MHz, δ, ppm): 166.6, 163.8, 163.4, 154.2, 132.1, 130.9, 128.3, 122.2, 120.4, 114.7, 68.0, 31.3, 28.9, 28.7, 28.5, 25.4, 22.1, 13.9.

FT-IR (KBr, ν: cm^{-1}): 3200 (-OH), 2920 (-C=H), 2853 (-C-H), 1735 (C=O), 1685 (C=O), 1602 (C=C), 1510 (C=C), 1252 (C-O), 1206 (C-O).

3.5.2.2 Synthesis of C_8BiCOOH (7)

Synthesis of **ethyl 4´-octyloxybiphenyl-4-carboxylate (6):** A mixture of ethyl 4´-hydroxybiphenyl-4-carboxylate **(5)** (0.30 g, 1.23 mmol), potassium carbonate (0.85 g, 6.17 mmol) and potassium iodide (spatula tip) were dissolved in acetonitrile (50 ml) and stirred under reflux for 30 minutes. Finally, 1-bromooctane (0.24 g, 1.23 mmol) was added to the solution and let react overnight. Then the solvent was evaporated, the solid redissolved in dichloromethane, and washed with water. The organic phase was dried with $MgSO_4$, filtered, and evaporated obtaining a white solid with a yield of 92%.

^{1}H-NMR ($CDCl_3$, 298K, 400 MHz, δ, ppm): 8.08 (m, 2H), 7.58 (m, 4H), 6.98 (m, 2H), 4.39 (q, J=6.9 Hz, 2H), 4.01 (t, J=6.6 Hz, 2H), 1.81 (m, 2H), 1.50-1.24 (m, 13H), 0.89 (t, J=6.9 Hz, 3H).

^{13}C-NMR ($CDCl_3$, 298K, 100 MHz, δ, ppm): 166.7, 159.6, 145.3, 132.4, 130.2, 128.7, 128.4, 126.5, 115.1, 68.3, 61.0, 32.1, 29.8, 29.7,29.6, 26.2, 22.8, 14.5, 14.3.

Synthesis of **4´-octyloxybiphenyl-4-carboxylic acid (7):** A solution of ethyl-4´-octyloxylbiphenyl-4-carboxylate **(6)** (400 mg, 1.13 mmol) was prepared in THF (10 ml); after that, a solution of LiOH (234 mg, 3.40 mmol) in water (10 ml) was added and stirred under reflux overnight. The crude was let cool down and HCl was added until pH=2. The solid obtained was filtered and washed with water, obtaining a white solid with a yield of 94%.

^{1}H-NMR (DMSO-d_6, 298K, 400 MHz, δ, ppm): 7.98 (m, 2H), 7.74 (m, 2H), 7.67 (m, 2H), 7.04 (m, 2H), 4.01 (t, J=6.5 Hz, 2H), 1.73 (q, J=7.89 Hz, 2H), 1.48-1.22 (m, 12H), 0.86 (t, J=6.96 Hz, 3H).

^{13}C-NMR ($CDCl_3$, 298K, 100 MHz, δ, ppm): 167.2, 150.0, 143.9, 131.1, 129.9, 128.8, 128.1, 126.0, 115.0, 67.5, 31.2, 28.7, 28.6, 25.5, 22.1, 13.9.

FT-IR (KBr, v: cm^{-1}): 3200 (-OH), 2920 (-C=H), 2846 (-C-H), 1684 (C=O), 1602 (C=C), 1435 (C=C), 1291 (C-O), 1202 (C-O).

3.5.2.3 Synthesis of C_8AzoCOOH (10)

Synthesis of **HOAzoCOOEt (8):** To a stirred solution of ethyl 4-aminobenzoate (5.00 g, 30.26 mmol) in 150 ml of water and 25 ml of HCl was added $NaNO_2$ (2.09 g, 33.26 mmol) in 50 ml of water at 0^{o}C. Finally, phenol (2.85 g, 33.26 mmol) was added and let react one hour. After that time the crude was neutralized with $NaHCO_3$, obtaining an orange solid that was filtered. The solid was purified with flash column chromatography with a mix of eluents hexane 8:1 ethyl acetate. Yield: 56%.

^{1}H-NMR (DMSO-d_6, 298K, 400 MHz, δ, ppm): 8.12 (m, 2H), 7.92 (m, 4H), 7.14 (m, 2H), 4.09 (t, J=6.5 Hz, 2H), 1.75 (q, J=7.8 Hz, 2H), 1.48-1.22 (m, 10H), 0.86 (t, J=6.96 Hz, 3H).

^{13}C-NMR ($CDCl_3$, 298K, 100 MHz, δ, ppm): 166.6, 159.4, 155.5, 147.2, 131.6, 130.7, 125.6, 122.5, 116.1, 61.5, 14.5.

Synthesis of **C_8AzoCOOEt (9):** A solution of **HOAzoCOOEt (8)** (2.00 g, 7.39 mmol), potassium carbonate (3.05 g, 22.17 mmol) and potassium iodide (spatula tip) was prepared in dimethylformamide (50 ml). The mixture was stirred under reflux and after 30 minutes 1-bromooctane (1.71 g, 8.87 mmol) was added to the mixture. After 16 hours the mixture was filtered over celite, and the solvent was evaporated. Finally, the crude was purified by flash column chromatography in an eluent mix of hexane 9:1 ethyl acetate. Yield: 86%.

^{1}H-NMR ($CDCl_3$, 298K, 400 MHz, δ, ppm): 8.18 (m, 2H), 7.92 (m, 4H), 7.01 (m, 2H), 4.41 (q, J=7.2 Hz, 2H), 4.05 (t, J=7.2 Hz, 2H), 1.82 (m, 2H), 1.51-1.25 (m, 13H), 0.89 (t, J=7.2 Hz, 3H)

^{13}C-NMR ($CDCl_3$, 298K, 100 MHz, δ, ppm): 166.3, 162.5, 155.5, 147.0, 131.6, 130.7, 125.3, 122.4, 114.9, 68.6, 61.3, 32.0, 29.5, 29.4, 29.3, 26.2, 22.8, 14.5, 14.2.

Synthesis of **C_8AzoCOOH (10):** Over a solution of **C_8AzoCOOEt (9)** (1.50 g, 3.92 mmol) in ethanol (20 ml) was added lithium hydroxide (0.88 g, 15.68 mmol) in water. The mixture was heated under reflux for 4 hours. The crude was allowed to cool down and HCl was added until pH=2. The solid obtained was filtered and washed with water, obtaining an orange solid with a yield of 89%.

^{1}H-NMR (DMSO-d_6, 298K, 400 MHz, δ, ppm): 8.12 (m, 2H), 7.91 (m, 4H), 7.15 (m, 2H), 4.09 (t, J=6.5 Hz, 2H), 1.75 (m, 2H), 1.49-1.20 (m, 10H), 0.88 (t, J=7.0 Hz, 3H).

^{13}C-NMR ($CDCl_3$, 298K, 100 MHz, δ, ppm): It could not be characterized because of low solubility.

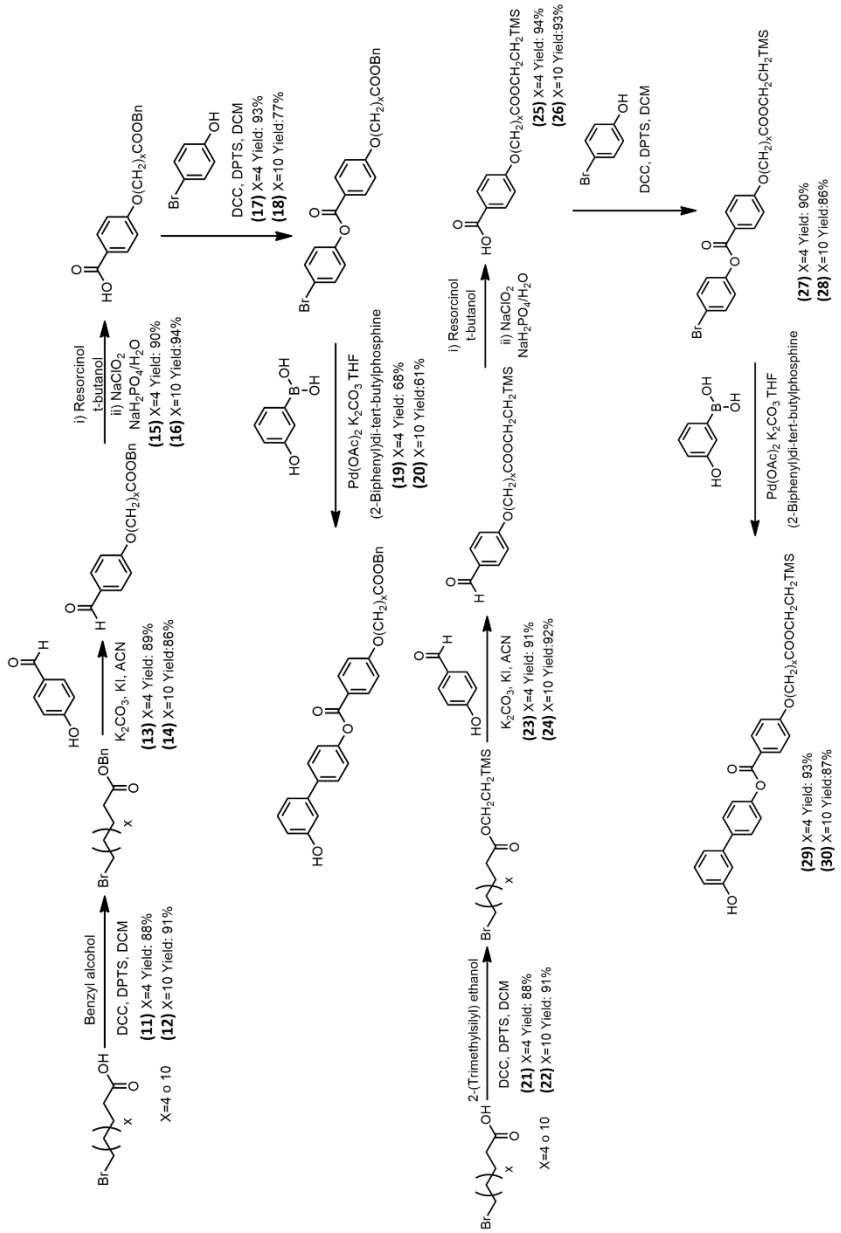

Scheme 3.2. *Synthesis of hydroxy-substituted biphenyl moieties.*

The synthesis of **HOBiC$_{10}$COOBn (19)** and **HOBiC$_4$COOBn (20)** was carried out with the same procedure. Here is described specifically the synthesis of **HOBiC$_{10}$COOBn.**

*3.5.2.4 Synthesis of **HOBiC$_{10}$COOBn (20)***

Synthesis of **benzyl 11-bromoundecanoate (12)**: In a flask was prepared a solution of 11-bromoundecanoic acid (3.00 g, 11.31 mmol), benzyl alcohol (1.22 g, 11.31 mmol) and DPTS (1.58 g, 5.63 mmol) in dry DCM (10 ml) at 0ºC. After that DCC (3.26 g, 15.83 mmol) was slowly added and let react overnight at room temperature. The crude was filtered over celite and the solvent was removed. The product was purified by flash column chromatography in an eluent mix of DCM 1:2 hexane. Yield: 88%.

^{1}H-NMR ($CDCl_3$, 298K, 400 MHz, δ, ppm): 7.33 (m, 5H), 5.12 (s, 2H), 3.41 (t, J=6.7 Hz, 2H), 2.34 (t, J=7.5 Hz, 2H), 1.81 (m, 2H), 1.65 (m, 2H), 1.41 (m, 2H), 1.28 (m, 10H).

^{13}C-NMR ($CDCl_3$, 298K, 100 MHz, δ, ppm): 173.7, 136.1, 128.5, 128.2, 66.1, 34.3, 34.0, 32.8, 29.3, 29.1, 29.0, 28.7, 28.1.

Synthesis of **benzyl 11-(4-formylphenoxy)undecanoate (14):** a solution of 4-hydroxybenzaldehyde (1.03 g, 8.44 mmol), potassium carbonate (5.82 g, 42.2 mmol) and potassium iodide (spatula tip) was prepared in acetonitrile (50 ml), and then benzyl 11-bromoundecanoate **(12)** (3.00 g, 8.44 mmol) was added. The mixture was stirred under reflux overnight. The crude was filtered over celite and the solvent evaporated. Finally, the product was purified by flash column chromatography in an eluent mix of DCM/hexane. Yield: 89%.

^{1}H-NMR ($CDCl_3$, 298K, 400 MHz, δ, ppm): 9.88 (s, 1H), 7.81 (m, 2H), 7.35 (m, 5H), 6.98 (m, 2H), 5.11 (s, 2H), 4.02 (t, J=6.3 Hz, 2H), 2.35 (t, J=7.6 Hz, 2H), 1.80 (m, 2H), 1.63 (m, 2H), 1.41 (m, 2H), 1.32 (m, 10H).

^{13}C-NMR ($CDCl_3$, 298K, 100 MHz, δ, ppm): 191.0, 173.8, 164.4, 136.3, 132.1, 129.9, 128.7, 128.3, 114.9, 68.6, 66.2, 34.4, 29.5, 29.4, 29.1, 26.1, 25.1.

Synthesis of **4-((11-benzyloxy-11-oxoundecyl)oxy)benzoic acid (16):** in a flask were dissolved benzyl 11-(4-formylphenoxy)undecanoate **(14)** (2.00 g, 5.04 mmol) and resorcinol (887.48, 8.06 mmol) in terc-butanol

(30 ml) at 35ºC. In another flask were dissolved $NaClO_2$ (2.87 g, 31.77 mmol) and NaH_2PO_4 (2.42 g, 20.16 mmol) in water (40 ml). This solution was slowly added over the first mixture and let react overnight at 35ºC. The crude was precipitated in HCl/H_2O (pH=1) and the solid obtained filtered and recrystallized in ethanol. Yield: 94%.

^{1}H-NMR ($CDCl_3$, 298K, 400 MHz, δ, ppm): 8.01 (d, J=8.9 Hz, 2H), 7.35 (m, 5H), 6.90 (d, J=8.9 Hz, 2H), 5.11 (s, 2H), 4.00 (t, J=6.5 Hz, 2H), 2.35 (t, J=7.6 Hz, 2H), 1.76 (m, 2H), 1.55-1.20 (m, 14).

^{13}C-NMR ($CDCl_3$, 298K, 100 MHz, δ, ppm): 173.9, 171.8, 163.9, 136.3, 132.4, 129.9, 128.3, 121.5, 114.3, 68.4, 66.2, 34.4, 29.5, 29.4, 29.1, 26.1, 25.1.

Synthesis of **4-bromophenyl 4-((11-benzyloxy-11-oxoundecyl)oxy) benzoate (18):** 4-((11-benzyloxy-11-oxoundecyl)oxy)benzoic **(16)** acid (180.00 mg, 0.55 mmol), 4-bromophenol (95.00 mg, 0.55 mmol) and DPTS (82.00 mg, 0.28 mmol) were dissolved in dry DCM (5 ml) under argon atmosphere at 0ºC. Then DCC (170.00 mg, 0.82 mmol) was added to the solution and let react overnight at room temperature. The mixture was filtered over celite and purified by column chromatography in dichloromethane, obtaining the product with a yield of 77%.

^{1}H-NMR ($CDCl_3$, 298K, 400 MHz, δ, ppm): 8.11 (d, J=8.9 Hz, 2H), 7.52 (d, J=8.9 Hz, 2H), 7.35 (m, 5H), 7.09 (d, J=8.8 Hz, 2H), 6.96 (d, J=8.8 Hz, 2H), 5.11 (s, 2H), 4.04 (t, J=6.5 Hz, 2H), 2.35 (t, J=7.6 Hz, 2H), 1.76 (m, 2H), 1.55-1.20 (m, 14).

^{13}C-NMR ($CDCl_3$, 298K, 100 MHz, δ, ppm): 173.8, 164.7, 163.8, 150.3, 139.9, 136.3, 132.6, 132.4, 128.7, 128.3, 123.8, 121.3, 118.9, 114.5, 68.5, 68.2, 34.4, 29.6, 29.5, 29.4, 29.3, 29.2, 29.2, 26.1, 25.1.

Synthesis of **3'-hydroxy-[1,1'-biphenyl]-4-yl 4-((11-benzyloxy-11-oxoundecyl)oxy)benzoate (20):** In a schlenk were dissolved compound **18** (3.00 g, 5.17 mmol), 3-hydroxyphenylboronic acid (1.06 g, 7.71 mmol), potassium carbonate (1.35 g, 23.26 mmol), (2-biphenyl)-di-tert-butylphosphine (154.3 mg, 0.52 mmol) and palladium acetate

(96.51 mg, 0.43 mmol) in 20 ml of dry THF. The mixture was stirred for 72h under argon atmosphere. After that time the crude was filtered over celite, the solvent was removed under vacuum and the product was purified by column chromatography in a mixture of DCM 8:2 hexane. Finally, it was recrystallized in ethanol, obtaining the pure product with a yield of 87%.

^{1}H-NMR ($CDCl_3$, 298K, 400 MHz, δ, ppm): 8.17 (m, 2H), 7.58 (m, 2H), 7.34 (m, 5H), 7.28 (m, 1H), 7.25 (m, 2H), 7.15 (m, 1H), 7.03 (m, 1H), 6.98 (m, 2H), 6.82 (m, 1H), 5.13 (s, 2H), 4.04 (t, J=6.5 Hz, 2H), 2.36 (t, J=7.6 Hz, 2H), 1.82 (m, 2H), 1.70-1.26 (m, 14).

^{13}C-NMR ($CDCl_3$, 298K, 100 MHz, δ, ppm): 174.0, 165.3, 163.7, 156.1, 150.7, 142.2, 138.5, 136.2, 132.5, 130.1, 128.7, 128.4, 128.3, 128.2, 122.2, 121.5, 119.7, 114.5, 114.2, 68.5, 66.3, 34.4, 29.6, 29.4, 29.2, 26.1, 25.1

The synthesis of **$HOBiC_{10}COOTMS$** and **$HOBiC_4COOTMS$** was carried out with the same procedure, here is described specifically the synthesis of **$HOBiC_4COOTMS$.**

3.5.2.5 *Synthesis of* ***$HOBiC_4COOTMS$ (29)***

Synthesis of **2-(trimethylsilyl)ethyl 5-bromopentanoate (21):** 5-bromopentanoic acid (6.12 g, 33.84 mmol), trimethylsilyl ethanol (4.00 g, 33.84 mmol) and DPTS (3.00 g, 10.16 mmol) were dissolved in dry DCM (20 ml) under argon atmosphere at 0^{o}C. Then DCC (10.48 g, 50.76 mmol) was added to the solution and let react overnight at room temperature. The mixture was filtered over celite and purified by column chromatography in hexane/ethyl acetate 97:3, obtaining the product with a yield of 89%.

^{1}H-NMR ($CDCl_3$, 298K, 400 MHz, δ, ppm): 4.18 (m, 2H), 3.42 (t, J=6.8 Hz, 2H), 2.31 (t, J=7.2 Hz, 2H), 1.90 (m, 2H), 1.79 (m, 2H), 0.98 (m, 2H), 0.05 (s, 9H).

^{13}C-NMR ($CDCl_3$, 298K, 100 MHz, δ, ppm): 173.4, 62.8, 33.6, 33.3, 33.2, 23.6, 17.5, 1.3.

Synthesis of **2-(trimethylsilyl)ethyl 5-(4-formylphenoxy)pentanoate (23):** a solution of 4-hydroxybenzaldehyde (1.74 g, 14.24 mmol), potassium carbonate (8.27 g, 59.96 mmol) and potassium iodide (spatula tip) was prepared in acetone (50 ml), and then 2-(trimethylsilyl)ethyl 5-bromopentanoate **(21)** (4.00 g, 14.24 mmol) was added. The mixture was stirred under reflux overnight. The crude was filtered over celite and the solvent evaporated. Finally, the product was purified by flash column chromatography in an eluent mix of hexane/ethyl acetate 85:15. Yield: 89%.

^{1}H-NMR ($CDCl_3$, 298K, 400 MHz, δ, ppm): 9.88 (s, 1H), 7.83 (m, 2H), 6.97 (m, 2H), 4.16 (m, 2H), 4.06 (t, J=6.8 Hz, 2H), 2.38 (t, J=7.2 Hz, 2H), 1.85 (m, 4H), 0.98 (m, 2H), 0.05 (s, 9H).

^{13}C-NMR ($CDCl_3$, 298K, 100 MHz, δ, ppm): 190.8, 173.5, 164.2, 132.1, 130.0, 114.9, 68.0, 62.7, 34.1, 28.6, 21.6, 17.5, 1.3.

Synthesis of **4-(5-oxo-5-(2-(trimethylsilyl)ethoxy)pentyloxy)benzoic acid (25):** in a flask were dissolved 2-(trimethylsilyl)ethyl 5-(4-formylphenoxy)pentanoate (2.96 g, 9.16 mmol) and resorcinol (1.61 g, 14.68 mmol) in terc-butanol (90 ml) at 35ºC. In other flask were dissolved $NaClO_2$ (5.20 g, 57.68 mmol) and NaH_2PO_4 (4.40 g, 36.64 mmol) in water (60 ml). This solution was slowly added over the first mixture and let react overnight at 35ºC. The solvent was removed and the crude redispersed in HCl/H_2O (pH=1), the solid obtained was filtered and recrystallized in ethanol. Yield: 91%.

^{1}H-NMR ($CDCl_3$, 298K, 400 MHz, δ, ppm): 8.04 (m, 2H), 6.92 (m, 2H), 4.16 (m, 2H), 4.06 (t, J=6.8 Hz, 2H), 2.38 (t, J=7.2 Hz, 2H), 1.85 (m, 4H), 0.98 (m, 2H), 0.05 (s, 9H).

^{13}C-NMR ($CDCl_3$, 298K, 100 MHz, δ, ppm): 173.7, 171.4, 163.6, 132.5, 121.7, 114.3, 67.8, 62.8, 34.1, 28.6, 21.6, 17.5, 1.4.

Synthesis of **4-bromophenyl 4-(5-oxo-5-(2-(trimethylsilyl)ethoxy) pentyloxy)benzoate (27):** compound **25** (2.80 g, 8.28 mmol), 4-bromophenol (1.43 g, 8.28 mmol) and DPTS (0.73 g, 2.48 mmol) were dissolved in dry DCM (15 ml) under argon atmosphere at 0ºC. Then

DCC (2.55 g, 12.40 mmol) was added to the solution and let react overnight at room temperature. The mixture was filtered over celite and purified by column chromatography in hexane/ethyl acetate 9:1, obtaining the product with a yield of 90%.

^{1}H-NMR ($CDCl_3$, 298K, 400 MHz, δ, ppm): 8.07 (m, 2H), 7.53 (m, 2H), 7.10 (m, 2H), 6.96 (m, 2H), 4.18 (m, 2H), 4.06 (t, J=6.8 Hz, 2H), 2.38 (t, J=7.2 Hz, 2H), 1.85 (m, 4H), 0.98 (m, 2H), 0.05 (s, 9H).

^{13}C-NMR ($CDCl_3$, 298K, 100 MHz, δ, ppm): 173.6, 164.7, 163.5, 150.1, 132.6, 132.4, 123.8, 121.3, 118.9, 114.5, 67.8, 62.8, 34.2, 28.7, 21.7, 17.5, 1.3.

Synthesis of **$HOBiC_4COOTMS$ (29):** In a schlenk were dissolved compound **27** (1.60 g, 3.15 mmol), 3-hydroxyphenylboronic acid (0.65 g, 4.72 mmol), potassium carbonate (1.30 g, 9.45 mmol), (2-biphenyl)-di-tert-butylphosphine (95.00 mg, 0.32 mmol) and palladium acetate (56.57 mg, 0.25 mmol) and were carried out vacuum-argon cycles. Then, the solids were dissolved in 15 ml of dry THF and again were carried out cycles of vacuum-argon. The mixture was stirred for 72h under argon atmosphere. After that time, the crude was filtered over celite and the solvent was removed under vacuum, the product was purified by column chromatography in a mixture of DCM 95:5 ethyl acetate. Finally, recrystallization in ethanol yielded the pure product with a yield of 93%.

^{1}H-NMR ($CDCl_3$, 298K, 400 MHz, δ, ppm): 8.16 (m ,2H), 7.59 (m, 2H), 7.31 (m, 1H), 7.25 (m, 2H), 7.15 (m, 1H), 7.05 (m, 1H), 6.98 (m, 2H), 6.82 (m, 1H), 5.13 (s, 1H), 4.18 (m, 2H), 4.07 (t, J=6.8 Hz, 2H), 2.39 (t, J=7.2 Hz, 2H), 1.85 (m, 4H), 0.98 (m, 2H), 0.05 (s, 9H).

^{13}C-NMR ($CDCl_3$, 298K, 100 MHz, δ, ppm): 173.8, 165.3, 163.5, 156.2, 150.8, 142.3, 138.5, 132.5, 130.1, 128.3, 122.1, 121.8, 119.7, 114.5, 114.3, 67.9, 62.8, 34.2, 28.6, 21.7, 17.5, 1.3.

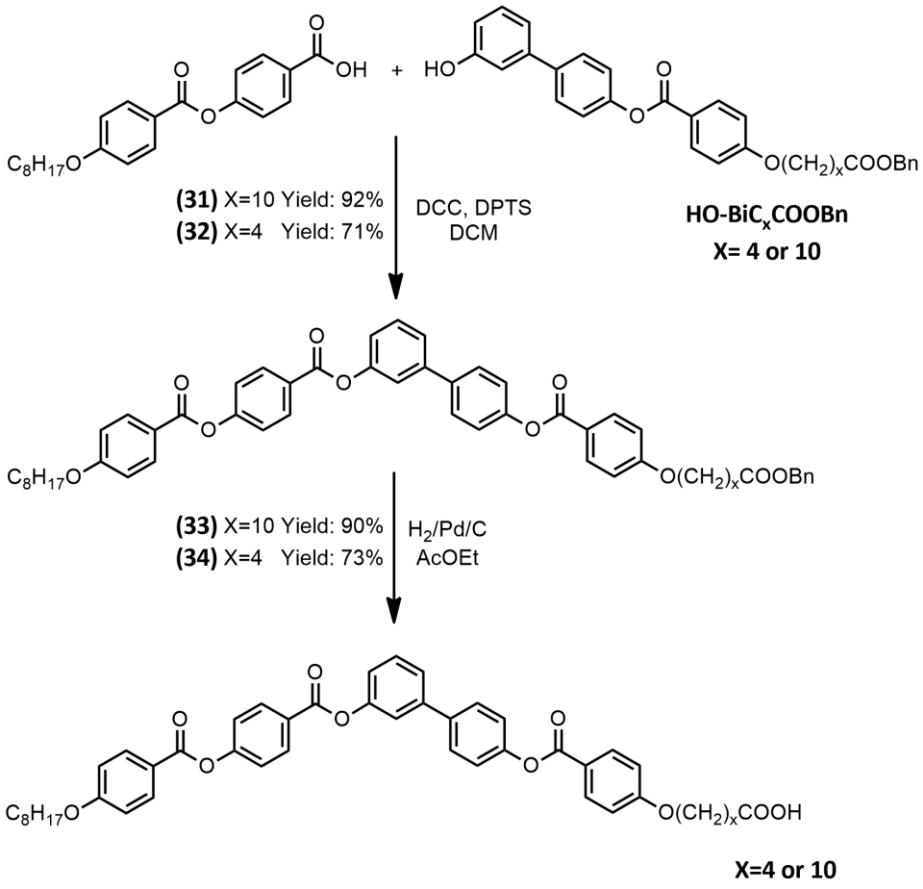

Scheme 3.3. *Synthesis of ester acids.*

3.5.2.6 Synthesis of C_8B1C_4COOH *(34)*

Synthesis of **8-B1-4-COOBn (32):** A mixture of 4-(4-(octyloxy) benzoyloxy)benzoic acid (685 mg, 1.85 mmol), **HO-BiC$_4$COOBn** (1.00 g, 1.85 mmol) and DPTS (163 mg, 0.56 mmol) were dissolved in dry DCM (10 ml) at 0^{o}C. After that, DCC (542 mg, 2.77 mmol) was slowly added and let react overnight at room temperature. The crude was filtered and the solvent evaporated. The product was purified by flash column chromatography in an eluent mix of DCM 9:1 AcOEt. Yield: 71%.

^{1}H-NMR ($CDCl_3$, 298K, 400 MHz, δ, ppm): 8.28 (m, 4H), 8.15 (m, 4H), 7.50 (t, J=8.2 Hz, 1H), 7.36 (m, 9H), 7.18 (m, 3H), 6.97 (m, 4H), 5.14 (s, 2H), 4.08 (m, 4H), 2.47 (t, J = 6.8 Hz, 2H), 1.85 (m, 6H), 1.53-1.23 (m, 12H), 0.91 (t, J = 6.8 Hz, 3H).

^{13}C-NMR ($CDCl_3$, 298K, 100 MHz, δ, ppm): 173.3, 164.5, 164.4, 164.2, 164.0, 163.7, 155.7, 155.6, 151.6, 136.1, 132.7, 132.6, 132.0, 128.7, 128.5, 128.4, 122.3, 121.3, 121.1 119.4, 116.0, 114.6, 114.5, 68.5, 67.9, 66.4, 34.0, 31.9, 29.5, 29.4, 29.2, 28.6, 26.1, 22.8, 21.7, 14.3.

Synthesis of **8-B1-4-COOH (34):** In a flask was prepared a solution of **8-B1-4-COOBn (32)** (1.25 g, 1.40 mmol) in 10 mL of AcOEt. Three cycles of vacuum/Ar were performed and Pd/C 10% wt (125 mg) was added. Again, three cycles of vacuum/Ar were performed, followed by three cycles of vacuum/hydrogen. The mixture was stirred under hydrogen atmosphere for 16 h. Then, the crude was redissolved in THF, filtered through celite and the solvent was evaporated. The product was recrystallized from ethanol to obtain a white solid. Yield: 73%.

^{1}H-NMR ($CDCl_3$, 298K, 400 MHz, δ, ppm): 8.30 (d, J=8.7 Hz, 2H), 8.15 (m, 4H), 7.64 (d, J=8.6 Hz, 2H), 7.47 (m, 3H), 7.38 (d, J=8.7 Hz, 2H), 7.28 (d, J=8.6 Hz, 2H), 7.22 (m, 1H), 6.97 (m, 4H), 4.08 (m, 4H), 2.48 (t, J = 6.8 Hz, 2H), 1.85 (m, 6H), 1.53-1.23 (m, 12H), 0.91 (t, J = 6.8 Hz, 3H).

^{13}C-NMR ($CDCl_3$, 298K, 100 MHz, δ, ppm): 178.8, 165.0, 164.6, 164.5, 163.9, 163.4, 155.6, 151.5, 150.9, 142.3, 137.9, 132.6, 132.5, 132.0, 130.0, 128.4, 127.0, 124.8, 122.3, 122.2, 121.8, 121.1, 120.7, 120.6, 114.6, 114.4, 68.5, 67.8, 33.5, 31.9, 29.4, 29.3, 29.2, 28.6, 26.1, 22.8, 21.5, 14.2.

FT-IR (KBr, ν: cm^{-1}): 3457 (OH), 2919 (=C-H), 2852 (C-H), 1738 (C=O), 1726 (C=O), 1699 (C=O dimeric), 1604 (C=C), 1257 (C-O), 1155(C-O).

MS (MALDI$^+$, dithranol, m/z): found 781.27 [M+Na^+] calculated with sodium 781.83 (758.85+22.98).

3.5.2.7 Synthesis of $C_8B1C_{10}COOH$

Synthesis of **8-B1-10-COOBn (31):** A mixture of 4-(4-(octyloxy) benzoyloxy)benzoic acid (1.65 g, 4.04 mmol), **HO-BiC_{10}COOBn** (2.34 g, 4.04 mmol) and DPTS (0.71 g, 2.42 mmol) were dissolved in dry DCM (10 ml) at 0^{o}C. After that, DCC (4.99 g, 24.2 mmol) was slowly added and let react overnight at room temperature. The crude was filtered

and the solvent evaporated. The product was purified by flash column chromatography in an eluent mix of DCM 1:1 hexane. Yield: 82%.

^{1}H-NMR (CD_2Cl_2, 298K, 400 MHz, δ, ppm): 8.30 (m, 2H), 8.15 (m, 4H), 7.79 (m, 2H), 7.55 (m, 2H), 7.49 (m, 1H), 7.40 (m, 2H), 7.35 (m, 5H), 7.30 (m, 2H), 7.24 (m, 1H), 7.01 (m, 4H), 5.12 (s, 2H), 4.08 (m, 4H), 2.47 (t, J = 6.8 Hz, 2H), 1.85 (m, 6H), 1.53-1.23 (m, 12H), 0.91 (t, J = 6.8 Hz, 3H).

^{13}C-NMR (CD_2Cl_2, 298K, 100 MHz, δ, ppm): 173.6, 165.4, 165.0, 164.8, 164.5, 164.1, 156.1, 152.1, 151.6, 142.6, 138.2, 136.9, 132.9, 132.7, 132.2, 130.4, 129.1, 128.8, 128.7 128.6, 125.2, 122.9, 122.8, 121.0, 115.0, 114.9, 69.1, 68.4, 66.6, 34.4, 32.5, 30.1, 29.9, 29.8, 29.7, 29.1, 26.5, 23.3, 22.1, 14.4.

Synthesis of **8-B1-10-COOH (33):** In a flask was prepared a solution of **8-B1-10-COOBn (31)** (120 mg, 0.14 mmol) in 10 mL of AcOEt. Three cycles of vacuum/Ar were performed and Pd/C 10% wt (15 mg) was added. Again, three cycles of vacuum/Ar were performed, followed by three cycles of vacuum/hydrogen. The mixture was stirred under hydrogen atmosphere for 16 h. Then, the crude was redissolved in THF, filtered through celite and the solvent was evaporated. The product was recrystallized from ethanol to obtain a white solid. Yield: 73%.

^{1}H-NMR (CD_2Cl_2, 298K, 400 MHz, δ, ppm): 8.30 (m, 2H), 8.15 (m, 4H), 7.79 (m, 2H), 7.55 (m, 2H), 7.49 (m, 1H), 7.40 (m, 2H), 7.30 (m, 2H), 7.24 (m, 1H), 7.01 (m, 4H), 4.08 (m, 4H), 2.47 (t, J = 6.8 Hz, 2H), 1.85 (m, 6H), 1.53-1.23 (m, 12H), 0.91 (t, J = 6.8 Hz, 3H).

^{13}C-NMR (CD_2Cl_2, 298K, 100 MHz, δ, ppm): 177.7, 165.4, 165.0, 164.8, 164.5, 156.1, 152.1, 151.6, 142.6, 138.2, 132.9, 132.8, 132.2, 130.4, 128.7 127.5, 125.2, 122.9, 122.8, 122.2, 121.6, 121.3, 121.0, 115.0, 114.9, 69.1, 68.4, 33.7, 32.5, 30.1, 29.9, 29.8, 29.7, 29.1, 26.5, 23.3, 21.9, 14.4.

FT-IR (KBr, v: cm^{-1}): 3450 (OH), 2921 (=C-H), 2842 (-C-H), 1733 (C=O), 1708 (C=O), 1699 (C=O dimeric), 1605 (C=C), 1252 (C-O), 1165 (C-O).

MS (MALDI$^+$, dithranol, m/z): found 866.35 [M+K$^+$] calculated with potassium 868.07 (828.98+39.09).

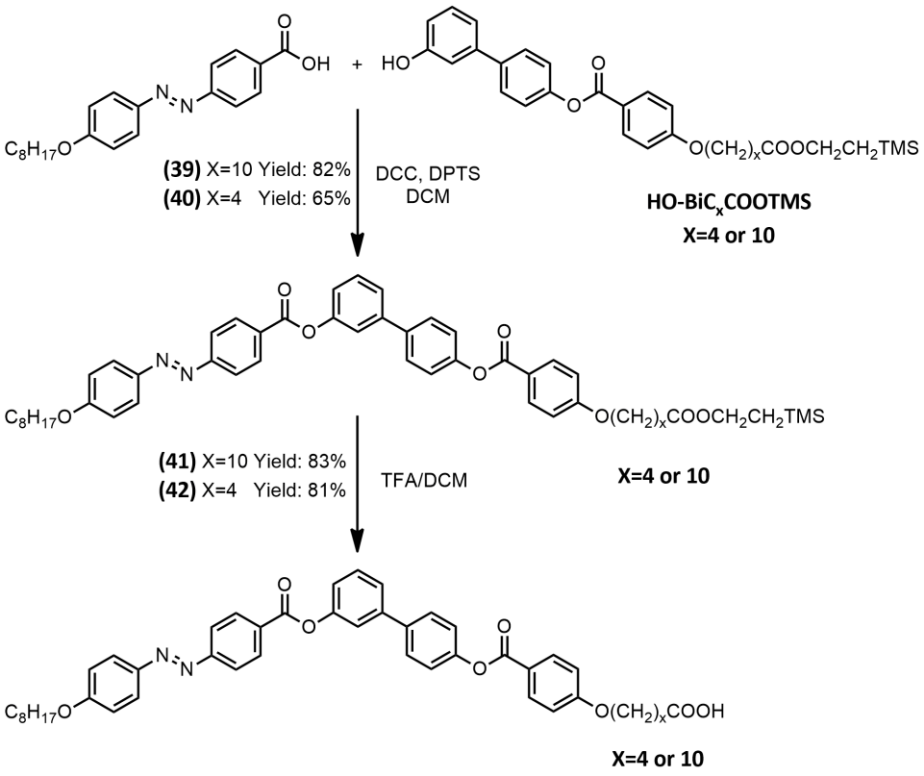

Scheme 3.4. *Synthesis of AZO acids.*

3.5.2.8 Synthesis of C_8AzoC_4COOH (42)

Synthesis of **8-Azo-4-COOTMS (40):** A mixture of 4-(4-octyloxyphenylazo)benzoic acid (400.00 mg, 1.13 mmol), **HO-BiC$_{10}$COOTMS** (573.00 mg, 1.13 mmol) and DPTS (100.00 mg, 0.34 mmol) were dissolved in dry DCM (5 ml) at 0^{o}C. After that, DCC (349.00 mg, 1.69 mmol) was slowly added and let react overnight at room temperature. The crude was filtered and the solvent evaporated. The product was purified by flash column chromatography in an eluent mix of DCM 1:1 hexane. Yield: 65%.

^{1}H-NMR (CD_2Cl_2, 298K, 400 MHz, δ, ppm): 8.35 (m ,2H), 8.15 (m, 2H), 7.98 (m, 4H), 7.70 (m, 2H), 7.54 (m, 3H), 7.31 (m, 2H), 7.26 (m, 1H), 7.05 (m, 2H), 7.00 (m, 2H), 4.16 (m, 2H), 4.08 (m, 2H), 2.37 (t, J= 6.8

Hz, 2H), 1.85 (m, 6H), 1.48 (m, 2H), 1.41-1.27 (m, 8H), 1.01 (m, 2H), 0.90 (t, J=6.8 Hz, 3H), 0.05 (s, 9H).

^{13}C-NMR (CD_2Cl_2, 298K, 100 MHz, δ, ppm): 173.8, 165.4, 163.2, 156.4, 152.1, 151.6, 147.4, 142.6, 138.2, 132.7, 131.7, 131.1, 128.7, 125.8, 123.1, 122.9, 122.2, 121.3, 121.0, 115.4, 69.2, 68.5, 63.0, 34.5, 32.4, 29.9, 29.8, 29.7, 29.1, 26.5, 23.2, 22.1, 17.8, 14.4, 1.3.

Synthesis of **8-Azo-4-COOH (42):** A solution of **8-Azo-10-COOTMS (40)** (250.00 mg, 0.30 mmol) was prepared in DCM (10 ml), over which was slowly added TFA (7 ml) at 0^{o}C. The mixture was stirred at room temperature for 3 hours. The crude was dispersed in 100 ml of water and extracted with DCM (3x50ml). The organic phase was dried with $MgSO_4$, filtered and evaporated. The crude was recrystallized in ethanol. Yield: 81%.

^{1}H-NMR (CD_2Cl_2, 298K, 400 MHz, δ, ppm): 8.35 (m ,2H), 8.17 (m, 2H), 7.98 (m, 2H), 7.67 (m, 2H), 7.52 (m, 2H), 7.30 (m, 2H), 7.24 (m, 1H), 7.03 (m, 2H), 6.98 (m, 2H), 4.08 (m, 4H), 2.48 (t, J= 6.8 Hz, 2H), 1.82 (m, 6H), 1.48 (m, 2H), 1.41-1.27 (m, 8H), 0.90 (t, J=6.8 Hz, 3H).

^{13}C-NMR (CD_2Cl_2, 298K, 100 MHz, δ, ppm): 177.5, 165.0, 164.9, 163.5, 162.7, 156.0, 151.5, 151.0, 147.0, 142.3, 137.9, 132.5, 131.4, 130.6, 130.0, 128.4, 125.5, 124.9, 122.7, 122.3, 121.9, 120.6, 115.0, 114.5, 68.6, 67.8, 33.4, 32.0, 31.1, 29.5, 29.4, 29.3, 28.6, 26.2, 22.8, 21.5, 14.2.

FT-IR (KBr, v: cm^{-1}): 3453 (OH), 2919 (=C-H), 2844 (-C-H), 1738 (C=O), 1721 (C=O), 1699 (C=O dimeric), 1602 (C=C), 1261 (C-O), 1161 (C-O).

MS (MALDI$^+$, dithranol, m/z): found 849.36 [M+Na$^+$] calculated with sodium 849.99 (827.01+22.98).

3.5.2.9 Synthesis of $C_8AzoC_{10}COOH$ (41)

Synthesis of **8-Azo-10-COOTMS (39):** A mixture of 4-(4-octyloxyphenylazo)benzoic acid (126.32 mg, 0.35 mmol), **HO-BiC_{10}COOTMS** (200 mg, 0.35 mmol) and DPTS (63.00 mg, 0.24 mmol) were dissolved in dry DCM (5 ml) at 0ºC. After that DCC (109.99 mg, 0.53 mmol) was slowly added and let react overnight at room temperature. The crude was filtered and the solvent evaporated. The product was purified by flash column chromatography in an eluent mix of DCM 1:1 hexane. Yield: 82%.

^{1}H-NMR ($CDCl_3$, 298K, 400 MHz, δ, ppm): 8.36 (m, 2H), 8.16 (m, 2H), 7.97 (m, 4H), 7.66 (m, 2H), 7.52 (m, 2H), 7.48 (s, 1H), 7.29 (m, 2H), 7.01 (m, 4H), 4.16 (m, 2H), 4.04 (m, 4H), 2.28 (t, J=7.5 Hz, 2H), 1.83 (m, 4H), 1.70-1.20 (m, 24H), 0.98 (m, 2H), 0.89 (t, J=6.8 Hz, 3H).

^{13}C-NMR ($CDCl_3$, 298K, 100 MHz, δ, ppm): 173.86, 165.43, 163.26, 156.43, 152.17, 151.63, 147.43, 142.68, 138.29, 132.74, 131.73, 131.16, 128.73, 125.83, 123.11, 122.96, 122.23, 121.37, 121.05, 115.43, 69.27, 68.57, 63.08, 34.58, 32.49, 29.96, 29.84, 29.77, 29.34, 29.28, 29.14, 26.53, 23.28, 22.13, 17.84, 14.45, 1.38.

Synthesis of **8-Azo-10-COOH (41):** A solution of **8-Azo-10-COOTMS (39)** (280 mg, 0.30 mmol) was prepared in DCM (10 ml), over which was slowly added TFA (7 ml) at 0ºC. The mixture was stirred at room temperature for 3 hours. The crude was dispersed in 100 ml of water and extracted with DCM (3x50ml). The organic phase was dried with $MgSO_4$, filtered and evaporated. The crude was recrystallized in ethanol. Yield: 83%.

^{1}H-NMR ($CDCl_3$, 298K, 400 MHz, δ, ppm): 8.36 (m, 2H), 8.16 (m, 2H), 7.97 (m, 4H), 7.66 (m, 2H), 7.52 (m, 2H), 7.48 (s, 1H), 7.29 (m, 2H), 7.01 (m, 4H), 4.04 (m, 4H), 2.28 (t, J=7.5 Hz, 2H), 1.83 (m, 4H), 1.70-1.20 (m, 24H), 0.89 (t, J=6.8 Hz, 3H).

^{13}C-NMR ($CDCl_3$, 298K, 100 MHz, δ, ppm): 179.22, 165.08, 164.89, 163.74, 162.64, 156.02, 151.52, 151.02, 147.04, 142.33, 137.90, 132.47, 131.39, 130.55, 130.01, 128.39, 125.46, 124.86, 122.69,

122.34, 121.62, 120.69, 120.56, 115.00, 114.48, 68.63, 68.47, 34.02, 31.96, 29.59, 29.49, 29.46, 29.37, 29.34, 29.32, 29.23, 29.18, 26.16, 26.11, 24.82, 22.80, 14.24.

FT-IR (KBr, v: cm^{-1}): 3450 (OH), 2925 (=C-H), 2851 (-C-H), 1730 (C=O), 1702 (C=O dimeric), 1602 (C=C), 1252 (C-O), 1168 (C-O).

MS (MALDI$^+$, dithranol, m/z): found 835.41 [M+Na^+] calculated with sodium 835.66 (812.98+22.98).

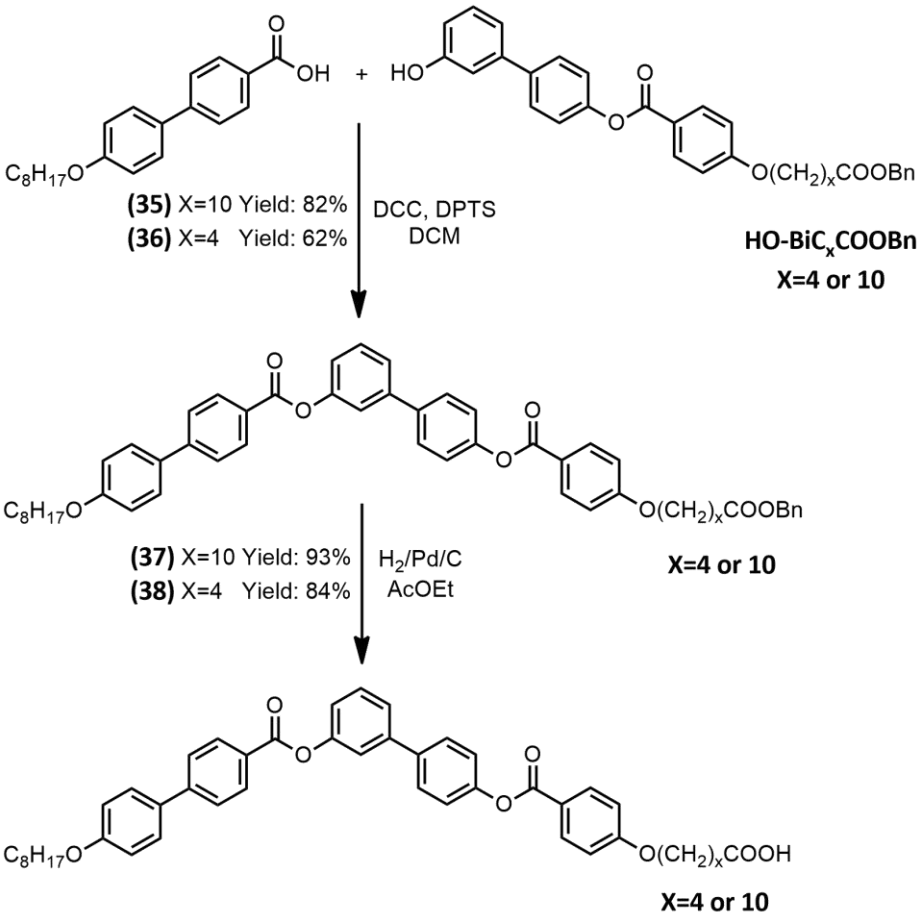

Scheme 3.5. *Synthesis of biphenyl acids.*

3.5.2.10 Synthesis of C_8BiC_4COOH (38)

Synthesis of **8-Bi-4-COOBn (36):** A mixture of 4´-octyloxybiphenyl-4-carboxylic acid (300.00 mg, 0.92 mmol), **HO-BiC_{10}COOBn** (447.00 mg, 0.92 mmol) and DPTS (81.00 mg, 0.28 mmol) was dissolved in dry DCM

(10 ml) at 0°C. After that, DCC (285.00 mg, 1.38 mmol) was slowly added and let react overnight at room temperature. The crude was filtered and the solvent evaporated. The product was purified by flash column chromatography in dichloromethane. Yield: 62%.

^{1}H-NMR ($CDCl_3$, 298K, 400 MHz, δ, ppm): 8.26 (m, 2H), 8.15 (m, 2H), 7.75 (m, 2H), 7.69 (m, 2H), 7.64 (m, 2H), 7.52 (m, 3H), 7.35 (m, 5H), 7.30 (m, 2H), 7.25 (m, 1H), 6.98 (m, 4H), 5.12 (s, 2H), 4.08 (t, J=6.0 Hz, 2H), 4.02 (t, J=6.4 Hz, 2H), 2.47 (t, J=7.5 Hz, 2H), 1.84 (m, 4H), 1.66 (m, 2H), 1.57-1.23 (m, 10 H), 0.90 (t, J=6.8 Hz, 3H).

^{13}C-NMR ($CDCl_3$, 298K, 100 MHz, δ, ppm): 173.5, 165.6, 165.3, 164.0, 160.3, 152.2, 151.6, 146.5, 142.5, 138.2, 136.9, 132.7, 132.3, 131.2, 130.4, 129.1, 128.9, 128.7, 128.1, 127.1, 125.1, 122.8, 122.2, 121.3, 121.0, 115.5, 114.9, 68.8, 68.4, 66.6, 34.3, 32.4, 29.9, 29.8, 29.1, 26.6, 23.2, 22.1, 14.4.

Synthesis of **8-Bi-4-COOH (38):** In a flask was prepared a solution of **8-Bi-10-COOBn (36)** (454.00 mg, 0.56 mmol) in ethyl acetate (15 ml). Three cycles of vacuum/argon were performed and then Pd/C was added (45.00 mg, 10% wt); after that, other three cycles of vacuum/argon were performed, followed by three cycles of vacuum/hydrogen. The mixture was stirred under hydrogen atmosphere overnight. The crude was filtered over celite and the solvent was evaporated. The product was recrystallized in ethanol Yield: 84%

^{1}H-NMR ($CDCl_3$, 298K, 400 MHz, δ, ppm): 8.26 (m, 2H), 8.17 (m, 2H), 7.71 (m, 2H), 7.66 (m, 2H), 7.61 (m, 2H), 7.52 (m, 3H), 7.29 (m, 2H), 6.99 (m, 4H), 4.08 (t, J=6.0 Hz, 2H), 4.02 (t, J=6.8 Hz, 2H), 2.48 (t, J=6.8 Hz, 2H), 1.82 (m, 4H), 1.62 (m, 2H), 1.54-1.23 (m, 10 H), 0.90 (t, J=6.8 Hz, 3H).

^{13}C-NMR ($CDCl_3$, 298K, 100 MHz, δ, ppm): 178.1, 165.3, 165.1, 163.5, 159.8, 151.6, 151.0, 146.2, 142.3, 138.0, 132.5, 132.1, 130.9, 130.0, 128.6, 128.4, 127.6, 126.8, 124.8, 122.3, 121.9, 120.8, 120.6, 115.2,

114.4, 68.3, 67.8, 33.4, 33.3, 33.2, 32.0, 29.5, 29.4, 28.6, 26.2, 22.8, 21.5, 14.3.

FT-IR (KBr, v: cm^{-1}): 3456 (OH), 2918 (=C-H), 2848 (-C-H), 1735 (C=O), 1724 (C=O), 1696 (C=O dimeric), 1602 (C=C), 1253 (C-O), 1163 (C-O).

MS (MALDI$^+$, dithranol, m/z): found 737.30 [M+Na^+] calculated with sodium 737.30 (714.31+22.98).

3.5.2.11 Synthesis of $C_8BiC_{10}COOH$ (37)

Synthesis of **8-Bi-10-COOBn (35):** A mixture of 4-octyloxybiphenyl-4-carboxylic acid (112.60 mg, 0.34 mmol), **HO-BiC_{10}COOBn** (200 mg, 0.34 mmol) and DPTS (60.58 mg, 0.24 mmol) was dissolved in dry DCM (10 ml) at 0^{o}C. After that, DCC (106 mg, 0.51 mmol) was slowly added and let react overnight at room temperature. The crude was filtered and the solvent evaporated. The product was purified by flash column chromatography in an eluent mix of DCM 1:1 hexane. Yield: 82%.

^{1}H-NMR ($CDCl_3$, 298K, 400 MHz, δ, ppm): 8.28 (d, J=8.3 Hz, 2H), 8.17 (d, J=8.8 Hz, 2H), 7.77 (d, J=8.3 Hz, 2H), 7.72 (d, J=8.6 Hz, 2H), 7.67 (d, J=8.7 Hz, 2H), 7.55 (m, 3H), 7.33 (m, 7H), 7.03 (m, 4H), 5.12 (s, 2H), 4.07 (m, 4H), 2.38 (t, J=7.5 Hz, 2H), 1.84 (m, 4H), 1.66 (m, 2H), 1.57-1.23 (m, 20 H), 0.93 (t, J=7.0 Hz, 3H).

^{13}C-NMR ($CDCl_3$, 298K, 100 MHz, δ, ppm): 173.51, 165.63, 165.37, 164.08, 160.35, 152.23, 151.69, 146.54, 142.50, 138.21, 136.90, 132.65, 132.60, 132.31, 130.43, 129.13, 128.90, 128.71, 128.16, 127.11, 125.13, 122.87, 122.20, 121.34, 115.51, 114.92, 68.83, 68.42, 66.63, 34.32, 32.45, 29.97, 29.84, 29.37, 29.35, 29.16, 26.64, 23.21, 22.13, 14.43.

Synthesis of **8-Bi-10-COOH (37):** In a flask was prepared a solution of **8-Bi-10-COOBn (35)** (260 mg, 0.28 mmol) in ethyl acetate (15 ml). Three cycles of vacuum/argon were performed and then Pd/C was added (26 mg, 10% wt); after that, another three cycles of vacuum/argon were performed, followed by three cycles of vacuum/hydrogen. The mixture was stirred under hydrogen

atmosphere overnight. The crude was filtered over celite and the solvent was evaporated. The product was recrystallized in ethanol Yield: 93%

^{1}H-NMR ($CDCl_3$, 298K, 400 MHz, δ, ppm): 8.26 (d, J=8.6 Hz, 2H), 8.16 (d, J=9.0 Hz, 2H), 7.71 (d, J=8.6 Hz, 2H), 7.66 (d, J=8.7 Hz, 2H), 7.61 (d, J=8.8 Hz, 2H), 7.52 (m, 3H), 7.29 (d, J=8.7 Hz, 2H), 6.99 (m, 4H), 4.03 (m, 4H), 2.29 (t, J=7.5 Hz, 2H), 1.82 (m, 4H), 1.62 (m, 2H), 1.54-1.23 (m, 20 H), 0.90 (t, J=7.0 Hz, 3H).

^{13}C-NMR ($CDCl_3$, 298K, 100 MHz, δ, ppm): 178.48, 174.07, 165.31, 165.09, 163.74, 159.76, 151.60, 150.99, 146.20, 142.28, 137.96, 132.46, 132.12, 130.90, 129.96, 128.54, 128.39, 127.61, 126.76, 124.74, 122.32, 121.62, 120.76, 120.63, 115.16, 114.47, 68.47, 68.33, 34.53, 33.89, 31.97, 29.61, 29.51, 29.46, 29.39, 29.34, 29.24, 29.17, 26.20, 26.11, 25.12, 24.82, 22.81, 14.20.

FT-IR (KBr, v: cm^{-1}): 3453 (OH), 2916 (=C-H), 2856 (-C-H), 1738 (C=O), 1721 (C=O), 1699 (C=O dimeric), 1602 (C=C), 1261 (C-O), 1161 (C-O).

MS (MALDI^{+}, dithranol, m/z): found 823.39 [M+K^{+}] calculated with potassium 823.99 (784.90+39.09).

3.5.2.12 *Synthesis of Ionic Bent-Core Pillar[5]arenes*

Azo 4-8-P5N10

^{1}H-NMR ($CDCl_3$, 298K, 400 MHz, δ, ppm): 8.33 (d, J=8.3 Hz, 20H), 8.12 (d, J=7.6 Hz, 20H), 7.95 (m, 40H), 7.62 (d, J=8.2 Hz, 20H), 7.47 (m, 30H), 7.24 (m, 20H), 7.01 (d, J=8.9 Hz, 20H), 6.93 (d, J=8.4 Hz, 20H), 4.99 (s, 30H), 4.05 (m, 40H), 3.75 (m, 20H), 3.43 (s, 10H), 2.41 (m, 20H), 1.83 (m, 40H), 1.54-1.23 (m, 120H), 0.90 (t, J=6.9 Hz, 30H).

^{13}C-NMR ($CDCl_3$, 298K, 100 MHz, δ, ppm): 178.22, 165.00, 164.88, 163.49, 162.62, 155.97, 151.48, 150.94, 147.01, 142.24, 137.87, 132.46, 131.38, 130.52, 130.01, 128.37, 125.46, 124.84, 122.69, 122.31, 121.75, 120.53, 114.97, 114.42, 68.61, 67.97, 39.83, 34.91, 31.96, 29.50, 29.38, 29.32, 28.83, 26.16, 22.81, 22.12, 14.26.

FT-IR (KBr, ν: cm^{-1}): 3441 (-NH_3^+), 2921 (=C-H), 2841 (-C-H), 1732 (C=O), 1604 (C=C), 1251 (C-O).

Azo 10-8-P5N10

^{1}H-NMR ($CDCl_3$, 298K, 400 MHz, δ, ppm): 8.36 (d, J=8.3 Hz, 20H), 8.16 (d, J=7.6 Hz, 20H), 7.98 (m, 40H), 7.66 (d, J=8.2 Hz, 20H), 7.50 (m, 30H), 7.29 (d, J=8.9 Hz, 20H), 7.00 (m, 40H), 4.05 (m, 40H), 3.87 (m, 30H), 2.35 (t, J=7.5 Hz, 20H), 1.82 (m, 40H), 1.64 (m, 20H), 1.54-1.23 (m, 200H), 0.90 (t, J=6.9 Hz, 30H).

^{13}C-NMR ($CDCl_3$, 298K, 100 MHz, δ, ppm): 178.46, 165.10, 164.90, 163.74, 162.63, 156.01, 152.33, 151.50, 151.39, 151.00, 150.97, 147.03, 137.90, 137.35, 132.59, 132.34, 131.49, 131.28, 130.54, 128.59, 128.22, 125.61, 125.30, 122.80, 122.55, 122.35, 121.95, 121.59, 120.68, 115.10, 114.88, 114.57, 114.37, 68.63, 68.46, 65.33, 34.10, 31.96, 29.61, 29.58, 29.49, 29.37, 29.23, 26.15, 24.92, 22.81, 13.67.

FT-IR (KBr, ν: cm^{-1}): 3427 (-NH_3^+), 2921 (=C-H), 2851 (-C-H), 1730 (C=O), 1604 (C=C), 1253 (C-O).

B1 4-8-P5N10

^{1}H-NMR ($CDCl_3$, 298K, 400 MHz, δ, ppm): 8.28 (d, J=8.2 Hz, 20H), 8.13 (m, 40H), 7.62 (d, J=9.0 Hz, 20H), 7.46 (m, 30H), 7.36 (d, J=8.5 Hz, 20H), 7.20 (m, 20H), 6.95 (m, 40H), 5.85 (s, 30H), 4.04 (m, 40H), 3.71 (s, 10H), 3.40 (s, 10H), 2.36 (m, 20H), 1.83 (m, 40H), 1.52-1.23 (m, 120H), 0.89 (t, J=6.9 Hz, 30H).

^{13}C-NMR ($CDCl_3$, 298K, 100 MHz, δ, ppm): 179.38, 165.01, 164.61, 164.46, 163.96, 163.50, 155.54, 151.45, 150.91, 142.16, 137.82, 132.56, 132.42, 131.95, 129.99, 128.33, 126.96, 124.78, 122.30, 122.26, 121.66, 121.08, 120.48, 114.55, 114.40, 110.14, 68.53, 68.02, 35.76, 31.94, 29.47, 29.36, 29.23, 28.92, 26.12, 22.80, 22.38, 14.24.

FT-IR (KBr, ν: cm^{-1}): 3437 (-NH_3^+), 2919 (=C-H), 2848 (-C-H), 1734 (C=O), 1606, 1580 (C=C), 1258, 1151 (C-O).

B1 10-8-P5N10

^{1}H-NMR ($CDCl_3$, 298K, 400 MHz, δ, ppm): 8.31 (d, J=8.8 Hz, 20H), 8.16 (m, 40H), 7.65 (d, J=8.7 Hz, 20H), 7.48 (m, 30H), 7.38 (d, J=8.8 Hz, 20H), 7.29 (d, J=8.6 Hz, 20H), 7.22 (m, 10H), 6.98 (m, 40H), 4.05 (m, 40H), 2.34 (t, J=7.5 Hz, 20H), 1.82 (m, 40H), 1.63 (m, 20H), 1.53-1.20 (m, 200H), 0.90 (t, J=6.9 Hz, 30H).

^{13}C-NMR ($CDCl_3$, 298K, 100 MHz, δ, ppm): 179.03, 165.10, 164.66, 164.50, 163.98, 163.73, 155.57, 151.46, 150.98, 142.29, 137.89, 132.58, 132.47, 131.99, 130.01, 128.39, 127.00, 124.84, 122.33, 122.28, 121.58, 121.09, 120.71, 120.56, 114.57, 114.46, 68.55, 68.46, 35.30, 31.95, 29.67, 29.60, 29.51, 29.48, 29.37, 29.25, 29.24, 26.14, 25.48, 22.81, 14.25.

FT-IR (KBr, ν: cm^{-1}): 3441 (-NH_3^+), 2921 (=C-H), 2856 (-C-H), 1735 (C=O), 1604, 1509 (C=C), 1256, 1163 (C-O).

Bi 4-8-P5N10

^{1}H-NMR ($CDCl_3$, 298K, 400 MHz, δ, ppm): 8.23 (d, J=8.4 Hz, 20H), 8.10 (d, J=8.7 Hz, 20H), 7.67 (d, J= 8.5 Hz, 20H), 7.59 (m, 40H), 7.45 (m, 30H), 7.22 (m, 30H), 6.99 (d, J=8.8 Hz, 20H), 6.90 (d, J=8.7 Hz, 20H), 5.19 (s, 30H), 4.00 (t, J=6.5 Hz, 40H), 3.74 (m ,20H), 3.43 (s, 10H), 2.99 (m, 20H), 2.37 (m, 20H), 1.81 (m, 60H), 1.54-1.17 (m, 120H), 0.89 (t, J=7.0 Hz, 30H).

^{13}C-NMR ($CDCl_3$, 298K, 100 MHz, δ, ppm): 165.30, 163.54, 159.86, 151.74, 151.08, 146.30, 142.32, 138.05, 132.51, 132.24, 131.19, 130.93, 129.97, 128.57, 128.41, 127.74, 126.81, 124.73, 122.32, 122.03, 120.80, 120.66, 118.28, 115.27, 114.53, 68.46, 68.43, 67.92, 33.44, 31.99, 29.57, 29.53, 29.45, 29.40, 28.70, 26.24, 22.81, 21.70, 14.23.

FT-IR (KBr, ν: cm^{-1}): 3439 (-NH_3^+), 2931 (=C-H), 2854 (-C-H), 1735 (C=O), 1604 (C=C), 1258 (C-O), 1167(C-O).

Bi 10-8-P5N10

^{1}H-NMR ($CDCl_3$, 298K, 400 MHz, δ, ppm): 8.26 (d, J=8.4 Hz, 20H), 8.16 (d, J=8.9 Hz, 20H), 7.71 (d, J=8.4 Hz, 20H), 7.66 (d, J=8.6 Hz, 20H), 7.61 (d, J=8.7 Hz, 20H), 7.51 (d, J=4.9 Hz, 20H), 7.46 (s, 10H), 7.26 (d, J=8.6 Hz, 20H), 7.00 (m, 40H), 4.04 (m, 40H), 3.87 (m, 20H), 2.36 (t, J=7.6 Hz, 20H), 1.82 (q, J=7.7 Hz, 40H), 1.70-1.23 (m, 200H), 0.90 (t, J=6.9 Hz, 30H).

^{13}C-NMR ($CDCl_3$, 298K, 100 MHz, δ, ppm): 174.05, 165.30, 165.09, 163.74, 159.76, 151.60, 150.99, 146.19, 142.28, 137.96, 132.46, 132.12, 132.10, 130.90, 129.96, 128.54, 128.40, 127.61, 126.76, 124.74, 122.32, 121.62, 120.76, 120.63, 115.15, 114.47, 68.47, 68.33, 34.53, 34.25, 31.97, 29.61, 29.51, 29.39, 29.27, 29.24, 26.20, 25.91, 25.12, 22.81, 14.25.

FT-IR (KBr, ν: cm^{-1}): 3426 ($-NH_3^+$), 2921 (=C-H), 2851 (-C-H), 1732 (C=O), 1704 (C=O dimeric), 1604 (C=C), 1251 (C-O), 1171 (C-O).

3.6 Appendix

3.6.1 NMR Spectra

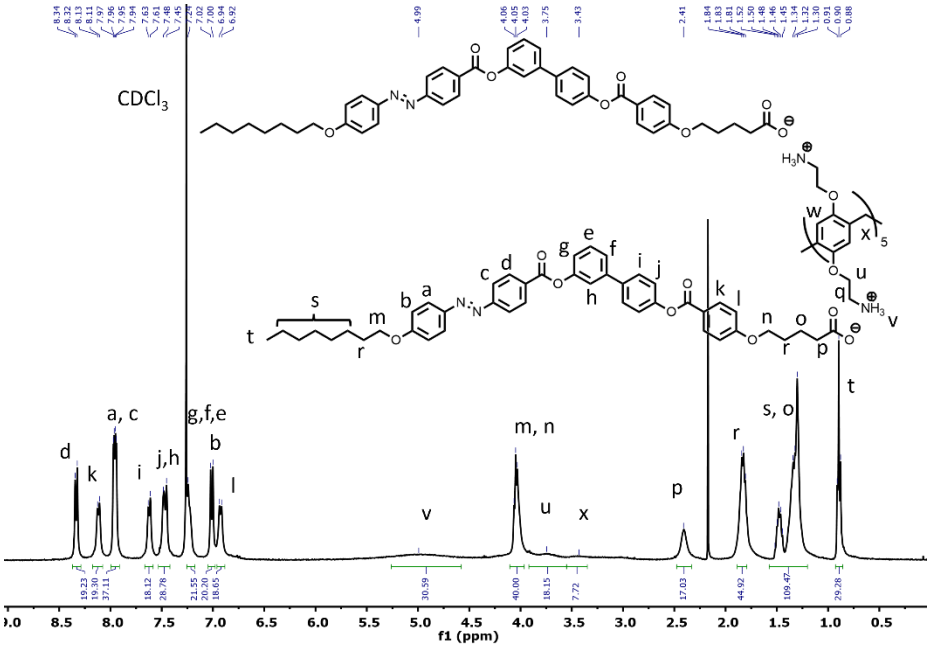

Figure 3.39. *^{1}H-NMR spectrum of* ***Azo 4-8-P5N10****, $CDCl_3$, 298K, 400 MHz.*

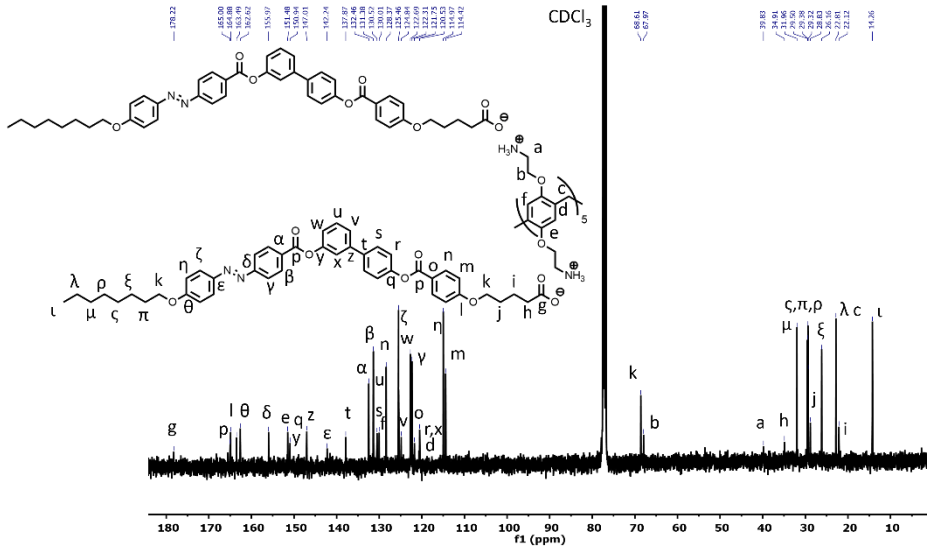

Figure 3.40. *^{13}C-NMR spectrum of* ***Azo 4-8-P5N10****, DMSO-d_6, 298K, 100 MHz.*

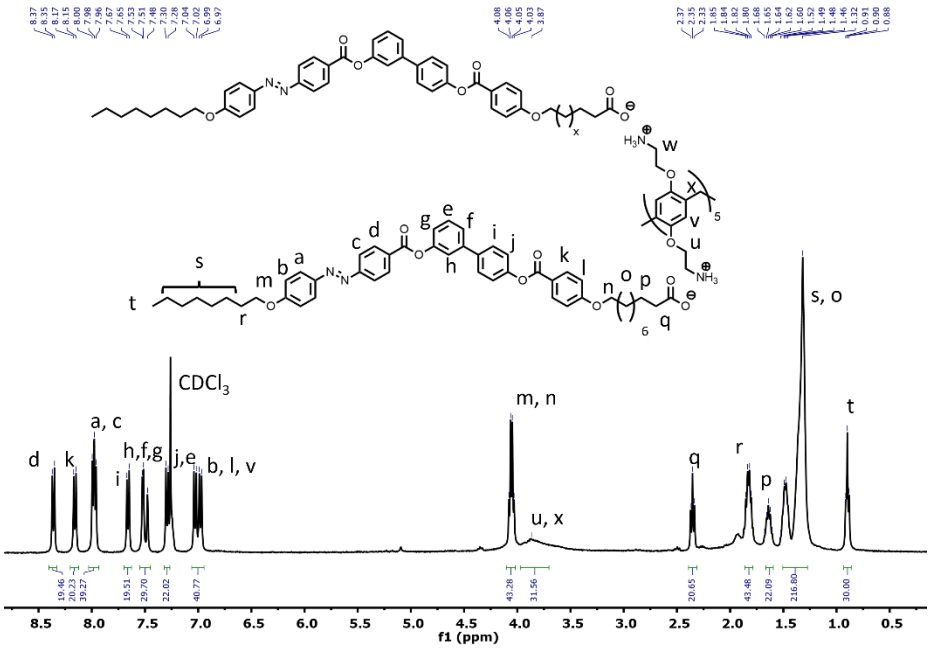

Figure 3.41. *^{1}H-NMR spectrum of* ***Azo 10-8-P5N10****, $CDCl_3$, 298K, 400 MHz.*

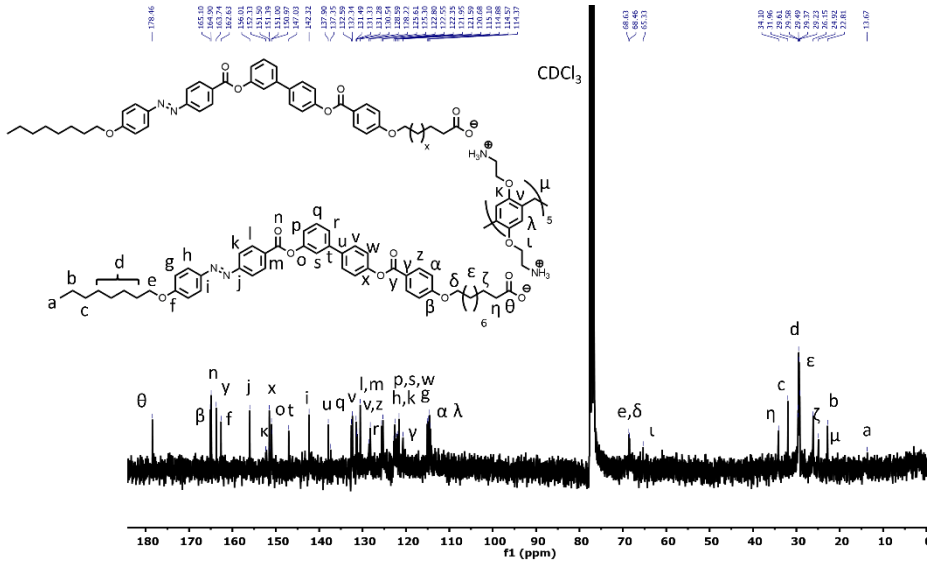

Figure 3.42. *^{13}C-NMR spectrum of* ***Azo 10-8-P5N10****, $CDCl_3$, 298K, 100 MHz.*

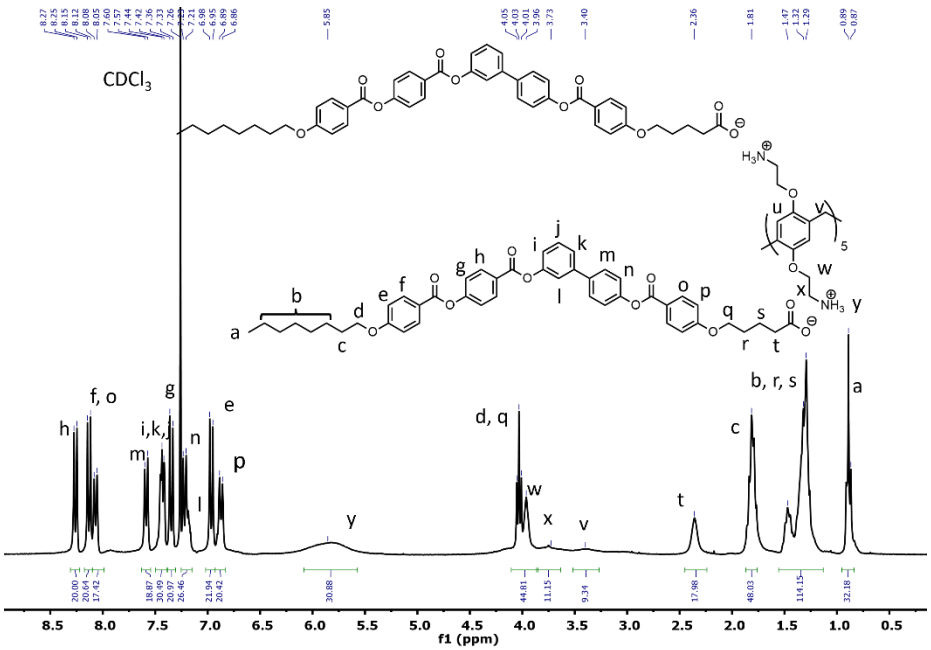

Figure 3.43. *^{1}H-NMR spectrum of **B1 4-8-P5N10**, $CDCl_3$, 298K, 400 MHz.*

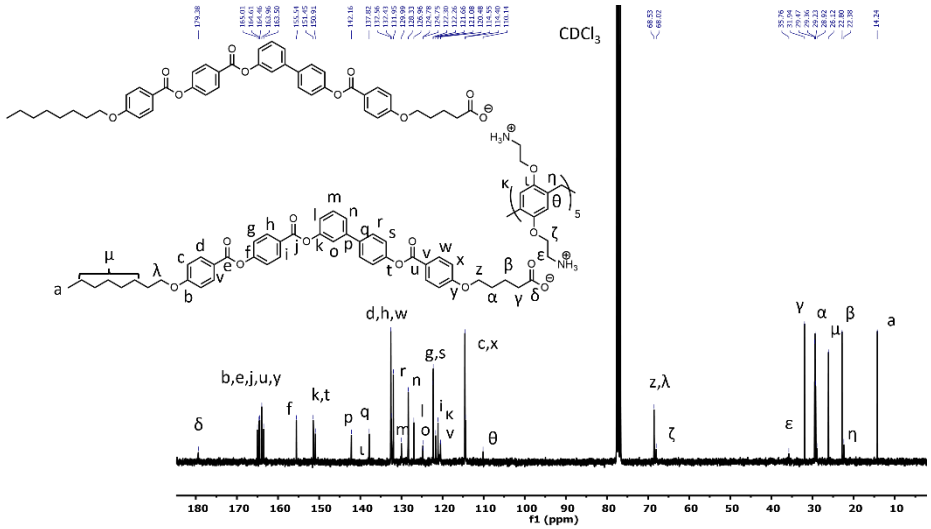

Figure 3.44. *^{13}C-NMR spectrum of **B1 4-8-P5N10**, $CDCl_3$, 298K, 100 MHz.*

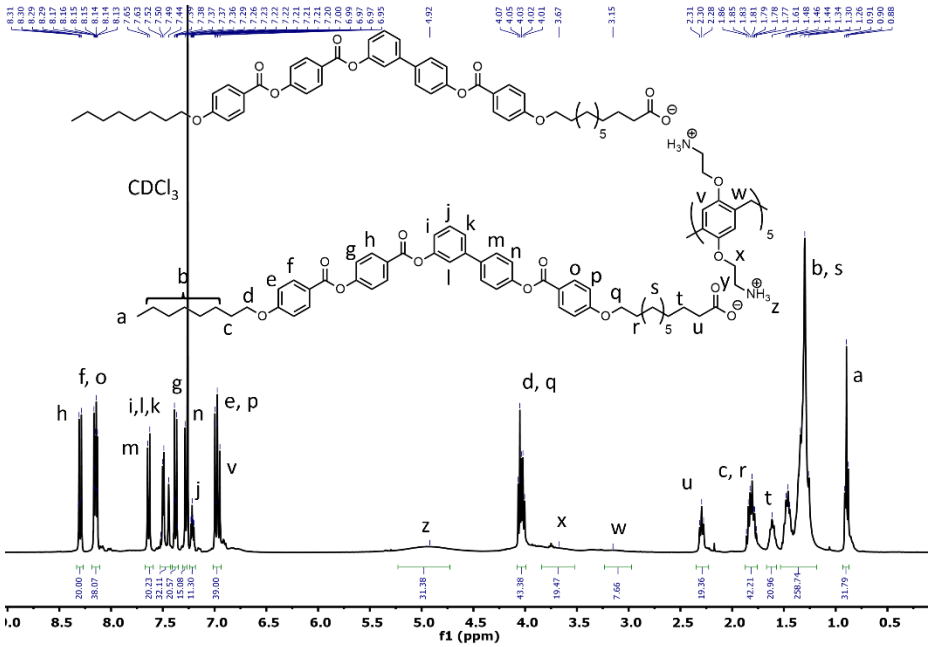

Figure 3.45. *^{1}H-NMR spectrum of **B1 10-8-P5N10**, $CDCl_3$, 298K, 400 MHz.*

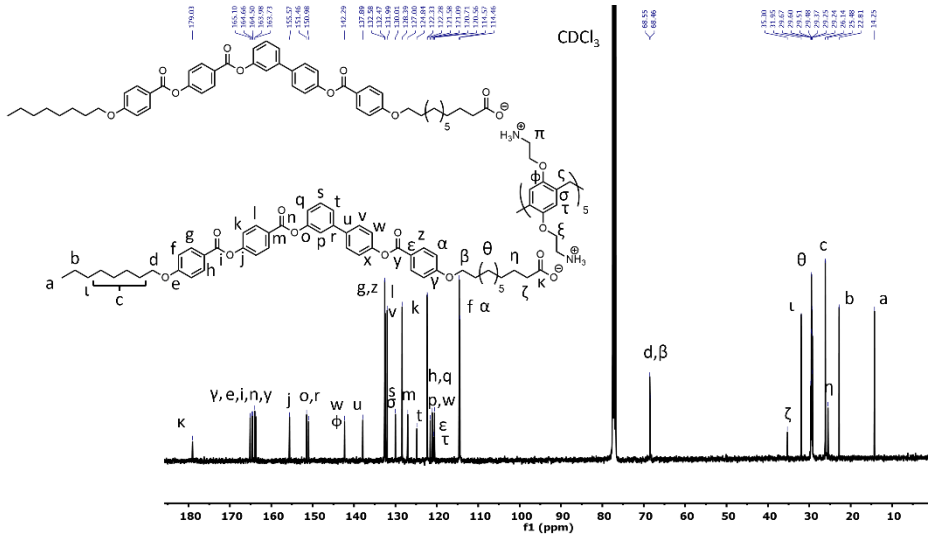

Figure 3.46. *^{13}C-NMR spectrum of **B1 10-8-P5N10**, $CDCl_3$, 298K, 100 MHz.*

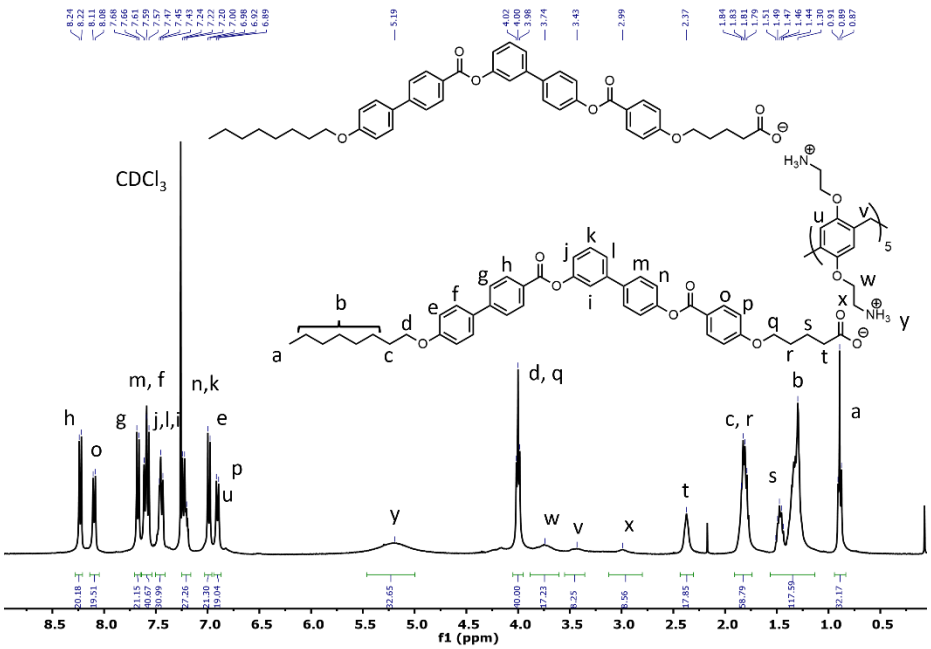

Figure 3.47. *^{1}H-NMR spectrum **Bi 4-8-P5N10**, $CDCl_3$, 298K, 400 MHz.*

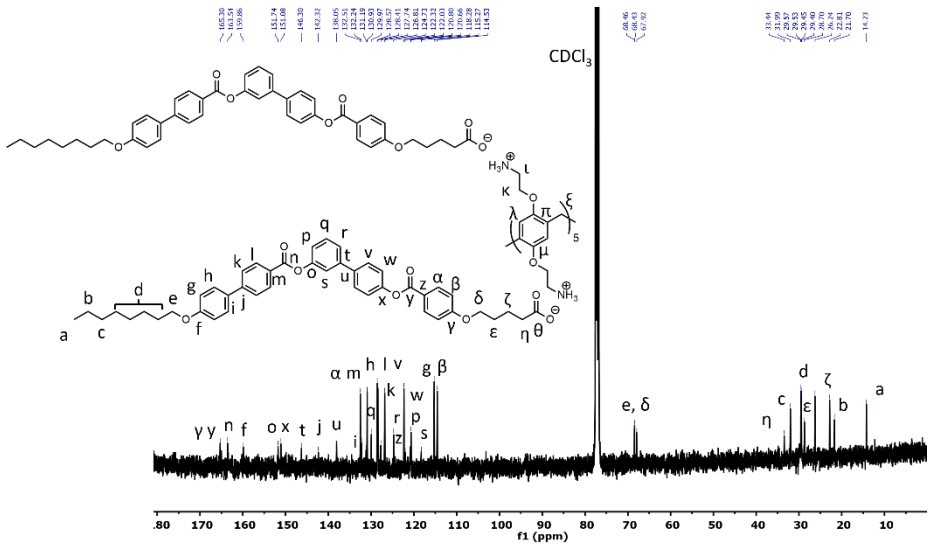

Figure 3.48. *^{13}C-NMR spectrum of **Bi 4-8-P5N10**, $CDCl_3$, 298K, 100 MHz.*

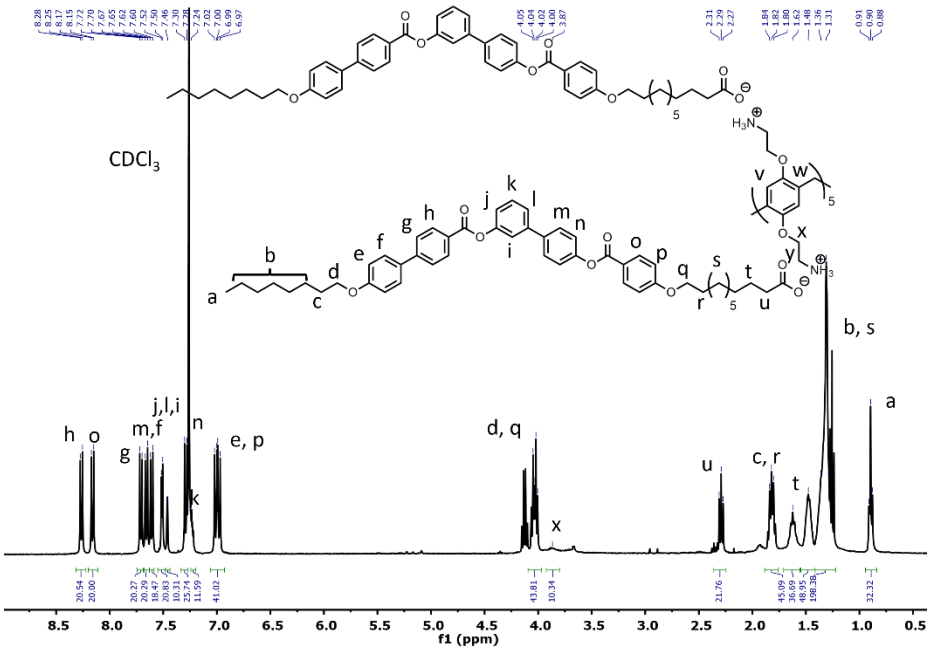

Figure 3.49. *^{1}H-NMR spectrum of **Bi 10-8-P5N10**, $CDCl_3$, 298K, 400 MHz.*

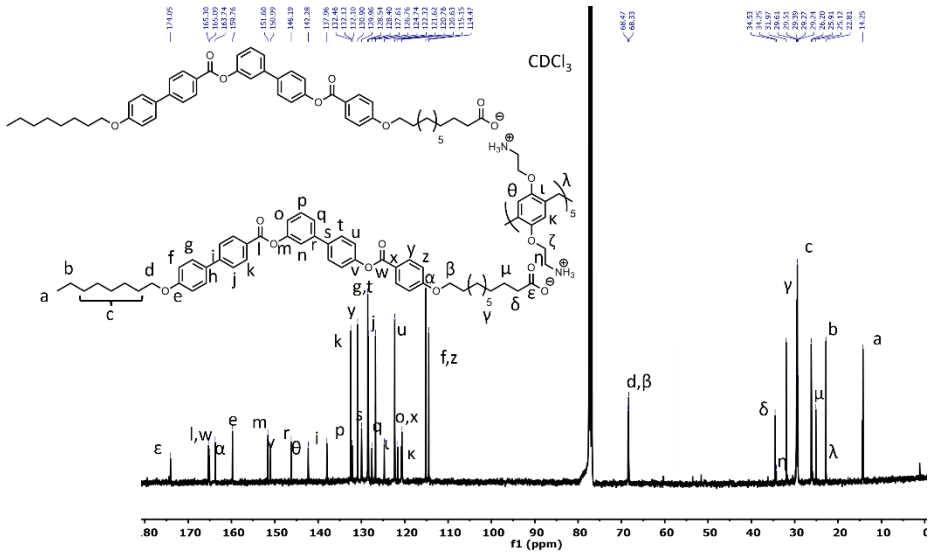

Figure 3.50. *^{13}C-NMR spectrum of **Bi 10-8-P5N10**, $CDCl_3$, 298K, 100 MHz.*

3.6.2 FT-IR spectra

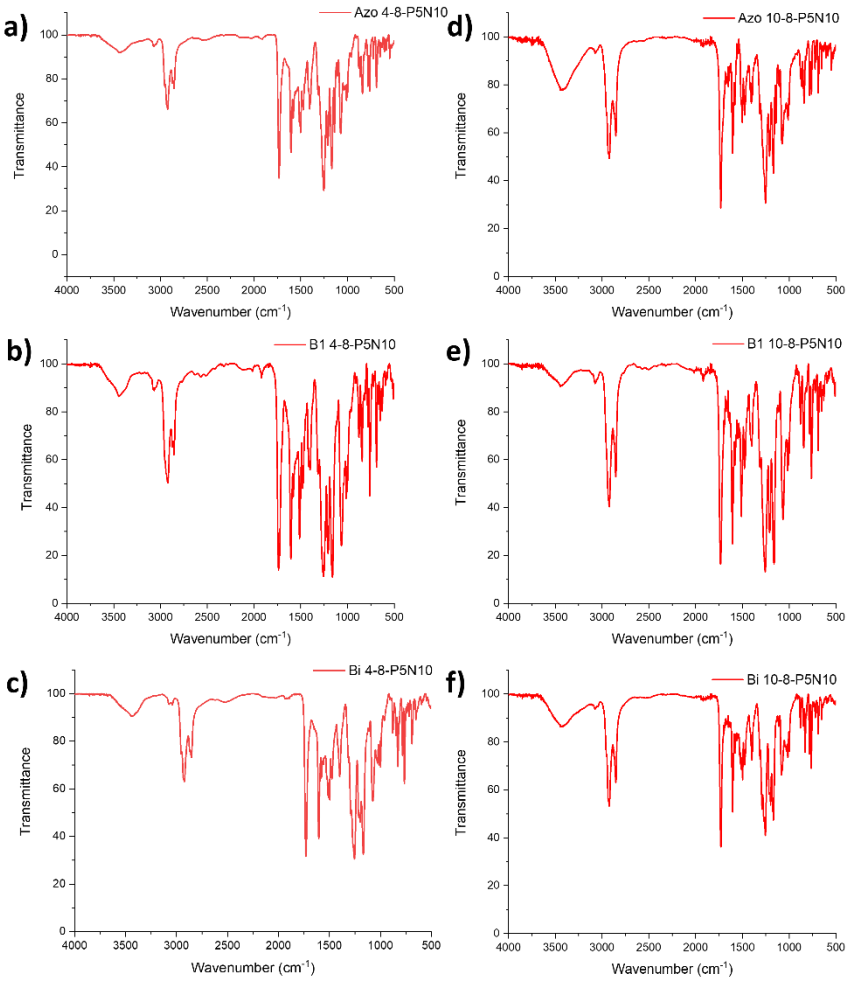

Figure 3.51. *FT-IR spectra in KBr of a)* ***Azo 4-8-P5N10****, b)* ***B1 4-8-P5N10****, c)* ***Bi 4-8-P5N10****, d)* ***Azo 10-8-P5N10****, d)* ***B1 10-8-P5N10*** *and* ***Bi 10-8-P5N10****.*

3.6.3 DSC Thermograms

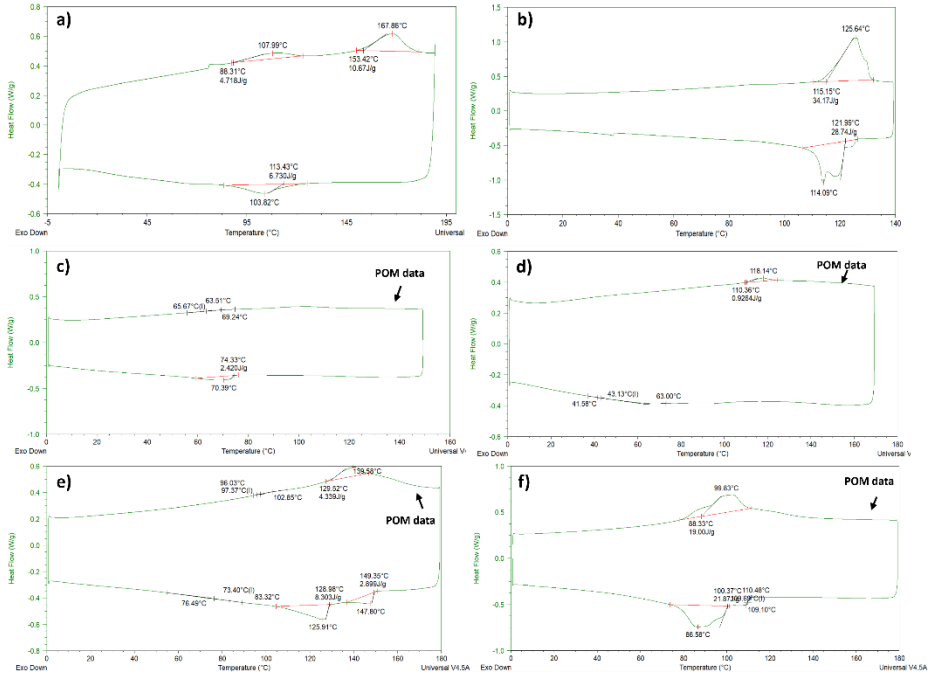

Figure 3.52. *DSC thermograms corresponding to the second heating-cooling cycle of a)* ***Azo 4-8-P5N10****, b)* ***Azo 10-8-P5N10****, c)* ***B1 4-8-P5N10*** *d)* ***B1 10-8-P5N10****, e)* ***Bi 4-8-P5N10*** *and f)* ***Bi 10-8-P5N10****.*

3.6.4 X-Ray Diffractograms

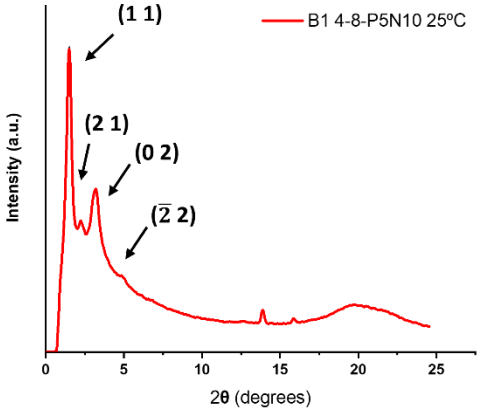

Figure 3.53. *XRD of* ***B1 4-8-P5N10*** *at 25ºC.*

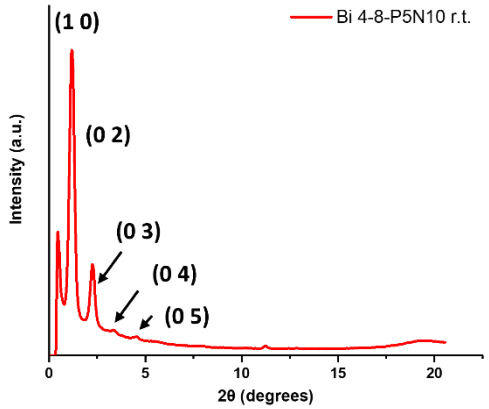

Figure 3.54. *XRD of* ***Bi 4-8-P5N10*** *at room temperature after a heating-cooling cycle.*

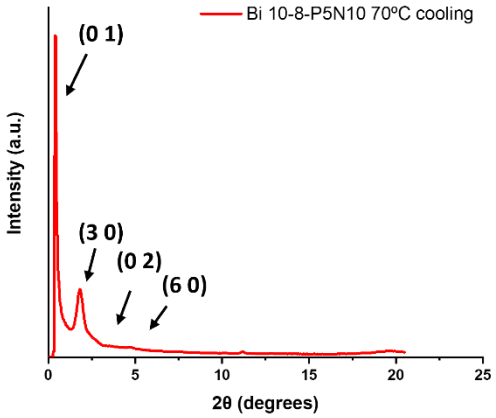

Figure 3.55. *XRD of* ***Bi 10-8-P5N10*** *at 70ºC in the cooling cycle.*

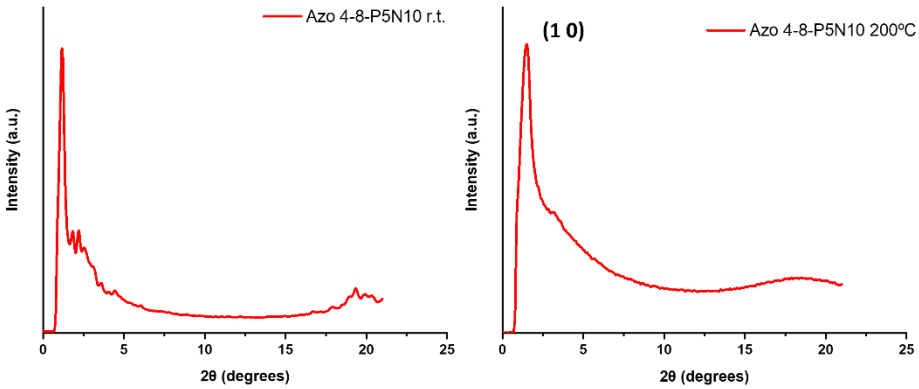

Figure 3.56. *XRD of* ***Azo 4-8-P5N10*** *at room temperature and at 200ºC in the heating cycle.*

3.6.5 Electrochemical impedance spectroscopy measurements

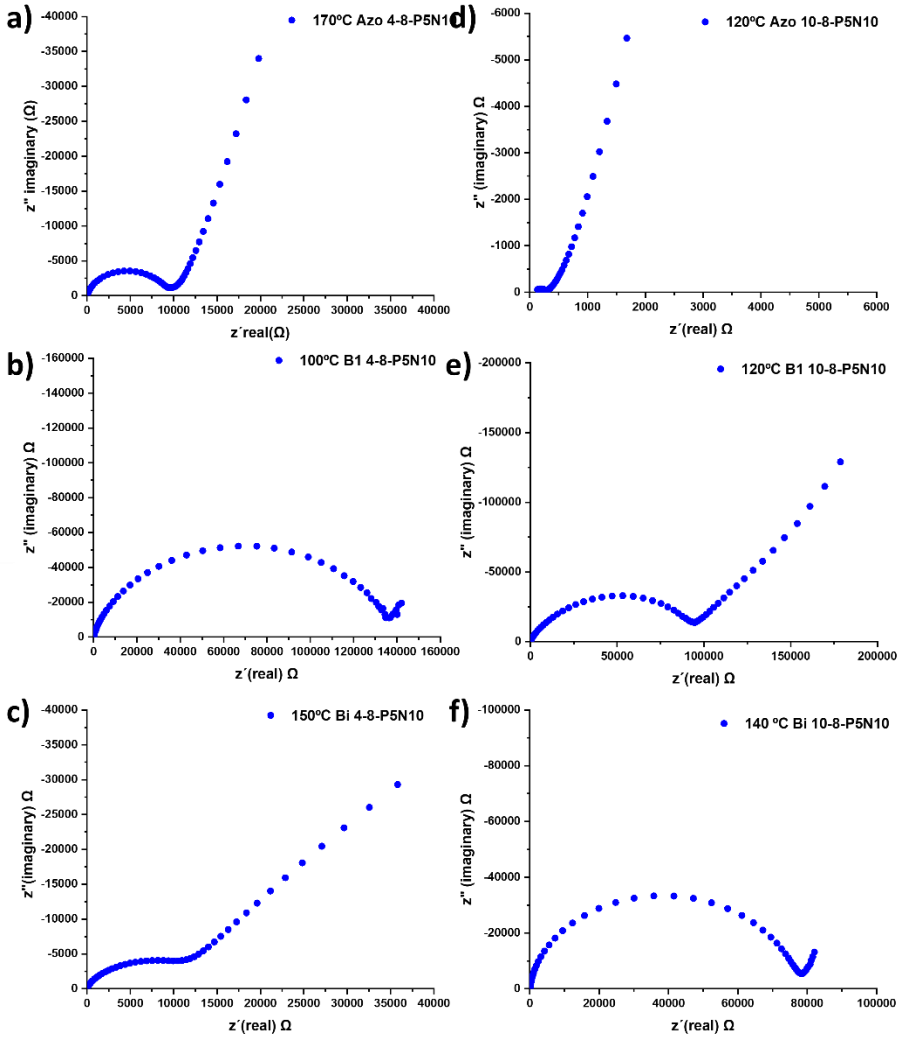

Figure 3.57. *Nyquist plots of the bent-core pillar[5]arenes at different temperatures: a)* ***Azo 4-8-P5N10*** *at 170°C, b)* ***B1 4-8-P5N10*** *at 100°C, c)* ***Bi 4-8-P5N10*** *at 150°C, d)* ***Azo 10-8-P5N10*** *at 120°C, e)* ***B1 10-8-P5N10*** *at 120°C and f)* ***Bi 10-8-P5N10*** *at 140°C.*

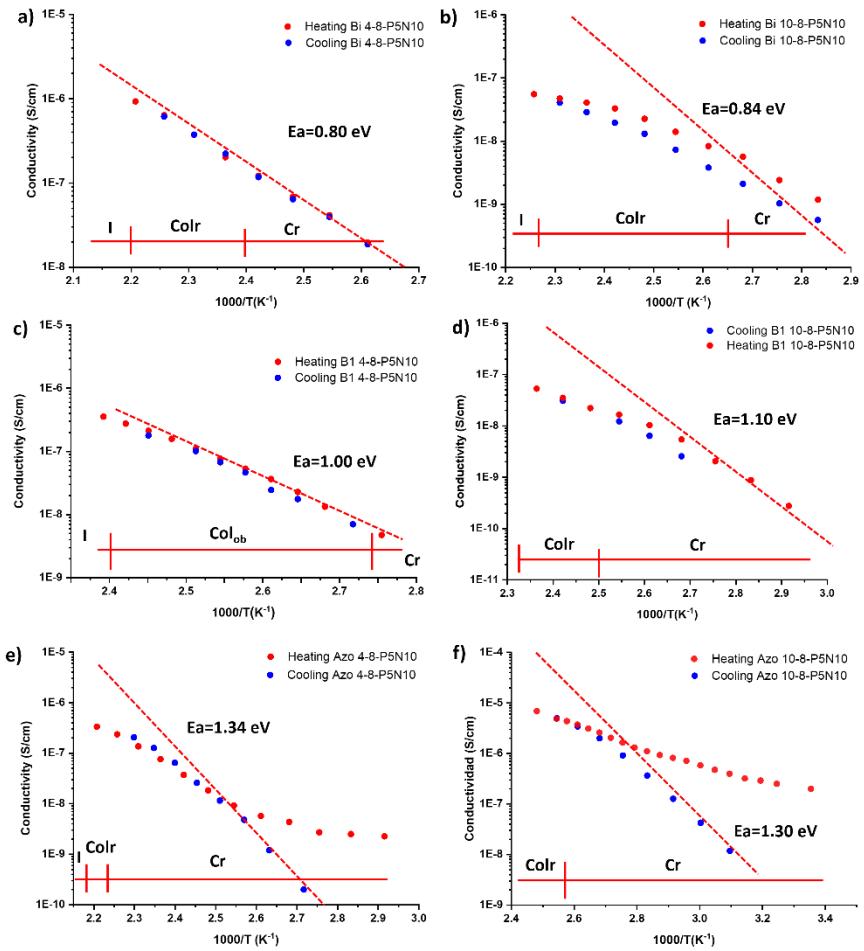

Figure 3.58. *Conductivity variation with temperature measured by EIS and activation energy of ionic bent-core pillar[5]arenes.*

3.7 References

[1] T. Niori, T. Sekine, J. Watanabe, T. Furukawa and H. Takezoe, Distinct ferroelectric smectic liquid crystals consisting of banana shaped achiral molecules, *J. Mater. Chem.,* 1996, **6**, 1231-1233.

[2] Y. Takanishi, New liquid crystal formation induced by nanoscale phase separation composed of bent-core liquid crystal and rod-like cholesteric liquid crystal mixtures, *Soft Matter,* 2021, **17**, 563-570.

[3] N. Gimeno, I. Pintre, M. Martínez-Abadia, J. L. Serrano and M. B. Ros, Bent-core liquid crystal phases promoted by azocontaining molecules: from monomers to side chain polymers*, RSC Adv.,* 2014, **4**, 19694–19702.

[4] R. A. Reddy, U. Baumeister and C. Tschierske, Influence of the core structure on the development of polar order and superstructural chirality in liquid crystalline phases formed by silylated bent-core molecules: naphthalene derivatives, *J. Mater. Chem.,* 2007, **17**, 62–75.

[5] R. A. Reddy and C. Tschierske, Bent-core liquid crystals: polar order, superstructural chirality and spontaneous desymmetrisation in soft matter systems, *J. Mater. Chem.,* 2006, **16**, 907–961.

[6] S. Shadpour, A. Nemati, M. Salamonczyk, M. E. Prévôt, J. Liu, N. J. Boyd, M. R. Wilson, C. Zhu, E. Hegmann, A. I. Jákli and T. Hegmann, Missing Link between Helical Nano- and Microfilaments in B4 Phase Bent-Core Liquid Crystals, and Deciphering which Chiral Center Controls the Filament Handedness, *Small*, 2020, **16**, 1905591-1905603.

[7] Y. Takanishi, F. Araoka and H. Iwayama, The effect of the structure of a helical nanofilament of the B4 phase of bent-core liquid crystals on the nano-phase separation mixed with a rod-like cholesteric liquid crystal mixture*, RSC Adv.,* 2022, **12**, 29346–29349.

[8] S. P. Sreenilayam, Y. P. Panarin, J. K. Vij, V. P. Panov, A. Lehmann, M. Poppe, M. Prehm and C. Tschierske, Spontaneous helix formation in non-chiral bent-core liquid crystals with fast linear electro-optic effect, *Nat. Commun.,* 2016, **7**, 11369-11377.

[9] M. Alaasar, M. Prehm, S. Belau, N. Sebastián, M. Kurachkina, A. Eremin, C. Chen, F. Liu and C. Tschierske, Polar Order, Mirror Symmetry Breaking, and Photoswitching of

Chirality and Polarity in Functional Bent-Core Mesogens, *Chem. Eur.J.,* 2019*,* **25**, 6362 -6377.

[10] I. Dominguez-Candela, I. Zulkhairi, I. Pintre, N. F. K. Aripin, J. Lora-García, V. Fombuena, M. B. Ros and A. Martínez-Felipe, Light-responsive bent-core liquid crystals as candidates for energy conversion and storage, *J. Mater. Chem. C,* 2022, **10,** 18200-18212.

[11] M. Martínez-Abadía, S. Varghese, B. Milián-Medina, J. Gierschner, R. Giménez and M. B. Ros, Bent-core liquid crystalline cyanostilbenes: fluorescence switching and thermochromism, *Phys. Chem. Chem. Phys*., 2015, **17**, 11715-11724.

[12] D. Shen, A. Pegenau, S. Diele, I. Wirth and C. Tschierske, Molecular Design of Nonchiral Bent-Core Liquid Crystals with Antiferroelectric Properties, *J. Am. Chem. Soc.,* 2000*,* **122**, 1593-1601.

[13] E. Westphal, H. Gallardo, N. Sebastián, A. Eremin, M. Prehm, M. Alaasar and C. Tschierske, Liquid crystalline self-assembly of 2,5-diphenyl1,3,4-oxadiazole based bent-core molecules and the influence of carbosilane end-groups, *J. Mater. Chem. C,* 2019*,* **7**, 3064-3081.

[14] H.-J. Kim, F. Liu, J.-H. Ryu, S.-K. Kang, X. Zeng, G. Ungar, J.-K. Lee, W.-C. Zin and M. Lee*,* Self-Organization of Bent Rod Molecules into Hexagonally Ordered Vesicular Columns, *J. Am. Chem. Soc.,* 2012*,* **134**, 13871–13880.

[15] X. Chen, K. K. Tenneti, C. Y. Li, Y. Bai, X. Wan, X Fan, Qi-F. Zhou, L. Rong, and B. S. Hsiao, Side-Chain Liquid Crystalline Poly(meth)acrylates with Bent-Core Mesogens, *Macromolecules,* 2007, **40**, 840-848.

[16] M. Castillo-Vallés, P. Romero, V. Sebastián and M. B. Ros, Microfluidics for the rapid and controlled preparation of organic nanotubes of bent-core based dendrimers, *Nanoscale Adv.,* 2021, **3**, 1682–1689.

[17] J. Vergara, N. Gimeno, M. Cano, J. Barberá, P. Romero, J. L. Serrano, and M. B. Ros, Mesomorphism from Bent-Core Based Ionic Dendritic Macromolecules, *Chem. Mater.,* 2011, **23**, 4931–4940.

[18] L. Guo, K. Gomola, E. Gorecka, D. Pociecha, S. Dhara, F. Araoka, K. Ishikawaa and H. Takezoe, Transition between two orthogonal polar phases in symmetric bent-core liquid crystals, *Soft Matter*, 2011, **7**, 2895-2899.

[19] L. E. Hough, H. T. Jung, D. Krüerke, M. S. Heberling, M. Nakata, C. D. Jones, D. Chen, D. R. Link, J. Zasadzinski, G. Heppke, J. P. Rabe, W. Stocker, E. Körblova, D. M. Walba, M. A. Glaser and N. A. Clark, Helical Nanofilament Phases, *Science*, 2009, **325**, 456-460.

[20] D. Chen, Y. Shen, C. Zhu, L. E. Hough, N. Gimeno, M. A. Glaser, J. E. Maclennan, M. B. Ros and N. A. Clark, Interface structure of the dark conglomerate liquid crystal phase, *Soft Matter*, 2011, **7**, 1879–1883.

[21] K. V. Le and F. Araoka, Abstract Book of TOYOTA RIKEN International Workshop on Bent-Core Liquid Crystals, 2015, p. 42.

[22] J. Liu, S. Shadpour, M. E. Prévôt, M. Chirgwin, A. Nemati, E. Hegmann, R. P. Lemieux and T. Hegmann, Molecular Conformation of Bent-Core Molecules Affected by Chiral Side Chains Dictates Polymorphism and Chirality in Organic Nano- and Microfilaments, *ACS Nano,* 2021, **15**, 4, 7249–7270.

[23] L. Li, M. Salamonczyk, A. Jákli, and T. Hegmann, A Dual Modulated Homochiral Helical Nanofilament Phase with Local Columnar Ordering Formed by Bent Core Liquid Crystals: Effects of Molecular Chirality, *Small*, 2016, **12**, 3944-3955.

[24] S. Pieraccini, S. Masiero, A. Ferrarini and G. P. Spada, Chirality transfer across length-scales in nematic liquid crystals: fundamentals and applications, *Chem. Soc. Rev.*, 2011, **40**, 258–271.

[25] N. Micali, H. Engelkamp, P. G. van Rhee, P. C. M. Christianen, L. Monsù Scolaro and J. C. Maan, Selection of supramolecular chirality by application of rotational and magnetic forces, *Nature Chem., 2012,* **4**, 201–207.

[26] D. Verreault, K. Moreno, É. Merlet, F. Adamietz, B. Kauffmann, Y. Ferrand, C. Olivier and V. Rodriguez, Hyper-Rayleigh Scattering as a New Chiroptical Method: Uncovering the Nonlinear Optical Activity of Aromatic Oligoamide Foldamers, *J. Am. Chem. Soc.,* 2020, **142**, 1, 257–263.

[27] J. Liu, Y. Molard, M. E. Prévôt and T. Hegmann, Highly Tunable Circularly Polarized Emission of an Aggregation Induced Emission Dye Using Helical Nano- and Microfilaments as Supramolecular Chiral Templates, *ACS Appl. Mater. Interfaces,* 2022, **14**, 29398−29411.

[28] M. Cano, A. Sánchez-Ferrer, J. L. Serrano, N. Gimeno and M. B. Ros, Supramolecular Architectures from Bent-Core Dendritic Molecules, *Angew. Chem. Int. Ed.,* 2014, **53**, 13449-13453.

[29] M. Castillo-Vallés, M. Cano, A. Bermejo-Sanz, N. Gimeno and M. B. Ros, Towards supramolecular nanostructured materials: control of the self-assembly of ionic bent-core amphiphiles, *J. Mater. Chem. C*, 2020, **8**, 1998-2007.

[30] M. Castillo-Vallés, C. L. Folcia, J. Ortega, J. Etxebarria and M. B. Ros, Self-assembly of bent-core amphiphiles joining the ethylene-oxide/lithium ion tandem, *Journal of Molecular Liquids*, 2023, **381**, 121825-121835.

[31] E. Westphal, D. H. da Silva, F. Molin and H. Gallardo, Pyridinium and imidazolium 1,3,4-oxadiazole ionic liquid crystals: a thermal and photophysical systematic investigation, *RSC Adv*., 2013, **3**, 6442-6454.

[32] G. F. Starkulla, S. Klenk, M. Butschies, S. Tussetschläger and S. Laschat, Towards room temperature ionic liquid crystals: linear versus bent imidazolium phenylpyrimidines*, J. Mater. Chem.*, 2012, **22**, 21987- 21997.

[33] S. Ciastek-Iskrzycka, J. Szczytko, H. Monobe, D. Pociecha, M. Jasinski and P. Kaszynski, Paramagnetic ionic liquid crystals: Ion conductive bent-core derivatives of stable radicals, *Journal of Molecular Liquids,* 2021, **337**, 116028-116035.

[34] T. Okamoto, Next-generation organic semiconductors driven by bent-shaped π-electron cores, *Polym. J.,* 2019, **51**, 825–833.

[35] S. Hernández-Ainsa, J. Barberá, M. Marcos and J.L. Serrano, Influence of the poly(propylene imine) generation in the LC properties of ionic codendrimers bearing fluorinated and perhydrogenated chains, *J. Polym. Sci. A Polym. Chem*., 2011, **49**, 278-285.

[36] A. Concellón, T. Liang, A. P. H. J. Schenning, J. L. Serrano, P. Romero and M. Marcos, Proton-conductive materials formed by coumarin photocrosslinked ionic liquid crystal dendrimers, *J. Matter. Chem. C,* 2018, ***6***, 1000-1007.

[37] M. Marcos, R. Alcalá, J. Barberá, P. Romero, C. Sánchez and J. L. Serrano, Photosensitive Ionic Nematic Liquid Crystalline Complexes Basedon Dendrimers and Hyperbranched Polymers and a Cyanoazobenzene Carboxylic Acid, *Chem. Mater*., 2008, **20**, 5209–5217.

[38] K. Bacha, J. Estager, S. Brassart-Pasco, C. Chemotti, A.E. Fernandes, J-P. Mbakidi, M. Deleu and S. Bouquillon, Synthesis and Activity of Ionic Antioxidant-Functionalized PAMAMs and PPIs Dendrimers, *Polymers*, 2022, ***14***, 3513-3538.

[39] M. Castillo-Vallés, P. Romero, V. Sebastián and M. B. Ros, Microfluidics for the rapid and controlled preparation of organic nanotubes of bent-core based dendrimers, *Nanoscale Adv.*, 2021, **3**, 1682-1689.

[40] X. Cheng, X. Bai, S. Jing, H. Ebert, M. Prehm and C. Tschierske, Self-Assembly of Imidazolium-Based Rodlike Ionic Liquid Crystals: Transition from Lamellar to Micellar Organization, *Chem. Eur. J.*, 2010, **16**, 4588-4601.

Chapter 4

Size and chirality selective nanoporous membranes based on coumarins

---

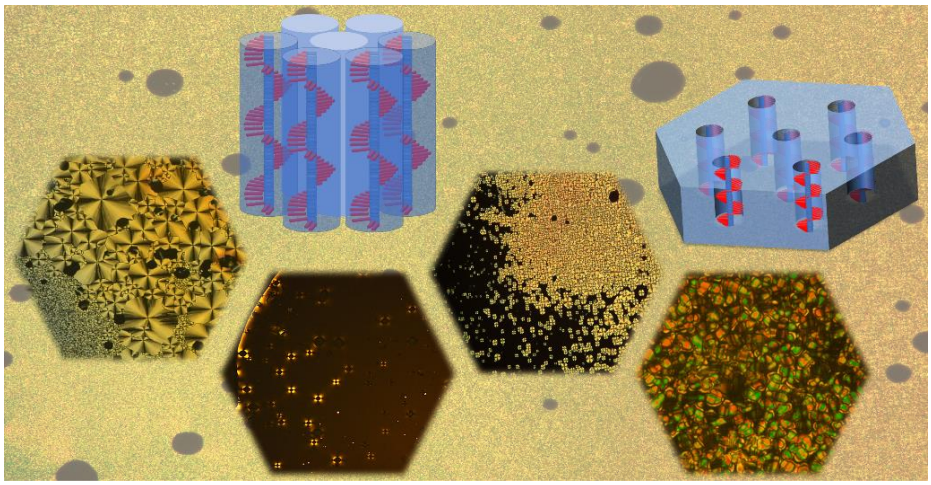

“All good things are on the other side of fear”

4.1 Introduction

4.1.1 Nanoporous materials based on liquid crystals

Since the discovery of liquid crystals (LCs) in the XIX century they have been studied in different areas such as chemistry,[1] physics,[2] biology[3] and engineering,[4] with remarkable advances in basic science and multiple applications like proton[5] and electronic transport[6] for conductive materials, sensors,[7] separation,[8] electrooptical effects…[9] One of the fields where liquid crystals have recently impacted is in nanoporous materials for separation. Some of the hottest topics in our society are related with the separation of substances, for example, getting clean water without contaminants,[10,11,12] separation of enantiomers in the pharmaceutical industry,[13,14] etc.

In contrast with other kind of nanoporous materials (inorganic zeolites[15] or organic block copolymers[16]), LCs provide homogeneous films without defects, uniform channels in the structure, tunable pores and controlled functionalized channels. In this context, hydrogen bond has been proved as an excellent tool for the preparation of supramolecular organized nanostructures yielding novel nanoporous materials. This directional bond allows new molecular designs that simplify the covalent synthesis used previously, allowing to obtain different types of LC phases.

In this approach, the nanostructure provided by the LC arrangement is fixed by the photopolymerization of different groups (acrylates,[17,18] dienes,[19] coumarins…[20]). The morphology of the pores obtained is related with the kind of mesophase; thus the columnar phases allow to obtain 1D pores in the direction of the column axis.[20] Alternatively, 2D pores are gotten with smectic mesophases with pores in the direction of the layer plane.[18] Finally, 3D pores are prepared with lyotropic LCs in bicontinuous cubic mesophases where the amount of water determines the pore size[10] (**Figure 4.1**).

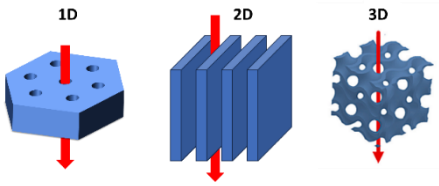

Figure 4.1. *Different kind of liquid crystal membranes.*

4.1.2 Materials with one-dimensional pores

The preparation of these 1D porous materials is based on a bottom-up strategy to synthesize disc shaped molecules that self-organize in columnar LCs. Commonly, supramolecular discotic mesogenic units are constructed by joining a flat aromatic central core functionalized with basic units derived from nitrogen, which acts as a template, interacting through hydrogen bonds with dendronic structures containing carboxylic acids in the apical position. The "core" plays a key role in the stacking of molecules, the alignment of the mesophase and the future pore size. Besides this, the dendronic units incorporate lateral alkyl chains to favor the LC behavior functionalized in their terminal positions with photopolymerizable units. After polymerization, the resulting polymeric film is subjected to different treatments to break the hydrogen bonds, releasing the template molecule and, consequently, obtaining the nanoporous material.

This methodology offers a wide variety of chemical structures both in the template molecules and the polymerizable acids. Some of the cores that have been widely studied are: benzotris(imidazoles),[21] triazines,[22] melamines etc. Sijbesma´s group has published several examples[23,24,25,26] of this approach using imidazole as template with remarkable results. In 2022 Lugger *et al.*[26] presented a photoresponsive membrane which incorporates azobenzenes in the photopolymerizable units; the *cis*/*trans* isomerization with UV light led to a modification of the pore size and, consequently, an increase in the adsorption rate (**Figure 4.2**).

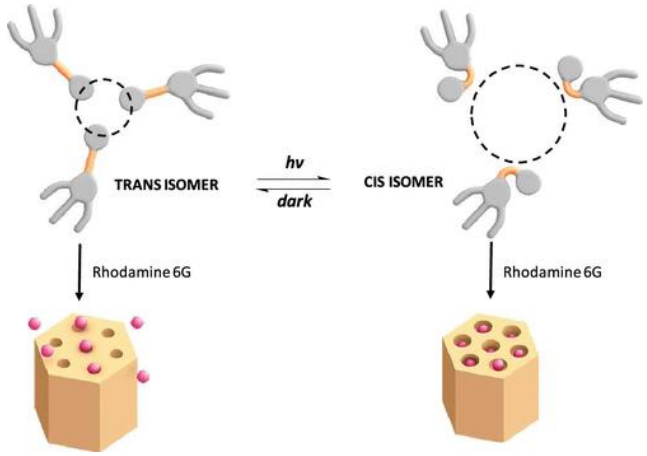

Figure 4.2. *Azo isomerization with UV light produces a modification of the pore size and the adsorption rate (adapted from reference 26).*

The structural characteristics and adsorption differences between a homeotropic and a planar alignment in a membrane were examined in 2018 by Sijbesma´s group.[25] The homeotropic alignment was achieved with a PEG derivative as dopant which aligns the mesophase. In the case of the planar membrane, the alignment was carried out with a unidirectional shearing of the LC macroscopic organization before polymerization. This change in the alignment resulted in an adsorption rate 3-4 times faster in the homeotropic membrane (**Figure 4.3**).

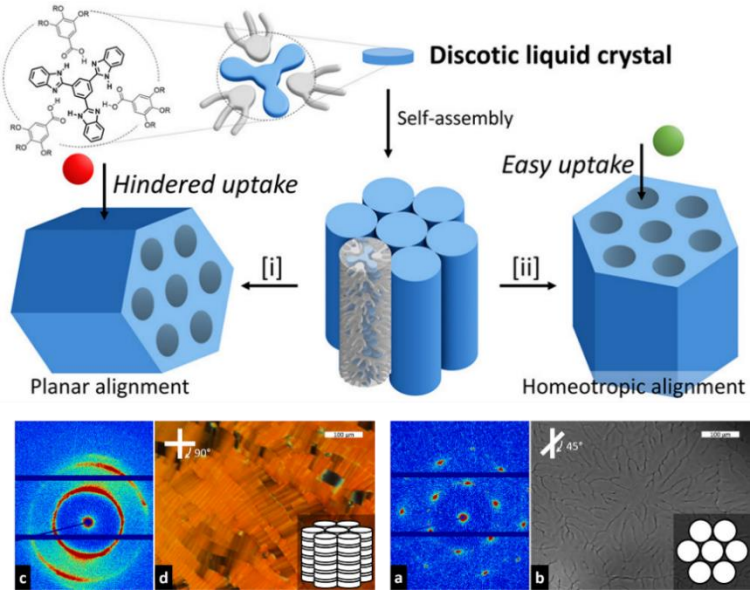

Figure 4.3. *Schematic representation of a planar (c,d) and homeotropic (a,b) alignment of a columnar liquid crystal (adapted from reference 25).*

In 2017 our group described an example of nanoporous membranes based on the fixation of the columnar structure through crosslinking of vinyl groups.[27] Later in 2018 our group reported the first example of columnar fixation by coumarin dimerization.[20] In this approach Concellón *et al.* prepared two different membranes with different pore sizes using melamine and triazine derivatives as template molecules. The columnar structure was fixed by the photo-dimerization of coumarins with light of 325 nm. Coumarins react by a [2+2] cyclodimerization producing a cyclobutane structure without any catalyst (**Figure 4.4**).

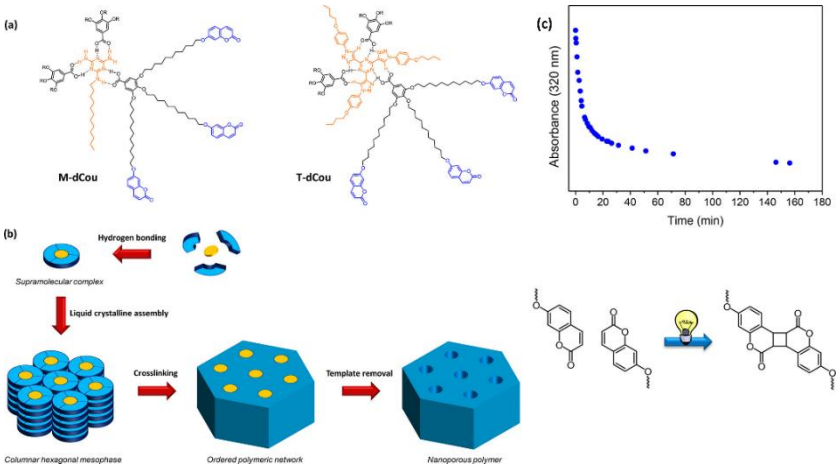

Figure 4.4. *a) Supramolecular complexes containing coumarin units, b) schematic representation of the membrane preparation and c) coumarin dimerization induced by UV light, obtained from reference 20.*

This approach is going to be studied in the following chapters. However, there are other methodologies to develop columnar LCs for nanoporous materials. Similarly, Ishida *et al.*[28,29] prepared chiral membranes based on chiral amino alcohols as template producing helical pores with potential applications on chiral separation, circularly polarized light (CPL) emitting devices, piezoelectric materials, etc. In the projects developed by Osuji *et al.*[30] nanoporous materials were set up without template molecules; instead, a gallic salt which self-assembled in columnar LC was aligned with magnetic fields, leading to membranes with pores of 1 nm.

4.1.3 Materials with two-dimensional pores

Nanoporous materials with 2D pores have been built based on smectic liquid crystals, hydrogen-bonded mesogens with photopolymerizable units being the most important approach in this field. Once the arrangement of the mesophase is fixed through polymerization, the hydrogen bonds can be broken inducing nanopores. However, the first attempts of getting this kind of materials led to the collapse of the nanostructure.[31] This problem was faced by different research groups adding to the layer structure different covalent units that act as "nanopillars" linking the different layers[32,33,34] (**Figure 4.5**).

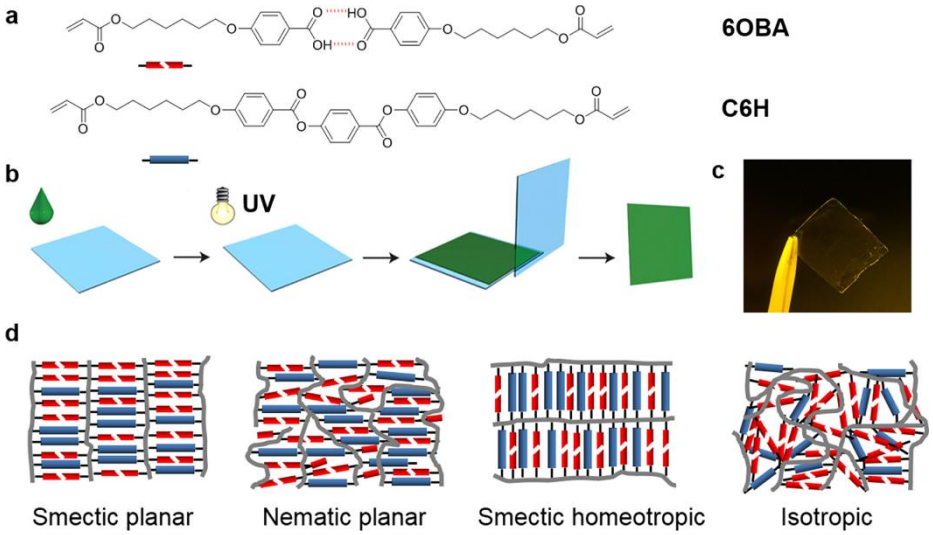

Figure 4.5. *a) Chemical structure of the mesogens employed in the fabrication of 2D porous membranes, b) schematic representation of the fabrication process to prepare the liquid crystal networks c) nanoporous membrane obtained after the treatment and d) different organizations of the material (obtained from reference 34).*

This strategy has been explored by many groups adding modifications,[35,36] for example, deprotecting the acids in the pores with basic treatments leading to charged pores,[37,38] adding "dopants" like azobenzene moieties[39,40] for photoresponsive materials[41] or substituting the hydrogen bond moieties for covalent structures easy to break.[42]

4.1.4 Materials with three-dimensional pores

In the synthesis of 3D nanoporous materials, lyotropic liquid crystals[43,44] excel over thermotropic LCs. These lyotropic mesophases yield continuous nanochannels within the membrane. This structural configuration proves advantageous in applications where alignment, as achieved in 1D and 2D membranes, is unnecessary. By avoiding alignment-related challenges, these membranes facilitate easy processing and harbor continuous channels whose functional groups dictate the permeation/rejection (**Figure 4.6**) of substances.[10]

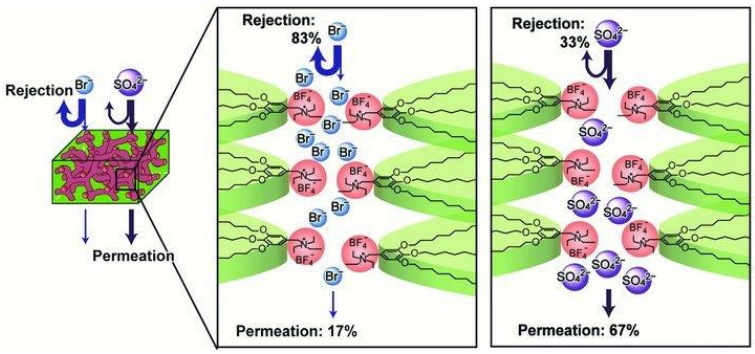

Figure 4.6. *Rejection/Permeation of a 3D membrane, obtained from reference 10.*

4.1.5 Generation of chirality in columnar liquid crystals with circularly polarized light

In the previous sections several examples of different membranes have been shown. In spite of their differences (kind of mesophase, kind of pores or alignment), they have in common the incorporation of other units to functionalize the membrane or improve their properties. One of the most studied systems is azobenzenes, which provide a well-studied photoresponse to the materials because of their *E/Z* isomerization. Recently, Wang and co-workers[45] have described in detail the irradiation of an azobenzene polymer with circularly polarized light (CPL) of different wavelengths and different times. This approach not only allows to obtain a chiral material without the presence of chiral center, but it also enables to photoswitch the chirality of the material irradiating with *right*-CPL or *left*-CPL.[46]

In our group we can find some examples of chirality generation in columnar liquid crystals. Vera *et al.*[47,48] presented several columnar organizations based on V-shaped acids which contained azobenzene moieties and interacted through hydrogen bond with a melamine derivative. The chiral signal of the mesophases was controlled upon irradiation with *right* or *left* CPL and the structure of the mesophase was studied before and after the irradiation.

4.2 Objectives

This study presents an innovative method to fabricate chiral membranes based on discotic supramolecules that self-organize into columnar liquid crystals phases. Supramolecules are formed by hydrogen bonds combining planar aromatic derivatives functionalized with basic groups derived from nitrogen with Percec-type promesogenic dendrons, which carry carboxyl groups in their apical position. Variations in the template size will lead to the creation of nanoporous materials with different pore sizes. The exposition of the material to circularly polarized light will induce chirality in the membranes due to azobenzene isomerization. In addition, the functionalization of the acids with coumarins in the periphery will provide a polymeric material through coumarin dimerization with light. As a result, the nanoporous material will effectively separate molecules by size and chirality (**Figure 4.8**).

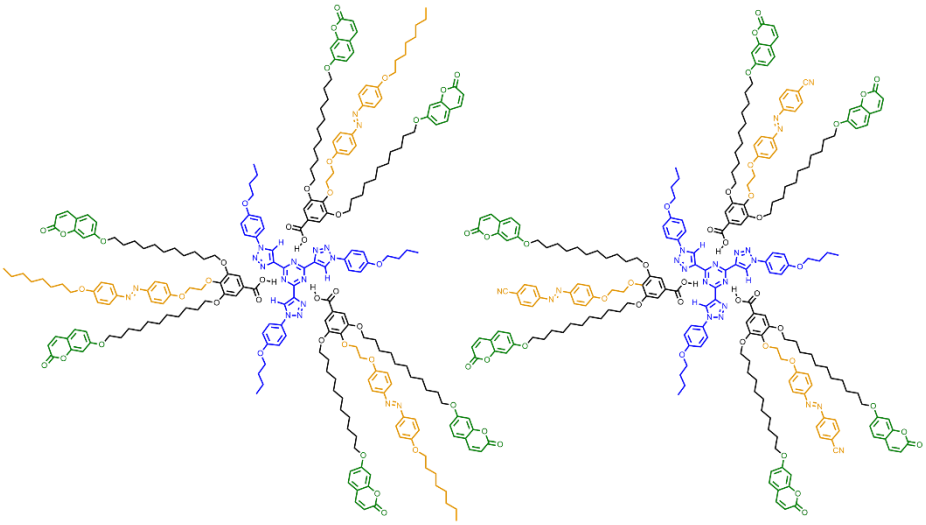

Figure 4.7. *Examples of disc-shaped supramolecular complexes prepared by hydrogen bond. The complex on the left includes an apolar azobenzene (AzoC$_8$H$_{17}$); the complex on the right includes a polar azobenzene (AzoCN).*

In the process of preparing chiral membranes, several critical factors come into play, with particular emphasis on the utilization of coumarins as the polymeric unit and azobenzenes as the source of chirality. While the prior experience of our group with coumarins has

shown the viability of constructing membranes using them, our specific case necessitates to corroborate coumarin dimerization in presence of azobenzenes. With this purpose a LED of the specific wavelength for coumarin dimerization (325 nm) is going to be used. Another key aspect lies in the application of azobenzenes to induce chirality using circularly polarized light (CPL). While this method has been extensively documented in the context of discotic supramolecular liquid crystals, its application in nanoporous membranes remains unexplored. In this study, we aim to investigate whether the chiral signal will be preserved in the polymeric material and, ultimately, in the nanoporous material. To study the influence of the azobenzene polarity, two different derivatives are going to be examined: one polar (**AzoCN**) and one apolar (**AzoC$_8$H$_{17}$**) (**Figure 4.7**). The inclusion of azobenzene as a chiral inductive unit broadens the spectrum of possibilities, as the chiral signal can be externally adjusted with either *right*-CPL or *left*-CPL. Furthermore, in the context of our specific project, we will investigate whether this signal can be reversed within the nanoporous material once the membrane has been fabricated.

To obtain the abovementioned chiral membranes, we have outlined the following specific objectives:

1. Synthesis and characterization of three different planar aromatic heterocycles (**Figure 4.9**) that contain aromatic amines in their structure to act as templates in the supramolecular complexes.
2. Synthesis and characterization of two benzoic acids holding substituents containing coumarin and azobenzene derivatives (cyano-azobenzene **dCouAzoCN** and octyloxy-azobenzene **dCouAzoC$_8$**, **Scheme 4.1**).
3. Preparation of supramolecular complexes by hydrogen bond and characterization of the new structures (^{1}H-NMR, ^{13}C-NMR, FT-IR, POM, DSC, TGA and XRD).
4. Irradiation with circularly polarized light of 450 nm to induce chirality in the supramolecular complex and

photopolymerization with light of 325 nm to obtain a polymeric material.

5. Template removal through acid treatment and characterization of the nanoporous membranes by FT-IR, XPS, XRD and CD.
6. Selective adsorption studies by size and chirality with different dyes monitored by UV.

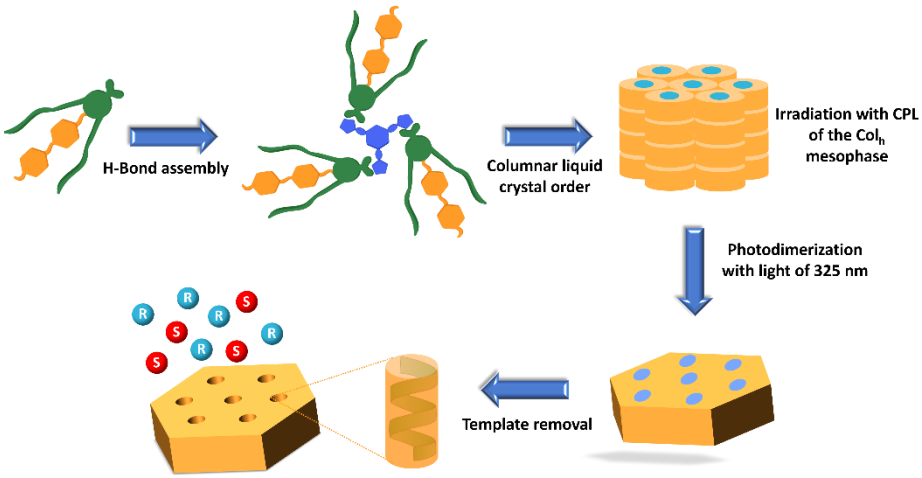

Figure 4.8. *Schematic representation of the different steps carried out to prepare the chiral membranes.*

4.3 Results and discussion

4.3.1 Synthesis and characterization of supramolecular complexes

Regarding template molecules used in this work (**Figure 4.9**), melamine (**M**), tris(triazolyl)triazine (**TTT**) and heptazine (**Hpz**) derivatives were synthesized following described procedures.[49,50,51] The details of the synthesis are included in the experimental part (**section 4.5.2**).

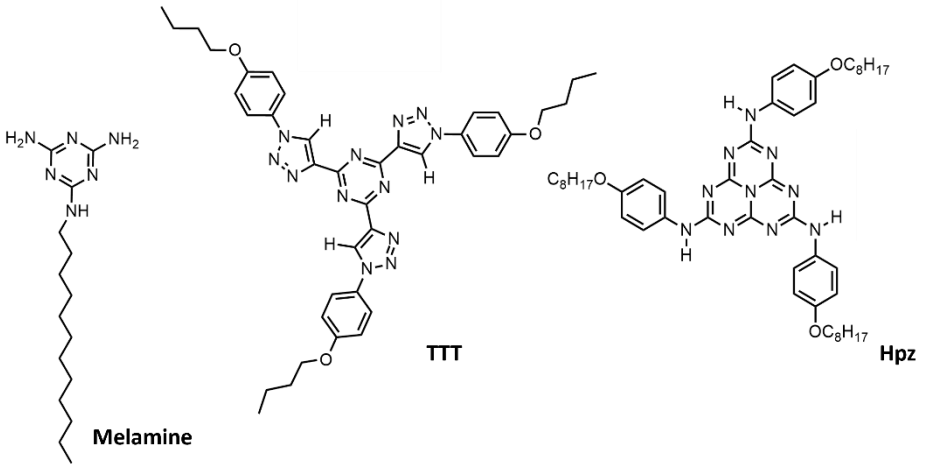

Figure 4.9. *Template molecules employed in the preparation of the supramolecular complexes.*

The synthetic route employed for the synthesis of **dCouAzoCN** and **dCouAzoC$_8$** is described in **Scheme 4.1.** The first step is a Williamson reaction carried out with the corresponding azobenzene derivative (the synthesis of both azobenzene derivative precursors has been described before[52,53] and it is detailed in the experimental part (**section 4.5.2**)), using potassium hydrogen carbonate as a base to functionalize the *para*-position of methyl gallate. The *para*-position is more acid than the two *meta*-positions and therefore the use of a weak base is appropriate to selectively generate the phenolate in *para*-position. The protected acids **(5)** and **(6)** were synthesized by Williamson reaction using a coumarin chain derivative synthesized before (**7-(11-bromoundecyloxy)-2H-chromen-2-one (13)**, ***Chapter 2***) and the gallate azobenzenes **(3)** and **(4)** using classical conditions for this kind of reaction. Finally, a hydrolysis with aqueous lithium

hydroxide was carried out to obtain both acids **dCouAzoCN** and **dCouAzoC$_8$** (**see Section 4.5.2** in the experimental part).

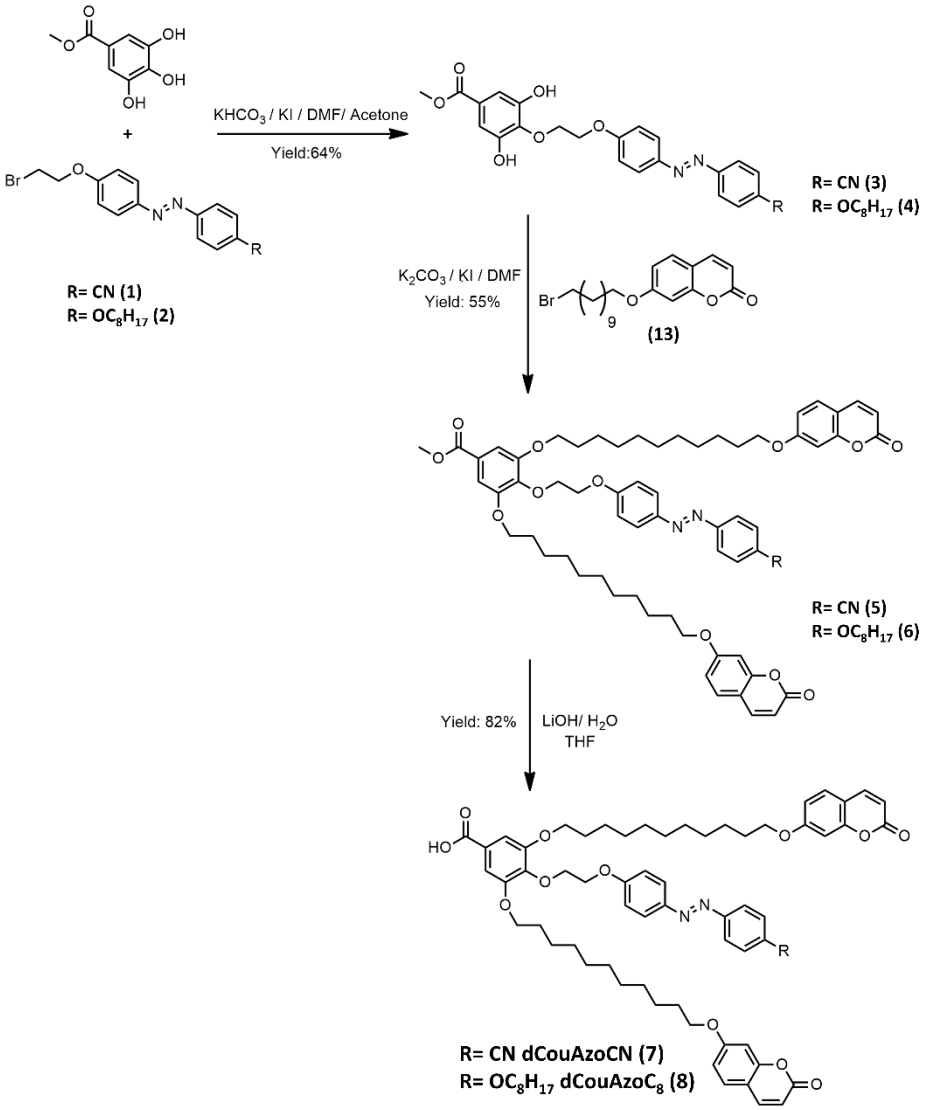

Scheme 4.1. *Synthetic procedure of* ***dCouAzoCN*** *and* ***dCouAzoC$_8$*** *dendrons.*

The chemical structure of all intermediates and final products was verified by FT-IR spectroscopy, MALDI-TOF experiments and ^{1}H-NMR, ^{1}H-^{1}H COSY, ^{13}C-NMR, ^{1}H-^{13}C HSQC and ^{1}H-^{13}C HMBC spectroscopy.

The supramolecular complexes were assembled by hydrogen-bond mixing the corresponding acid (**dCouAzoCN or dCouAzoC$_8$**) with the chosen template (**M, TTT or Hpz**) dissolved in DCM in a ratio 3:1. The

mixture was stirred and slowly evaporated at room temperature until the weight remained stable. Finally, a thermal treatment was carried out by heating up to the isotropic state and cooling down to room temperature. The hydrogen-bonded organization was characterized in the six supramolecular complexes by FT-IR, ^{1}H-NMR and ^{13}C-NMR.

As examples of the H-bond formation, the FT-IR spectra of **dCouAzoCN**, **TTT-dCouAzoCN**, **dCouAzoC$_8$** and **TTT-dCouAzoC$_8$** are shown in **Figure 4.10**. The interaction between the carboxyl group of **dCouAzoC$_8$** and the amino groups of the template produces several changes in the C=O band of the acid. The band produced by the dimeric form of **dCouAzoC$_8$** at 1677 cm^{-1} was displaced to 1695 cm^{-1} in the supramolecule **TTT-dCouAzoC$_8$** indicating the formation of the hydrogen bond. Also, the **dCouAzoCN** carbonyl band that appears at 1685 cm^{-1} shifted to 1718 cm^{-1} in complex **TTT-dCouAzoCN**.

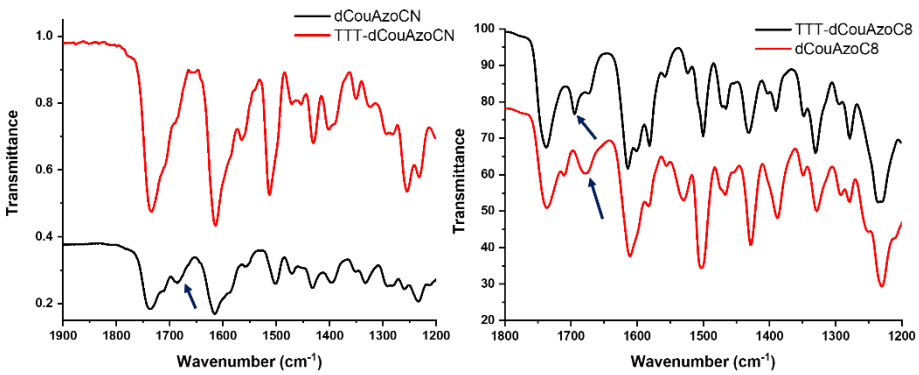

*Figure 4.10. FT-IR spectra comparison of **dCouAzoCN**, **TTT-dCouAzoCN** (left) and **dCouAzoC$_8$**, **TTT-dCouAzoC$_8$** (right).*

The structural characterization was completed with ^{1}H-NMR studies. In **Figure 4.11** the most relevant protons and carbons involved in the formation of the supramolecular complexes are labelled to indicate the main shifts (for both acids **dCouAzoCN** and **dCouAzoC$_8$**). It is worth mentioning that these studies were carried out in solution assuming that the supramolecular complexes are in a quick equilibrium with their own components.

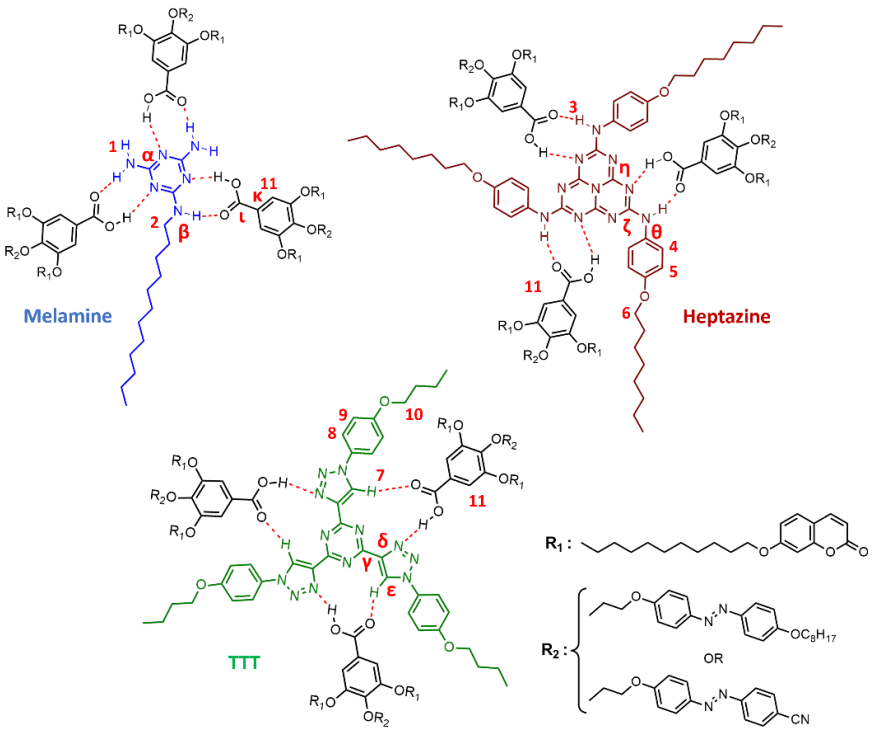

Figure 4.11. *Schematic representation of the supramolecular complexes.*

In **Figures 4.12-17**, ^{1}H-NMR spectra of the template molecules, supramolecular complexes and the corresponding dendrons (**dCouAzoCN** and **dCouAzoC$_8$**) are compared. These comparisons revealed important shifts in some of the peaks involved in the hydrogen bond formation and those in close proximity. The corresponding chemical shift data are summarized in **Table 4.1** (for **dCouAzoCN**) and **Table 4.2** (for **dCouAzoC$_8$**). In the complexes involving melamine **M**, the formation of hydrogen bonds was confirmed by the downfield shift observed in the NH protons (***H$_1$*** and ***H$_2$***) of melamine, shifting from 4.85 to 6.27 ppm, as observed in the case of **dCouAzoCN** (**Figure 4.12**). Additionally, the **TTT** complexes exhibited changes in the proton shifts within the triazole ring (***H$_7$***). For instance, in the **TTT-dCouAzoC$_8$** complex (**Figure 4.16**), the proton shifted from 8.86 to 9.07 ppm, providing further confirmation of its interaction with the carbonyl group of the acid. Finally, NH protons from heptazine core (***H$_3$***) shifted downfield approximately 1 ppm in both complexes (**Figures 4.14** and **4.17**).

Table 4.1. *Most relevant shifts in ^{1}H-NMR spectra of* ***melamine M***, ***tris(triazolyl)triazine TTT***, ***heptazine Hpz*** *and their supramolecular complexes with* ***dCouAzoCN***.

	H_1	H_2	H_3	H_4	H_5	H_6	H_7	H_8	H_9	H_{11}
M	4.85	3.30								
Supra M	6.27	3.37								7.33
TTT							8.86	7.79	7.10	
Supra TTT							9.05	7.78	7.09	7.33
Hpz			7.75	7.40	6.85	3.92				
Supra Hpz			8.62	7.45	6.90	3.94				7.34
dCouAzoCN										7.32

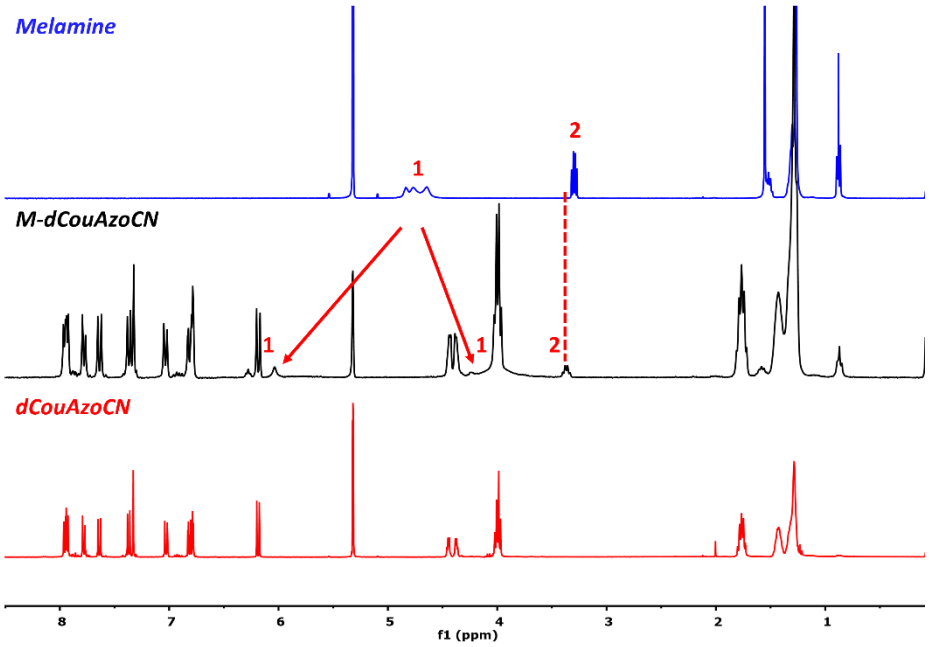

Figure 4.12. *^{1}H-NMR (CD_2Cl_2, 298K, 400 MHz) spectra of* ***melamine M*** *(blue line),* ***dCouAzoCN*** *(red line) and* ***M-dCouAzoCN*** *complex (black line).*

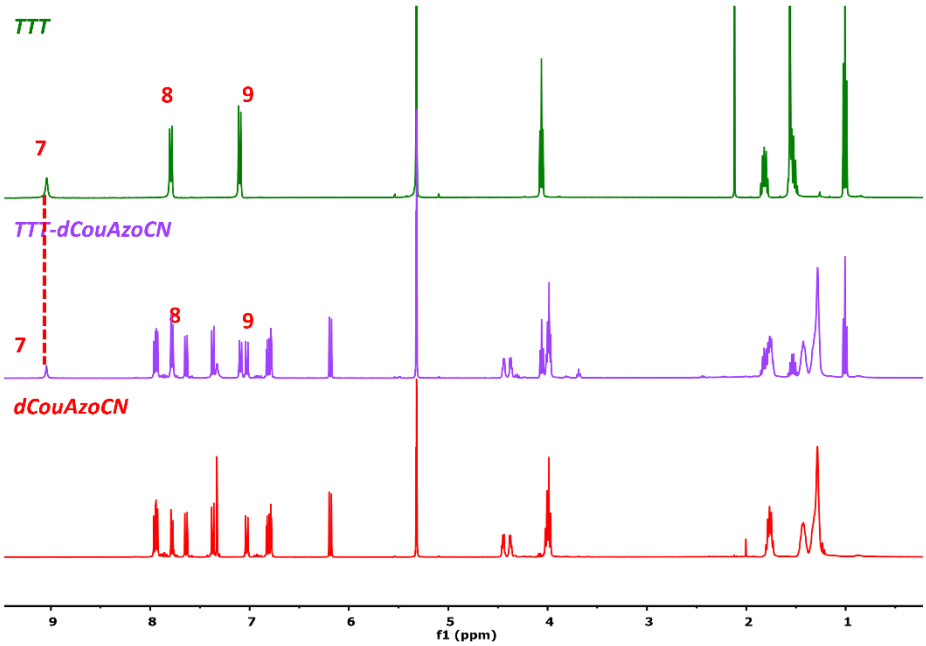

Figure 4.13. *^{1}H-NMR (CD_2Cl_2, 298K, 400 MHz) spectra of **TTT** (green line), **dCouAzoCN** (red line) and **TTT-dCouAzoCN** complex (purple line).*

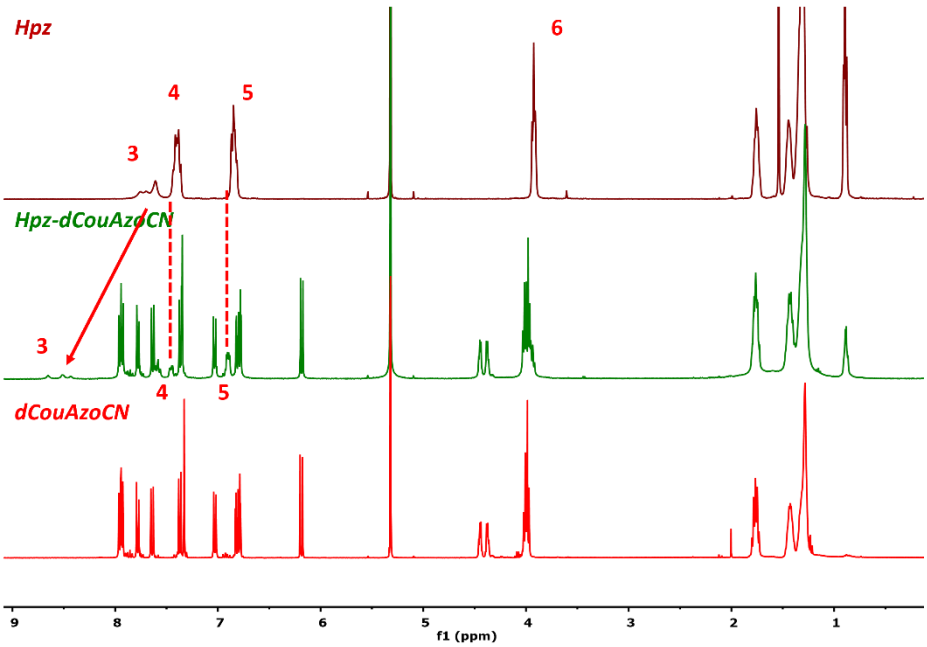

Figure 4.14. *^{1}H-NMR (CD_2Cl_2, 298K, 400 MHz) spectra of **heptazine Hpz** (burgundy line), **dCouAzoCN** (red line) and **Hpz-dCouAzoCN** complex (green line).*

Table 4.2. *Most relevant shifts in ^{1}H-NMR spectra of* ***melamine M***, ***tris(triazolyl)triazine TTT***, ***heptazine Hpz*** *and their supramolecular complexes with* ***dCouAzoC$_8$***.

	H_1	H_2	H_3	H_4	H_5	H_6	H_7	H_8	H_9	H_{11}
M	4.85	3.30								
Supra M	6.25	3.36								7.32
TTT							8.86	7.79	7.10	
Supra TTT							9.07	7.78	7.09	7.32
Hpz			7.75	7.40	6.85	3.92				
Supra Hpz			8.85	7.46	6.90	3.93				7.35
dCouAzoC$_8$										7.31

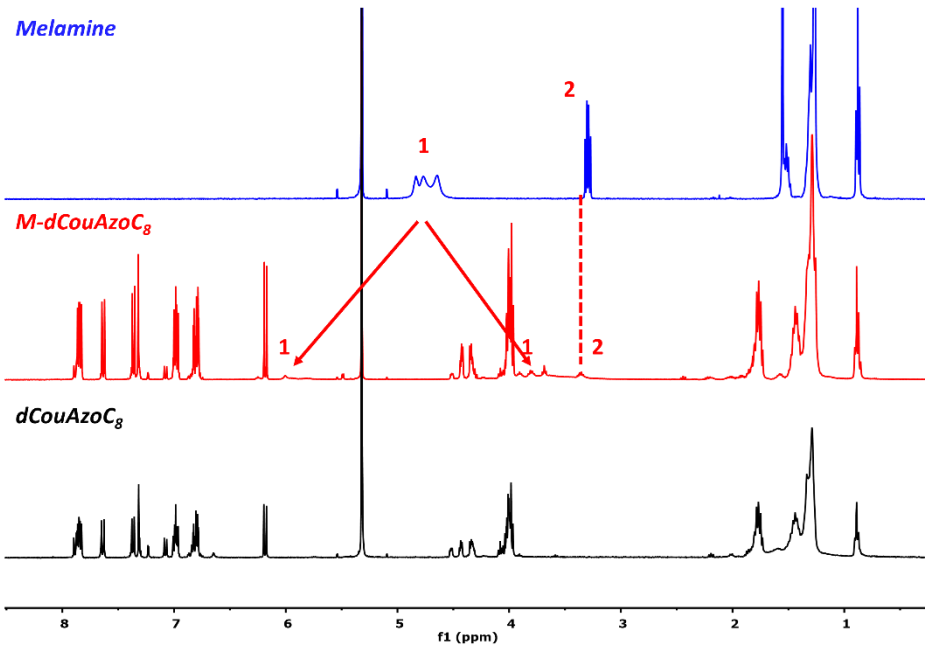

Figure 4.15. *^{1}H-NMR (CD_2Cl_2, 298K, 400 MHz) spectra of* ***melamine M*** *(blue line),* ***dCouAzoC$_8$*** *(black line) and* ***M-dMetAzoC$_8$*** *complex (red line).*

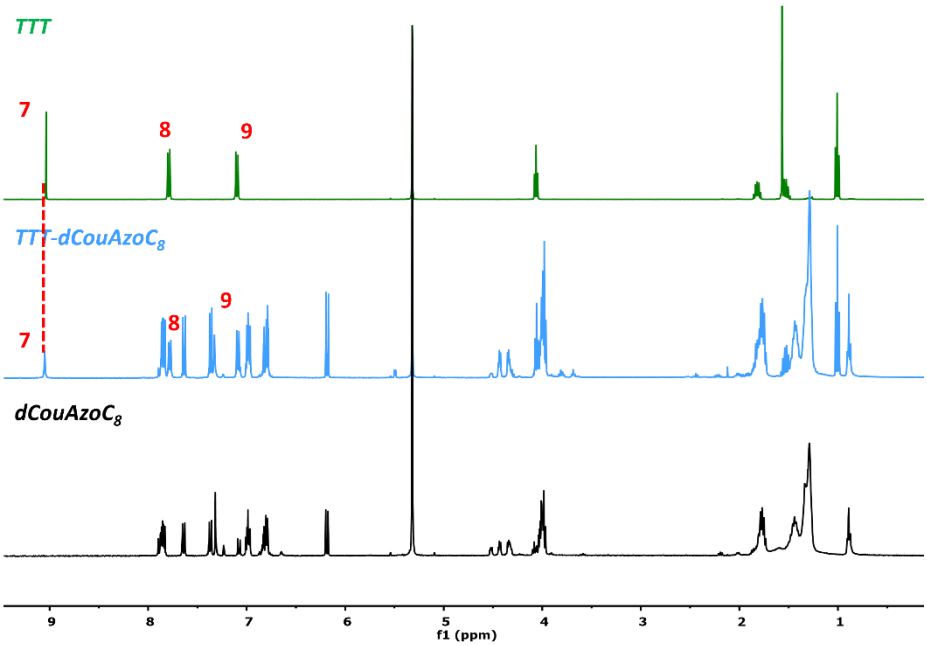

Figure 4.16. ^{1}H-NMR (CD_2Cl_2, 298K, 400 MHz) spectra of **TTT** (green line), **dCouAzoC$_8$** (black line) and **TTT-dCouAzoC$_8$** complex (blue line).

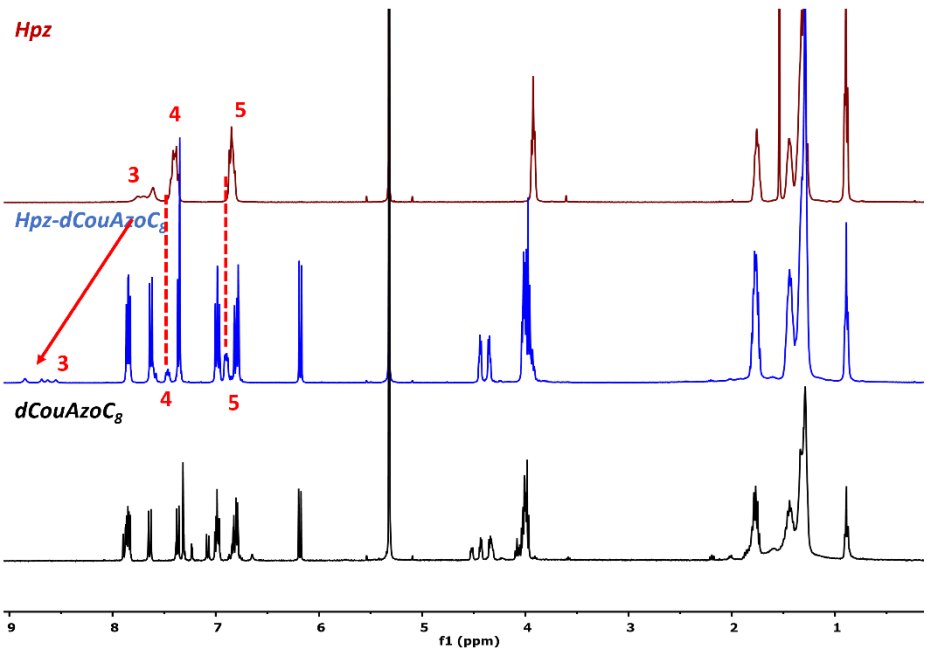

Figure 4.17. ^{1}H-NMR (CD_2Cl_2, 298K, 400 MHz) spectra of **heptazine Hpz** (burgundy line), **dCouAzoC$_8$** (black line) and **Hpz-dCouAzoC$_8$** complex (blue line).

To conclude the structural characterization, ^{13}C-NMR experiments were carried out. In **Table 4.3** the most significantly changes in the signals involved in the hydrogen bond formation are summarized. Among these changes stands out the shift in the carbonyl peak of the acids which changes, for example, from 170.92 in **dCouAzoCN** to 169.74 in **TTT-dCouAzoCN**.

Table 4.3. *Main shifts in ^{13}C-NMR spectra of the complexes, templates and acids (100 MHz, CD_2Cl_2). See* ***Figure 4.11***

	C_α	C_θ	C_γ	C_δ	C_ε	C_η	C_ζ	C_ϑ	C_ι	C_κ
M	167.47	41.19								
M-dCouAzoCN	164.13	41.41							170.50	126.26
TTT			167.42	146.40	126.20					
TTT-dCouAzoCN			167.40	145.81	125.62				169.74	124.39
Hpz						157.28	157.05	130.48		
Hpz-dCouAzoCN						156.99	156.95	124.13	170.13	125.05
dCouAzoCN									170.92	124.89
	C_α	C_θ	C_γ	C_δ	C_ε	C_η	C_ζ	C_ϑ	C_ι	C_κ
M	167.47	41.19								
M-dCouAzoC$_8$	164.31	41.39							170.49	126.10
TTT			167.42	146.40	126.20					
TTT-dCouAzoC$_8$			167.45	145.80	125.55				169.74	126.24
Hpz						157.28	157.05	130.48		
Hpz-dCouAzoC$_8$						156,96		130.53	170.52	124.81
dCouAzoC$_8$									170.30	124.90

4.3.2 Thermal characterization and liquid crystal behavior

The thermal stability of the supramolecular complexes and acids was assessed using thermogravimetry (TGA). The results indicate favorable stability for all compounds, exhibiting a 2% weight loss at temperatures 100°C higher than the isotropization temperature. Furthermore, the DSC results showed repetitive behavior between the second scan and subsequent ones. The mesomorphic behavior was studied by polarized optical microscopy (POM), differential scanning calorimetry (DSC) and X-ray diffraction (XRD), and the main results are summarized in **Table 4.4**. Three cycles were carried out by DSC, using the data from second cycle to assign the phase transitions; in some of the cases isotropic temperatures were taken from POM observations.
In order to interpret the structural parameters, the lattice constant *a* of the hexagonal columnar mesophase was deduced from the relationship between the observed reflections and parameter *a*:

$$a = 2/\sqrt{3} * ((d_{10}) + \sqrt{3} * (d_{11}) + \sqrt{4} * (d_{20}) + \sqrt{7} * (d_{21}) + \ldots)/n_{reflections}$$

*Table 4.4. Thermal behavior and structural parameters of **dCouAzo** complexes.*

Compound	$T_{2\%}$[a](°C)	Phase transitions[b]	d (Å)[c]	h k l[d]	Structural parameters
dCouAzoCN	345	Cr 28 N_D 130 I			
M-dCouAzoCN	228	Cr 33 N_D 122 I*			
TTT-dCouAzoCN	235	g 22 N_D 127 I*			
Hpz-dCouAzoCN	209	Cr 72 Col_h 111 I	44.7 25.7 22.1 16.7 4.3	1 0 0 1 1 0 2 0 0 2 1 0 br	a = 51.5 Å
dCouAzoC$_8$	320	Cr 114 I			
M-dCouAzoC$_8$	245	Cr 31 Col_h 100 I*	43.3 24.9 21.6 13.2 4.1	1 0 0 1 1 0 2 0 0 2 2 0 br	a = 49.9 Å
TTT-dCouAzoC$_8$	264	Cr 20 Col_h 105 I*	53.4 30.7 26.4 20.0 13.3 4.4	1 0 0 1 1 0 2 0 0 2 1 0 4 0 0 br	a = 61.5 Å
Hpz-dCouAzoC$_8$	315	Cr 69 Col_h 106 I	48.1 27.6 24.0 18.1 12.0 4.3	1 0 0 1 1 0 2 0 0 2 1 0 4 0 0 br	a = 55.4 Å

[a] Decomposition temperature corresponding to 2% weight loss.

*[b] DSC data obtained at a rate of 10°C/min in the second heating-cooling cycle. Cr: crystal, N_D: discotic nematic, g: mesomorphic glass, Col_h: hexagonal columnar and I: isotropic liquid.*Data obtained from POM observations.*

[c] Observed reflections.

[d] Miller indices.

All supramolecular complexes obtained from **dCouAzoCN** showed mesogenic behavior, but their thermal properties and mesophases were different. For **M-dCouAzoCN** and **TTT-dCouAzoCN,** POM observations revealed classical textures of discotic nematic mesophases after applying mechanical stress (**Figure 4.18 c-d**). DSC studies revealed that on cooling **M-dCouAzoCN** crystallized at 33°C and **TTT-dCouAzoCN** exhibited a glass transition at 22°C. The XRD patterns confirmed the discotic nematic nature of the mesophases, as they yielded only diffuse scattering without any sharp reflection characteristic of positional order (**Figure 4.18 a-b**).

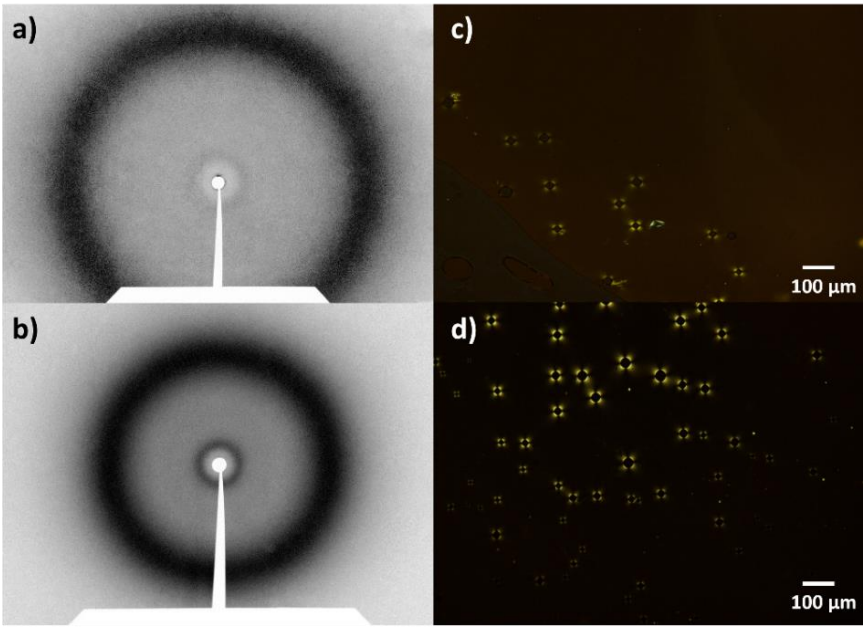

Figure 4.18*. XRD patterns at room temperature of* ***M-dCouAzoCN*** *(a) and* ***TTT-dCouAzoCN*** *(b). POM microphotographs of* ***M-dCouAzoCN*** *(c) and* ***TTT-dCouAzoCN*** *(d) obtained at room temperature in the cooling process.*

In the case of **Hpz-dCouAzoCN**, POM observations (**Figure 4.19a**) revealed a homogeneous material which displayed a characteristic mosaic texture more birefringent and colorful in comparison with the previously studied complexes (**M-dCouAzoCN** and **TTT-dCouAzoCN**). In the DSC curves two different peaks were observed during the cooling process, corresponding to the transition from isotrope to mesophase at 111°C and the crystallization at 72°C. The peaks were stable and reversible after several thermal cycles, indicating the stability of the

supramolecular complex and the formation of hydrogen bonds. The specific kind of mesophase was examined by X-ray diffraction (XRD) (**Figure 4.19 b-c**); the small angle region showed an intense sharp diffraction peak corresponding to a distance of 44.7 Å and three weaker peaks with spacings related to the main reflection by 1:1/√3: 1/√4: 1/√7. These reflections correspond to the (100), (110), (200) and (210) planes of a Col_h mesophase. In the high angle region, the diffractogram showed a broad peak at 4.3 Å that corresponds to the chain-chain interactions.

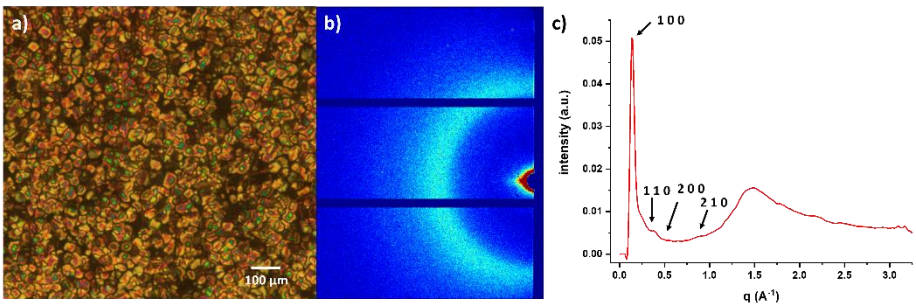

Figure 4.19. *a) POM microphotograph taken at 105ºC in the cooling process, (b) 2D XRD pattern and (c) 1D XRD pattern of* ***Hpz-dCouAzoCN****.*

The modification of the terminal group in the azobenzene from a cyano group to an octyloxy chain favored the stacking of the supramolecules into columnar mesophases, since all **dCouAzoC$_8$** supramolecules organized in columnar liquid crystals with similar thermal properties. At POM all supramolecular complexes (**M-dCouAzoC$_8$, TTT-dCouAzoC$_8$ and Hpz-dCouAzoC$_8$**) were homogeneous and stable after several thermal cycles as it was confirmed by DSC. In the case of **M-dCouAzoC$_8$**, POM observations (**Figure 4.20a**) revealed colorful textures typical of columnar mesophases with a tendency to crystallize at room temperature. DSC cycles showed a crystallization process close to room temperature (31ºC) and the clearing point was established by POM (100ºC). The assignment of the mesophase was carried out by XRD (**Figure 4.20 b-c**), confirming the columnar arrangement with several reflections in the low-angle region: at 43.3 Å and 24.9 Å two intense and sharp peaks stand out in a relationship 1:1/√3 ((100) and (110) planes). Moreover, two more diffraction

maxima in a ratio $1/\sqrt{4}$: $1/\sqrt{12}$ with the main reflection supported the Col_h nature of the mesophase ((200) and (220) planes). In the high angle region, a broad diffuse halo was observed typical of the alkyl chain interactions at 4.1 Å. WAXS diffractogram (**Figure 4.20b**) also provided additional information about the packing of the supramolecular complex, coming into view several spots instead of circular diffraction maxima, indicating a macroscopic orientation of the material.

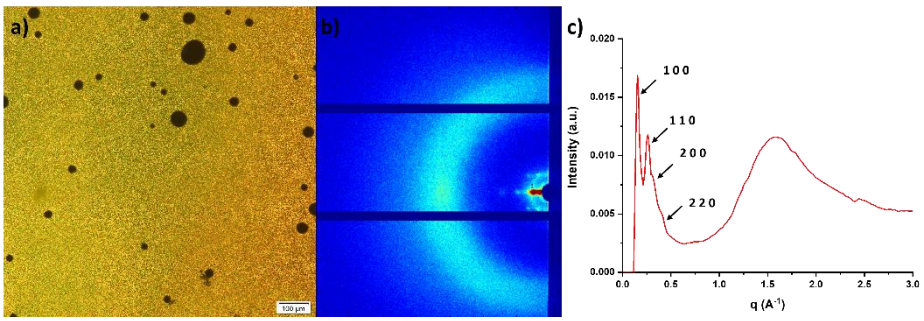

Figure 4.20. *(a) POM microphotograph taken at 55ºC in the cooling process, (b) 2D XRD pattern and (c) 1D XRD pattern of* ***M-dCouAzoC$_8$****.*

TTT-dCouAzoC$_8$ showed LC behavior at POM with birefringent Maltese crosses textures (**Figure 4.21a**). In the cooling cycle the material showed an homeotropic order with dark zones, and Maltese crosses appear after applying mechanical stress, demonstrating a highly ordered structure in the material. DSC studies exhibited crystallization at 20ºC and the clearing point was established by POM (105ºC). The mesophase assignation was performed by XRD (**Figure 4.21 b-c**). The patterns exhibit multiple reflections in the low angle region and a diffuse halo at 4.4 Å in the high-angle region. Similarly to complex **M-dCouAzoC$_8$**, two sharp peaks appeared in a ratio $1:1/\sqrt{3}$ at 53.4 and 30.8 Å. The small angle region contains three more peaks in a ratio $1/\sqrt{4}$: $1/\sqrt{7}$: $1/\sqrt{16}$ with the fundamental reflection, confirming a Col_h mesophase with the observed planes (100), (110), (200), (210) and (400). POM observations and 2D-diffractograms (**Figure 4.21b**) suggest a highly ordered material with macroscopic orientation.

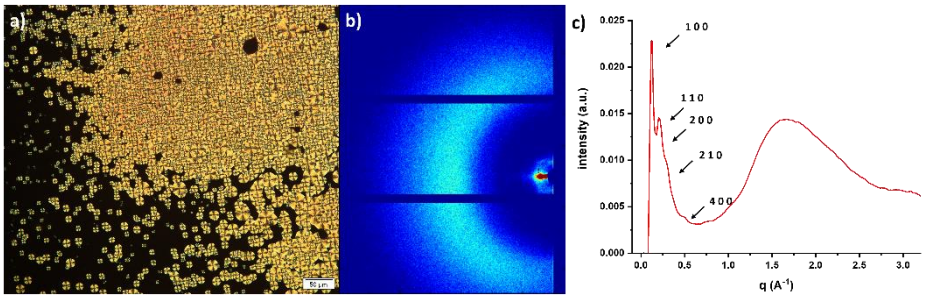

Figure 4.21. *(a) POM microphotograph taken at 85ºC in the cooling process, (b) 2D XRD pattern and (c) 1D XRD pattern of* ***TTT-dCouAzoC$_8$.***

Finally, the supramolecular complex **Hpz-dCouAzoC$_8$** exhibited similar textures at POM (**Figure 4.22a**) as **Hpz-dCouAzoCN**, manifesting the influence of the **Hpz** template in the behavior of the complex. Each DSC cycle showed two peaks corresponding to the transition from crystal to mesophase and from mesophase to isotrope (**Figure 4.51** in **Appendix**, **section 4.6.3**). Those transitions appear in both process (heating-cooling) indicating the enantiotropic nature of the mesophase. The structure of the mesophase was confirmed by WAXS and SAXS **(Figure 4.22 b-c)**, obtaining five reflections in the low-angle region with a distance ratio of: 1:1/√3: 1/√4: 1/√7: 1/√16 that correspond to the reflections (100), (110), (200), (210) and (400) with a high alignment of the columns in the plane perpendicular to the film. In the high angle region, a broad peak at 4.3 Å appeared because of the chain-chain interactions. This kind of patterns confirmed the hexagonal columnar nature of the mesophase.

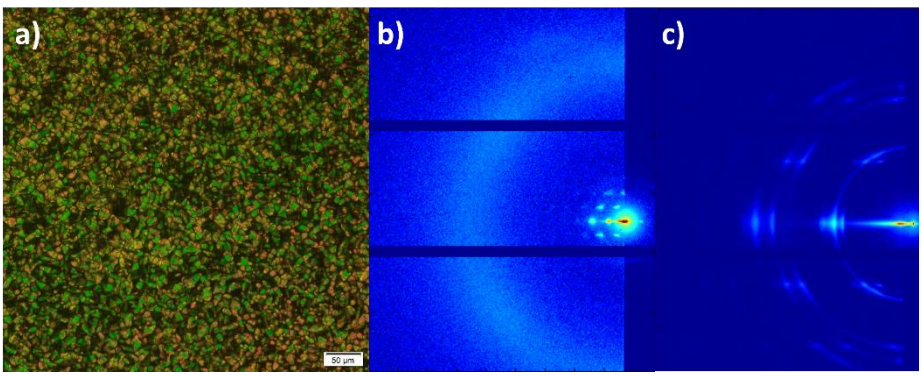

Figure 4.22. *(a) POM microphotograph taken at 25ºC in the cooling process, (b) WAXS pattern and (c) SAXS pattern of* ***Hpz-dCouAzoC$_8$.***

4.3.3 Preparation of chiral membranes

After the characterization of the materials, those which exhibited columnar mesophases were selected for the preparation of chiral membranes. The preparation of the chiral membranes includes several steps that had to be completed and characterized:

1. Preparation of the film by spin-coating.
2. Chiral induction in the films with circularly polarized light.
3. Photopolymerization of coumarins with 325 nm light.
4. Template removal by acid treatment and verification of the chirality in the nanoporous material.

Films were prepared on clean quartz substrates that were previously treated with a polyamide solution by spin-coating to obtain a homeotropic alignment. Then a solution of the corresponding material in DCM was spin-coated (1500 rpm, 30s, 25 mg/ml) resulting in homogeneous films. The presence of azobenzene moieties in the supramolecular complexes enabled us to induce chirality in these complexes without the presence of any chiral centers. As it is previously described in the literature,[46,47,54] supramolecular chirality can be induced in columnar mesophases by irradiating them with circularly polarized light (CPL). Azobenzenes, known for their well-studied *E*/*Z* isomerization induced by external photoirradiation, undergo a process that alters the compound polarity and geometry, resulting in macroscopic dichroism.

In our materials, the irradiation of the films with CPL for 1 minute at room temperature generated a chiral signal at the wavelength of the maximum absorption of the coumarin and the azobenzene chromophores, which are overlapped (325-400 nm) (**Figure 4.23b**). Moreover, if we change the sign of the CPL irradiation to the opposite handedness, the CD spectra obtained has the opposite sign, which demonstrates that the supramolecular chirality can be tuned externally with the sign of the CPL employed (**Figure 4.23a** blue and red line). The CD signal is the result of a helical arrangement of the

chromophores along the columns of the material which can be modulated with the sign of the CPL. These results were reproducible with all supramolecular complexes studied.

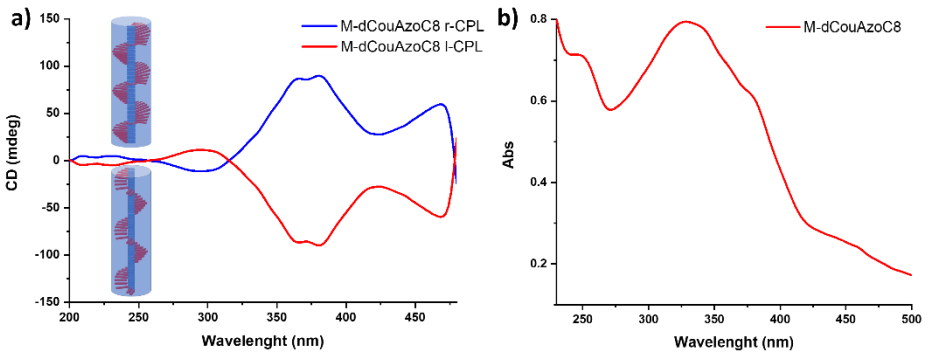

Figure 4.23. *a) Circular dichroism spectra of a* ***M-dCouAzoC$_8$*** *film after being irradiated with r-CPL (blue) and l-CPL (red) b) UV spectrum of a* ***M-dCouAzoC$_8$*** *film.*

It is worth mentioning that the signal generated by CPL remains after 24 hours, its intensity decreasing slightly when the sample is kept in darkness (**Figure 4.24**).

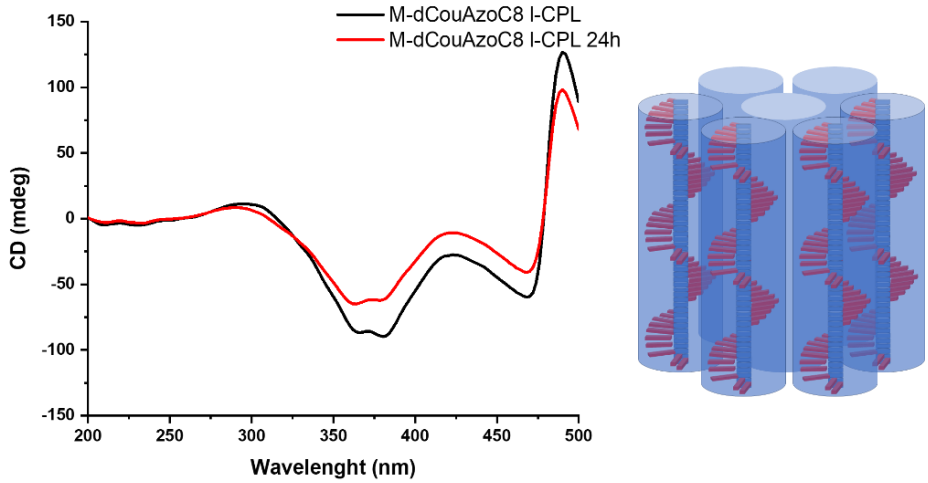

Figure 4.24. *Evolution of the CD signal after 24h.*

After successfully transmitting the chirality to the supramolecular complexes, the next step was to develop a polymeric material capable of maintaining the characteristic columnar order of the mesophase. This material was achieved through the crosslinking of coumarins using 325 nm light. When the material was exposed to 325 nm light, coumarins undergo a [2+2] photodimerization process to produce a

cyclobutane dimer, which should preserve the structural organization and does not require any catalyst or initiator. The photoreaction was monitored using UV-vis spectroscopy, FT-IR and POM. Furthermore, the structure of the resulting material was confirmed through X-ray diffraction (XRD) and circular dichroism (CD).

The UV spectra of the selected complexes (**Hpz-dCouAzoCN**, **M-dCouAzoC$_8$**, **TTT-dCouAzoC$_8$** and **Hpz-dCouAzoC$_8$**) showed an absorption band at 325 nm in films caused by the coumarin π-π* transition. The exposition of the films to light of 325 nm produced the [2+2] cycloaddition, decreasing the intensity of the coumarin absorption band. This decrease was monitored by UV until it remained stable (**Figure 4.25a**).

For further knowledge of the photoreaction, the films were studied by FT-IR: in the case of **M-dCouAzoC$_8$** the carbonyl (C=O) stretching band of the dimeric form shifted from 1748 cm^{-1} to 1726 cm^{-1} and the intensity of the C=C band of the coumarins at 1613 cm^{-1} decreased because of the dimerization (**Figure 4.25b**).

The film that had been irradiated with light was studied by POM (**Figure 4.25c**) and, in contrast with the non-irradiated film, the sample was not colorful and birefringent. After heating until isotropization temperature of the complex, the sample did not melt and did not flow, confirming the formation of the polymeric material.

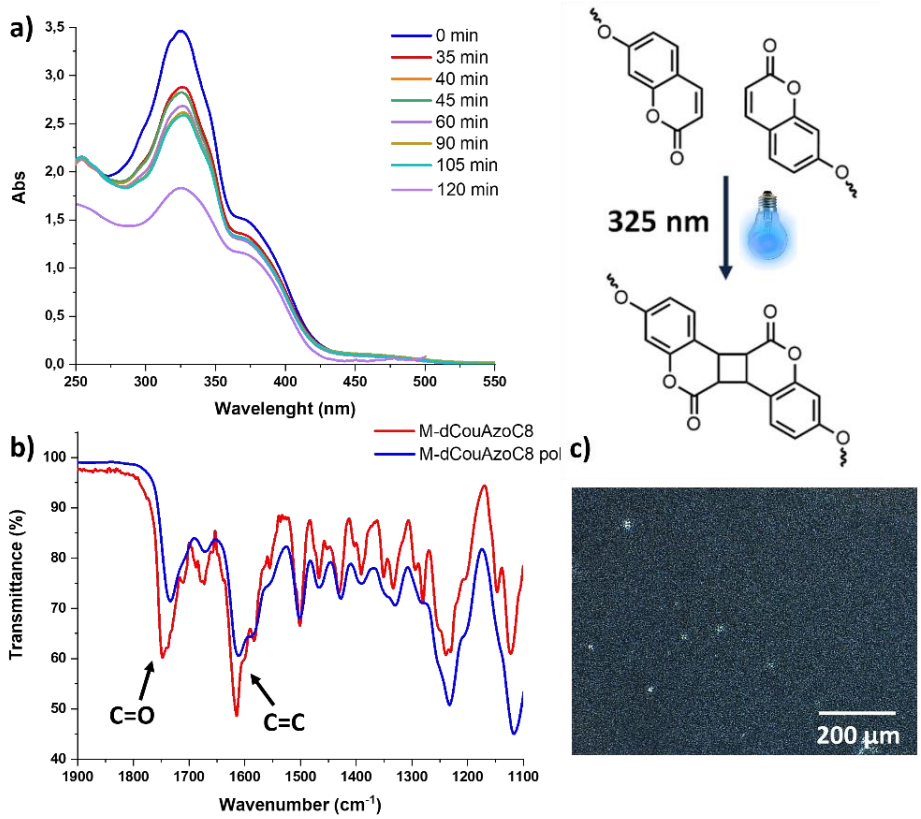

Figure 4.25. *a)* ***M-dCouAzoC$_8$*** *photodimerization process followed by UV in film at different times b) FT-IR spectra comparison before and after photodimerization and c) POM image after photodimerization.*

Once the photodimerization was carried out and characterized, the structural analysis of the polymeric films was conducted using X-ray diffraction (XRD). **Figure 4.26 a-b** presents a comparison of the 1D XRD patterns before and after photodimerization. Significantly, the key peaks corresponding to the columnar structure ((100) and (110)) were preserved, indicating the retention of the columnar arrangement within the polymeric films. Moreover, these signals exhibited broadening and slight shifting to larger angles, suggesting that dimerization of coumarins led to a reduction in the column cross-section and altered the lattice distances. Remarkably, some of the peaks observed prior to polymerization disappeared; for instance, the signals (210) and (400) were not detected in the spectrum after polymerization. Regarding heptazine derivatives, their diffractograms showed a highly oriented material with multiple signals in the small-

angle region after polymerization (**Figure 4.26 e-f**) manifesting the tendency to the homeotropic alignment of the heptazine. Overall, these experiments provided strong evidence of the persistence of the columnar organization in the polymeric materials.

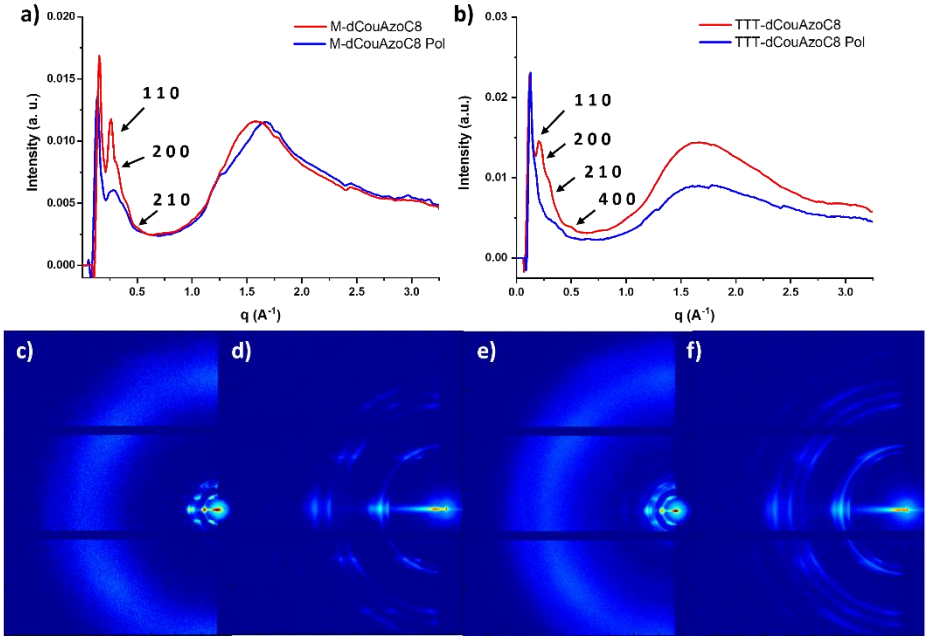

Figure 4.26. *XRD patterns before and after photodimerization of a)* ***M-dCouAzoC$_8$*** *b)* ***TTT-dCouAzoC$_8$****. WAXS and SAXS diffractograms of* ***Hpz-dCouAzoC$_8$*** *before (c and d) and after (e and f) photodimerization.*

Across the preparation of the nanoporous membranes, the chirality of the material was verified. The CD spectra of the photopolymerized materials are presented in **Figure 4.27**, revealing lower CD values compared to the pre-dimerization state. The dimerization of the coumarins had an impact on the helical arrangement within the columnar structure, resulting in a decrease in the CD signal intensity. In addition, the exposure of the films to 325 nm light could potentially influence the azobenzenes, which had previously absorbed circularly polarized light (CPL). This reduction in the CD signal is correlated with the specific template used: larger templates, such as **TTT** and **Hpz**, exhibited a more pronounced decrease in CD signal intensity. The reason could be that the azobenzenes, which induce the helical state in the columnar structure, are positioned farther away from the

template in comparison to the melamine **M** template, which displayed the highest CD signal intensity.

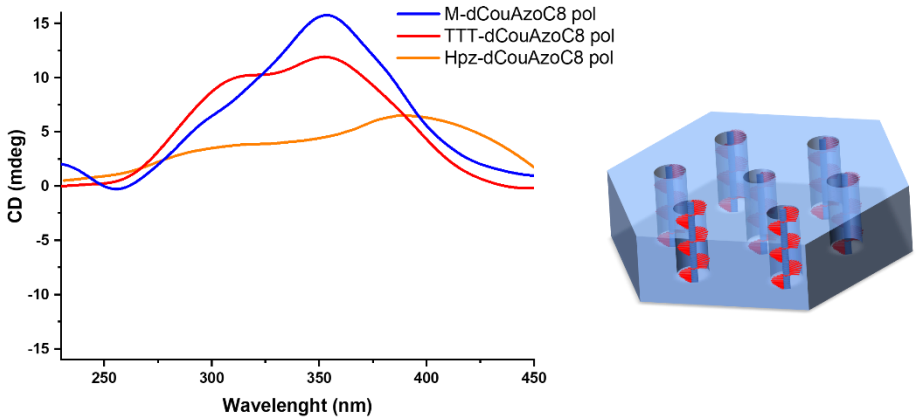

Figure 4.27. *CD spectra of* ***dCouAzoC$_8$*** *supramolecular complexes after photodimerization.*

Finally, liquid crystal membranes were obtained after a chemical treatment of the polymeric films. To produce the self-standing nanoporous materials, the films were immersed in a 3M solution of HCl in EtOH for **M** and **TTT**. However, in the case of **Hpz** its poor solubility led to search more aggressive conditions with a solution of HCl (3M)/DMSO (1%)/EtOH. After shaking the films in the proper solution for 14 hours, the nanoporous materials were washed with water, dried and characterized by XPS, FT-IR and XRD.

First, the XPS spectrum of the dendron **dCouAzoC$_8$** was studied (**Figure 4.28a**) revealing that the azobenzene bond (-N=N-) did not appear in the same nitrogen region as the templates (-N=C- and -N-C- ~398 eV). Secondly, XPS experiments of the polymeric films and the nanoporous films were carried out (**Figure 4.28 b-d**). The analysis of the N 1s region of the polymeric films exhibited an intense peak at 398 eV attributed to the abundance of nitrogen atoms in the **M**, **TTT** and **Hpz** templates. However, after the acid treatment, the intensity of these peaks decreased drastically, indicating the successful removal of the templates.

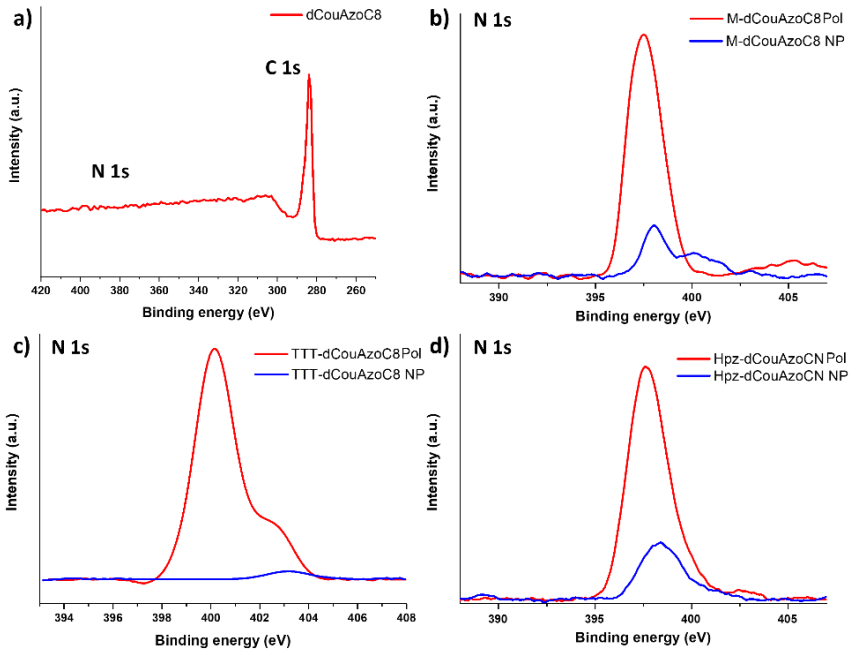

Figure 4.28. *a) XPS spectrum of* ***dCouAzoC$_8$****. b-d) XPS spectra comparison before (red line) and after (blue line) template removal.*

To determine the percentage of template eliminated, the integration of the N 1s peaks was calculated both before and after the acid treatment (**Table 4.5**). The results indicated a similar percentage of removal for **melamine** and **TTT** templates. However, **heptazine** was less effectively eliminated, due to its poor solubility.

Table 4.5. *Percentage of template removal in the nanoporous films.*

	$N_{integral}$	$\%_{removal}$
M-dCouAzoC$_8$ Pol	*3847*	
M-dCouAzoC$_8$ NP	*220*	*95%*
TTT-dCouAzoC$_8$ Pol	*5853*	
TTT-dCouAzoC$_8$ NP	*170*	*97%*
Hpz-dCouAzoC$_8$ Pol	*6923*	
Hpz-dCouAzoC$_8$ NP	*1002*	*86%*
Hpz-dCouAzoCN Pol	*1472*	
Hpz-dCouAzoCN NP	*323*	*79%*

The FT-IR spectra of the nanoporous films confirmed the template removal by the disappearance of the -NH_2 stretching band at 3356 cm^{-1} of the template molecules (**Figure 4.29a**). Moreover, the formation of the pores in the films modifies the stretching vibration of the carboxylic acids since the hydrogen bond disappeared, and this is reflected in a new stretching at 1685 cm^{-1} that corresponds to the free acid (**Figure 4.29b**).

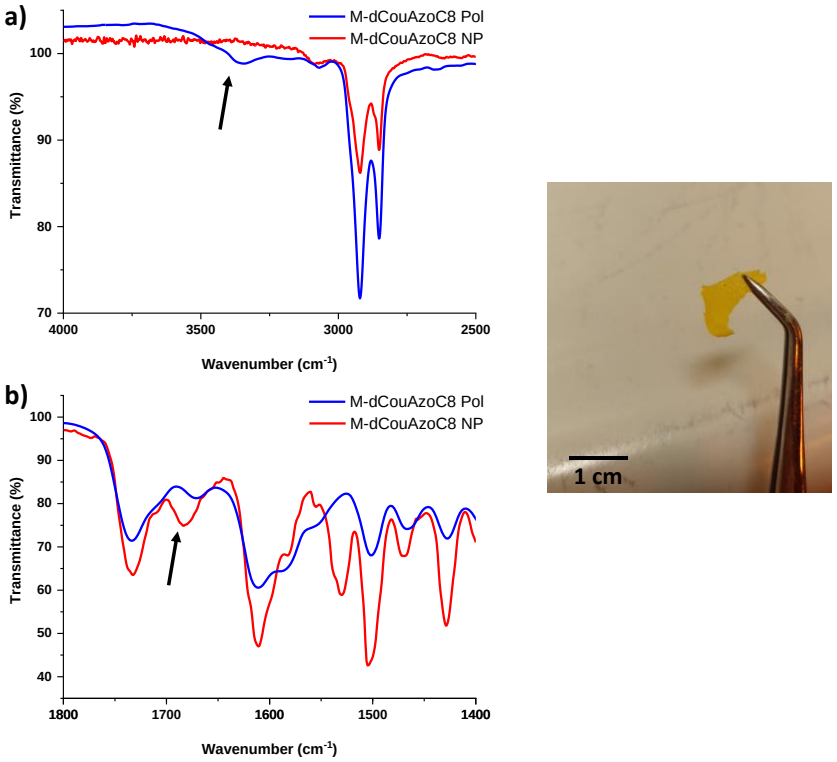

Figure 4.29. *FT-IR spectra of the polymerized films before (blue line) and after (red line) the acid treatment. Example of a chiral nanoporous membrane.*

The structural details of the nanoporous materials were examined by XRD, and in **Figure 4.30** the XRD patterns of the **dCouAzoC$_8$** complexes are shown. These patterns revealed multiple reflections in the low angle region that indicates the conservation of the columnar hexagonal arrangement. However, after the template removal the column cross-section was reduced in some angstroms, as was

described in the bibliography, due to the shrinkage of the disc-shaped complex.

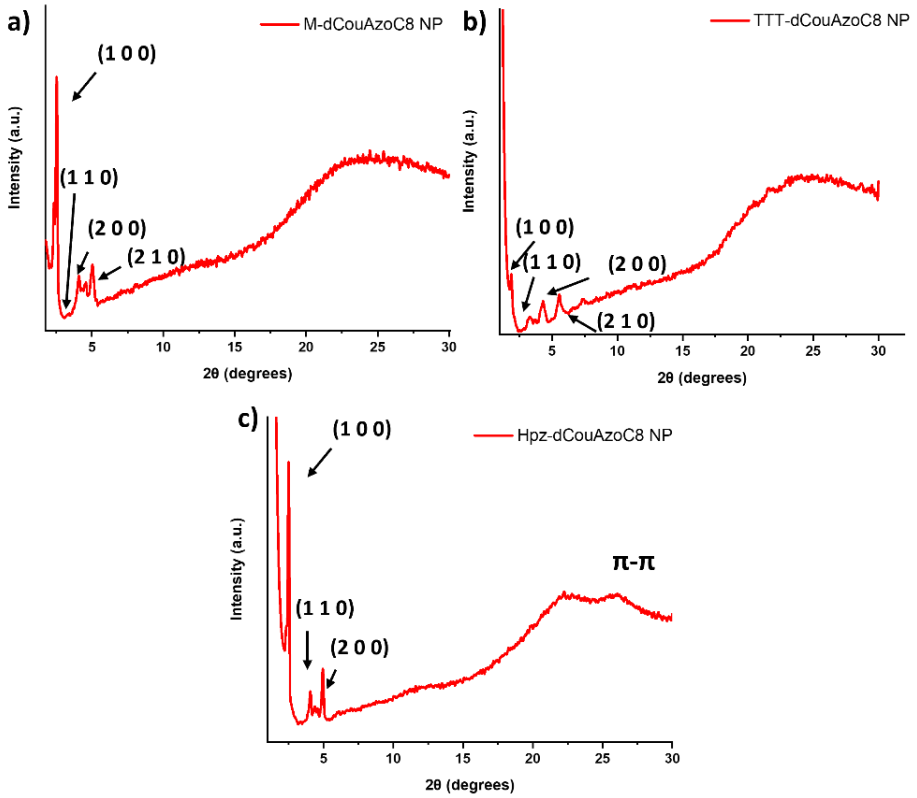

Figure 4.30. *XRD patterns after the template removal of the* ***dCouAzoC$_8$*** *membranes.*

After the acid treatment, all compounds exhibited chiral signal in the CD spectra at the wavelength of the azobenzene absorption (**Figure 4.31a**), verifying the formation of chiral membranes through the irradiation with CPL. Regarding the intensity of the signal, the CD value decreased after the template removal, being highest in the **melamine** complex as it happened after the dimerization process. It is worth emphasizing that none of the spectra exhibited a chiral signal at the wavelengths corresponding to coumarin absorption (325 nm) or template absorption (200-350 nm), providing evidence of both photodimerization and template elimination. After successfully demonstrating the preparation of chiral membranes, we explored whether the azobenzenes would be capable of reversing their isomerization when they were exposed to circularly polarized light

(CPL) of the opposite sign. To test this, the films were subjected to irradiation with CPL of the opposite sign to that was used during the initial process. A 1-minute exposure to CPL resulted in the generation of CD signal with the opposite value (**Figure 4.31b**), proving the formation of tunable chiral membranes with CPL.

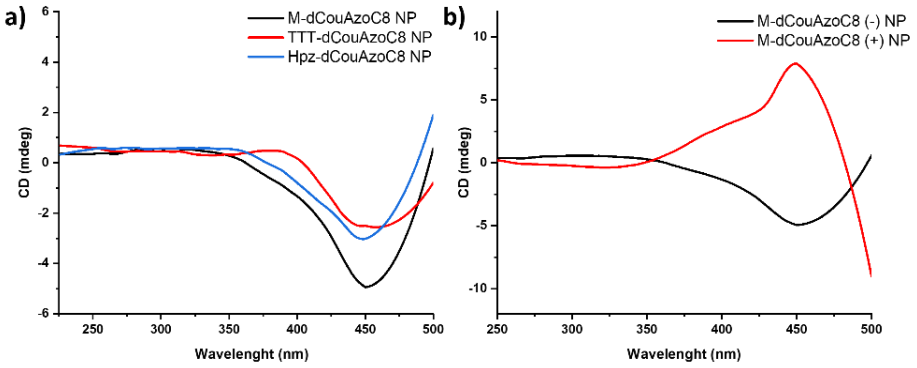

Figure 4.31. *a) CD spectra of some complexes after acid treatment. b) CD spectra after irradiation with CPL of the opposite sign.*

4.3.4 Selective adsorption studies

4.3.4.1 Selective adsorption by size

The employment of different molecules that act as templates led to the preparation of membranes that exhibit a range of pore sizes, including a small pore resulting from **melamine** with a size of 5 Å, as well as two larger pores originated from **TTT** and **Hpz**, measuring 10 Å and 9 Å, respectively (calculated by MM2 force field method using Chem3D software). These differences in the pore size turn them suitable materials for the adsorption of organic molecules. To test the ability of rejection or adsorption by size, three different molecules containing amine groups have been employed: (*S*)-(hexan-2-yl)-4-nitroaniline (**NA*** size= 11.7x4.2 Å), (*S*)-tryptophan (**Tryp*** size= 8.2x4.8 Å) and (*S*)-(hexan-2-yl)pyrene (**Pyr*** size= 13.9x7.7 Å) (**Figure 4.32**). These molecules were chosen for their biological activity and their luminescence properties (UV and fluorescence).

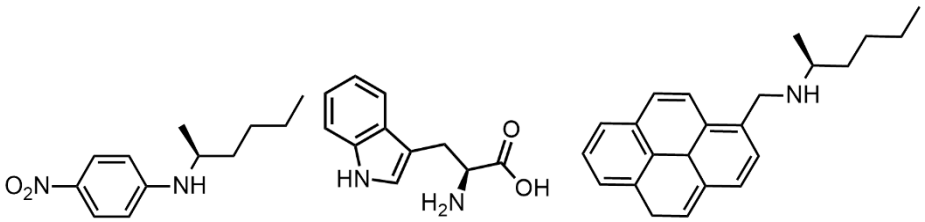

Figure 4.32. *Molecules used in the selective adsorption by size studies:* ***(S)-(hexan-2-yl)-4-nitroaniline*** *(left),* ***(S)-tryptophan*** *(middle) and* ***(S)-(hexan-2-yl)pyrene*** *(right).*

Initially, the thinnest molecule (**(*S*)-(hexan-2-yl)-4-nitroaniline**), **NA***, was tested with the four nanoporous materials that exhibited columnar mesophases (**Figure 4.33**). To investigate the kinetics of the membrane adsorption, the absorbance of the aniline solution was measured at different times of immersion of the membrane in a solution of the compound to be adsorbed. It was observed that all materials exhibited adsorption of nitroaniline, with variations in the time-dependent evolution of the process. The maximum adsorption was achieved after 24 hours, indicating that, by this point, the materials had largely adsorbed the nitroaniline derivative.

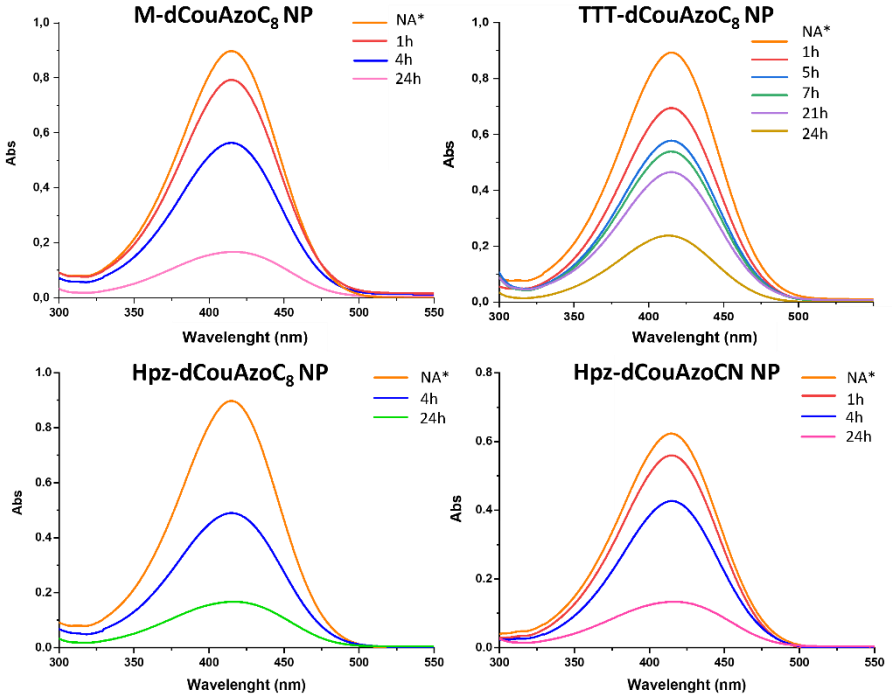

Figure 4.33. *UV spectra of* ***(S)-(hexan-2-yl)-4-nitroaniline*** *in water before and after adsorption at different times with the four nanoporous membranes.*

The adsorption capacity was explored for each nanoporous material by UV in water: in the case of **M-dCouAzoC$_8$** 29% of the carboxyl groups in the pores were occupied with nitroaniline, which represents 0.87 molecules per disc. For **TTT-dCouAzoC$_8$** the occupation rate was 47%, which corresponds to 1.44 molecules per disc (**Figure 4.34**). Finally, heptazine derivative **Hpz-dCouAzoC$_8$** adsorbed with an occupancy of 38% (1.15 molecules per disc) and for **Hpz-dCouAzoCN** the occupancy was 43% (1.31 molecules per disc).

Figure 4.34. *Vial of* ***TTT-dCouAzoC$_8$ NP*** *material after 24h of immersion in a* ***(S)-(hexan-2-yl)-4-nitroaniline*** *solution (left) and* ***(S)-(hexan-2-yl)-4-nitroaniline*** *solution in water (right).*

After the successful adsorption of a small molecule, we focused on the study of a bigger molecule. Tryptophan **Tryp*** was chosen because it possesses a primary amine and two aromatic rings in its structure, in comparison with the nitroaniline derivative that only possesses one. The evolution of the maximum absorbance of tryptophan at 280 nm was followed by UV, revealing an occupation of: 16% for **M-dCouAzoC$_8$ NP** (0.48 molecules per disc), 36% for **TTT-dCouAzoC$_8$ NP** (1.10 molecules per disc), 29% for **Hpz-dCouAzoC$_8$ NP** (0.87 molecules per disc) and 31 % for **Hpz-dCouAzoCN NP** (0.94 molecules per disc).
Finally, the nanoporous materials were tested with a big molecule: the absorbance of the pyrene derivative **Pyr*** was followed by UV between 200 nm and 400 nm (**Figure 4.35**). **M-dCouAzoC$_8$** rejected the pyrene because of its small pore size with an occupation of 1% (0.03 molecules per disc). The bigger pores adsorbed the pyrene derivative with a percentage of 34% for **TTT-dCouAzoC$_8$ NP** (1.04 molecules per

disc), 22% for **Hpz-dCouAzoC$_8$ NP** (0.67 molecules per disc) and 16% for **Hpz-dCouAzoCN NP** (0.48 molecules per disc).

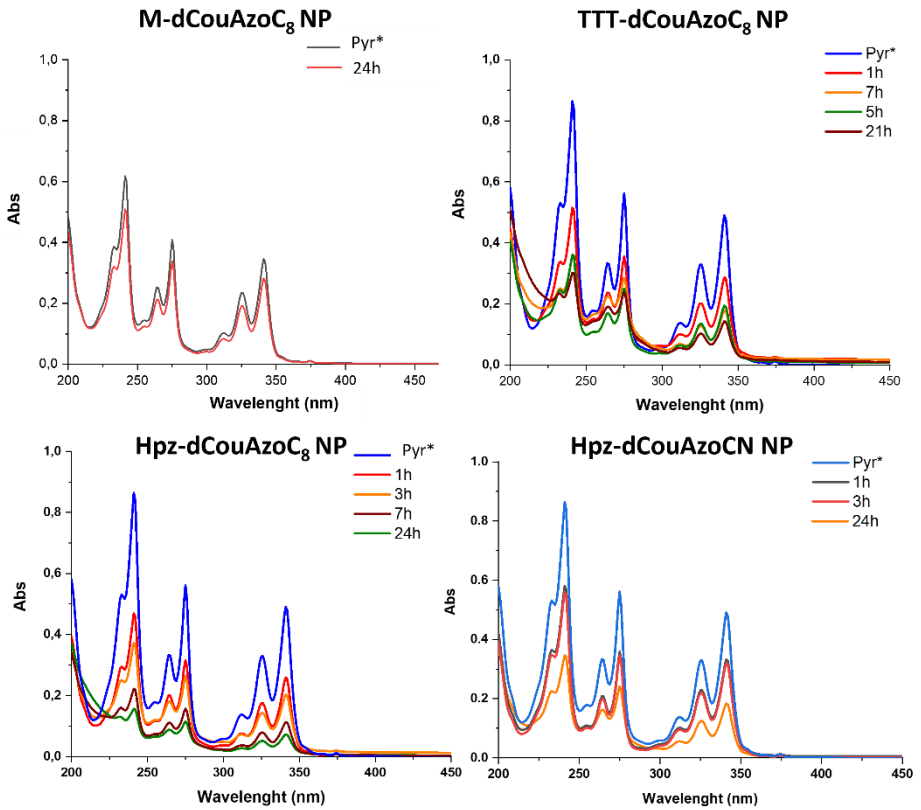

Figure 4.35. *Absorption spectra of* ***(S)-(hexan-2-yl)pyrene*** *in water after membrane immersion at different times.*

The adsorption capacity of the LC membranes was measured in relation to the milligrams of dye per gram of membrane as a function of time:

$$q_t = \frac{(C_0 - C_f)V}{m}$$

Where C_0 is the initial concentration (mg/L) of the dye, C_f is the final concentration (mg/L), V is the volume (L) of the solution and m is the mass of membrane (g). **Table 4.6** shows a summary of the adsorption capacities of the four prepared nanoporous membranes with respect to the three molecules selected for the studies.

Table 4.6. Capacity of adsorption of the four prepared nanoporous membranes.

	M-dCouAzoC$_8$ NP	TTT-dCouAzoC$_8$ NP	Hpz-dCouAzoC$_8$ NP	Hpz-dCouAzoCN NP
q_t NA* (mg/g)	56	94	74	91
q_t Tryp* (mg/g)	15	31	27	25
q_t Pyr* (mg/g)	1	67	59	57

For a better understanding of the quantitative analysis, we tried to adjust these results to a first order kinetic adsorption whose equation is:

$$q_t = q_e(1 - e^{-kt})$$

Where q_e is the maximum amount of molecules adsorbed in the equilibrium, t is the time in that equilibrium and k is the kinetic constant. This model fitted with precision for the adsorption capacity. As an example, in **Figure 4.36** the curve, the equation and the R value are shown for the adsorption of the nitroaniline derivative **NA*** with **M-dCouAzoC$_8$ NP** and **TTT-dCouAzoC$_8$ NP**.

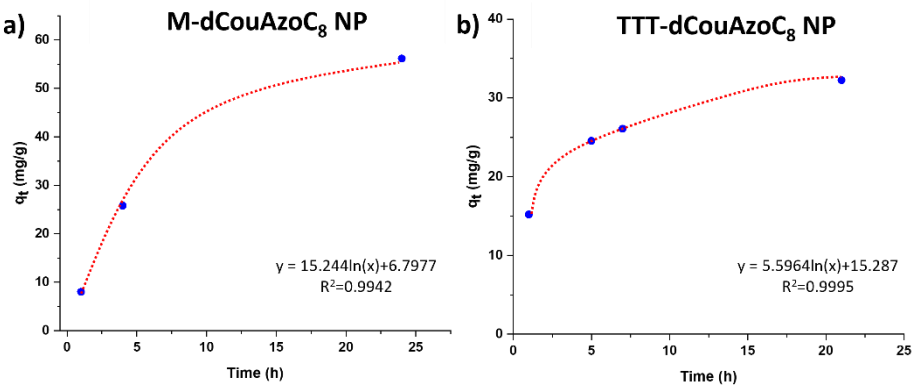

*Figure 4.36. First order kinetic adjustment of a) **M-dCouAzoC$_8$ NP** and b) **TTT-dCouAzoC$_8$ NP** with the nitroaniline derivative.*

These studies revealed that the **melamine** derivatives, which possess the smallest pore, cannot adsorb big molecules as pyrene. **TTT** membranes adsorbed all the molecules studied; however, they showed a higher tendency to adsorb small molecules like the nitroaniline derivative as could be measured with the q_t calculations. Finally, **Hpz** membranes, which also adsorbed all molecules, revealed a lower capacity of adsorption in comparison with **TTT**. Furthermore, it is noteworthy that the nature of the adsorbed molecule plays a key role. For instance, tryptophan **Tryp***, despite being smaller than the pyrene derivative **Pyr***, did not exhibit as facile adsorption as pyrene. This difference in behavior may be attributed to the type of amine present in the molecule: tryptophan possesses a primary amino group, while the other studied molecules contain secondary amino groups.

The ability to desorb molecules in solution is a critical aspect of membrane preparation, as it allows for the retrieval of valuable adsorbates and the reusability of the membrane. As it was previously demonstrated, the nanoporous materials adsorbed a substantial amount of nitroaniline derivative in a water solution. To assess the desorption capability, the membranes were immersed in a 1M solution of KOH in water, which deprotonates the carboxylic acids and releases the previously adsorbed nitroaniline derivative. The release of this dye was monitored via UV spectroscopy until the signal reached a constant level. This adsorption-desorption cycle was repeated three times, demonstrating the reversibility of the process (**Figure 4.37**).

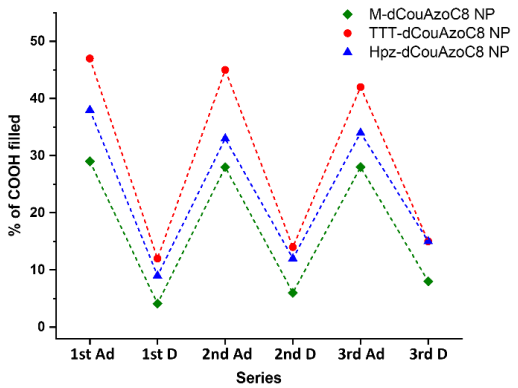

Figure 4.37. *Adsorption-desorption cycles of* ***(S)-(hexan-2-yl)-4-nitroaniline*** *studied by UV in different membranes.*

4.3.4.2 Selective adsorption by chirality

After successfully demonstrating the size-selective adsorption, our next goal was to investigate the selective adsorption based on the chirality of the studied dye. To achieve this, **(*S*)-(hexan-2-yl)-4-nitroaniline** and **(*R*)-(hexan-2-yl)-4-nitroaniline** were synthesized, and their adsorption on chiral nanoporous materials was examined.

Two films of **M-dCouAzoC$_8$ NP** were prepared, one irradiated with *right*-CPL and the other with *left*-CPL. Each film was individually immersed in a solution of **(*S*)-(hexan-2-yl)-4-nitroaniline** in water. The progression of **(*S*)-nitroaniline** adsorption was monitored in both cases. Interestingly, a decrease in the UV signal was observed in only one case. After 30 hours, the film irradiated with *r*-CPL had adsorbed the majority of **(*S*)-nitroaniline**, whereas the UV absorption remained nearly unchanged in the film irradiated with *l*-CPL (**Figure 4.38**).

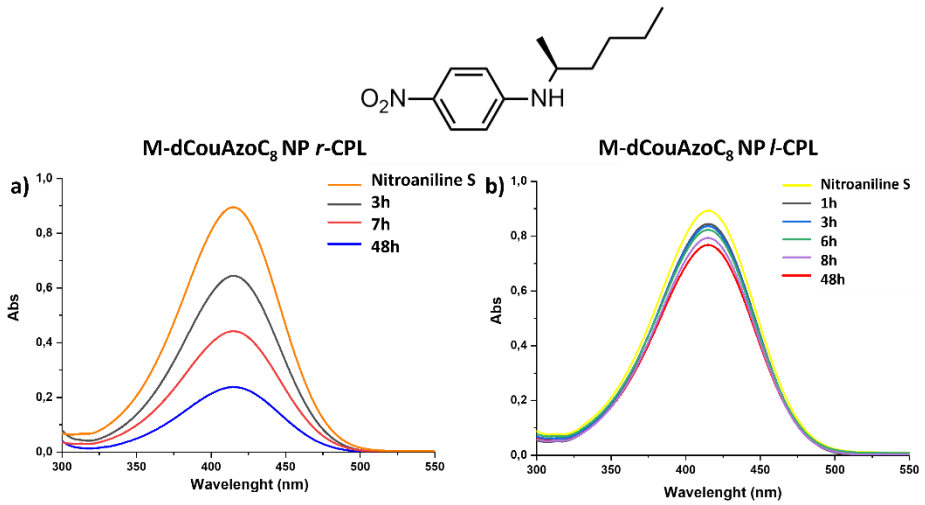

Figure 4.38. *Chemical structure of* ***(S)-(hexan-2-yl)-4-nitroaniline and*** *adsorption progress followed by UV of a)* ***M-dCouAzoC$_8$ NP*** *r-CPL and b)* ***M-dCouAzoC$_8$ NP*** *l-CPL.*

The chiral dependent adsorption was further studied using the other enantiomer **(*R*)-(hexan-2-yl)-4-nitroaniline**. Again, two films of **M-dCouAzoC$_8$ NP** were prepared, one irradiated with *right*-CPL and the other with *left*-CPL. In accordance with the previous experiment only one of them adsorbed most of the nitroaniline derivative. In this case, it was observed that the film irradiated with *left*-CPL exhibited

significant adsorption of the dye, while the other film (irradiated with *right*-CPL) showed minimal adsorption even after 48 hours (**Figure 4.39**).

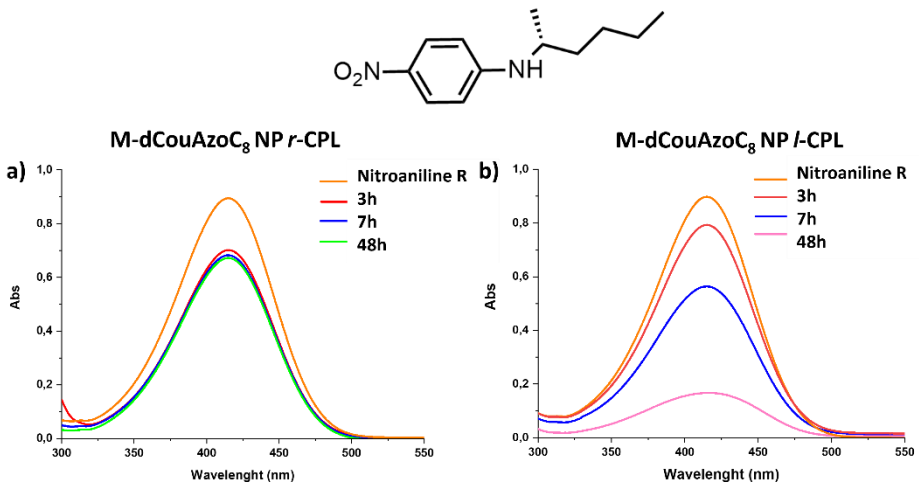

Figure 4.39. *Chemical structure of* ***(R)-(hexan-2-yl)-4-nitroaniline and*** *adsorption progress followed by UV of a)* ***M-dCouAzoC$_8$ NP*** *r-CPL and b)* ***M-dCouAzoC$_8$ NP*** *l-CPL.*

The successful demonstration of chiral selective adsorption with the smallest molecule invited to predict similar outcomes with larger templates (**TTT** and **Hpz**) and larger molecules (tryptophan **Tryp*** and pyrene **Pyr***). **M-dCouAzoC$_8$ NP** was dismissed for the following experiments because, as it was demonstrated in the previous section, its pore size does not allow the adsorption of tryptophan and pyrene derivatives.

The methodology employed to investigate the chiral selective adsorption of tryptophane and pyrene was the same used for **M-dCouAzoC$_8$ NP**. Different films of **TTT-dCouAzoC$_8$ NP**, **Hpz-dCouAzoC$_8$ NP** and **Hpz-dCouAzoCN NP** were prepared and irradiated with either *left*-CPL or *right*-CPL; then they were immersed separately in a solution of **(*S*)-tryptophan**, **(*R*)-tryptophan**, **(*S*)-(hexan-2-yl)pyrene** and **(*R*)-(hexan-2-yl)pyrene** and their adsorption was followed by UV at different wavelengths.

As an example of the results obtained, the UV progress of the pyrene absorption is shown in **Figures 4.40** and **4.41** for the membranes **TTT-dCouAzoC$_8$ NP** and **Hpz-dCouAzoC$_8$ NP**. The studies revealed that the

irradiation with CPL influenced the kinetics of the process, showing a faster adsorption when the film was irradiated with *right*-CPL for **(*S*)-(hexan-2-yl)pyrene**. However, after 48 hours the nanoporous film irradiated with *left*-CPL adsorbed most of the dye, as its counterpart.

Regarding the smaller dyes, such as nitroaniline **NA*** and tryptophan **Tryp***, irradiation with CPL did not result in any alterations in the adsorption process for **TTT** and **Hpz** membranes. This lack of difference in selective adsorption ability can be attributed to the substantial pore size in these materials, which exceeds the size of the molecules under study.

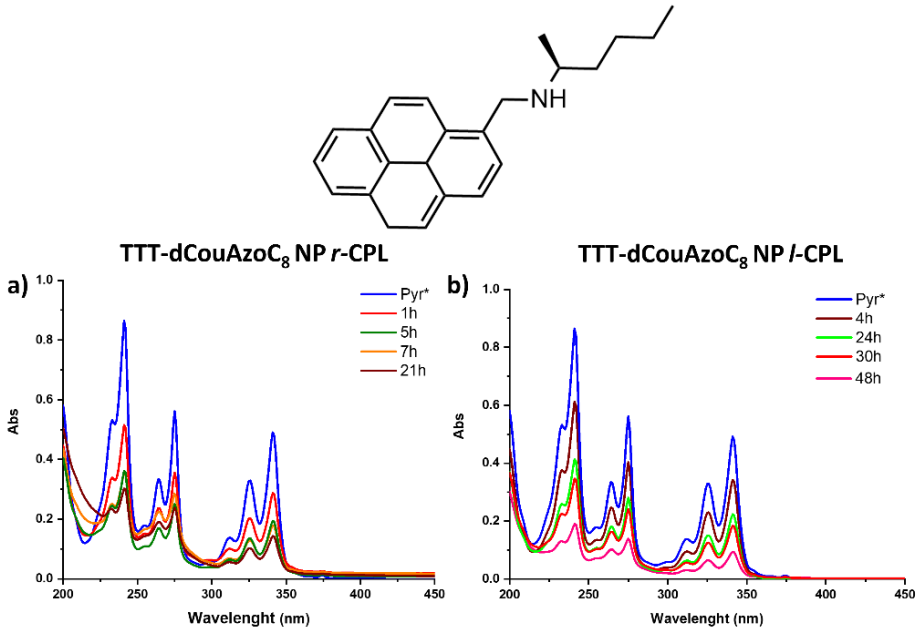

Figure 4.40. *Pyrene adsorption by* ***TTT-dCouAzoC$_8$ NP*** *irradiated with r-CPL (a) and l-CPL (b).*

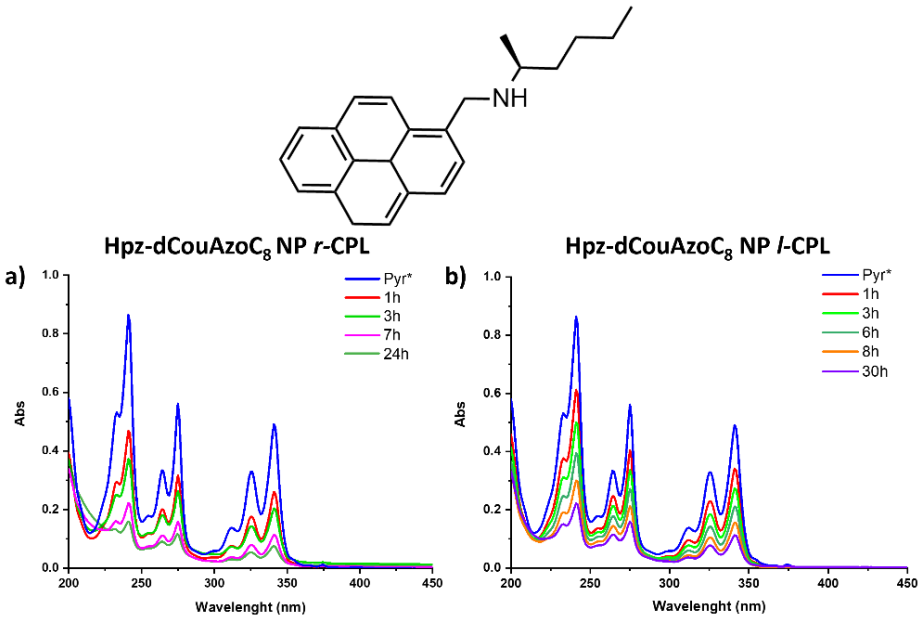

Figure 4.41. *Pyrene adsorption by* ***Hpz-dCouAzoC$_8$ NP*** *irradiated with r-CPL (a) and l-CPL (b).*

These results disclose the importance of the pore size in the separation process: the membrane obtained from **M-dCouAzoC$_8$** with pores generated from melamine facilitated the separation of nitroaniline enantiomers due to their closely matched dimensions. In the nanoporous materials obtained from **heptazine** and **TTT**, their large pore allowed an effective and fast adsorption of small molecules such as nitroaniline **NA*** no matter the chirality of the film and the molecule. In spite of that, their application with bigger molecules resulted in a clear preference of adsorption of the appropriate enantiomer.

4.3.4.3 Separation of racemic mixtures

In light of the chiral membranes capacity to adsorb/reject molecules by their chirality, we considered their use to separate racemic mixtures. Therefore, an equimolar solution of both **NA*** enantiomers was prepared and immersed in a *left*-CPL irradiated film. The solution was studied by chiral HPLC (high performance liquid chromatography) after 24 hours, showing an enantiomer relation of 80/20 (*R*)/(*S*)

demonstrating the enantioseparation from the racemic mixture (**Figure 4.42a**).

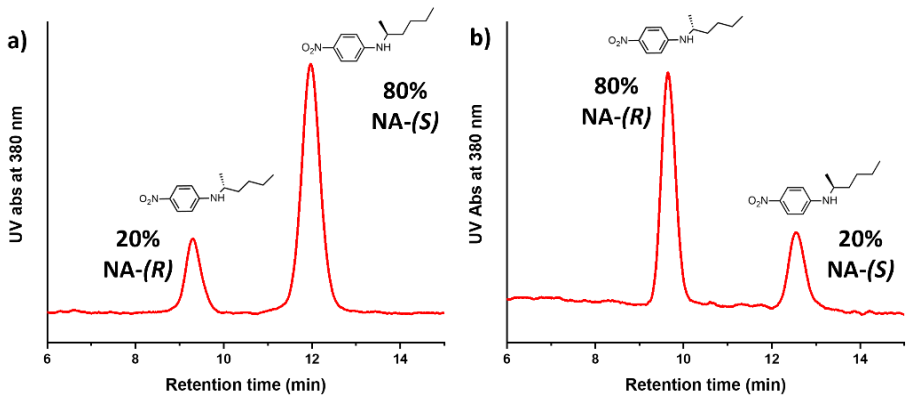

Figure 4.42. *HPLC traces of: a) enantiomeric mixture after l-CPL membrane adsorption b) KOH/H_2O solution after l-CPL membrane desorption.*

The inverse film (*right*-CPL irradiated) was investigated, obtaining the opposite relation between the (*R*)/(*S*) enantiomers (**Figure 4.43a**). These experiments confirm the ability of the chiral nanoporous membranes to separate racemic mixtures and their tuneability to adsorb the desired enantiomer with the same material irradiating with *right* or *left*-CPL. Finally, both membranes were immersed in a solution of KOH/H_2O and the solution turned yellow after 24 hours. These solutions were analyzed by chiral HPLC, resulting in the opposite concentration of enantiomers than that previously studied (**Figures 4.42b** and **4.43b**).

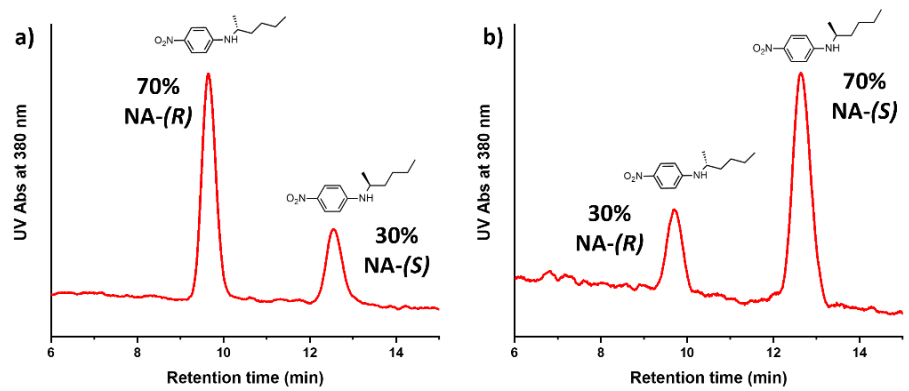

Figure 4.43. *HPLC traces of: a) enantiomeric mixture after r-CPL membrane adsorption b) KOH/H_2O solution after r-CPL membrane desorption.*

4.4 Conclusions

In this chapter we have developed an effective approach for the preparation of chiral nanoporous membranes based on columnar liquid crystals. These mesophases have exhibited a highly ordered structure which has been fixed through coumarin photodimerization. Moreover, the irradiation with circularly polarized light has allowed to obtain tunable chiral membranes. The different template molecules employed in the formation of the disc shaped supramolecules by hydrogen bond have led to the formation of different pore sizes. Finally, the application of these materials in molecular recognition and separation has been tested with different molecules by size and chirality, proving an effective separation by size depending on the template used and by chirality depending on the sign of the CPL employed, as well as resolution of specific racemic mixtures with the melamine derivative membrane.

4.5 Experimental part

4.5.1 Characterization techniques

All reagents were purchased from Aldrich and used without further purification. Anhydrous CH_2Cl_2 and THF were purchased from Scharlab and dried by using a solvent purification system.

^{1}H-NMR and **^{13}C-NMR** spectra were acquired on a Bruker AV400 spectrometer. The experiments were performed at room temperature in different deuterated solvents ($CDCl_3$, CD_2Cl_2 or DMSO-d_6). Chemical shifts are given in ppm relative to TMS and the solvent residual peak was used as the internal standard.

Infrared spectra were recorded on a Bruker Vertex 70 FT-IR spectrometer. The samples were prepared on KBr pellets with a concentration of the product of 1-2% (w/w).

MALDI-TOF mass spectrometry was performed on an Autoflex Bruker mass spectrometer with a dithranol matrix. Positive and negative ion electrospray ionization high resolution (**ESI HRMS**) was performed on a Bruker Q-TOF-MS in a positive or negative ESI mode.

Mesophase textures were investigated by **polarized-light optical microscopy** (POM) using an Olympus BH-2 polarizing microscope fitted with a Linkam THMS600 hot stage and a Linkam TMS94 controller.
Thermogravimetric analysis (TGA) was performed using a Q5000IR from TA instruments at heating rate of 10 °C min^{-1} under a nitrogen atmosphere.
Thermal transitions were determined by **differential scanning calorimetry** (DSC) using a DSC Q2000 from TA instruments with powdered samples (2−5 mg) sealed in aluminum pans. The apparatus was previously calibrated with indium (156.6 °C, 28.44 J*g-1). Glass transition temperatures (Tg) were determined at the half height of the

baseline jump, and first order transition temperatures were read at the maximum of the corresponding peak.

X-ray diffraction measurements were carried out using an XRD-PANanalytical Empyrean diffractometer equipped with platform Scatter X78. Photographic patterns were recorded with a Pinhole camera (Anton Paar) operating with a point-focused Ni-filtered Cu-Kα beam. Samples were contained in Lindemann glass capillaries (0.9 or 0.7 mm diameter) and, when necessary, a variable-temperature attachment was used to heat the sample. The patterns were collected on flat photographic film perpendicular to the X-ray beam. X-Ray Diffraction in films (XRD) images were recorded on a Ganesha lab instrument equipped with a Genix-Cu ultra-low divergence source producing X-ray photons with a wavelength of 1.54 Å and a flux of 1 x 108 photons/second. Diffraction patterns were collected on a Pilatus Nanoporous polymer | 59 300K detector with reversed-biased silicon diode array sensor. The detector contains 487 x 619 pixels of 172 x 172 µm2 and consists out of three modules with an intermodule gap of 17 pixels in between, resulting in two dark bands on the image. Grazing Incidence X-Ray Scattering (GIXS) measurements were performed on a sample to detector distance of 1080 mm (WAXS) or 1530 mm (SAXS). Temperature-dependent measurements were executed with a Linkam HFSX350 heating stage and cool unit. Azimuthal integration of the obtained diffraction patterns was performed by utilizing the SAXSGUI software. The beam centre and the q-range were calibrated by utilizing silver behenate (0.107 $Å^{-1}$; 58.43 Å).

UV-Vis absorption spectra were recorded on an ATI-Unicam UV4-200 spectrophotometer.

Circular dichroism spectra were recorded on a Jasco J-810 spectropolarimeter. CD spectra were recorded at different rotation angles around the light beam showing the same trace, in the graphs the average of the six rotations were shown.

Photocrosslinking of coumarin units (photodimerization) was carried out by exposing the aligned LC films of 10 µm of thickness to 325 nm LED light (ThorsLab) for 180 min with a UV power of 8 mW/cm^2.

XPS spectra were recorded on a Kratos AXIS ultra DLD spectrometer equipped with an Al Kα X-ray monochromatic source (1486.6 eV) and using 20 eV as pass energy. Binding energies were calibrated according to the C1s peak at 284.6 eV.

Chiral HPLC: Waters HPLC chromatograph: Waters Delta 600 multi-solvent quaternary gradient pump, a Waters 2996 photodiode detector (PDA) and a Rheodyne® 7125 injector. Data were acquired and processed with Waters Empower® software.

The column is a Chiralpak® IA (tris packed (3,5-dimethylphenylcarbamate cellulose immobilized on silica, size particle 5 µm) with dimensions 250 x 4.6 mm ID. A 90/10 hexane/EtOH mixture with a flow of 1mL/min. Detection: UV absorption at 380 nm. 10 microliters were injected directly from the solution obtained after extraction of the samples with 1mL of AcOEt.

4.5.2 Synthetic procedures

4.5.2.1** Synthesis of the two azobenzene derivative precursors:(E)-4-((4-(2-bromoethoxy)phenyl)diazenyl)benzonitrile **BrAzoCN (1)** and (E)-1-(4-(2-bromoethoxy)phenyl)-2-(4-(octyloxy)phenyl)diazene **BrAzoC$_8$ (2)

The synthesis of the two azobenzene derivative precursors is gathered in the **Scheme 4.2**.

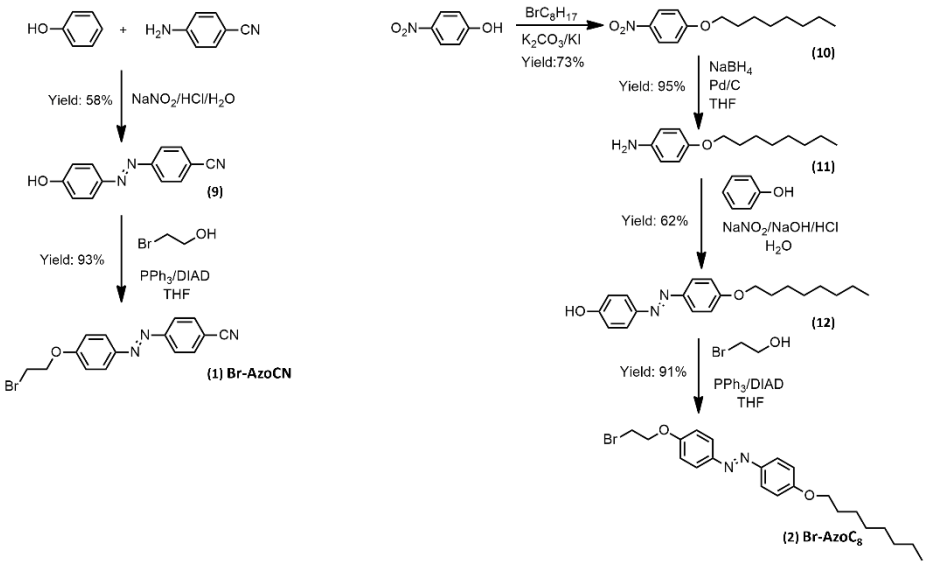

***Scheme 4.2**. Synthetic procedures of the two precursor azobenzene derivatives **BrAzoCN** and **BrAzoC$_8$**.*

*4.5.2.1.1 Synthesis and characterization of compound **Br-AzoCN (1)***

Synthesis of **HO-AzoCN (9)**: in a flask of 500 ml was dissolved 4-aminobenzonitrile (15.00 g, 0.17 mol) in 240 ml of water and 80 ml of HCl at 0ºC. In another flask was dissolved $NaNO_2$ (14.07 g, 0.20 mol) in 100 ml of water at 0ºC and it was slowly added to the first solution until pH=7. After that, phenol (18.82 g, 0.20 mol) was added and let react for one hour. The reaction was neutralized with $NaHCO_3$, and the solid obtained was filtered and purified by flash column chromatography in a mix of hexane 8:2 ethyl acetate. The product was obtained with a yield of 58%.

^{1}H-NMR ($CDCl_3$, 298K, 400 MHz, δ, ppm): 7.93 (m, 4H), 7.78 (m, 2H), 6.98 (m, 2H), 5.25 (s, 1H).

^{13}C-NMR (CDCl$_3$, 298K, 100 MHz, δ, ppm): 133.33, 125.84, 123.26, 116.17.

Synthesis of **Br-AzoCN (1)**: in a flask were dissolved **HO-AzoCN (9)** (2.50 g, 11.21 mmol), triphenylphosphine (3.60 g, 14.01 mmol) and 2-bromoethanol (1.75 g, 14.01 mmol) in THF (80 ml) and the solution was stirred under argon atmosphere. Finally, DIAD (3.00 g, 14.01 mmol) was added dropwise and let react at room temperature for 48 hours. The crude was filtered, the solvent evaporated and the product purified by recrystallization in ethanol obtaining **Br-AzoCN** with a yield of 93%.

^{1}H-NMR (CDCl$_3$, 298K, 400 MHz, δ, ppm): 7.95 (m, 4H), 7.79 (m, 2H), 7.05 (m, 2H), 4.40 (t, J=6.2 Hz, 2H), 3.69 (t, J=6.2 Hz, 2H).

^{13}C-NMR (CDCl$_3$, 298K, 100 MHz, δ, ppm): 161.60, 154.82, 147.37, 133.31, 125.62, 123.28, 118.73, 115.20, 113.52, 68.22, 28.73.

*4.5.2.1.2 Synthesis and characterization of compound **Br-AzoC$_8$ (2)***

Synthesis of **1-nitro-4-(octyloxy)benzene (10):** in a flask were dissolved in acetone (100 ml) 4-nitrophenol (10 g, 71.94 mmol) and K_2CO_3(19.86 g, 143.88 mmol). After vigorous stirring during one hour at reflux, 1-bromooctane (20.84 g, 107.91 mmol) and a spatula tip of KI were added. The mixture was stirred under reflux for 10 hours, filtered over celite and the solvent removed. The crude was purified by column chromatography in an eluent mix of dichloromethane 1:1 hexane with a yield of 73%.

^{1}H-NMR (CDCl$_3$, 298K, 400 MHz, δ, ppm): 8.18 (d, J=9.3 Hz, 2H), 6.93 (d, J=9.3 Hz, 2H), 4.04 (t, J=6.5 Hz, 2H), 1.82 (q, J=7.9 Hz, 2H), 1.50-1.23 (m, 10H), 0.89 (t, J=7.1 Hz, 3H)

^{13}C-NMR (CDCl$_3$, 298K, 100 MHz, δ, ppm): 164.40, 141.42, 126.03, 114.52, 69.04, 31.91, 29.40, 29.32, 29.10, 26.04, 22.77, 14.21.

Synthesis of **4-(octyloxy)aniline (11):** in a flask was prepared a solution of 1-nitro-4-(octyloxy)benzene **(10)** (10 g, 39.78 mmol) in 100 ml of THF. Under argon atmosphere was added $NaBH_4$ (3 g, 79.57 mmol)

and 1.00 g of Pd/C, and the mixture was stirred at room temperature for 3 hours. The crude was filtered over celite and the solvent removed obtaining the product with a yield of 95%.

^{1}H-NMR ($CDCl_3$, 298K, 400 MHz, δ, ppm): 6.74 (d, J=8.8 Hz, 2H), 6.63 (d, J=8.8Hz, 2H), 3.87 (t, J=6.6 Hz, 2H), 3.40 (s, 2H), 1.74 (q, J=7.9 Hz, 2H), 1.50-1.20 (m, 10H), 0.88 (t, J=6.9 Hz, 3H).

^{13}C-NMR ($CDCl_3$, 298K, 100 MHz, δ, ppm): 152.49, 139.94, 116.55, 115.80, 68.86, 31.96, 29.58, 29.53, 29.39, 26.21, 22.80, 14.24.

Synthesis of **HO-AzoC_8 (12):** over a solution of 4-(octyloxy)aniline **(11)** (1.30 g, 5.87 mmol) in THF/H_2O/HCl (50 ml/50 ml/10 ml) was slowly added an aqueous solution of $NaNO_2$ (0.77 g, 11.15 mmol) at 0^{o}C. The mixture was stirred 30 minutes at 0^{o}C and a solution of phenol (0.60 g, 6.45 mmol) in aqueous NaOH (2M, 20ml) was added. The mixture was kept at pH 9-10 for 10 hours at room temperature. After that time, it was neutralized with HCl (10%), obtaining a biphase. The organic phase was extracted, dried with $MgSO_4$, filtered and the solvent removed. The crude was purified by column chromatography in dichloromethane obtaining the product with a yield of 62%.

^{1}H-NMR ($CDCl_3$, 298K, 400 MHz, δ, ppm): 7.85 (m, 4H), 6.99 (m, 2H), 6.93 (m, 2H), 5.11 (s, 1H), 4.03 (t, J=6.5 Hz, 2H), 1.81 (q, J=7.9 Hz, 2H), 1.52-1.24 (m, 10H), 0.89 (t, J=7.0 Hz, 3H).

^{13}C-NMR ($CDCl_3$, 298K, 100 MHz, δ, ppm): 161.37, 158.13, 147.28, 146.99, 124.66, 124.47, 115.89, 114.82, 68.49, 31.95, 31.09, 29.49, 29.37, 29.35, 26.17, 22.80, 14.24.

Synthesis of **Br-AzoC_8 (2):** in a flask were dissolved **HO-AzoC_8 (13)** (1.00 g, 3.06 mmol), triphenylphosphine (1.00 g, 3.83 mmol) and 2-bromoethanol (0.48 g, 3.83 mmol) in THF (40 ml) under argon atmosphere. Finally, was slowly added DIAD (0.77 g, 3.83 mmol) and let react 24 hours. The salts were filtered and the solvent removed. The product was purified by column chromatography in an eluent mix of dichloromethane 6:4 hexane with a yield of 91%.

^{1}H-NMR ($CDCl_3$, 298K, 400 MHz, δ, ppm): 7.87 (m ,4H), 7.00 (m, 4H), 4.37 (t, J=6.3 Hz, 2H), 4.03 (t, J=6.6 Hz, 2H), 3.67 (t, J=6.3 Hz, 2H), 1.82 (q, J=8.0 Hz, 2H), 1.52-1.24 (m, 10H), 0.89 (t, J=7.0 Hz, 3H).

^{13}C-NMR ($CDCl_3$, 298K, 100 MHz, δ, ppm): 161.49, 160.03, 147.68, 146.99, 124.55, 124.49, 115.02, 114.82, 68.49, 68.14, 31.95, 29.49, 29.37, 29.35, 28.95, 26.17, 22.80, 14.24.

4.5.2.2 *Synthesis and characterization of the dendrons* ***dCouAzoCN (7)*** *and* ***dCouAzoC$_8$ (8)*** *(see Scheme 4.1 in section 4.3.1)*

4.5.2.2.1 *Synthesis and characterization of the dendron* ***dCouAzoCN (7)***

Synthesis of **MedOHAzoCN (3):** in a two-neck flask were dissolved methyl gallate (8.37 g, 45.40 mmol), potassium hydrogen carbonate (4.54 g, 45.40 mmol) and potassium iodide (spatula tip) under argon atmosphere in a mix of DMF/Acetone (40/10 ml). The mixture was vigorously stirred at 80°C and finally **Br-AzoCN (1)** was added (1.50 g, 4.54 mmol) and let react overnight. The crude was let cool down and was precipitated in 100 ml of H_2O. It was extracted with ethyl acetate (3x100 ml), dried with $MgSO_4$, filtered and the solvent evaporated. The product was purified by recrystallization in ethanol with a yield of 70%.

^{1}H-NMR (DMSO-d$_6$, 298K, 400 MHz, δ, ppm): 9.49 (s, 2H), 8.05 (m, 2H), 7.96 (m, 4H), 7.17 (m, 2H), 6.97 (s, 2H), 4.39 (m, 4H), 3.78 (s, 3H).

^{13}C-NMR (DMSO-d$_6$, 298K, 100 MHz, δ, ppm): 166.01, 162.24, 154.19, 150.66, 146.18, 138.59, 133.77, 125.29, 122.90, 115.34, 108.50, 70.18, 67.94, 51.93.

Synthesis of **MedCouAzoCN (5):** in a two-neck flask was dissolved **MedOHAzoCN (3)** (2.00 g, 4.61 mmol) in dry DMF (20 ml) and then potassium carbonate was added (1.91 g, 13.83 mmol) under argon atmosphere. The mixture was stirred at 80°C and finally **CouC$_{11}$Br (13)** (1.10g, 2.79 mmol) and a spatula tip of KI were added to the reaction. After 16 hours, the crude was let cool down and was precipitated in 200 ml of H_2O. It was extracted with ethyl acetate (3x100 ml), dried with $MgSO_4$, filtered and the solvent evaporated. The product was

purified by flash column chromatography in dichloromethane with a yield of 92%.

^{1}H-NMR ($CDCl_3$, 298K, 400 MHz, δ, ppm): 7.93 (m, 4H), 7.77 (m, 2H), 7.63 (d, J=9.4 Hz, 2H), 7.33 (m, 4H), 7.02 (m, 2H), 6.80 (m, 4H), 6.24 (d, J=9.5 Hz, 2H), 4.47 (m, 2H), 4.38 (m, 2H), 3.99 (m, 8H), 3.89 (s, 3H), 1.77 (m, 8H), 1.43 (m, 8H), 1.36-1.20 (m, 20H).

^{13}C-NMR ($CDCl_3$, 298K, 100 MHz, δ, ppm): 165.91, 162.54, 162.49, 159.38, 157.12, 154.85, 152.81, 147.04, 144.51, 142.44, 132.61, 128.84, 125.56, 124.81, 123.21, 118.73, 114.75, 113.42, 113.13, 111.81, 111.17, 109.46 104.12, 71.20, 69.37, 68.78, 68.18, 51.51, 29.67, 29.63, 29.49, 29.44, 29.35, 29.08, 26.14, 25.98.

Synthesis of **dCouAzoCN (7):** Over a solution of **MedCouAzoCN (5)** (2.00 g, 1.87 mmol) in THF (50 ml) at 60ºC was added a solution of LiOH (210 mg, 8.79 mmol) in water (20 ml). The mixture was stirred overnight at 60ºC and then poured in a solution of HCl/H_2O 4M, obtaining an orange solid. The crude was purified by flash column chromatography using dichloromethane as eluent and then recrystallized in methanol with a yield of 85%.

^{1}H-NMR ($CDCl_3$, 298K, 400 MHz, δ, ppm): 7.93 (m, 4H), 7.77 (m, 2H), 7.63 (d, J=9.4 Hz, 2H), 7.33 (m, 4H), 7.02 (m, 2H), 6.80 (m, 4H), 6.24 (d, J=9.5 Hz, 2H), 4.47 (m, 2H), 4.38 (m, 2H), 3.99 (m, 8H), 1.77 (m, 8H), 1.43 (m, 8H), 1.36-1.20 (m, 20H).

^{13}C-NMR ($CDCl_3$, 298K, 100 MHz, δ, ppm): 170.66, 162.54, 162.49, 161.49, 156.05, 154.85, 152.81, 147.04, 143.62, 142.44, 133.29, 128.84, 125.56, 124.41, 123.21, 118.73, 115.11, 113.37, 113.13, 113.06, 112.51, 108.47, 101.44, 71.20, 69.37, 68.78, 68.18, 29.67, 29.63, 29.49, 29.44, 29.35, 29.08, 26.14, 26.07.

FT-IR (KBr, ν: cm^{-1}): 3447 (OH), 2926 (-C=C-H), 2842 (-C-C-H), 2226 (CN), 1729 (C=O), 1685 (C=O), 1613 (C=C), 1503 (C=C), 1231 (C-O), 1128 (C-O).

MS (MALDI$^+$, dithranol, m/z): found 1071.5 [M+Na$^+$] calculated with sodium 1071.18 (1048.20+22.98).

*4.5.2.2.2 Synthesis and characterization of the dendron **dCouAzoC$_8$ (8)***

Synthesis of **MedOHAzoC$_8$ (4)**: in a flask were dissolved methyl gallate (4.25 g, 23.07 mmol), potassium hydrogen carbonate (2.31 g, 23.07 mmol) and a spatula tip of potassium iodide under argon atmosphere in a mix of DMF/Acetone (30/10 ml) at 80^{o}C and the mixture was stirred vigorously. Finally, was added compound **AzoC$_8$ (2)** (1.00g, 2.31 mmol) and let react overnight. Once the reaction was completed, it was let cool down and the salts were filtered over celite. The solution was dissolved in a mix of ethyl acetate/hexane (50/50 ml) and extracted with water (5x100 ml), dried with $MgSO_4$, filtered and the solvent removed in vacuum. The crude product was purified by column chromatography on silica gel with an eluent mix of dichloromethane 8/2 hexane with a yield of 64%.

^{1}H-NMR (CD_2Cl_2, 298K, 400 MHz, δ, ppm): 7.91 (m, 2H), 7.87 (m, 2H), 7.19 (s, 2H), 7.12 (m, 2H), 7.00 (m, 2H), 6.34 (s, 2H), 4.42 (m, 4H), 4.05 (t, J=6.6 Hz, 2H), 3.86 (s, 3H), 1.82 (q, J=7.8 Hz 2H), 1.48 ppm (q, J=8 Hz, 2H), 1.32 (m, 8H), 0.90 (t, J=6.9 Hz, 3H).

^{13}C-NMR (CD_2Cl_2, 298K, 100 MHz, δ, ppm): 166.83, 162.19, 160.02, 150.01, 148.47, 147.33, 138.04, 127.75, 124.98, 124.94, 115.43, 115.27, 109.97, 73.31, 69.05, 67.95, 52.63, 32.41, 29.92, 29.82, 29.78, 26.57, 23.25, 14.44.

Synthesis of **MedCouAzoC$_8$ (6):** In a flask were dissolved **MedOHAzoC$_8$ (4)** (0.6 g, 1.12 mmol), potassium carbonate (0.46 g, 3.35 mmol) and a spatula tip of potassium iodide in DMF (20 ml) under argon atmosphere. The compound **CouC$_{11}$Br (13)** (1.10g, 2.79 mmol) was added to the solution and let react at 80^{o}C overnight. The mixture was precipitated in 100 ml of H_2O and extracted with ethyl acetate (3x50 ml). The organic phase was dried with $MgSO_4$, filtered and the solvent evaporated. The crude was purified by column chromatography on silica gel with dichloromethane as eluent with a yield of 92%.

^{1}H-NMR (CD_2Cl_2, 298K, 400 MHz, δ, ppm): 7.86 (m, 4H), 7.63 (d, J=9.5 Hz, 2H), 7.36 (d, J=8.5 Hz, 2H), 7.27 (s, 2H), 6.99 (m, 4H), 6.78 (m, 4H), 6.18 (d, J=9.5 Hz, 2H), 4.38 (dt, J=5 Hz, 4H), 3.99 (m, 10H), 3.87 (s, 3H), 1.77 (q, J=7.8 Hz, 10H), 1.50-1.20 (m, 40H), 0.89 (t, J=7 Hz, 3H)

^{13}C-NMR (CD_2Cl_2, 298K, 100 MHz, δ, ppm): 167.15, 163.02, 161.93, 161.43, 156.55, 153.25, 147.66, 147.37, 143.93, 142.07, 129.32, 125.98, 124.81, 124.79, 115.27, 115.19, 113.37, 113.28, 112.95, 108.07, 101.77, 71.78, 69.75, 69.31, 68.98, 68.62, 52.56, 32.40, 30.13, 30.10, 29.95, 29.92, 29.90, 29.85, 29.82, 29.78, 29.56, 26.61, 26.57, 26.48, 23.24, 14.44.

Synthesis of **dCouAzoC$_8$ (8):** Over a solution of **MedCouAzoC$_8$ (6)** (0.40 g, 0.34 mmol) in THF (10 ml) at 60^{o}C, was added a solution of LiOH (41 mg, 1.17 mmol) in water (5 ml), and the mixture was stirred overnight. The crude was precipitated in a solution of HCl/H_2O 4M, obtaining an orange solid. The solid obtained was filtered and recrystallized in methanol obtaining an orange solid with a yield of 82%.

^{1}H-NMR (DMSO-d$_6$, 298K, 400 MHz, δ, ppm): 7.96 (d, J=9.5 Hz, 2H), 7.80 (m, 4H), 7.58 (d, J=8.5 Hz, 2H), 7.19 (s, 2H), 7.01 (m, 4H), 6.68 (m, 4H), 6.26 (d, J=9.5 Hz, 2H), 4.31 (s, 4H), 3.95 (m, 10H), 1.64 (m, 8H), 1.22 (m, 40H), 0.84 (t, J=7 Hz, 3H).

^{13}C-NMR (DMSO-d$_6$, 298K, 100 MHz, δ, ppm): 163.86, 161.87, 160.28, 155.41, 152.10, 144.30, 129.41, 124.06, 114.82, 114.78, 112.64, 112.20, 110.48, 107.31, 101.04, 68.49, 68.32, 68.24, 67.86 31.23, 29.01, 28.83, 28.77, 28.74, 28.65, 28.59, 28.44, 25.50, 25.40, 22.07, 13.94.

FT-IR (KBr, ν: cm^{-1}): 3369 (OH), 2921 (-C=C-H), 2854 (C-C-H), 1742 (C=O), 1677 (C=O), 1618 (C=C), 1511 (C=C), 1239 (C-O), 1125 (C-O).

MS (MALDI^{+}, dithranol, m/z): found 1173.5 [M+Na^{+}] calculated with sodium 1174.38 (1151.4+22.98).

4.5.2.3 Synthesis and characterization of the planar aromatic heterocyclic templates

*4.5.2.3.1 Synthesis and characterization of **N-dodecylmelamine (M)***

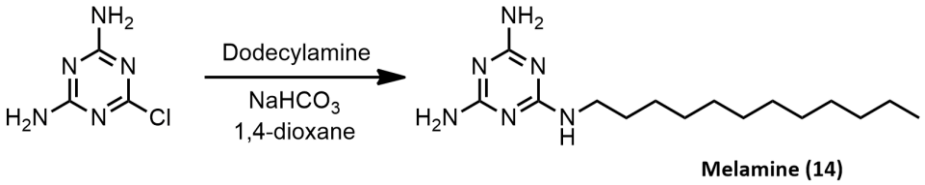

***Scheme 4.3**. Synthetic route of N-dodecylmelamine (**M**).*

Synthesis of **N-dodecylmelamine (14)**: A mixture of 2,4-diamino-6-chloro-1,3,5-triazine (2.77 g, 19 mmol), dodecylamine (3.52 g, 19 mmol) and sodium hydrogen carbonate (1.60 g, 19 mmol) was dissolved in 1,4-dioxane (75 ml). The mixture was stirred under argon atmosphere for 6h at reflux. The reaction was poured into water and the precipitate was filtered off and washed with water. The crude was purified by flash column chromatography on silica gel using DCM/MeOH (10:1) as eluent. Finally, the product was recrystallized in ethanol with a yield of 53%.

^{1}H-NMR (CD_2Cl_2, 298K, 400 MHz, δ, ppm): 4.88 (m, 5H), 3.30 (m, 2H), 1.51 (m, 2H), 1.44-1.20 (m, 18H), 0.8 (t, J=6.7 Hz, 3H).

^{13}C-NMR (CD_2Cl_2, 298K, 100 MHz, δ, ppm): 167.39, 41.06, 32.52, 30.39, 30.21, 29.96, 27.51, 23.28, 14.45.

FT-IR (KBr, *v*, cm^{-1}): 3495, 3440, 3330 (N-H), 1665 (C=C).

MS (ESI^+, m/z): found 295.26 [$M+H^+$] calculated 294.44.

4.5.2.3.2 *Synthesis of* ***2,4,6-tris(1-(4-butoxyphenyl)-1H-1,2,3-triazol-4-yl)-1,3,5-triazine (TTT)***

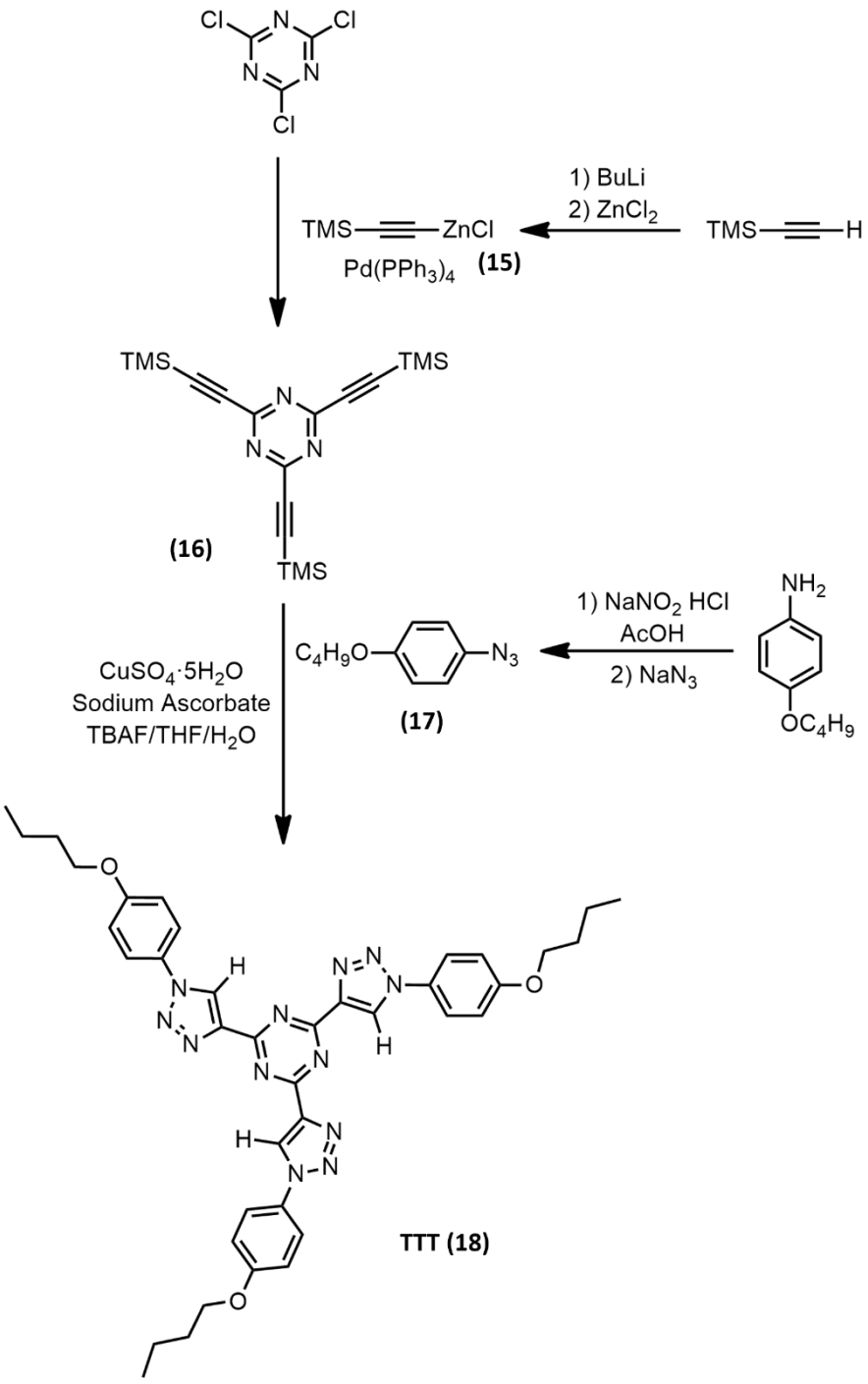

Scheme 4.4. *Synthetic procedure of tris(triazolyl)triazine (**TTT**).*

Synthesis of **(trimethylsilyl)ethynyl zinc chloride (15)**: (trimethylsilyl)acetylene (12.5 ml, 86.5 mmol) was dissolved in anhydrous THF (50 ml) at -78ºC in a Schlenk flask. Then, butyllithium (34.6 ml, 86.5 mmol) dissolved in THF (2.5 M) was added dropwise to the mixture and it was stirred at -78ºC for 30 minutes. After that, a solution of anhydrous zinc chloride (12 g, 86.5 mmol) in THF (60 ml) was added carefully. The mixture was slowly warmed to room temperature and used in the following reaction without further purification.

Synthesis of **2,4,6-tris((trimethylsilyl)ethynyl)-1,3,5-triazine (16)**: the previous solution of **15** (86.5 mmol) was added dropwise to a mixture of cyanuric chloride (3.22 g, 17.3 mmol) and $Pd(PPh_3)_4$ (1.01 g, 0.87 mmol) in anhydrous THF (40 ml) and the mixture was stirred at room temperature for 3h. The crude was poured into HCl 1M (aq.) (175 ml) and extracted three times with ether. The combined organic phases were dried over anhydrous magnesium sulfate. The solution was filtered and the solvent was removed under vacuum. The crude product was recrystallized in methanol with a yield of 53%.

^{1}H-NMR ($CDCl_3$, 298K, 400 MHz, δ, ppm): 0.27 (s, 27H).

^{13}C-NMR ($CDCl_3$, 298K, 100 MHz, δ, ppm): 159.72, 102.21,100.50, -0.83.

FT-IR (KBr, *ν*, cm^{-1}): 2169 (C≡C), 1480 (C=N Ar).

Synthesis of **1-azido-4-butoxybenzene (17)**: a mixture of 4-butoxyaniline (2.6 ml, 15.1 mmol), water (40 ml), glacial acetic acid (90 ml) and concentrated HCl (8 ml) was cooled in an ice bath. Sodium nitrite (9 ml, 2M) was added dropwise to the mixture and it was stirred in the ice bath. Then, a solution of sodium azide (1.10 g, 16.9 mmol) in water (10 ml) was slowly added. The mixture was stirred at 0ºC for 90 minutes and then it was extracted twice with DCM. The combined organic phases were washed twice with sodium hydroxide 10% (aq.), with brine and dried over anhydrous magnesium sulfate. The product was purified by flash chromatography on silica gel using hexane as eluent. Yield: 89%.

^{1}H-NMR ($CDCl_3$, 298K, 400 MHz, δ, ppm): 6.98 (m, 2H), 6.88 (m, 2H), 3.95 (t, J=7.0 Hz, 2H), 1.77 (m, 2H), 1.50-1.40 (m, 2H), 0.97 (t, J=7.0 Hz, 3H).

^{13}C-NMR ($CDCl_3$, 298K, 100 MHz, δ, ppm): 156.72, 132.18, 120.10, 116.20, 68.23, 31.44, 19.41, 14.01.

FT-IR (KBr, *v*, cm^{-1}): 2111 (N_3), 1504 (C=C), 1230 (C-O), 1011 (C-O).

Synthesis of **2,4,6-tris(1-(4-butoxyphenyl)-1,2,3-triazol-4-yl)-1,3,5-triazine (18):** a Schlenk flask was charged with compound **17** (1.00 g, 2.71 mmol), 1-azido-4-butoxybenzene **(17)** (1.61 g, 8.41 mmol), sodium ascorbate (0.16 g, 0.82 mmol), copper (II) sulfate pentahydrate (0.10 g, 0.39 mmol) and THF/H_2O (1:1, 35 ml). The reaction was degassed by three freeze-pump-thaw cycles and flushed with argon. The reaction mixture was stirred at room temperature for 5 minutes and then tetrabutylammonium fluoride (1M in THF, 8.40 ml) was added. The reaction was stirred at room temperature in the dark overnight. Then, the crude was poured into water and extracted with DCM. The combined organic phases were dried over anhydrous magnesium sulfate and the solvent was removed under vacuum. The crude was purified by flash chromatography on silica gel with DCM as eluent. Finally, the product was recrystallized in ethanol with a yield of 42%.

^{1}H-NMR (CD_2Cl_2, 298K, 400 MHz, δ, ppm): 8.86 (s, 3H), 7.61 (m, 6H), 6.95 (m, 6H), 3.97 (t, J=7.0 Hz, 6H), 1.78 (m, 6H), 1.55-1.46 (m, 6H), 1.00 (t, J=7.0 Hz, 9H).

^{13}C-NMR (CD_2Cl_2, 298K, 100 MHz, δ, ppm): 167.26, 160.40, 146.22, 130.14, 126.04, 122.60, 115.81, 68.70, 31.62, 19.62, 14.01.

FT-IR (KBr, *v*, cm^{-1}): 1611 (C=N), 1566 (C=C), 1513 (C=C), 1247 (C-O), 1169 (C-O).

MS (MALDI$^+$, dithranol, m/z): found 749.5 [M+Na^+] calculated with sodium 749.38 (726.40+22.98).

4.5.2.3.3 *Synthesis and characterization of* ***N2,N5,N8-tris(4-(octyloxy)phenyl)-1,3,3a[1],4,6,7,9-heptaazaphenalene-2,5,8-triamine (Hpz)***

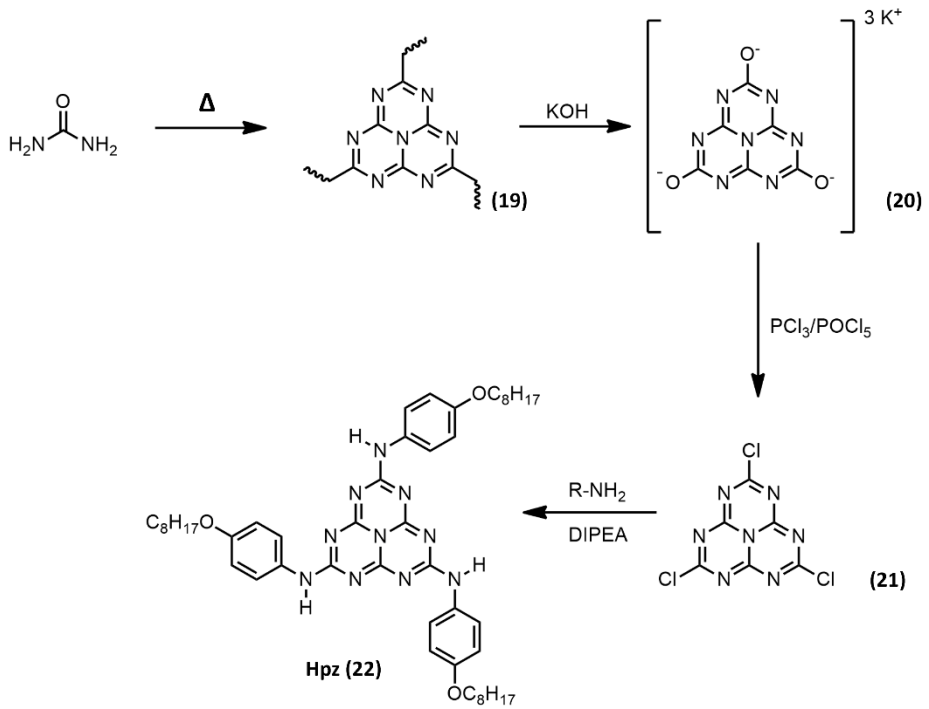

Scheme 4.5*. Synthetic procedure of Heptazine (**Hpz**).*

Synthesis of **heptazine polymer (19):** a melting pot was charged with urea (25.00 g, 416.25 mmol) and it was dried under vacuum at 80°C for 24 hours. Then it was introduced in a Muffle Furnace and heated to 550°C for 3 hours to complete the reaction, obtaining a yellow solid.

Synthesis of **potassium heptaazaphenalene (20):** the yellow solid **(19)** was dissolved in 100 ml of KOH (2.5M) and heated under reflux for 5 hours. The solution was filtered and then poured in EtOH obtaining a solid that was filtered.

Synthesis of **trichloroheptaazaphenalene (21):** the potassium salt of heptaazaphenalene **(20)** (1.00 g, 3.63 mmol), PCl_5 (2.27 g, 10.89 mmol) and $POCl_3$ (29.49 g, 192.39 mmol) were heated at 110°C.

Synthesis of **Hpz (22)**: trichloro heptaazaphenalene **(21)** (0.12 g, 0.45 mmol) was dissolved in 10 ml of dry THF, then 4-octyloxyaniline was added to the solution dropwise (0.33 g, 1.80 mmol) and DIPEA (0.2 g, 1.57 mmol) was finally added. The mixture was stirred overnight, then was washed with methanol several times and filtered obtaining a solid.

^{1}H-NMR (CD_2Cl_2, 298K, 400 MHz, δ, ppm): 7.71 (m, 3H), 7.41 (m, 6H), 6.85 (m, 6H), 3.92 (t, J=6.4 Hz, 6H), 1.76 (m, 6H), 1.50-1.22 (m, 30H), 0.89 (t, J=6.7 Hz, 9H).

^{13}C-NMR (CD_2Cl_2, 298K, 100 MHz, δ, ppm): 157.28, 145.14, 130.48, 123.95, 114.94, 68.85, 32.45, 30.03, 29.91, 26.71, 26.63, 26.58, 23.26, 14.46

FT-IR (KBr, *ν*, cm^{-1}): 3339 (N-H), 3148 (N-H), 2918 (C=C-H), 2846 (C-C-H), 1638 (C=N), 1541 (C=C), 1513 (C=C), 1440 (C=C).

MS (MALDI^{+}, dithranol, m/z): found 853.51 [M+Na^{+}] calculated with sodium 854.08 (831.10+22.98).

4.5.2.4 *Preparation and characterization of supramolecular complexes*

All supramolecular complexes were prepared dissolving the corresponding acid and template in dichloromethane in a molar proportion of 3:1. Then, the solvent was slowly evaporated under agitation and the resulting solid was melted before using.

M-dCouAzoCN

^{1}H-NMR (CD_2Cl_2, 298K, 400 MHz, δ, ppm): 7.95 (m, 12H), 7.78 (m, 6H), 7.64 (d, J=9.5 Hz, 6H), 7.37 (d, J=8.6 Hz, 6H), 7.32 (s, 6H), 7.03 (m, 6H), 6.80 (m, 12H), 6.22 (s, 2H), 6.18 (d, J=9.5 Hz, 6H), 5.98 (s, 2H), 4.43 (m, 6H), 4.37 (m, 6H), 3.98 (m, 24H), 3.37 (m, 2H), 1.75 (m, 24H), 1.53-1.21 (m, 120 H), 0.87 (t, J=7.0 Hz, 3H).

^{13}C-NMR (CD_2Cl_2, 298K, 100 MHz, δ, ppm): 170.50, 164.13, 163.02, 161.53, 156.55, 155.32, 153.24, 147.51, 143.99, 142.25, 133.80, 129.35, 126.26, 125.95, 123.57, 115.54, 113.87, 113.40, 113.31,

112.99, 108.51, 101.79, 71.71, 69.78, 69.32, 68.83, 41.40, 32.50, 30.23, 30.11, 30.08, 29.94, 29.88, 29.55, 26.61, 26.47, 23.27, 14.46.

FT-IR (KBr, ν: cm^{-1}): 3453 (OH), 2927 (C=C-H), 2855 (C-C-H), 2227 (CN), 1731 (C=O), 1709 (C=O), 1615 (C=C), 1552 (C=C), 1228 (C-O), 1120 (C-O).

TTT-dCouAzoCN

^{1}H-NMR (CD_2Cl_2, 298K, 400 MHz, δ, ppm): 9.05 (s, 3H), 7.95 (m, 12H), 7.78 (m, 12H), 7.64 (d, J=9.5 Hz, 6H), 7.37 (d, J=8.5 Hz, 6H), 7.33 (s, 6H), 7.09 (d, J=9.0 Hz, 6H), 7.03 (d, J=9.0 Hz, 6H), 6.80 (m, 12H), 6.18 (d, J=9.5 Hz, 6H), 4.45 (m, 6H), 4.37 (m, 6H), 4.06 (t, J=6.6 Hz, 6H), 3.99 (m, 24H), 1.85-1.71 (m, 30H), 1.58-1.24 (m, 90H), 1.01 (t, J=7.4 Hz, 9H).

^{13}C-NMR (CD_2Cl_2, 298K, 100 MHz, δ, ppm): 169.74, 167.40, 163.00, 162.96, 161.55, 160.55, 156.51, 155.28, 153.32, 147.48, 146.37, 144.00, 142.63, 133.78, 130.29, 129.34, 126.24, 125.94, 123.55, 122.78, 119.09, 115.96, 115.50, 113.84, 113.36, 113.30, 112.96, 101.75, 71.71, 69.77, 69.30, 68.85, 68.82, 31.77, 30.09, 30.06, 29.92, 29.86, 29.80, 29.52, 26.57, 26.45, 19.77, 14.18.

FT-IR (KBr, ν: cm^{-1}): 3363 (OH), 2932 (C=C-H), 2854 (C-C-H), 2226 (CN), 1735 (C=O), 1718 (C=O), 1615 (C=C), 1511 (C=C), 1255 (C-O), 1121 (C-O).

Hpz-dCouAzoCN

^{1}H-NMR (CD_2Cl_2, 298K, 400 MHz, δ, ppm): 8.65 (s, 1H), 8.51 (s, 1H), 8.43 (s, 1H), 7.94 (m, 12H), 7.77 (m, 6H), 7.63 (d, J=9.5 Hz, 6H), 7.45 (m, 6H), 7.35 (m, 12H), 7.03 (m, 6H), 6.90 (m, 6H), 6.80 (m, 12H), 6.18 (d, J=9.5 Hz, 6H) 4.45 (m, 6H), 4.37 (m, 6H), 3.98 (m, 30H), 1.76 (m, 30H), 1.50-1.22 (m, 114), 0.89 (m, 9H).

^{13}C-NMR (CD_2Cl_2, 298K, 100 MHz, δ, ppm): 169.28, 163.02, 162.63, 161.55, 156.99, 156.95, 156.54, 153.30, 147.51, 146.82, 144.00, 133.80, 133.20, 129.92, 129.35, 125.96, 124.13, 123.69, 123.57, 115.54, 115.35, 115.18, 114.52, 113.87, 113.39, 113.32, 112.99,

108.64, 101.79, 71.73, 69.84, 69.33, 68.95, 68.84, 32.43, 30.10, 30.07, 29.99, 29.95, 29.87, 29.55, 26.60, 26.47, 23.25, 14.45.

FT-IR (KBr, ν: cm^{-1}): 3441 (OH), 2926 (C=C-H), 2847 (C-C-H), 2228 (CN), 1738 (C=O), 1711 (C=O), 1614 (C=C), 1507 (C=C), 1234 (C-O), 1127 (C-O).

M-dCouAzoC$_8$

^{1}H-NMR (CD_2Cl_2, 298K, 400 MHz, δ, ppm): 7.85 (m, 12H), 7.63 (d, J= Hz, 6H), 7.36 (d, J=Hz, 6H), 7.32 (s, 6H), 6.99 (m, 12H), 6.82 (m, 12H), 6.25 (s, 1H), 6.18 (d, J= Hz, 6H), 6.01 (s, 2H), 4.37 (m, 12H), 3.99 (m, 30H), 3.37 (m, 2H), 1.77 (m, 34H), 1.52-1.21 (m, 140 H), 0.89 (m, 12H).

^{13}C-NMR (CD_2Cl_2, 298K, 100 MHz, δ, ppm): 170.49, 164.31, 163.05, 161.95, 161.53, 161.45, 156.55, 153.26, 147.68, 147.39, 143.99, 129.34, 126.10, 124.80, 115.29, 115.21, 113.32, 112.97, 108.53, 101.80, 71.81, 69.78, 69.34, 69.00, 68.63, 41.39, 32.51, 32.40, 30.21, 30.09, 29.94, 29.89, 29.83, 29.80, 29.56, 26.62, 26.58, 26.48, 23.24, 14.44.

FT-IR (KBr, ν: cm^{-1}): 3423 (OH), 2925 (C=C-H), 2846 (C-C-H), 1748 (C=O), 1712 (C=O), 1614 (C=C), 1502 (C=C), 1238 (C-O), 1121 (C-O).

TTT-dCouAzoC$_8$

^{1}H-NMR (CD_2Cl_2, 298K, 400 MHz, δ, ppm): 9.05 (s, 3H), 7.82 (m, 12H), 7.78 (d, J=9.0 Hz, 6H), 7.63 (d, J=9.5 Hz, 6H), 7.34 (m, 12H), 7.09 (d, J=9.0 Hz, 6H), 6.98 (m, 12H), 6.80 (m, 12H), 6.18 (d, J=9.5 Hz, 6H), 4.44 (m, 6H), 4.36 (m, 6H), 4.00 (m, 36H), 1.77 (m, 36H), 1.62-1.21 (m, 120H), 1.01 (t, J=7.4 Hz, 9H), 0.89 (t, J=6.9 Hz, 9H).

^{13}C-NMR (CD_2Cl_2, 298K, 100 MHz, δ, ppm): 169.74, 167.45, 163.05, 161.96, 161.56, 161.42, 160.59, 156.55, 153.35, 147.69, 147.39, 145.80, 144.00, 142.78, 130.33, 129.34, 126.24, 125.55, 124.82, 124.80, 122.81, 116.00, 115.29, 115.21, 113.36, 113.33, 112.97, 101.80, 71.84, 69.83, 69.34, 69.01, 68.89, 68.64, 32.41, 31.79, 30.10, 30.08, 29.93, 29.82, 29.55, 26.60, 26.47, 23.24, 19.79, 14.18.

FT-IR (KBr, ν: cm^{-1}): 3445 (OH), 2924 (C=C-H), 2847 (C-C-H), 1749 (C=O), 1695 (C=O), 1611 (C=C), 1516 (C=C), 1251 (C-O), 1123 (C-O).

Hpz-dCouAzoC_8

^{1}H-NMR (CD_2Cl_2, 298K, 400 MHz, δ, ppm): 9.11 (s, 1H), 8.90 (s, 1H), 8.75 (s, 1H), 7.85 (m, 12H), 7.62 (m, 10H), 7.35 (m, 12H), 6.98 (m, 12H), 6.89 (m, 6H), 6.80 (m, 12H), 6.18 (d, J=9.5 Hz, 6H), 4.44 (m, 6H), 4.36 (m, 6H), 4.00 (m, 36H), 1.77 (m, 36H), 1.52-1.21 (m, 144H), 0.89 (m, 18H).

^{13}C-NMR (CD_2Cl_2, 298K, 100 MHz, δ, ppm): 170.52, 163.03, 161.94, 161.52, 161.43, 156.96, 156.53, 153.31, 147.68, 147.37, 143.97, 142.71, 130.53, 129.98, 129.32, 125.33, 124.81, 122.22, 115.28, 115.19, 115.10, 114.43, 113.36, 113.31, 112.96, 108.67, 101.77, 71.84, 69.85, 69.33, 68.99, 68.91, 68.64, 32.40, 30.13, 30.09, 29.97, 29.82, 29.79, 29.55, 26.63, 26.57, 26.47, 23.24, 14.46, 14.44.

FT-IR (KBr, ν: cm^{-1}): 3445 (OH), 2931 (C=C-H), 2846 (C-C-H), 1738 (C=O), 1694 (C=O), 1610 (C=C), 1499 (C=C), 1229 (C-O), 1114 (C-O).

4.5.3 Experimental procedures

4.5.3.1 Preparation of the chiral nanoporous membranes

Liquid crystal polymers were prepared by sandwiching 2 mg of product between two glasses that were previously spin-coated (1500 rpm, 30s) with a solution of poly(vinyl alcohol) (1% in water) with spacers of 10 µm. The sandwich was heated above isotropization temperature and let slowly cool down until room temperature. After that, it was irradiated with 325 nm LED for 180 min and introduced in hot water until PVA was dissolved, obtaining the corresponding self-standing polymeric material.

To remove the template molecules, the polymeric material was immersed in a solution of HCl/Ethanol 3M for 24 hours in the case of **melamine** and **TTT**. For **heptazine** stronger conditions were necessary,

using DMSO (1%) HCl/EtOH (3M). Finally, the nanoporous materials were washed with water and dried under vacuum before using.

4.5.3.2 *Adsorption experiments*

A piece of 2 mg of the nanoporous material was immersed in a solution (0.6 ml) of the corresponding molecule that was previously studied by UV spectroscopy with a maximum absorbance of 1. Then the adsorption process was followed by UV monitoring the changes. In the case of the chiral selective experiments the vial with the membrane and the solution was protected from the light.

4.6 Appendix

4.6.1 NMR spectra

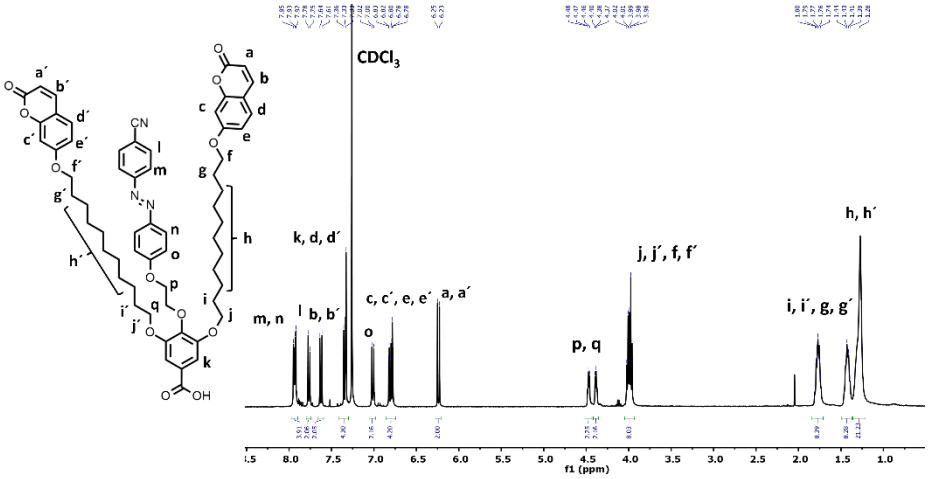

*Figure 4.44. [1]H-NMR spectrum of **dCouAzoCN**, $CDCl_3$, 298K, 400 MHz.*

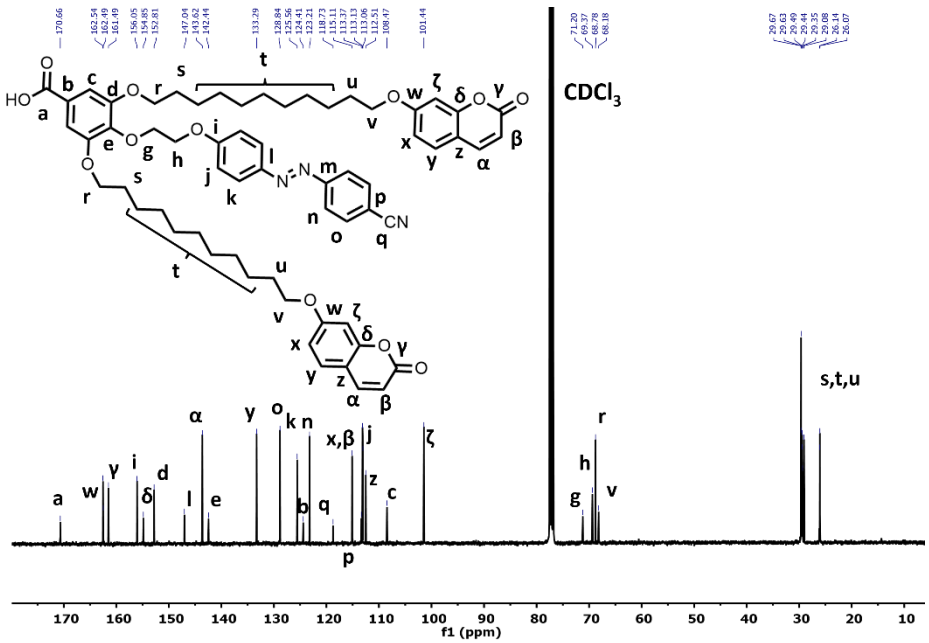

*Figure 4.45. [13]C-NMR spectrum of **dCouAzoCN**, $CDCl_3$, 298K, 100 MHz.*

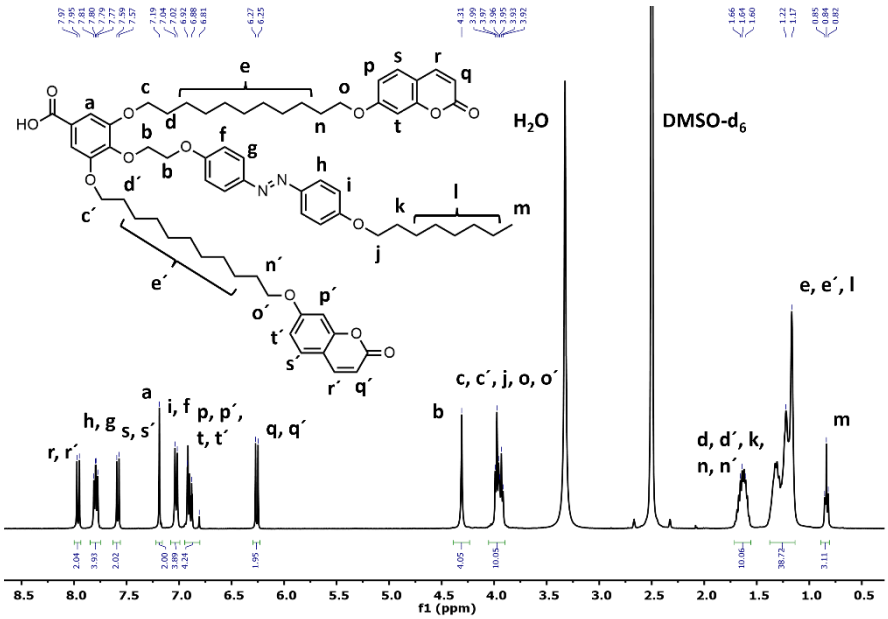

Figure 4.46. *^{1}H-NMR spectrum of **dCouAzoC$_8$**, DMSO-d$_6$, 298K, 400 MHz.*

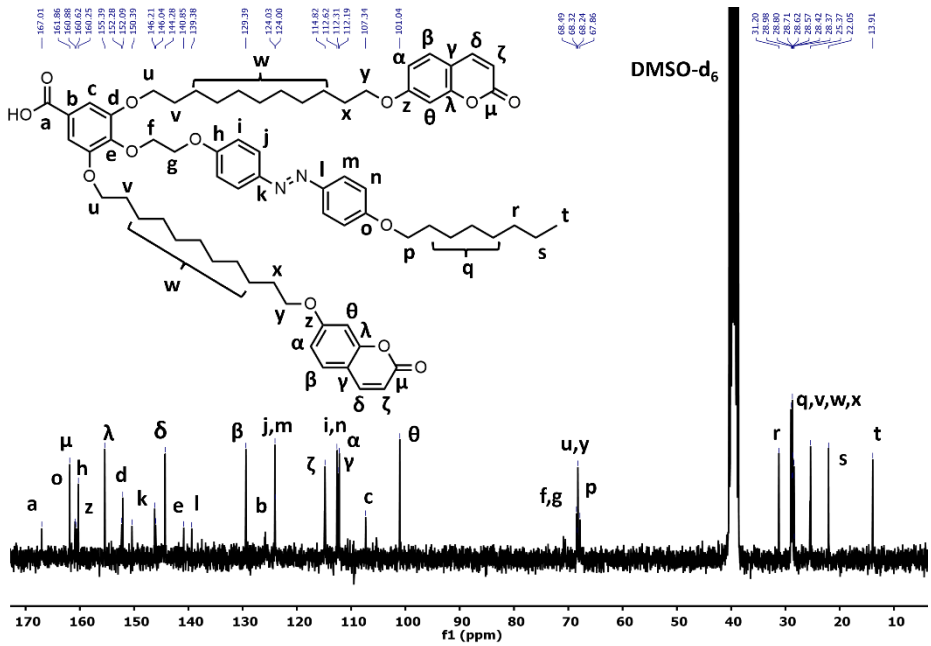

Figure 4.47. *^{13}C-NMR spectrum of **dCouAzoC$_8$**, DMSO-d$_6$, 298K, 100 MHz.*

4.6.2 Mass spectrometry spectra

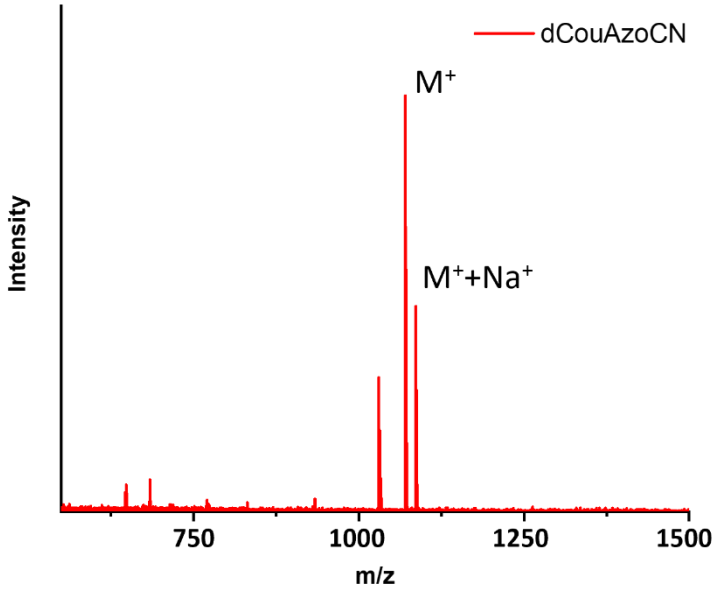

Figure 4.48. *MALDI spectrum of* ***dCouAzoCN*** *(matrix dithranol).*

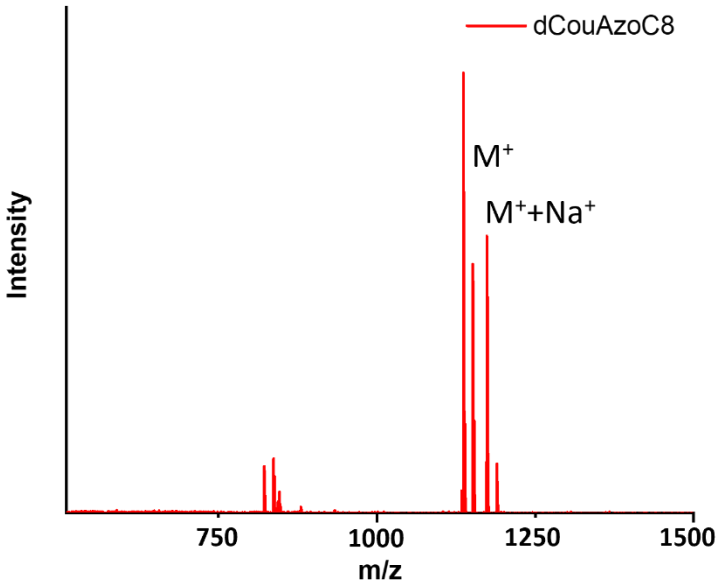

Figure 4.49. *MALDI spectrum of* ***dCouAzoC$_8$*** *(matrix dithranol).*

4.6.3 DSC thermograms

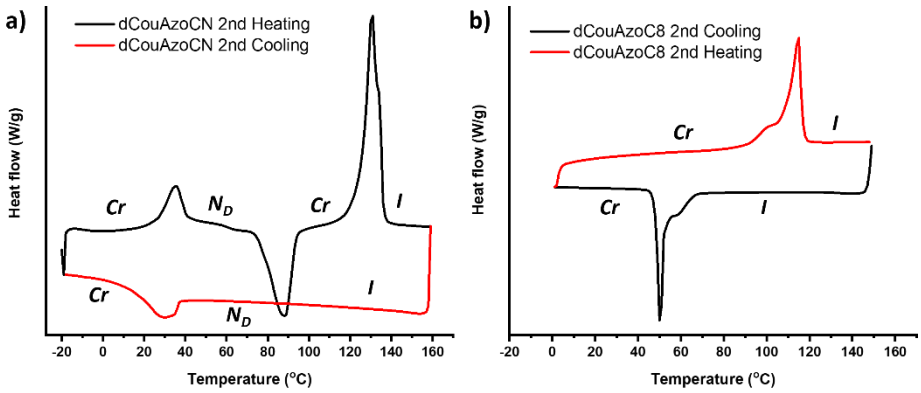

Figure 4.50. *Second DSC cycle (10 °C/min) of a)* ***dCouAzoCN*** *and b)* ***dCouAzoC$_8$****.*

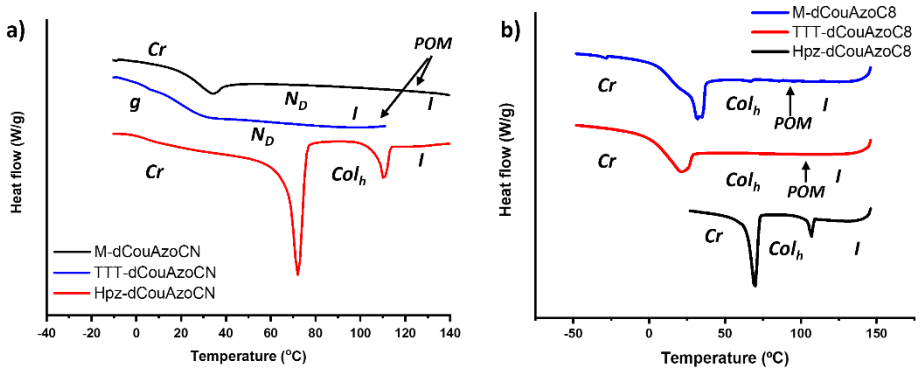

Figure 4.51. *DSC traces of the second cooling (10 °C/min) of the supramolecular complexes.*

4.6.4 Adsorption experiments

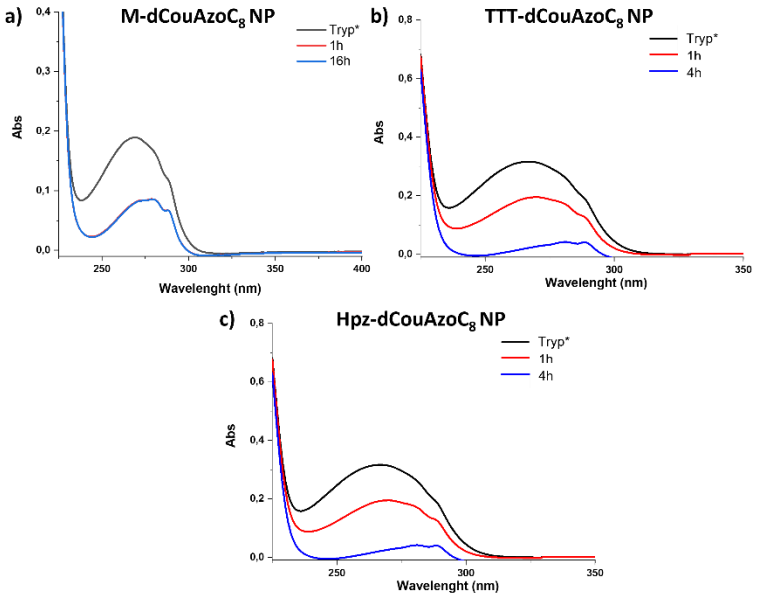

Figure 4.52. *Tryptophan* ***Tryp**** *adsorption of different membranes a)* ***M-dCouAzoC$_8$ NP****, b)* ***TTT-dCouAzoC$_8$ NP*** *and c)* ***Hpz-dCouAzoC$_8$ NP*** *followed by UV in water.*

4.7 References

[1] S. J. D. Lugger, S. J. A. Houben, Y. Foelen, M. G. Debije, A. P. H. J. Schenning and D. J. Mulder, Hydrogen-Bonded Supramolecular Liquid Crystal Polymers: Smart Materials with Stimuli-Responsive, Self-Healing, and Recyclable Properties, *Chem. Rev.,* 2022, **122**, 5, 4946–4975.

[2] D. Foster, C. Kind, P. J. Ackerman, J-S. B. Tai, M. R. Dennis and I. I. Smalyukh, Two-dimensional skyrmion bags in liquid crystals and ferromagnets, *Nat. Phys.*, 2019, **15**, 655–659.

[3] Y. Shang, J. Wang, T. Ikeda and L. Jiang, Bio-inspired liquid crystal actuator materials, *J. Mater. Chem. C*, 2019, **7**, 3413—3428.

[4] M. P. da Cunha, M. G. Debije and A. P. H. J. Schenning, Bioinspired light-driven soft robots based on liquid crystal polymers, *Chem. Soc. Rev*., 2020, **49**, 6568-6578.

[5] A. Concellón, T. Liang, A. P. H. J. Schenning, J. L. Serrano, P. Romero and M. Marcos, Proton-conductive materials formed by coumarin photocrosslinked ionic liquid crystal dendrimers, *J. Mater. Chem. C*, 2018, **6**, 1000-1006.

[6] A. Concellón, M. Marcos, P. Romero, J. L. Serrano, R. Termine and A. Golemme, Not Only Columns: High Hole Mobility in a Discotic Nematic Mesophase Formed by Metal-Containing Porphyrin-Core Dendrimers, *Angew. Chem. Int. Ed*., 2017, **56**, 1259–1263.

[7] H. Wang, T. Xu, Y. Fu, Z. Wang, M. S. Leeson, J. Jiang and T. Liu, Liquid Crystal Biosensors: Principles, Structure and Applications, *Biosensors*, 2022, **12**, 639-666.

[8] J. Kloos, N. Joosten, A. P. H. J. Schenning and K. Nijmeijer, Self-assembling liquid crystals as building blocks to design nanoporous membranes suitable for molecular separations, *Journal of Membrane Science*, 2021, **620**, 118849-118867.

[9] S. Lagerwall, A. Dahlgren, P. Jägemalm, P. Rudquist, K. D´havé, H. Pauwels, R. Dabrowski and W. Drzewinski, Unique Electro-Optical Properties of LiquidCrystals Designed for Molecular Optics, *Adv. Funct. Mater.,* 2001, **11**, 87-94.

[10] M. Henmi, K. Nakatsuji, T. Ichikawa, H. Tomioka, T. Sakamoto, M. Yoshio and T. Kato, Self-Organized Liquid-Crystalline Nanostructured Membranes for Water Treatment: Selective Permeation of Ions, *Adv. Mater*., 2012, **24**, 2238-2241.

[11] N. Marets, D. Kuo, J. Torrey, T. Sakamoto, M. Henmi, H. Katayama and T. Kato, Highly Efficient Virus Rejection with Self-Organized Membranes Based on a Crosslinked Bicontinuous Cubic Liquid Crystal, *Adv. Healthcare Mater*., 2017, **6**, 1700252-1700258.

[12] D. Devadiga and T. N. Ahipa, Liquid Crystal-Based Water Treatment Membranes, *Adv. Mater. Interfaces,* 2022, **9**, 2101276-2101294.

[13] K. Shimomura, T. Ikai, S. Kanoh, E. Yashima and K. Maeda, Switchable enantioseparation based on macromolecular memory of a helical polyacetylene in the solid state, *Nature Chem.*, 2014, **6**, 429-434.

[14] B. Wang, L. Wang, Z. Zha, Y. Hu, L. Xu and H. Wang, Hydrogen-Bonded, Hierarchically Structured Single-Component Chiral Poly(ionic liquid) Porous Membranes: Facile Fabrication and Application in Enantioselective Separation, *CCS Chem*., 2022, **4**, 2930–2937.

[15] Y. Li and J. Yu, Emerging applications of zeolites in catalysis, separation and host–guest assembly, *Nat. Rev. Mater.,* 2021*,* **6**, 1156–1174.

[16] L. Guo, Y. Wang and M. Steinhart, Porous block copolymer separation membranes for 21st century sanitation and hygiene, *Chem. Soc. Rev*., 2021, **50**, 6333–6348.

[17] Z.-Z. Nie, B. Zou, L. Liu, M. Wang, S. Huang, X.-M. Chen and H. Yang, Nanoporous Supramolecular Liquid Crystal Polymeric Material for Specific and Selective Uptake of Melamine, *Macromolecules,* 2020, **53***,* 4204-4213.

[18] H. P. C. van Kuringen, G. M. Eikelboom, I. K. Shishmanova, D. J. Broer, A. P. H. J. Schenning, Responsive Nanoporous Smectic Liquid Crystal Polymer Networks as Efficient and Selective Adsorbents, *Adv. Funct. Mater*., 2014, **24**, 5045-5051.

[19] S. Bhattacharjee, J. A. M. Lugger and R. P. Sijbesma, Pore size dependent cation adsorption in a nanoporous polymer film derived from a plastic columnar phase, *Chem. Commun*., 2018, **54**, 9521-9524.

[20] A. Concellon, A. P. H. J. Schenning, P. Romero, M. Marcos and J. L. Serrano, Size-Selective Adsorption in Nanoporous Polymers from Coumarin Photo-Cross-Linked Columnar Liquid Crystals, *Macromolecules,* 2018, **51**, 2349−2358.

[21]H. K. Lee, H. Lee, Y. H. Ko, Y. J. Chang, N. K. Oh, W. C. Zin and K. Kim, Synthesis of a Nanoporous Polymer with Hexagonal Channels from Supramolecular Discotic Liquid Crystals, *Angew. Chem. Int. Ed*., 2001, **40**, 2669-2671.

[22] S. Bhattacharjee, J. A. M. Lugger and R. P. Sijbesma, Tailoring Pore Size and Chemical Interior of near 1 nm Sized Pores in a Nanoporous Polymer Based on a Discotic Liquid Crystal, *Macromolecules*, 2017, **50**, 2777−2783.

[23] G. M. Bögels, J. A. M. Lugger, O. J. G. M. Goor and R. P. Sijbesma, Size-Selective Binding of Sodium and Potassium Ions in Nanoporous Thin Films of Polymerized Liquid Crystals, *Adv. Funct. Mater*., 2016, **26**, 8023–8030.

[24] P. Marin San Roman, K. Nijmeijer and R. P. Sijbesma, Sulfonated polymerized liquid crystal nanoporous membranes for water purification, *Journal of Membrane Science*, 2022, **644**, 120097-120110.

[25] J. A. M. Lugger, D. J. Mulder, S. Batthacharjee and R. P. Sijbesma, Homeotropic Self-Alignment of Discotic Liquid Crystals for Nanoporous Polymer Films, *ACS Nano*, 2018, **12**, 6714−6724.

[26] J. A. M. Lugger, P. Marín San Román, C. C. E. Kroonen and R. P. Sijbesma, Nanoporous Films with Photoswitchable Absorption Kinetics Based on Polymerizable Columnar Discotic Liquid Crystals, *ACS Appl. Mater. Interfaces,* 2021, **13**, 4385−4392.

[27] I. Gracia, P. Romero, J. L. Serrano, J. Barberá, A. Omenat, Templated nanoporous membranes based on hierarchically self-assembled materials, *J. Mater. Chem. C,* 2017, **5**, 2033-2042.

[28] C. Li, J. Cho, K. Yamada, D. Hashizume, F. Araoka, H. Takezoe, T. Aida and Y. Ishida, Macroscopic ordering of helical pores for arraying guest molecules noncentrosymmetrically, *Nat. Commun.,* 2015*,* **6**, 8418-8427.

[29] Y. Ishida, S. Amano, N. Iwahashi and K. Saigo, Switching of Structural Order in a Cross-Linked Polymer Triggered by the Desorption/Adsorption of Guest Molecules, *J. Am. Chem. Soc.,* 2006, **128**, 13068-13069.

[30] X. Feng, M. E. Tousley, M. G. Cowan, B. R. Wiesenauer, S. Nejati, Y. Choo, R. D. Noble, M. Elimelech, D. L. Gin and C. O. Osuji, Scalable Fabrication of Polymer Membranes with Vertically Aligned 1 nm Pores by Magnetic Field Directed Self-Assembly, *ACS Nano*, 2014, **8**, 11977-11986.

[31] T. Kato, J. M. J. Frèchet, P. G. Wilson, T. Saito, T. Uryu, A. Fujishima, C. Jin and F. Kaneuchi, Hydrogen-bonded liquid crystals. Novel mesogens incorporating nonmesogenic bipyridyl compounds through complexation between hydrogen-bond donor and acceptor moieties, *Chem. Mater.,* 1993, **5**, 1094–1100.

[32] K. Kishikawa, A. Hirai and S. Kohmoto, Fixation of Multilayered Structures of Liquid-Crystalline 2:1 Complexes of Benzoic Acid Derivatives and Dipyridyl Compounds and the Effect of Nanopillars on Removal of the Dipyridyl Molecules from the Polymers, *Chem. Mater.,* 2008, **20**, 5, 1931–1935.

[33] D.J. Mulder, T. Liang, Y. Xu, J. Ter Schiphorst, L.M.W. Scheres, B.M. Oosterlaken, Z. Borneman, K. Nijmeijer and A.P.H.J. Schenning, Proton conductive cationic nanoporous polymers based on smectic liquid crystal hydrogen-bonded heterodimers, *J. Mater. Chem. C*, 2018, **6**, 5018–5024.

[34] T. Liang, H.P.C. Van Kuringen, D.J. Mulder, S. Tan, Y. Wu, Z. Borneman, K. Nijmeijer and A.P.H.J. Schenning, Anisotropic dye adsorption and anhydrous proton conductivity in smectic liquid crystal networks: the role of cross-link density, order, and orientation, *ACS Appl. Mater. Interfaces*, 2017, **9**, 35218–35225.

[35] A. H. Gelebart, D. Liu, D. J. Mulder, K. H. J. Leunissen, J. van Gerven, A. P. H. J. Schenning and D. J. Broer, Photoresponsive Sponge-Like Coating for On-Demand Liquid Release, *Adv. Funct. Mater*., 2018, **28**, 1705942-1705950.

[36] X. Pang, J-an. Lv, C. Zhu, L. Qin and Y. Yu, Photodeformable Azobenzene-Containing Liquid Crystal Polymers and Soft Actuators, *Adv. Mater.,* 2019, **31**, 1904224-1904250.

[37] C. L. Gonzalez, C. W. M. Bastiaansen, J. Lub, J. Loos, K. Lu, H. J. Wondergem and D. J. Boer, Nanoporous Membranes of Hydrogen-bridged Smectic Networks with Nanometer Transverse Pore Dimensions, *Adv. Mater.*, 2008, **20**, 1246–1252.

[38] S. J. A. Houben, S. A. van Merwijk, B. J. H. Langers, B. M. Oosterlaken, Z. Borneman and A. P. H. J. Schenning, Smectic Liquid Crystalline Polymer Membranes with Aligned Nanopores in an Anisotropic Scaffold, *ACS Appl. Mater. Interfaces,* 2021, **13**, 6, 7592–7599.

[39] Y. Zhan, D. J. Broer and D. Liu, Perspiring Soft Robotics Skin Constituted by Dynamic Polarity-Switching Porous Liquid Crystal Membrane, *Adv. Mater.*, 2023, **35**, 2211143-2211151.

[40] Y. Zhan, W. Zhang, A. Özden, S. Houben, M. Schuster, H. Gojzewski, G. Zhou, D. J. Broer and D. Liu, Localized Liquid Secretion from a Photopatterned Liquid-Crystal Polymer Skin, *ACS Appl. Polym. Mater*., 2020, **2**, 4071−4077.

[41] Y. Zhan, S. Calierno, J. Peixoto, L. Mitzer, D. J. Broer and D. Liu, Light- and Field-Controlled Diffusion, Ejection, Flow and Collection of Liquid at a Nanoporous Liquid Crystal Membrane, *Angew. Chem. Int. Ed.*, 2022, **61**.

[42] D. J. Mulder, L. M. W. Scheres, J. Dong, G. Portale, D. J. Broer and A. P. H. J. Schenning, Fabrication and Postmodification of Nanoporous Liquid Crystalline Networks via Dynamic Covalent Chemistry, *Chem. Mater*., 2017, **29**, 6601-6605.

[43] T. Ichikawa, M. Yoshio, A. Hamasaki, J. Kagimoto, H. Ohno and T. Kato, 3D Interconnected Ionic Nano-Channels Formed in Polymer Films: Self-Organization and Polymerization of Thermotropic Bicontinuous Cubic Liquid Crystals, *J. Am. Chem. Soc.,* 2011, **133**, 7, 2163–2169.

[44] Y. Saadat, K. Kim and R. Foudazi, Two-Step Thermoresponsive Ultrafiltration Membranes from Polymerization of Lyotropic Liquid Crystals, *ACS Applied Polymer Materials*, 2022, ***4***, **11**, 8156-8165.

[45] L. Wang, L. Yin, W. Zhang, X. Zhu and M. Fujiki, Circularly Polarized Light with Sense and Wavelengths To Regulate Azobenzene Supramolecular Chirality in Optofluidic Medium, *J. Am. Chem. Soc.,* 2017, **139**, 13218−13226.

[46] A. B. Kanj, J. Bürck, N . Vankova, C. Li, D. Mutruc, A. Chandresh, S. Hecht, T. Heine and L. Heinnke, Chirality Remote Control in Nanoporous Materials by Circularly Polarized Light, *J. Am. Chem. Soc.,* 2021, **143**, 7059−7068.

[47] F. Vera, J. L. Serrano, M. P. De Santo, R. Barberi, M. B. Ros and T. Sierra, Insight into the supramolecular organization of columnar assemblies with phototunable chirality, *J. Mater. Chem.*, 2012, **22**, 18025.

[48] F. Vera, J. Barberá, P. Romero, J. L. Serrano, M. B. Ros and T. Sierra, Orthogonal Action of Noncovalent Interactions for Photoresponsive Chiral Columnar Assemblies, *Angew. Chem. Int. Ed.,* 2010, **49**, 4910 –4914.

[49] J. Barberá, L. Puig, P. Romero, J. L. Serrano and T. Sierra, Propeller-like Hydrogen-Bonded Banana-Melamine complexes inducing helical supramolecular organizations, *J. Am. Chem. Soc.,* 2006, **128**, 4487-4492.

[50] B. Feringán, P. Romero, J. L. Serrano, R. Giménez and T. Sierra, Supramolecular columnar liquid crystals formed by hydrogen bonding between a clicked star-shaped s-Triazine and benzoic acids, *Chem. Eur. J.*, 2015, **21**, 8859-8866.

[51] I. Bala, S. P. Gupta, S. Kumar, H. Singh, J. De, N. Sharma, K. Kailasam and S. K. Pal, Hydrogen-bond mediated columnar liquid crystalline assemblies of C3-symmetric heptazine derivatives at ambient temperature, *Soft Matter*, 2018, **14**, 6342-6352.

[52] S. Pan, M. Ni, B. Mu, Q. Li, X-Yu. Hu, C. Lin, D. Chen and L. Wang, Well-Defined Pillararene-Based Azobenzene Liquid Crystalline Photoresponsive Materials and Their Thin Films with Photomodulated Surfaces, *Adv. Funct. Mater*., 2015, **25**, 3571–3580.

[53] J. Royes, C. Provenzano, P. Pagliusi, R. M. Tejedor, M. Piñol and L. Oriol, A Bifunctional Amorphous Polymer Exhibiting Equal Linear and Circular Photoinduced Birefringences, *Macromol. Rapid Commun*., 2014, **35**, 1890−1895.

[54] J. R. A. Moreno, J. J. L. González, F. P. Ureña, F. Vera, M. B. Ros and T. Sierra, Study of the Photoinduced Supramolecular Chirality in Columnar Liquid Crystals by Infrared and VCD Spectroscopies, *J. Phys. Chem. B,* 2012, 116, **16**, 5090–5096.

Chapter 5

Preparation of discotic shaped molecules through H-bond for chiral nanoporous membranes based on methacrylates

---

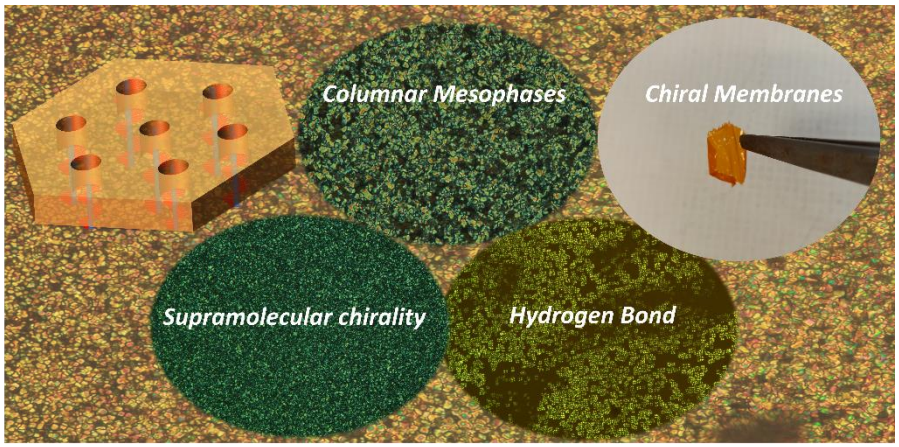

"Success is the sum of small efforts repeated day after day"
Stephen Curry

5.1 Introduction

After the successful preparation of chiral nanoporous materials described in ***Chapter* 4** based on columnar LCs with coumarins as polymerizable units, in this chapter we want to expand the knowledge on this kind of materials. In this context one of the most interesting polymerizable groups is methacrylate, which provides stronger and mechanically stable materials in comparison with coumarin because its high polymerization degree. Furthermore, as the chirality is not intrinsic to the structure of the materials and will be generated with the irradiation with CPL, this change of coumarin for methacrylate (with different thermal properties) may affect the retention of chirality through the preparation process. In **Figure 5.1** two schematic models of the supramolecular complexes prepared in this chapter are represented.

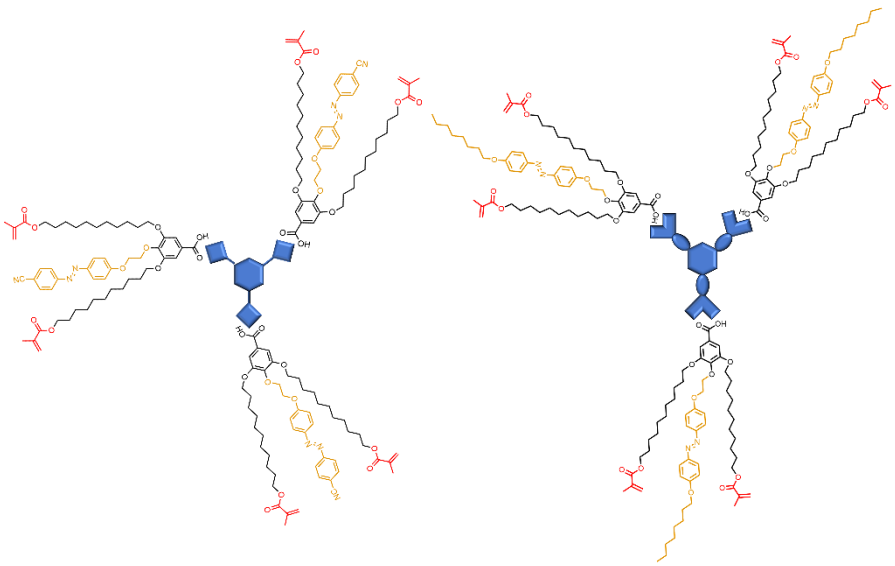

Figure 5.1. *Schematic models of the supramolecular complexes prepared in this chapter.*

5.2 Objectives

In order to obtain the chiral nanoporous membranes with methacrylates, we set the following specific objectives:

1. Synthesis and characterization of two dendrons containing terminally-appended 11-undecyloxymethacrylate and azobenzene moieties (**AzoCN (1)** and **AzoC$_8$(2)**, **Scheme 5.1**) functionalized with a carboxylic acid in their apical positions.
2. Preparation and characterization (^{1}H-NMR, ^{13}C-NMR, FT-IR, POM, DSC, TGA and XRD) of the supramolecular complexes formed by hydrogen bonding between the two dendrons synthesized in objective 1 with the template molecules described previously in ***Chapter 4***.
3. 3.a. Preparation and characterization of the polymeric films obtained after irradiating with circularly polarized light and photopolymerization of the methacrylate groups.
   3.b. Immersion of the films in acid solutions to remove the template molecules and characterization of the nanoporous membranes by FT-IR, XPS, XRD and CD.
4. Selective adsorption studies by size and chirality with different dyes, monitored by UV.

The specific structural details of the methacrylate membranes will be studied to determine the alignment of the material (analyzing the stacking of molecules with XRD). Moreover, in this kind of materials, the contraction of the pores after the template removal has been described, reducing the pore size.[1,2] Then again XRD studies will provide information about this.

5.3 Results and discussion

5.3.1 Synthesis and characterization of supramolecular complexes

The synthesis of the methacrylate-containing benzoic acids is described in **Scheme 5.1**; the procedure applied was similar to the synthesis of **dCouAzoCN** and **dCouAzoC$_8$** described in ***Chapter 4***. First, a Williamson reaction with a weak base was carried out to introduce the azobenzene moiety in the *para*-position of methyl gallate (facilitated by its acidity), and then two alkyl chains carrying a protected terminal hydroxy group were attached to the gallate derivative, giving rise to the protected dendrons. The deprotection of the carboxyl and hydroxyl groups was completed in a one-pot reaction using aqueous lithium hydroxide for the hydrolysis of the ester, while the deprotection of *tert*-butyldimethylsilane was accomplished with an acid treatment. Finally, the desired acids **dMetAzoCN** and **dMetAzoC$_8$** were obtained after adding dropwise methacryloyl chloride (the acronym **dMet** refers to the dendron containing methacrylates and **AzoCN** or **AzoC$_8$** to the kind of azobenzene introduced in the structure). The methacryloyl chloride reacts favorably with the deprotected alcohol producing the methacrylate ester. However, the anhydride subproduct obtained from the reaction of methacryloyl chloride with the carboxyl group was obtained and separated during the column chromatography. Moreover, in these reactions the flask was protected from light to prevent the uncontrolled photopolymerization. The chemical structure of all intermediates and final products was verified by FT-IR spectroscopy, MALDI-TOF spectrometry and ^{1}H-NMR, ^{1}H-^{1}H COSY, ^{13}C-NMR, ^{1}H-^{13}C HSQC, ^{1}H-^{13}C HMBC spectroscopy (see **Appendix**, **section 5.6**).

Regarding the template molecules employed in the formation of the supramolecular complexes, which will produce the pores of the membranes, they are the same used in ***Chapter 4***: **Melamine (M)**, **TTT** and **Heptazine (Hpz)** derivatives (see experimental part of ***Chapter 4*** for synthesis and characterization details).

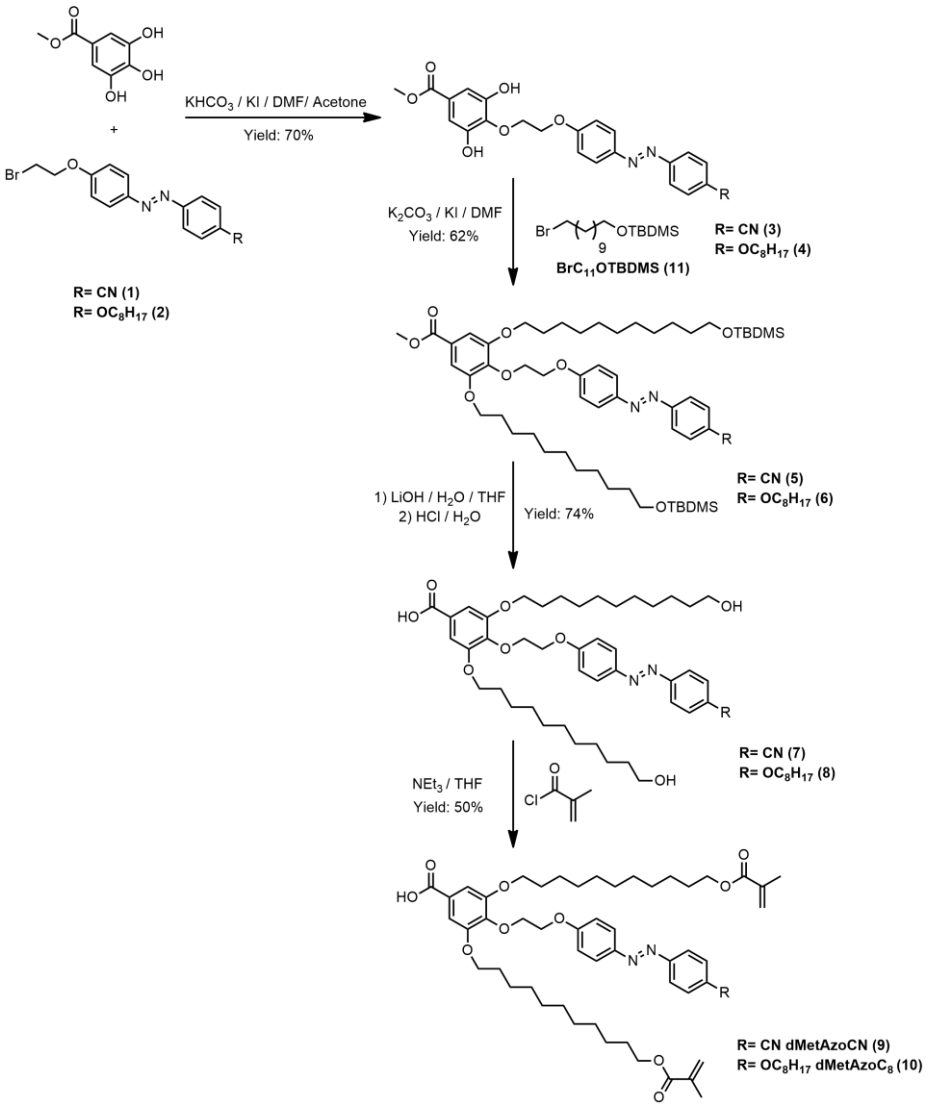

Scheme 5.1. *Synthetic route of the dendrons* ***dMetAzoCN*** *and* ***dMetAzoC$_8$****.*

Once the dendrons **dMetAzoCN** and **dMetAzoC$_8$** were characterized, each of them was mixed with the abovementioned templates derived from **Melamine**, **TTT** and **Heptazine** in a ratio 3:1. The DCM used as solvent was slowly evaporated at room temperature, while the mixture was protected from light until the weight was stable, obtaining six supramolecular complexes. Their structures were confirmed by FT-IR, ^{1}H-NMR and ^{13}C-NMR.

In **Figure 5.2** the FT-IR spectra of some methacrylate complexes are shown; in the case of **M-dMetAzoCN** (**Figure 5.2a**) important changes were observed in the 3250 cm^{-1} region because of the hydrogen bond formation. The stretching bands of the melamine (blue line) produced by the amino groups disappeared, resulting in a broad band (red line) due to the H-bond. Regarding the carbonyl region (**Figure 5.2b**) the stretching band of the dimerized carboxyl group in the **dMetAzoCN** spectrum at 1687cm^{-1} (blue line) disappeared after the formation of the supramolecular complex (red line).

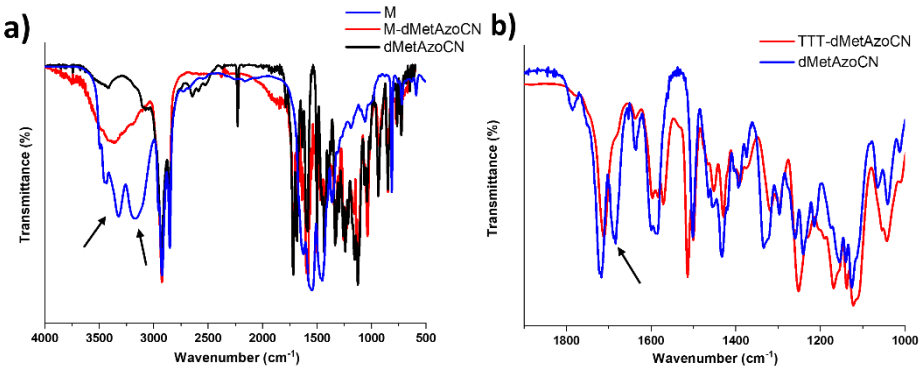

Figure 5.2. *Comparison of the FT-IR spectra of a)* ***M-dMetAzoCN*** *and b)* ***TTT-dMetAzoCN****, carbonyl region before (blue) and after (red) complex formation.*

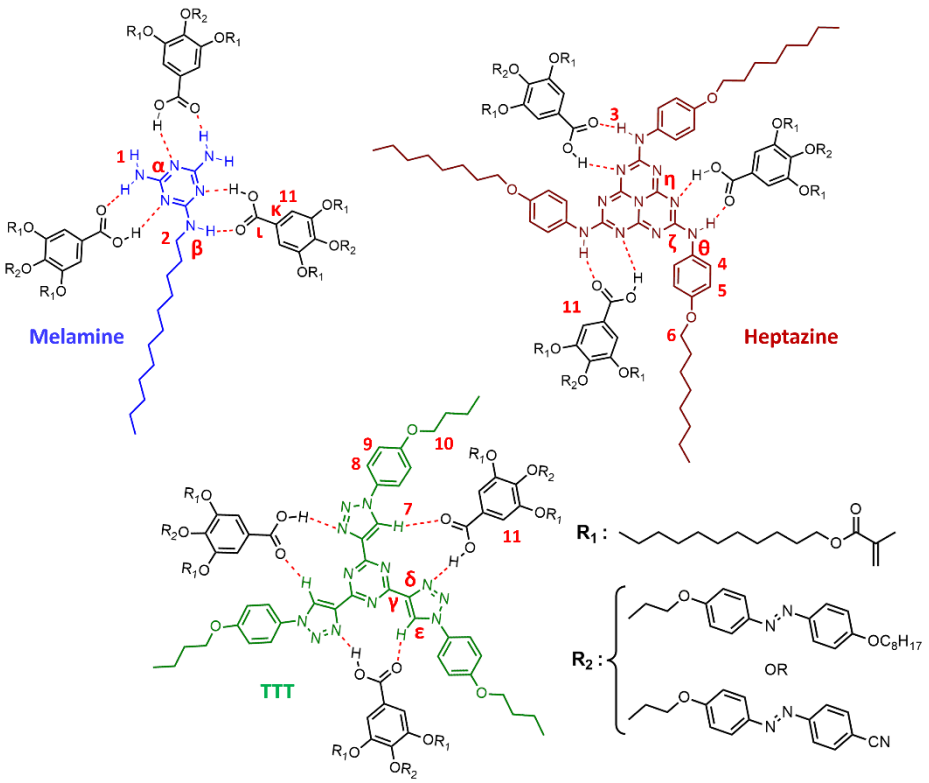

Figure 5.3. *Supramolecular complexes prepared in* ***Chapter 5*** *and meaningful signals.*

The six supramolecules studied in this chapter are represented in **Figure 5.3**, labelling the most important signals involved in the H-bond formation as can be observed in the ^{1}H-NMR and ^{13}C-NMR spectra. Concerning ^{1}H-NMR, the spectra of the supramolecular complexes are shown in **Figures 5.4-9**. In the case of **dMetAzoCN** complexes, the most relevant shifts were detected in the template molecules. For example, melamine protons (***H₁***) shifted from 4.85 to 6.85 ppm (**Figure 5.4**), amine protons (***H₃***) of heptazine shifted from 7.75 ppm to 10.09 and the aromatic signals (***H₄*** and ***H₅***) from 7.40 and 6.85 to 7.54 and 6.65 ppm respectively (**Figure 5.6**). In complex **TTT-dMetAzoCN** not only shifted the triazole proton ***H₇*** (from 8.86 to 9.04 ppm), but the aromatic protons (***H₈*** and ***H₉***) also shifted, suggesting the stack between supramolecules (**Figure 5.5**). For acid **dMetAzoC₈** analogous changes were exhibited in the amine protons of heptazine (from 7.75 to 9.73 ppm **Figure 5.9**) and melamine (from 4.85 to 6.32 ppm **Figure 5.7**). All

shifts produced in the H-bond formation are gathered in **Tables 5.1** and **5.2**.

Table 5.1. *Proton shifts in the supramolecular complexes of* ***dMetAzoCN****.*

	H_1	H_2	H_3	H_4	H_5	H_6	H_7	H_8	H_9	H_{11}
M	4.85	3.30								
Supra M	6.85	3.36								7.31
TTT							8.86	7.79	7.10	
Supra TTT							9.04	7.75	7.05	7.30
Hpz			7.75	7.40	6.85	3.92				
Supra Hpz			10.09	7.54	6.65	3.83				7.31
dMetAzoCN										7.32

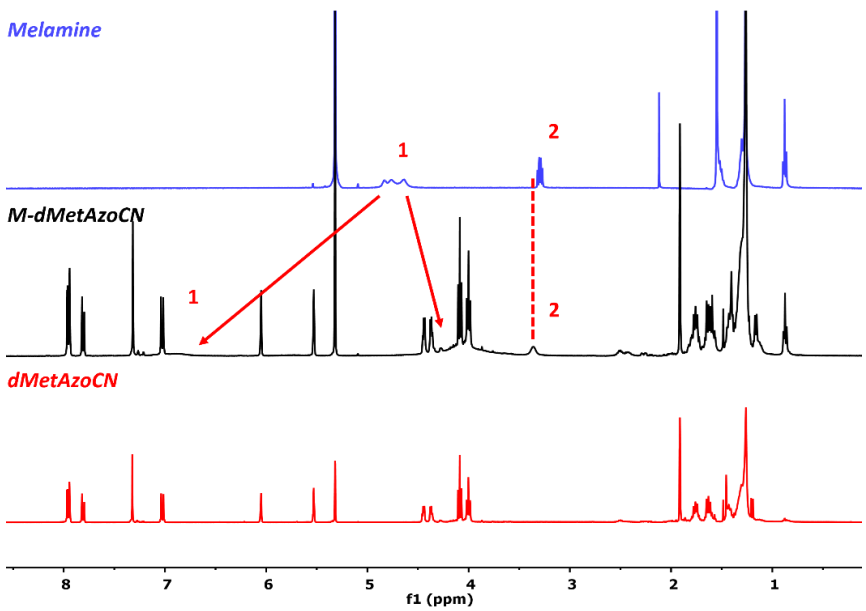

Figure 5.4. *^{1}H-NMR (CD_2Cl_2, 298K, 400 MHz) spectra of* ***melamine M*** *(blue line),* ***dMetAzoCN*** *(red line) and* ***M-dMetAzoCN*** *complex (black line).*

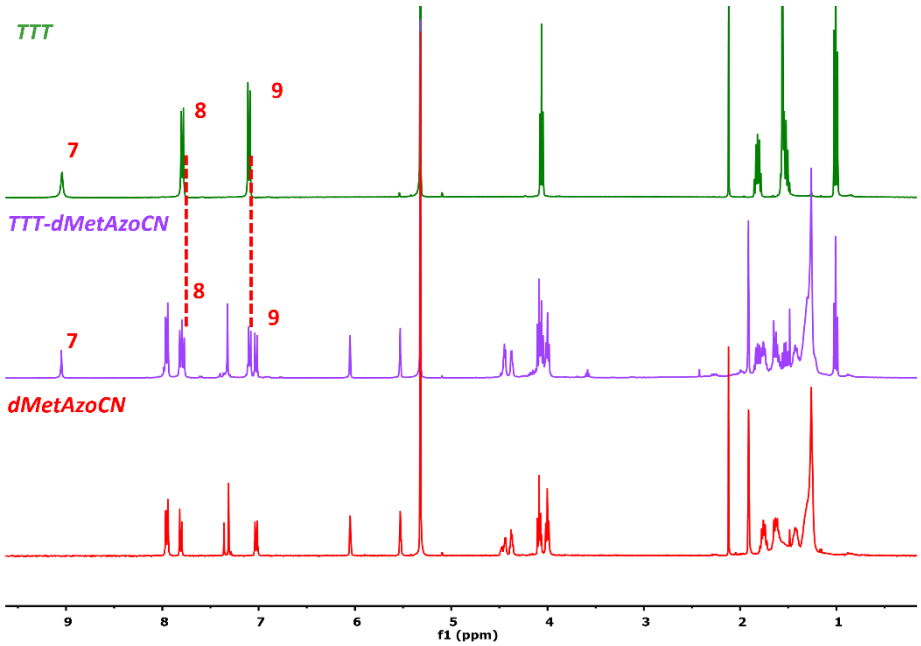

Figure 5.5. *^{1}H-NMR (CD_2Cl_2, 298K, 400 MHz) spectra of **TTT** (green line), **dMetAzoCN** (red line) and **TTT-dMetAzoCN** complex (purple line).*

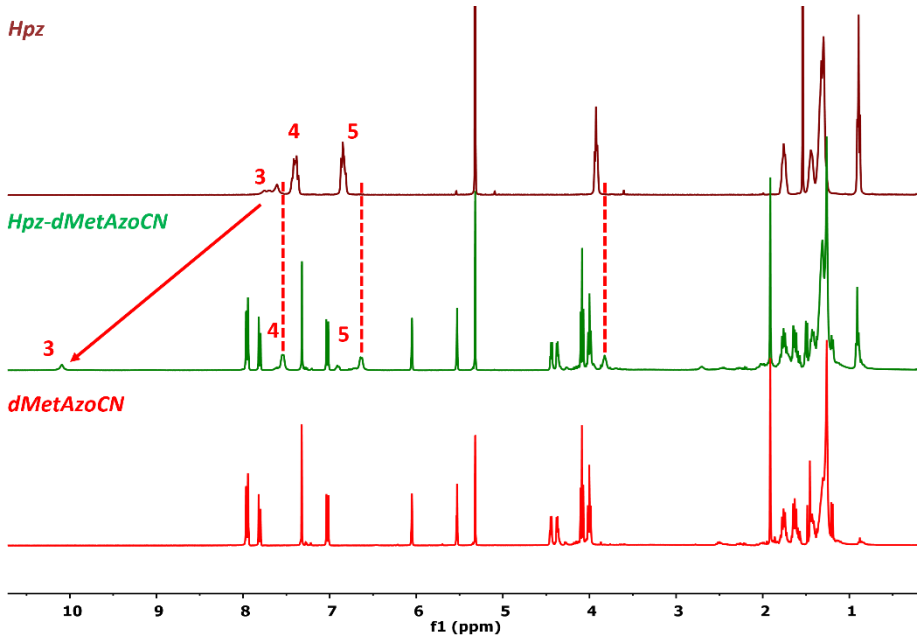

Figure 5.6. *^{1}H-NMR (CD_2Cl_2, 298K, 400 MHz) spectra of **heptazine Hpz** (burgundy line), **dMetAzoCN** (red line) and **Hpz-dMetAzoCN** complex (green line).*

Table 5.2. *Proton shifts in the supramolecular complexes of* ***dMetAzoC$_8$.***

	H_1	H_2	H_3	H_4	H_5	H_6	H_7	H_8	H_9	H_{11}
M	4.85	3.30								
Supra M	6.32	3.38								7.32
TTT							8.86	7.79	7.10	
Supra TTT							9.05	7.78	7.08	7.32
Hpz			7.75	7.40	6.85	3.92				
Supra Hpz			9.73	7.60	6.73	3.84				7.33
dMetAzoC$_8$										7.33

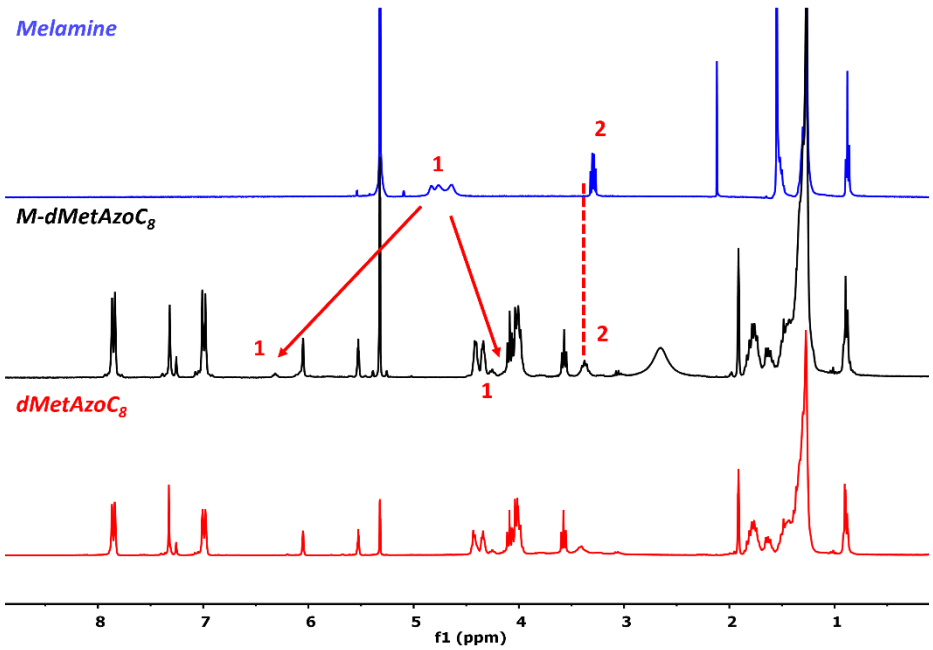

Figure 5.7. *^{1}H-NMR(CD_2Cl_2, 298K, 400 MHz) spectra of* ***melamine M*** *(blue line),* ***dMetAzoC$_8$*** *(red line) and* ***M-dMetAzoC$_8$*** *complex (black line).*

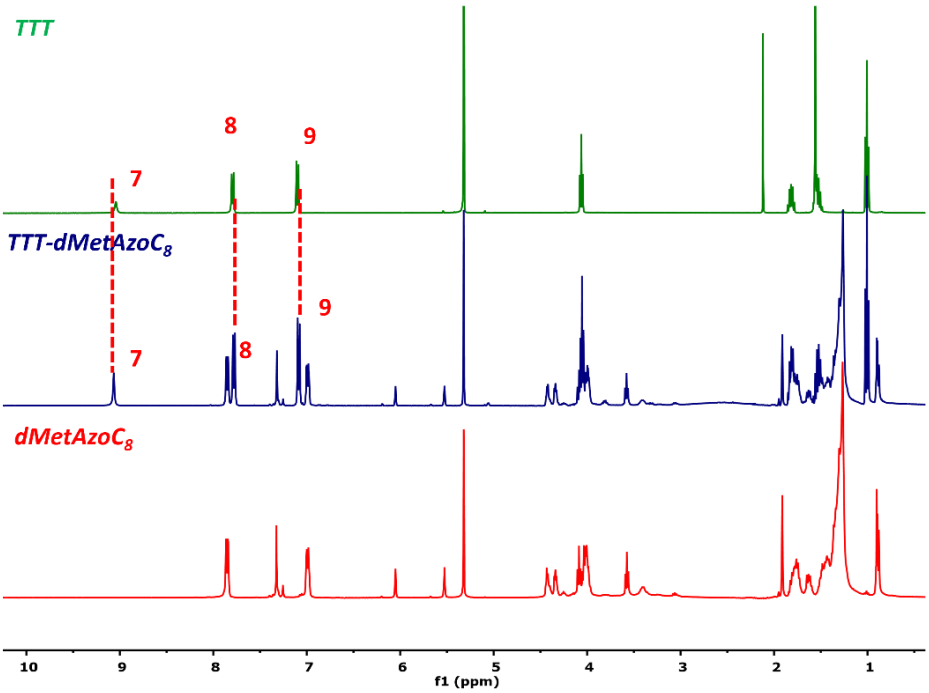

Figure 5.8. ^{1}H-NMR (CD_2Cl_2, 298K, 400 MHz) spectra of **TTT** (green line), **dMetAzoC$_8$** (red line) and **TTT-dMetAzoC$_8$** complex (blue line).

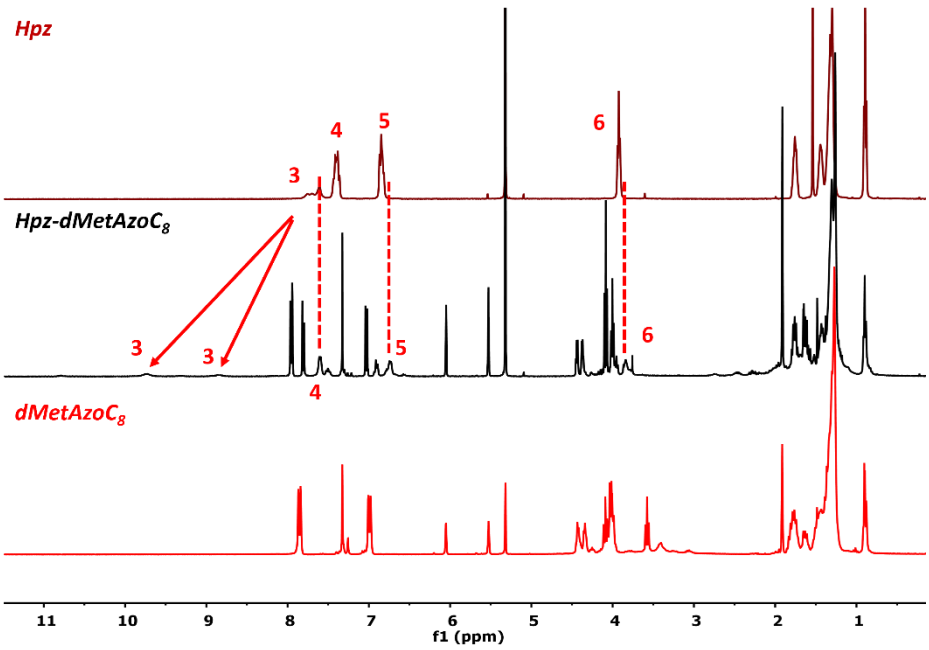

Figure 5.9. ^{1}H-NMR (CD_2Cl_2, 298K, 400 MHz) spectra of **heptazine Hpz** (burgundy line), **dMetAzoC$_8$** (red line) and **Hpz-dMetAzoC$_8$** complex (black line).

^{13}C-NMR spectra exhibited important changes for the carbonyl signal of the acids (**dMetAzoCN** and **dMetAzoC$_8$**) and the carbons close to the H-bond interaction, like the aromatic carbons of heptazine or the triazole carbons in TTT. In **Table 5.3** those variations are collected, indicating the specific carbon and its shift before and after the preparation of the supramolecular complex.

Table 5.3. *Shifts in the ^{13}C-NMR signals affected by the hydrogen bond formation (see **Figure 5.3**).*

	C_α	C_β	C_γ	C_δ	C_ε	C_η	C_ζ	C_ϑ	C_ι	C_κ
M	167.47	41.19								
M-dMetAzoCN		41.65							170.29	125.11
TTT			167.42	146.40	126.20					
TTT-dMetAzoCN			165.29	145.89	126.33				170.19	124.81
Hpz						157.28	157.05	130.48		
Hpz-dMetAzoCN						156.61	155.96	131.05	170.40	124.86
dMetAzoCN									170.64	124.74
	C_α	C_β	C_γ	C_δ	C_ε	C_η	C_ζ	C_ϑ	C_ι	C_κ
M	167.47	41.19								
M-dMetAzoC$_8$	176.34	41.44							170.15	125.22
TTT			167.42	146.40	126.20					
TTT-dMetAzoC$_8$			167.88	147.69	126.25				169.55	124.79
Hpz						157.28	157.05	130.48		
Hpz-dMetAzoC$_8$						157.45	157.21	129.78	171.52	125.22
dMetAzoC$_8$									169.95	125.23

Some examples of the ^{13}C-NMR variations are shown in **Figure 5.10**. The carbonyl signal of **dMetAzoCN** shifted from 170.64 to 170.19 ppm in **TTT-dMetAzoCN** and the carbon peak of triazine from 167.72 to 165.29 ppm (**Figure 5.10a**). This displacement could be produced not only by the hydrogen bond formation, but also the stacking interaction between molecules. This tendency to the stacking will be analyzed in the liquid crystal section. In the case of **dMetAzoC$_8$** the carbonyl peak shifted from 169.95 to 171.52 ppm in the heptazine complex (**Figure 5.10b)**, observing similar shifts in the template molecule as observed for **dMetAzoCN** complexes.

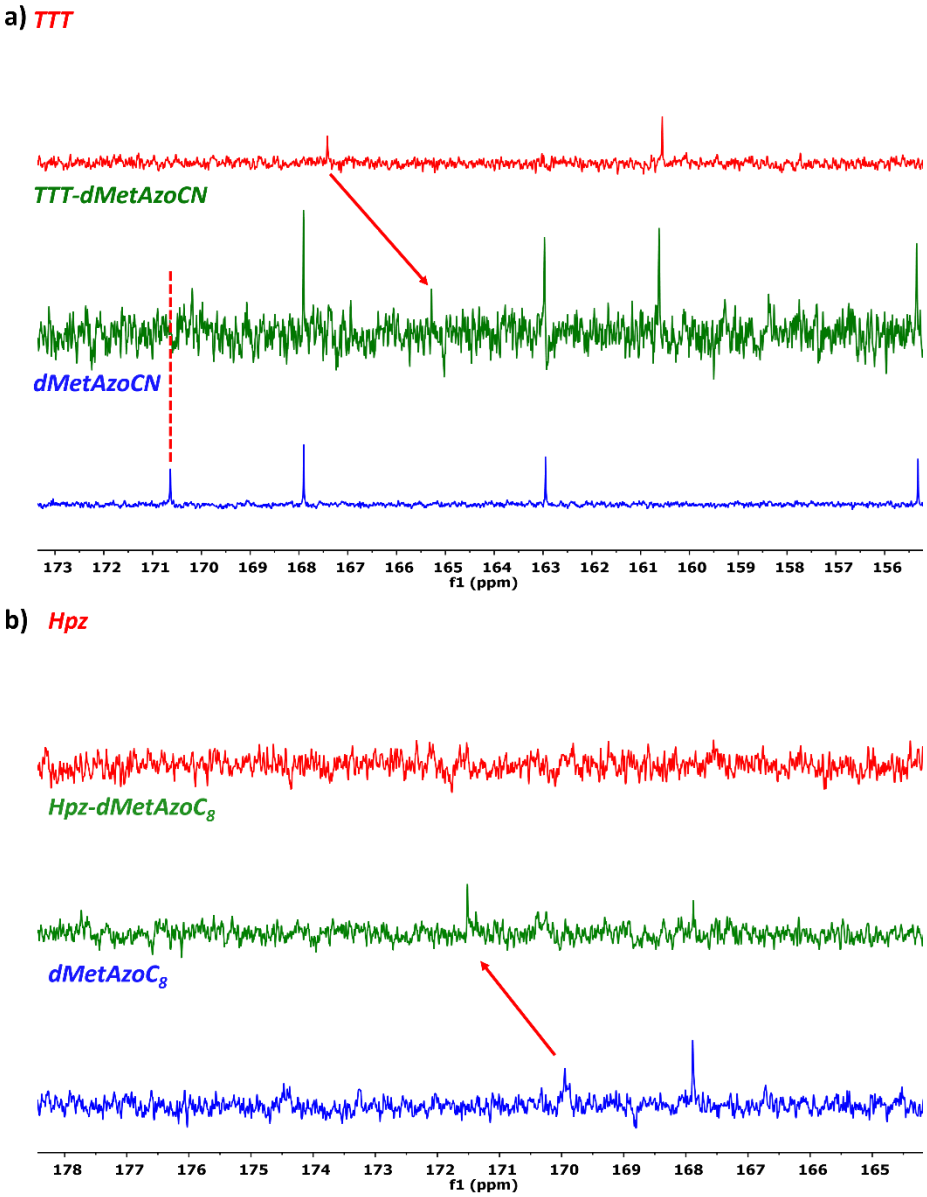

Figure 5.10. *Meaningful region of the ^{13}C-NMR (CD_2Cl_2, 298K, 100 MHz) spectra of a)* ***TTT-dMetAzoCN*** *and b)* ***Hpz-dMetAzoC$_8$****, the corresponding acids and templates.*

5.3.2 Thermal characterization and liquid crystal behavior

The thermal properties of the dendrons and the six supramolecular complexes were characterized using a combination of thermogravimetry (TGA), polarized optical microscope (POM), differential scanning calorimetry (DSC) and several X-ray measurements

(XRD, WAXS, MAXS). The TGA experiments showed in all cases a weight loss temperature of 2% clearly higher than the isotropization points of the dendrons and supramolecular complexes. DSC cycles showed several transitions during the heating and cooling processes. These data and the structural parameters obtained by X-ray diffraction are collected in **Table 5.4**.

Table 5.4. *Thermal properties and structural parameters of the studied compounds.*

Compound	$T_{2\%}$[a](°C)	Phase transitions[b]	d (Å)	h k l	Structural parameters
dMetAzoCN	171	g -8 Cr 55 I*			
M-dMetAzoCN	98	g -8 Col_h 65 I*	30.8 18.3 15.4 4.2	1 0 0 1 1 0 2 0 0 br	a = 35.6 Å
TTT-dMetAzoCN	180	g -9 Col_h 60 I*	33.3 19.1 12.2 9.7 4.1	1 0 0 1 1 0 2 1 0 2 2 0 br	a = 38.3 Å
Hpz-dMetAzoCN	166	Col_h 75 I	34.0 17.0 13.5 4.2	1 0 0 2 0 0 2 1 0 br	a = 39.2 Å
dMetAzoC$_8$	158	Cr_1 4 Cr_2 56 I*			
M-dMetAzoC$_8$	140	Cr 9 Col_h 56 I*	40.5 23.4 20.3 15.3 4.2	1 0 0 1 1 0 2 0 0 2 1 0 br	a = 46.8 Å
TTT-dMetAzoC$_8$	127	g -12 Col_h 29 I*	44.5 25.6 22.2 16.8 11.0 4.3	1 0 0 1 1 0 2 0 0 2 1 0 4 0 0 br	a = 51.3 Å

Hpz-dMetAzoC$_8$	129	Col$_h$ 56 I	40.6 23.4 20.3 15.3 4.2	1 0 0 1 1 0 2 0 0 2 1 0 br	a = 46.9 Å

[a] Decomposition temperature corresponding to 2% weight loss.

*[b] DSC data obtained at a rate of 10°C/min in the second heating-cooling cycle. Cr: crystal, g: glass, Col$_h$: columnar hexagonal and I: isotropic liquid. *Data obtained from POM observations.*

The acid **dMetAzoCN** was studied by POM and XRD to determine unequivocally the presence or not of a mesophase. However, the patterns revealed many sharp peaks in all diffractogram indicating its crystalline nature.

The complexes **M-dMetAzoCN** and **TTT-dMetAzoCN** were found to be mesomorphic materials at POM (**Figure 5.11a-b**). Homogeneous and classical textures of columnar hexagonal liquid crystals (Maltese crosses) with large dark areas that may be produced by an homeotropic alignment confirm the formation of liquid crystal phase. The behavior of both complexes in the DSC cycles was similar: a glass transition was detected during the cooling cycle at -10°C approximately. However, the transition from LC to isotropic liquid could not be detected by DSC and was determined by POM. XRD experiments provided structural information about the materials (**Figure 5.11c-d**). For **M-dMetAzoCN** three reflections in the low angle region were obtained with spacings in the ratio 1:1/$\sqrt{3}$:1/$\sqrt{4}$ which correspond to the (100), (110) and (200) planes of the hexagonal lattice. The high angle region of the diffractogram showed a diffuse scattering produced by the alkyl chain interactions with a tendency to crystallize after some time. The low-angle reflections yielded a disc diameter (*a* constant) of 35.6 Å. For the supramolecular complex **TTT-dMetAzoCN** the results of the X-ray measurements were similar, obtaining in this case the reflections (100), (110), (210) and (220) with spacings in a ratio 1:1/$\sqrt{3}$:1/$\sqrt{7}$:1/$\sqrt{12}$, which yielded a hexagonal lattice constant *a* = 38.3 Å. The increase in the value of the parameter *a* was produced by the bigger size of the TTT template in comparison with melamine template.

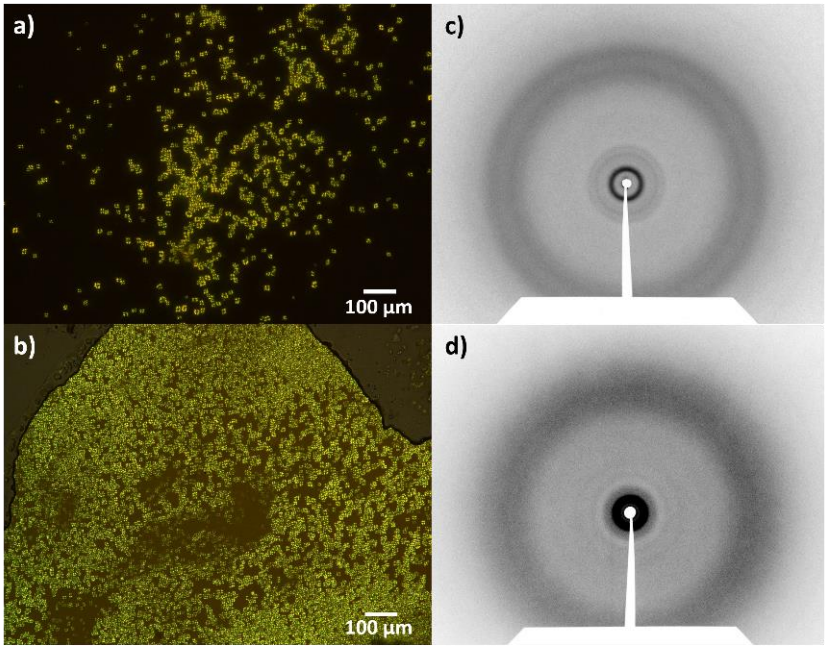

Figure 5.11. *a-b) POM microphotograph at room temperature during the cooling process of* ***M-dMetAzoCN*** *and* ***TTT-dMetAzoCN.*** *c) and d) XRD diffractogram at room temperature of* ***M-dMetAzoCN*** *and* ***TTT-dMetAzoCN****.*

Complex **Hpz-dMetAzoCN** exhibited a colorful texture (**Figure 5.12a**) by POM previously described in heptazine derivatives.[3]

The material was studied by DSC in three cycles of heating-cooling, showing the clearing point at 85°C. It is worth mentioning that the material did not suffer any crystallization or vitrification during the cooling cycle, remaining in the mesomorphic state until -50°C (limit reached by DSC). XRD patterns (**Figure 5.12b-c**) revealed a Col_h arrangement, as revealed by the presence of multiple reflections in the low angle region with spacings in a ratio of $1:1/\sqrt{4}: 1/\sqrt{7}$ and a broad peak at 4.2 Å in the high angle region produced by the alkyl chain interactions. These distances were indexed in a columnar hexagonal mesophase with a disc size of 39.2 Å, the highest in the **dMetAzoCN** family.

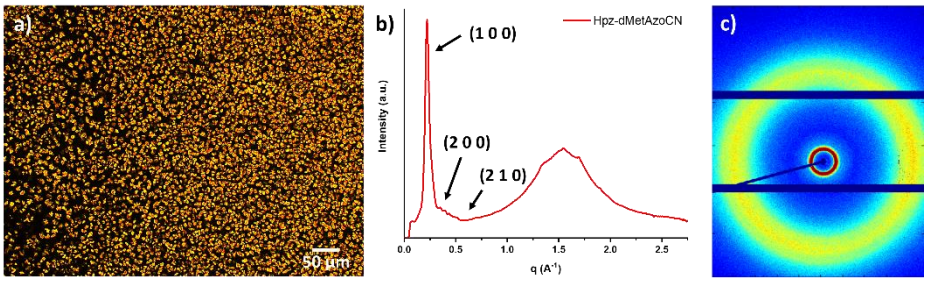

Figure 5.12. *a) POM microphotograph of* ***Hpz-dMetAzoCN*** *at r.t. after a heating-cooling cycle. b-c) 1D and 2D XRD patterns of* ***Hpz-dMetAzoCN****.*

The octyloxy derivative **dMetAzoC$_8$** exhibited several peaks in the DSC cycles of heating-cooling with high enthalpies (**Figure 5.37b**), which is a sign of crystalline material. POM observations revealed a birefringent material with certain degree of fluidity (**Figure 5.13a**). Finally, XRD experiments (**Figure 5.13b**) were carried out to determine the structure of the material, obtaining a diffractogram with multiple reflections in the low and high-angle regions, confirming the crystalline structure.

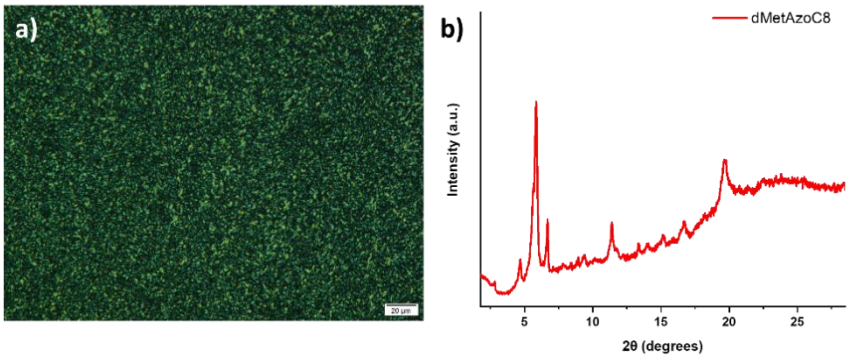

Figure 5.13. *a) POM microphotograph of* ***dMetAzoC$_8$*** *at room temperature and b) XRD pattern of* ***dMetAzoC$_8$****.*

The melamine complex **M-dMetAzoC$_8$** displayed a colorful, birefringent, spherulitic texture that melted at 56ºC (**Figure 5.14a**). In the cooling process from isotropic liquid, a birefringent texture appeared confirming the appearance of mesophase. The transitions observed after the repetition of the heating-cooling cycles did not present significant changes, which indicates the stability of the formation of hydrogen bonds. In the DSC studies, crystallization phenomena were observed around 9ºC in the cooling process; however,

the temperatures of the transition to isotropic liquid could only be determined by POM observations.

Finally, the structural details of the material were determined by X-ray experiments (**Figure 5.14 b-c-d**). 1D XRD displayed an intense sharp maximum (100) and several weak reflections which index in a columnar hexagonal mesophase with spacings in the ratio $1:1/\sqrt{3}:1/\sqrt{4}:1/\sqrt{7}$. The value found for parameter *a* (46.8 Å) is considerably large compared with its analogue of **dMetAzoCN** (35.5 Å). This fact may be explained in two terms: first of them is the length of the alkyl chain in the azobenzene moiety in contrast with a shorter cyanoazobenze; secondly, the homeotropic disposition of the material in **M-dMetAzoC$_8$** can only be adopted if the chains are totally stretched; however, in complex **M-dMetAzoCN** these chains may be folded, reducing the size of the disc.

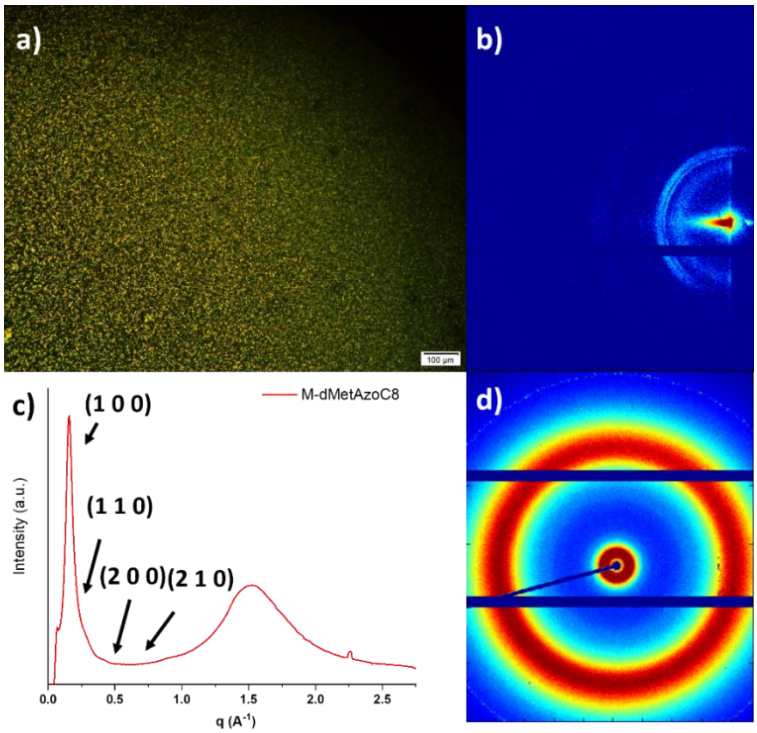

Figure 5.14. *a) POM microphotograph of **M-dMetAzoC$_8$** at r.t. during the cooling cycle. b) MAXS diffractogram c) 1D and d) 2D XRD diffractograms of **M-dMetAzoC$_8$**.*

The triazole derivative **TTT-dMetAzoC$_8$** showed a different texture under the microscope (**Figure 5.15a**) with dark areas and Maltese

crosses, which melted to the isotropic liquid at 29ºC and appeared again on cooling as a fluid material until room temperature. DSC cycles were carried out to determine the phase transitions in the material, yielding a glass transition at -12ºC and a clearing point to isotropic liquid at 29ºC. This range of mesophase was narrow, but it guaranteed the LC state at room temperature. The columnar hexagonal mesophase was confirmed with x-ray experiments. The 1D XRD pattern (**Figure 5.15c**) exhibited several reflections in the low angle region with an intense sharp maximum which indicates a disc size of 51.3 Å, a value larger than the one found for the previous complex of melamine because of the TTT size. At low angles five reflections were observed with spacings in the ratio 1:1/√3:1/√4:1/√7:1/√16.

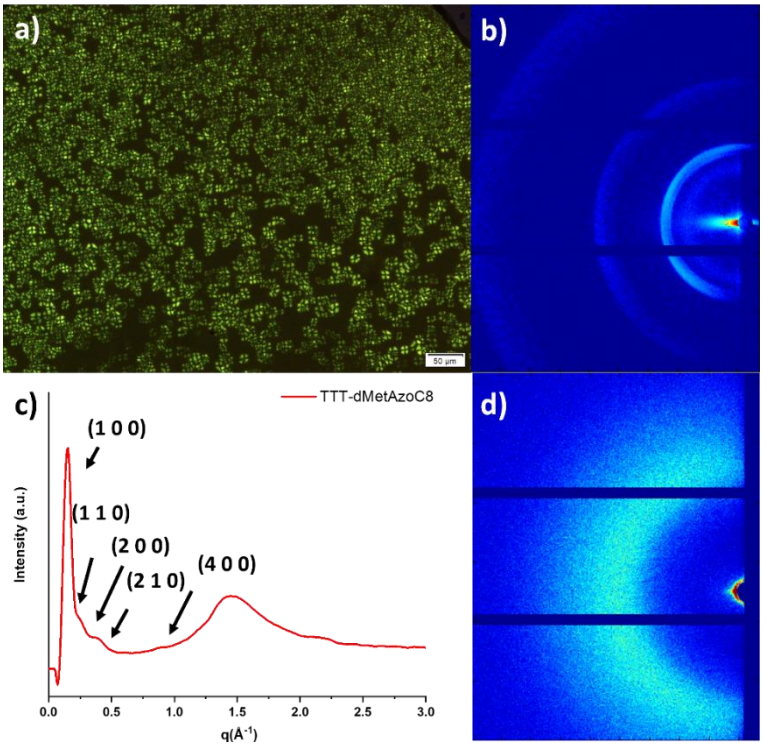

Figure 5.15. *a) POM microphotograph of* ***TTT-dMetAzoC$_8$*** *at r.t. during the cooling cycle. b) MAXS pattern c) 1D and d) 2D XRD patterns of* ***TTT-dMetAzoC$_8$****.*

Finally, complex **Hpz-dMetAzoC$_8$** exhibited colorful and birefringent textures with dark areas at POM (**Figure 5.16 a-b**) which indicates the tendency to the homeotropic alignment if the material is slowly cooled

down (0.1ºC/min) from the isotrope. Despite its similar behavior to the other **dMetAzoC$_8$** complexes, the textures observed reminded more to those of the other heptazine derivatives (**Hpz-dCouAzoC$_8$** and **Hpz-dMetAzoCN**), which suggests a clear influence of the core in the resulting mesophase. Their transitions were studied by DSC with three cycles of heating and cooling, observing the transition from the LC phase to the isotropic liquid at 56ºC. During the cooling cycle, the material was cooled until -50ºC without observing any change. The structural details and the kind of mesophase were determined by XRD (**Figure 5.16 b-c**). Again an intense sharp peak and several reflections were observed with spacings in a ratio of $1/\sqrt{3}:1/\sqrt{4}:1/\sqrt{7}$, supporting the columnar hexagonal arrangement. At high angles the classical diffuse halo produced by the alkyl chains interactions was observed.

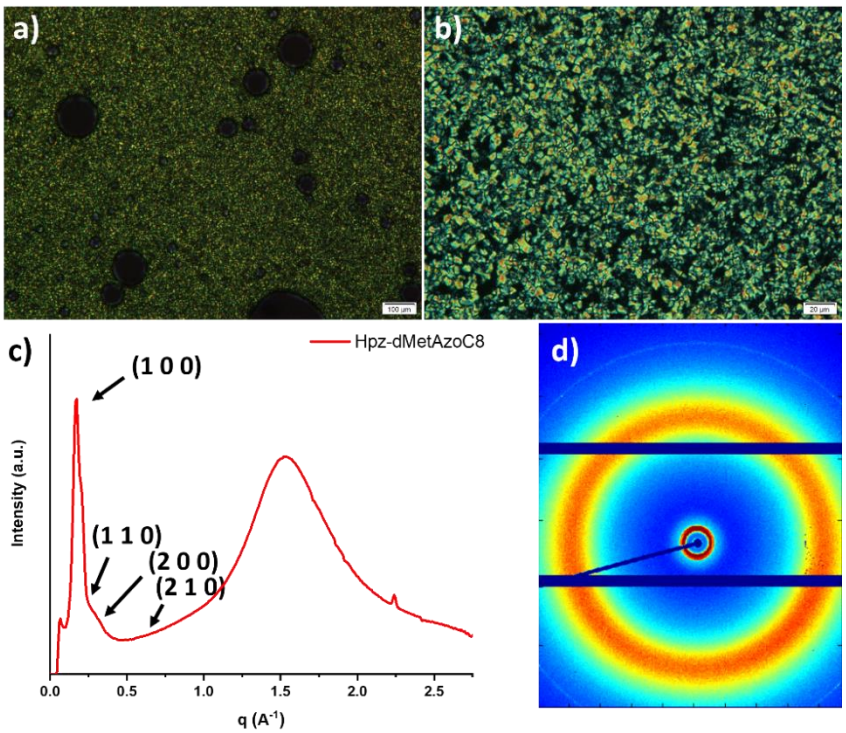

Figure 5.16. *a-b) POM microphotograph of **Hpz-dMetAzoC$_8$** at r.t. during the cooling cycle. c-d) 1D and 2D X-ray patterns of **Hpz-dMetAzoC$_8$**.*

The analysis of all these results indicates that all supramolecular complexes present columnar hexagonal order, which turn them in

potential materials for the preparation of chiral membranes. **dMetAzoCN** complexes exhibited a broad thermal range of mesophase including room temperature and a clear relationship between the template size and the diameter of the columns, increasing from melamine to heptazine. For **dMetAzoC$_8$** the thermal ranges of mesophase of its complexes were narrower, but covering room temperature in the three cases. This behavior indicates the influence of the azobenzene in the stacking of molecules in the mesophase.

5.3.3 Preparation of chiral membranes

Once the supramolecular complexes were structurally classified as columnar hexagonal LCs, this made these materials potentially suitable for the preparation of membranes. In contrast with the coumarin complexes which were polymerized irradiating with light of 325 nm (maximum absorbance of coumarin) and without any photoinitiator, for the methacrylate polymerization it was necessary to add a photoinitiator and irradiate at the wavelength which produces the photopolymerization.[4,5,6] Additionally, the irradiation of the azobenzene with CPL will produce the asymmetrical isomerization of the photoactive units and therefore chirality in the columns, considering that after generation of chirality the photoinitiator should absorb at a wavelength that does not revert the effect of the azobenzene units. Consequently, the preparation of the chiral membranes was carried out following these steps:

1. A solution of the supramolecular complex was mixed with a solution of the photoinitiator (bis(cyclopenta-1,3-diene)bis(1-(2,4-difluorophenyl)-3H-pyrrol-3-yl)titanium 2% weight) and the solvent was evaporated.
2. The solid obtained was melted between two glasses and was let to cool down at 0.1^{o}C/min, to obtain the macroscopic columnar organization.
3. The columnar organization was irradiated with 400 nm CPL to induce chirality in the material.

4. The helical columnar hexagonal arrangement was fixed irradiating with light of 720 nm for 30 minutes to obtain a polymeric film.
5. The polymeric films were immersed in an acid solution to remove the template molecule and obtain the chiral nanoporous material.

The irradiation of the non-polymerized films with *left*-CPL for 1 minute produced a chiral signal in all the complexes prepared at the maximum absorbance of the azobenzene units (**Figure 5.17 a-b**). As can be observed in **Figure 5.17a**, the intensity of the ellipticity decreases as the template size increases, the smallest template (M) producing the more intense signal. Similarly, to the results obtained in ***Chapter 4***, the irradiation with the opposite handedness resulted in the production of a helical structure with the opposite sign, confirming that the chirality of the films can be tuned externally.

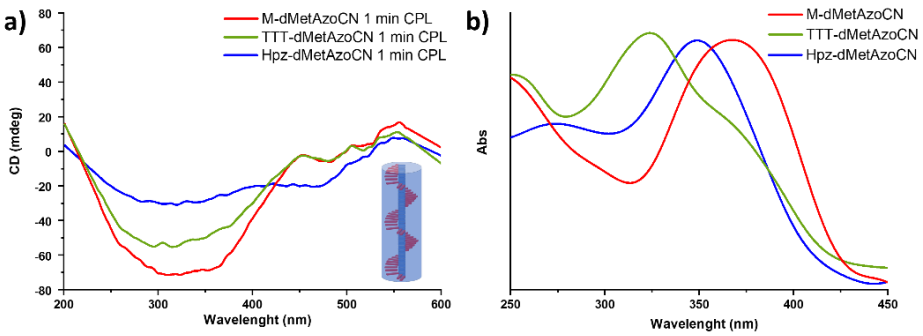

Figure 5.17. *a) CD spectra of **M-dMetAzoCN, TTT-dMetAzoCN** and **Hpz-dMetAzoCN** complexes after being irradiated with CPL b) UV spectra of **M-dMetAzoCN, TTT-dMetAzoCN** and **Hpz-dMetAzoCN** complexes.*

To fix the hexagonal columnar arrangement, the chiral films were exposed to 700 nm wavelength light for one hour to induce photoreaction. The polymerization was studied by FT-IR, verifying the conversion of the complex to a polymeric film. As examples, in **Figure 5.18** the spectra of **M-dMetAzoC$_8$** and **M-dMetAzoCN** are compared before and after the exposure to light. The carbonyl bands of the polymerized methacrylate shifted from 1736 cm^{-1} to 1711 cm^{-1} and from 1726 cm^{-1} to 1710 cm^{-1} in **M-dMetAzoC$_8$** and **M-dMetAzoCN** respectively, as well as changes in the symmetric and antisymmetric

bands (C-O). Furthermore, the vibration band of the C=C bond, which is involved in photopolymerization, suffered a significant decrease in intensity (indicated with black arrows in the **Figure 5.18**).

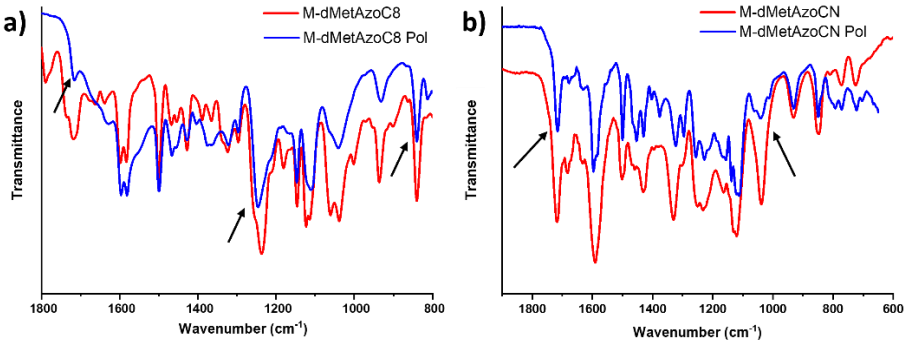

Figure 5.18. *FT-IR spectra before (red) and after (blue) polymerization of a)* ***M-dMetAzoC$_8$*** *and b)* ***M-dMetAzoCN****.*

The structural details were studied by XRD (**Figure 5.19**). The patterns confirmed the fixation of the columnar order after the methacrylate polymerization. In the low angle region, most of the abovementioned reflections found for the non-polymerized complexes remain and can be indexed again to a columnar hexagonal arrangement. In the high angle region, the diffuse halo was observed, supporting the fixation of the mesophase. However, the structural parameters of the polymeric films indicate a reduction of the disc size (around 5 Å) caused by the contraction of the material after the polymerization.

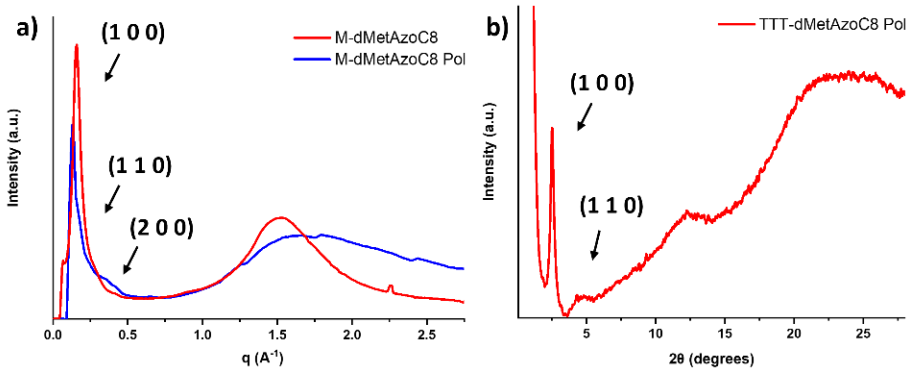

Figure 5.19. *a) 1D XRD patterns before and after polymerization of* ***M-dMetAzoC$_8$*** *and b) 1D XRD of* ***TTT-dMetAzoC$_8$*** *after polymerization.*

Before the acid treatment, the films were analyzed again by circular dichroism to check the stability of the chiral signal produced by the irradiation with CPL and the impact of the polymerization in the ellipticity generated in the columns. In **Figure 5.20** the CD spectra of the **dMetAzoCN** complexes are compared, observing a small reduction of the signal in all of them, which may be caused by the thermal reversion of the isomerization or by the irradiation with light of 700 nm. However, these ellipticity values are much higher than those described in ***Chapter 4*** for the polymeric films of coumarin. These differences in the chiral retention may be related with the thermal behavior of the compounds: for coumarins a tendency to crystallize was described. On the contrary, methacrylates retain the mesophase or vitrify at lower temperatures, "freezing" the mesophase and reducing the mobility of the compounds, thus avoiding the loss of chirality.

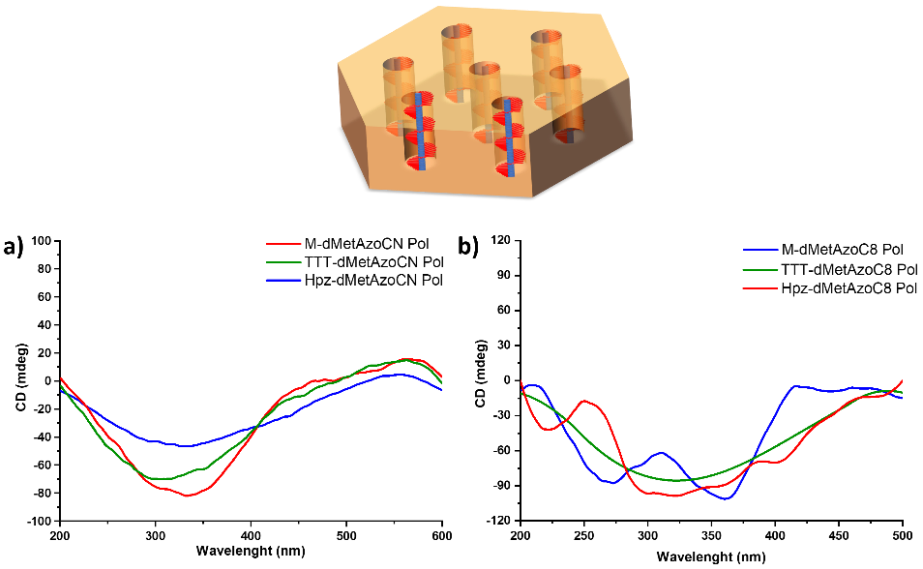

Figure 5.20. *CD spectra after polymerization of a)* ***M-dMetAzoCN***, ***TTT-dMetAzoCN*** *and* ***Hpz-dMetAzoCN*** *and b)* ***M-dMetAzoC$_8$***, ***TTT-dMetAzoC$_8$*** *and* ***Hpz-dMetAzoC$_8$*** *complexes.*

The obtained polymeric materials were immersed in an acid solution to remove the template molecules by breakup of the hydrogen bond. The procedure was similar to that described in ***Chapter 4***. Depending on the template, the acid treatment was more aggressive using HCl/EtOH (3M) for melamine and TTT or HCl(3M)/DMSO(1%)/EtOH for heptazine. After

shaking the films in the appropriate solution for 14 hours, the films were washed with water and dried under vacuum, obtaining nanoporous materials that were characterized by XPS, FT-IR and XRD (**Figure 5.22b**).

The XPS experiments revealed that the nanoporous (NP) materials of both **dMetAzoCN** and **dMetAzoC$_8$** dendrons (**Figure 5.21a**) did not present any peak in the nitrogen region corresponding to the template nitrogens. In **Figures 5.21 b-d** the template removal in the photopolymerized films is analyzed. The intense peak that appeared in the complexes before the acid treatment at 398 eV produced by the different N=C bonds was reduced drastically after the treatment, supporting the removal of the templates.

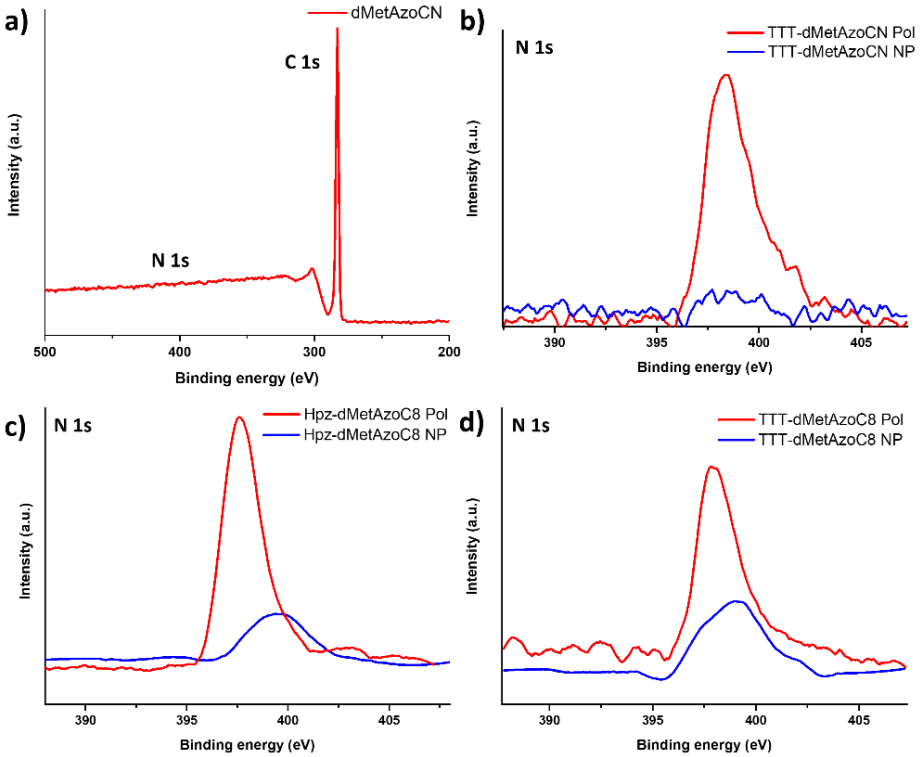

Figure 5.21. *a) XPS spectrum of* ***dMetAzoCN b-d)*** *XPS spectra before and after acid treatment of some polymerized supramolecular complexes.*

The integration of these peaks in the nitrogen area allowed to determine the percentage of template elimination. The low solubility of the heptazine core caused the least effective removal of this template.

Furthermore, this elimination is more effective in the complexes with **dMetAzoCN** dendron than in complexes with **dMetAzoC$_8$** (**Table 5.5**).

Table 5.5. *Analysis of the template removal by XPS.*

	$N_{integral\ (P/NP)}$	$\%_{removal}$
M-dMetAzoCN	631/12	98
TTT-dMetAzoCN	462/29	94
Hpz-dMetAzoCN	410/59	86
M-dMetAzoC$_8$	507/25	95
TTT-dMetAzoC$_8$	351/78	78
Hpz-dMetAzoC$_8$	584/111	81

The FT-IR spectra also supported the template elimination. In **Figure 5.22a** the FT-IR of **M-dMetAzoCN** before and after the acid treatment are compared. The appearance of a band at 1684 cm^{-1} supports the removal of melamine in this case, corresponding to the free acid band of the carbonyl generated after template elimination.

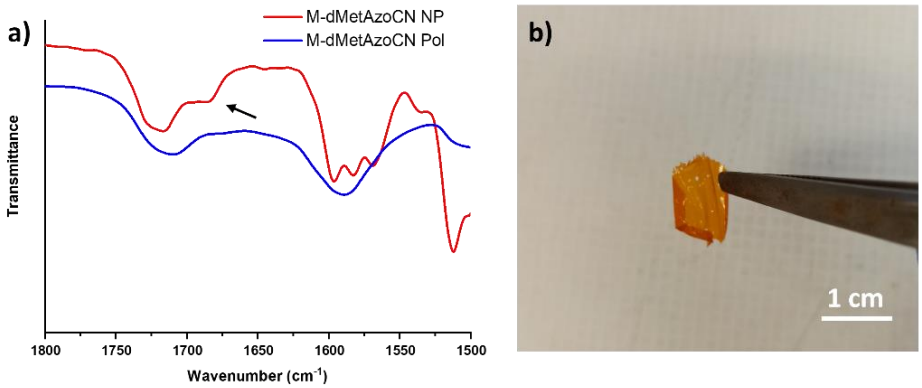

Figure 5.22. *a) FT-IR spectra comparison of the nanoporous material and the polymeric film. b) Self-standing membrane.*

Finally, the structural details of the nanoporous materials were studied by XRD (**Figure 5.23**). The diffractograms showed the retention of the columnar hexagonal arrangement. In the low angle region, the reflections were found in a ratio 1:1/√3 (1:1/√3:1/√4 for heptazine derived membranes), obtaining in this case a more ordered material. In

the high angle region, all diffractograms exhibited a broad halo, confirming the fixation of the liquid crystal arrangement in the membranes.

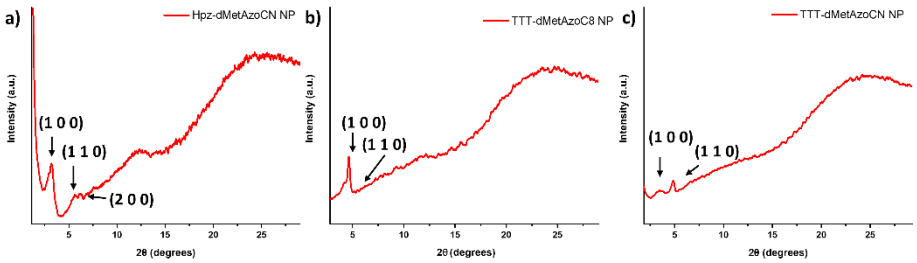

Figure 5.23. *1D XRD patterns of a)* ***Hpz-dMetAzoCN****, b)* ***TTT-dMetAzoC$_8$*** *and c)* ***TTT-dMetAzoCN*** *membranes.*

5.3.4 Selective adsorption studies

5.3.4.1 Selective adsorption by size

The size discrimination was studied in all complexes with the previous considered molecules, (*S*)-(hexan-2-yl)-4-nitroaniline (**NA***, size= 11.7x4.2 Å), (*S*)-tryptophan (**Tryp***, size= 8.2x4.8 Å) and (*S*)-(hexan-2-yl)pyrene (**Pyr***, size= 13.9x7.7 Å). These studies will focus on the different pore sizes and their capacity of adsorbing/rejecting molecules with special attention to the abovementioned contraction of the material during the membrane preparation.

Figure 5.24 represents the adsorption of **NA*** as a function of time with the different membranes prepared. The absorbance of the solution was measured at increasing times until it remained stable, which is considered the maximum adsorption of the membrane. The adsorption kinetics of **NA*** were examined up to a maximum of 24 hours. After this time, the membranes derived from the complexes with **TTT** and **Hpz** templates had adsorbed most of the molecules. However, melamine-derived membranes showed adsorption of approximately 55% of the molecules in solution. This value contrasts with the previously studied **M-dCouAzoC$_8$ NP** membrane (***Chapter 4***), which adsorbed

approximately 77%. This difference can be attributed to the reduction in pore size observed in the XRD studies.

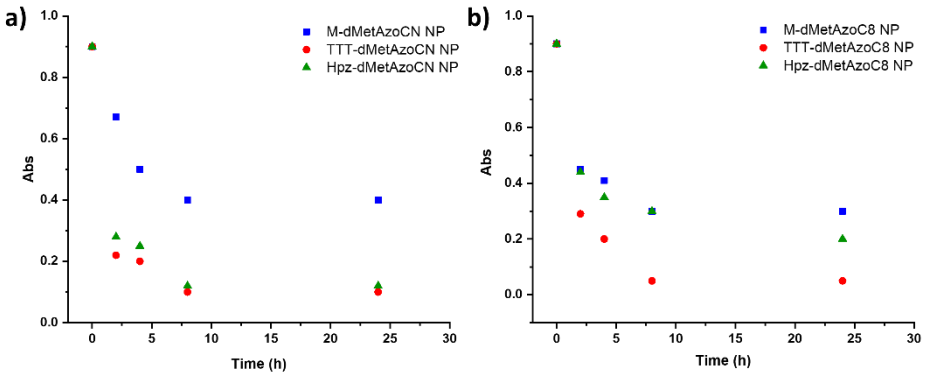

Figure 5.24. *Nitroaniline* ***NA**** *adsorption followed by UV spectroscopy in water of a)* ***M-dMetAzoCN****,* ***TTT-dMetAzoCN*** *and* ***Hpz-dMetAzoCN NP*** *membranes and b)* ***M-dMetAzoC$_8$****,* ***TTT-dMetAzoC$_8$*** *and* ***Hpz-dMetAzoC$_8$ NP*** *membranes.*

This limitation affected the membrane capacity of adsorption of **NA*** with a pore occupation of 25% and 32% for **M-dMetAzoCN NP** and **M-dMetAzoC$_8$ NP** respectively, which represents 0.87 and 0.96 molecules per disc. The membranes with bigger pores **TTT-dMetAzoCN NP** and **TTT-dMetAzoC$_8$ NP** adsorbed 42% and 43% (1.26 and 1.29 molecules per disc respectively) and 42%/35% for **Hpz-dMetAzoCN NP** and **Hpz-dMetAzoC$_8$ NP** (1.26 and 1.05 molecules per disc).

The adsorption of the tryptophan aminoacid **Tryp*** was also studied at 280 nm by UV (**Figure 5.25**). Melamine membranes **M-dMetAzoCN NP** and **M-dMetAzoC$_8$ NP** adsorbed it with an occupancy of 34% and 28% respectively, which represents 1.02 and 0.84 molecules of aminoacid per disc. TTT derivatives showed an occupancy of 42% and 50% of the pores for **TTT-dMetAzoCN NP** and **TTT-dMetAzoC$_8$ NP** respectively, which is traduced in 1.26 and 1.5 molecules per disc. Finally, heptazine **Hpz** derivatives adsorbed 34% for **Hpz-dMetAzoCN NP** and 27% for **Hpz-dMetAzoC$_8$ NP** (1.02 and 0.81 tryptophan molecules per disc respectively).

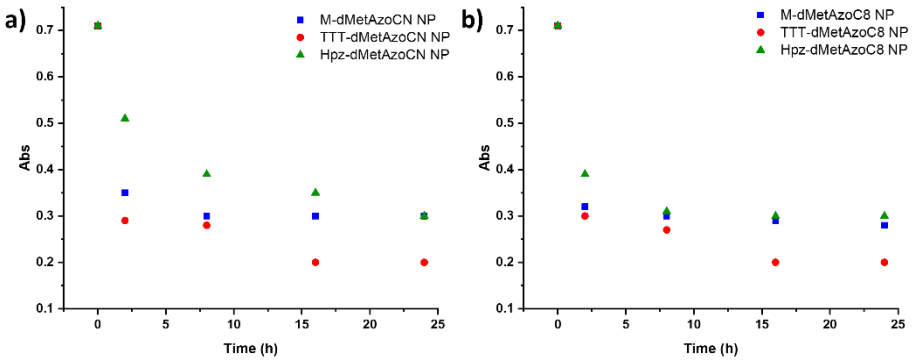

Figure 5.25. *Tryptophan **Tryp*** adsorption of a) **M-dMetAzoCN**, **TTT-dMetAzoCN** and **Hpz-dMetAzoCN NP** membranes and b) **M-dMetAzoC$_8$**, **TTT-dMetAzoC$_8$** and **Hpz-dMetAzoC$_8$ NP** membranes, followed by UV spectroscopy in water.*

Finally, the adsorption capacity was analyzed with a big dye. In **Figure 5.26** the absorbance variation of the pyrene **Pyr*** solution was followed by UV spectroscopy at 240 nm. The melamine membranes **M-dMetAzoCN NP** and **M-dMetAzoC$_8$ NP** hardly adsorbed because of their small pore with an occupancy of 2% and 0.04% (0.06 and 0.001 molecules per disc) . TTT membranes showed a reduced adsorption in comparison with the coumarin membrane studied in ***Chapter 4***; this reduction is related with the material contraction after the acid treatment. The percentage of adsorption was 29% (0.87 molecules per pore) and 28% (0.84 molecules per pore) for **TTT-dMetAzoCN NP** and **TTT-dMetAzoC$_8$ NP** respectively. Finally, **Hpz-dMetAzoCN NP** and **Hpz-dMetAzoC$_8$ NP** reached the highest adsorption of pyrene **Pyr*** with an occupancy of 43% and 55% (1.29 and 1.65 molecules adsorbed per disc).

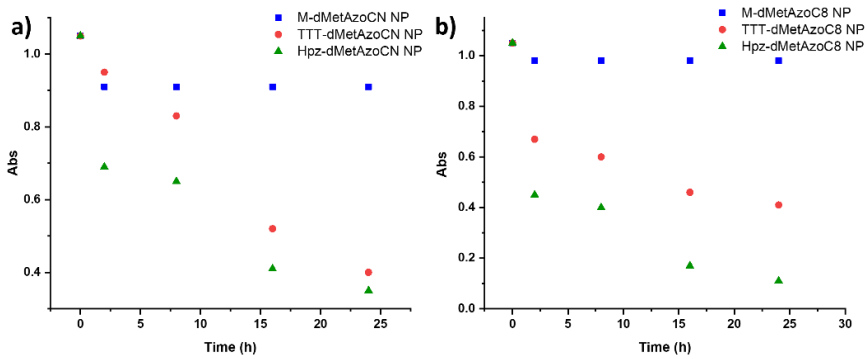

Figure 5.26. *Pyrene **Pyr*** adsorption of a) **M-dMetAzoCN**, **TTT-dMetAzoCN** and **Hpz-dMetAzoCN NP** membranes and b) **M-dMetAzoC$_8$**, **TTT-dMetAzoC$_8$** and **Hpz-dMetAzoC$_8$ NP** membranes followed by UV spectroscopy in water.*

The adsorption capacity of the LC membranes was measured as a function of the milligrams of dye and membrane, following the same equation described in ***Chapter 4*** (see **section 4.3.4.1**). **Tables 5.6** and **5.7** include the adsorption capacities of the membranes with the chosen dyes for these studies.

Table 5.6. *Adsorption capacity of the* ***dMetAzoCN NP*** *membranes.*

	M-dMetAzoCN NP	**TTT-dMetAzoCN NP**	**Hpz-dMetAzoCN NP**
q_t **NA*** (mg/g)	54	86	84
q_t **Tryp*** (mg/g)	40	50	40
q_t **Pyr*** (mg/g)	2	25	26

Table 5.7. *Adsorption capacity of the* ***dMetAzoC$_8$ NP*** *membranes.*

	M-dMetAzoC$_8$ NP	**TTT-dMetAzoC$_8$ NP**	**Hpz-dMetAzoC$_8$ NP**
q_t **NA*** (mg/g)	64	91	75
q_t **Tryp*** (mg/g)	42	59	39
q_t **Pyr*** (mg/g)	1	24	35

For a complete understanding of the dye adsorption, the results obtained in **Table 5.6** and **5.7** were adjusted to a second-order kinetic curve[7]:

$$\frac{t}{q_t} = \frac{1}{k_{ad} * q_e^2} + \frac{1}{q_e} * t$$

where q_e is the maximum capacity of dye adsorbed at equilibrium, t is the necessary time to reach that adsorption, and k_{ad} is the pseudo-second-order (g mg^{-1} h^{-1}) kinetic constant. The linear regression of t/q_t

vs t(h) for nitroaniline **NA*** adsorption with **dMetAzoCN** membranes is shown in **Figure 5.27**. The correlation coefficient obtained in all cases was superior to 0.99, confirming the precision of this model to the nitroaniline **NA*** adsorption.

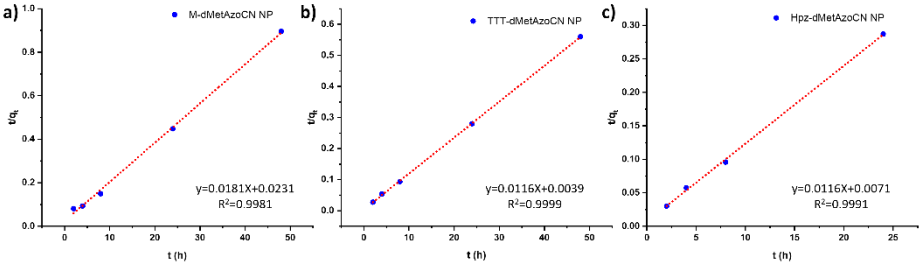

Figure 5.27**. Kinetic adjustment of the **NA adsorption in a) **M-dMetAzoCN**, b) **TTT-dMetAzoCN** and c) **Hpz-dMetAzoCN NP** membranes.*

In the case of **M-dMetAzoC$_8$**, **TTT-dMetAzoC$_8$** and **Hpz-dMetAzoC$_8$ NP** membranes, the linear representation is exhibited in **Figure 5.28**, fitting to the second order kinetics with correlation coefficients over 0.998 in the three membranes.

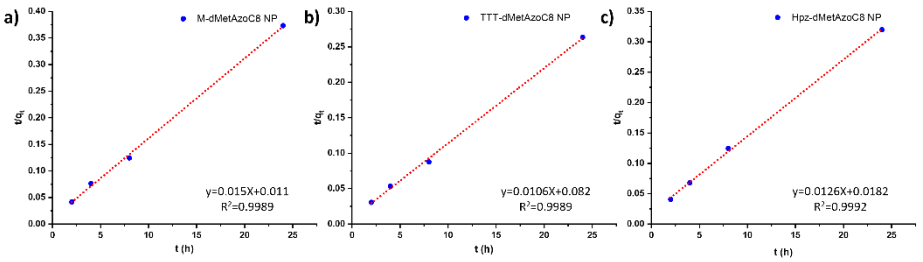

Figure 5.28.** Kinetic adjustment of the **NA adsorption in a) **M-dMetAzoC$_8$**, b) **TTT-dMetAzoC$_8$** and c) **Hpz-dMetAzoC$_8$ NP** membranes.*

The ability to release molecules from a solution is a crucial factor in membrane preparation (as it was commented in ***Chapter 4***), enabling the recovery of valuable adsorbates and the reusability of the membrane. To evaluate desorption capability, the membranes were immersed in a 1M KOH solution in water to release the previous adsorbed nitroaniline **NA***. This solution deprotonates the carboxyl groups, releasing the previously adsorbed **NA***. The UV spectroscopy monitored the release of **NA*** until a constant signal level was reached. This cycle of adsorption and desorption was repeated three times, highlighting the process reversibility (see **Figure 5.29**).

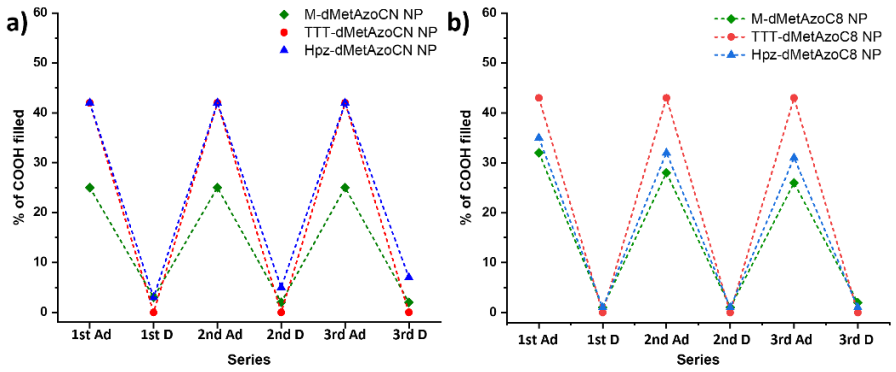

Figure 5.29. *Adsorption/Desorption of nitroaniline* ***NA**** *in a)* ***M-dMetAzoCN, TTT-dMetAzoCN and Hpz-dMetAzoCN NP*** *membranes and b)* ***M-dMetAzoC$_8$, TTT-dMetAzoC$_8$*** *and* ***Hpz-dMetAzoC$_8$ NP*** *membranes.*

5.3.4.2 Selective adsorption by chirality

Once the adsorption/rejection capacity of the materials by size was demonstrated, the chiral recognition was examined in the chiral membranes **M-dMetAzoCN NP** and **M-dMetAzoC$_8$ NP**. For this purpose, two films of each membrane were irradiated with *right*-CPL and *left*-CPL respectively. The adsorption of these membranes was investigated with a solution of **(S)-(hexan-2-yl)-4-nitroaniline NA***, and the process was followed by UV spectroscopy (**Figure 5.30**). In both materials the outcome of the experiments was the same: the *left*-CPL membranes adsorbed more molecules of dye in the first hours; however, if the membrane was left in the solution after 24 hours the materials had absorbed most of the nitroaniline derivative. These studies confirmed a tendency of the chiral membrane to adsorb the corresponding enantiomer with a kinetic control.

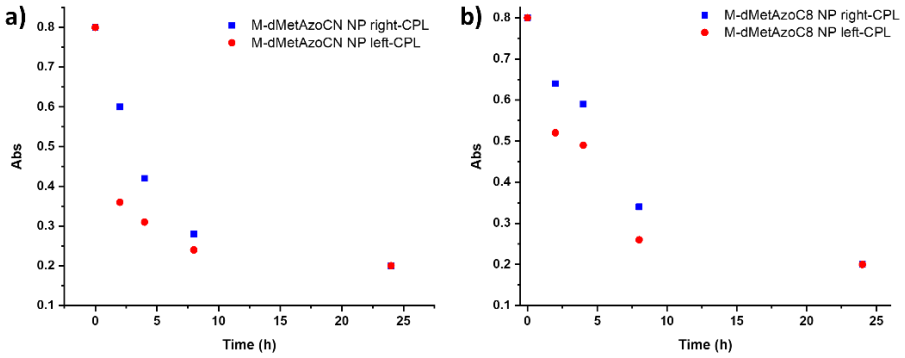

Figure 5.30. *Nitroaniline* ***NA**** *adsorption of a)* ***M-dMetAzoCN NP*** *and b)* ***M-dMetAzoC$_8$ NP*** *after irradiation with CPL followed by UV spectroscopy in water.*

5.4 Conclusions

In this chapter two different substituted benzoic acids have been synthesized which contain methacrylate groups and azobenzene moieties. The assembly of these acids with different aromatic planar molecules that contain amino groups has led to the formation of six supramolecular complexes through hydrogen bond. All complexes exhibit a columnar hexagonal arrangement. Their irradiation with CPL has produced a chiral signal of high intensity in all materials, which is maintained after the photopolymerization of the methacrylate units. The columnar order at room temperature allowed to obtain a high CD value in the polymeric films. This order is kept after the acid treatment, which successfully removed the template molecules. However, this treatment produced a contraction in the material, as has been described in the bibliography before for other methacrylate films. Finally, these chiral membranes have demonstrated molecular recognition by size, because of the different size of the template molecules used in their preparation.

5.5 Experimental part

5.5.1 Characterization techniques

All reagents were purchased from Aldrich and used without further purification. Anhydrous CH_2Cl_2 and THF were purchased from Scharlab and dried by using a solvent purification system.

^{1}H-NMR and **^{13}C-NMR** spectra were acquired on a Bruker AV400 spectrometer. The experiments were performed at room temperature in different deuterated solvents ($CDCl_3$, CD_2Cl_2 or DMSO-d_6). Chemical shifts are given in ppm relative to TMS and the solvent residual peak was used as the internal standard.

Infrared spectra were recorded on a Bruker Vertex 70 FT-IR spectrometer. The samples were prepared on KBr pellets with a concentration of the product of 1-2% (w/w).

MALDI-TOF mass spectrometry was performed on an Autoflex Bruker mass spectrometer with a dithranol matrix. Positive and negative ion electrospray ionization high resolution (**ESI HRMS**) was performed on a Bruker Q-TOF-MS in a positive or negative ESI mode.

The optical textures of the mesophases were investigated by **polarized-light optical microscopy** (POM) using an Olympus BH-2 polarizing microscope fitted with a Linkam THMS600 hot stage and a Linkam TMS94 controller. **Thermogravimetric analysis** (TGA) was performed using a Q5000IR from TA instruments at heating rate of 10 °C min^{-1} under a nitrogen atmosphere. Thermal transitions were determined by **differential scanning calorimetry** (DSC) using a DSC Q2000 from TA instruments with powdered samples (2−5 mg) sealed in aluminum pans. The apparatus was previously calibrated with indium (156.6 °C, 28.44 J*g-1). Glass transition temperatures (Tg) were determined at the half height of the baseline jump, and first order transition temperatures were read at the maximum of the corresponding peak. **X-ray diffraction** measurements were carried out using an XRD-PANanalytical Empyrean

diffractometer equipped with platform Scatter X78. Photographic patterns were recorded with a Pinhole camera (Anton Paar) operating with a point-focused Ni-filtered Cu-Kα beam. Samples were contained in Lindemann glass capillaries (0.9 or 0.7 mm diameter) and, when necessary, a variable-temperature attachment was used to heat the sample. The patterns were collected on flat photographic film perpendicular to the X-ray beam. X-Ray Diffraction in films (XRD) images were recorded on a Ganesha lab instrument equipped with a Genix-Cu ultra-low divergence source producing X-ray photons with a wavelength of 1.54 Å and a flux of 1 x 108 photons/second. Diffraction patterns were collected on a Pilatus Nanoporous polymer | 59 300K detector with reversed-biased silicon diode array sensor. The detector contains 487 x 619 pixels of 172 x 172 µm2 and consists out of three modules with an intermodule gap of 17 pixels in between, resulting in two dark bands on the image. Grazing Incidence X-Ray Scattering (GIXS) measurements were performed on a sample to detector distance of 1080 mm (WAXS) or 1530 mm (SAXS). Temperature-dependent measurements were executed with a Linkam HFSX350 heating stage and cool unit. Azimuthal integration of the obtained diffraction patterns was performed by utilizing the SAXSGUI software. The beam centre and the q-range were calibrated by utilizing silver behenate (0.107 $Å^{-1}$; 58.43 Å).

UV-Vis absorption spectra were recorded on an ATI-Unicam UV4-200 spectrophotometer.

Circular dichroism spectra were recorded on a Jasco J-810 spectropolarimeter. CD spectra were recorded at different rotation angles around the light beam showing the same trace, in the graphs the average of the six rotations were shown.

Photocrosslinking of methacrylates was carried out by exposing the aligned LC films of 10 µm of thickness to 740 nm LED light (ThorsLab) for 60 min with a UV power of 8 mW/cm^2.

XPS spectra were recorded on a Kratos AXIS ultra DLD spectrometer equipped with an Al Kα X-ray monochromatic source (1486.6 eV) and using 20 eV as pass energy. Binding energies were calibrated according to the C1s peak at 284.6 eV.

5.5.2 Synthetic procedures

*5.5.2.1 Synthesis of ((11-bromoundecyl)oxy)(tert-butyl)dimethylsilane **BrC$_{11}$OTBDMS (11)***

Synthesis of **BrC$_{11}$OTBDMS (11):** In a two-neck flask were dissolved 11-bromo-1-undecanol (8.12 g, 32. mmol), DMAP (0.79 g, 6.47 mmol) and imidazole (2.64 g, 38.8 mmol) under argon atmosphere at 0ºC in dichloromethane (150 ml). After 2 hours *tert*-butyldimethylsilyl chloride (5.84 g, 38.8 mmol) was added and the mixture was stirred overnight. The crude was poured into 100 ml of NH_4Cl and washed with 100 ml of NaCl. The aqueous phase was extracted three times with ethyl acetate (100 ml). The organic phases were collected and washed with NaCl (100 ml), dried with $MgSO_4$, filtered and the solvent evaporated. The product was purified by column chromatography in DCM 1:1 hexane with a yield of 64%.

^{1}H-NMR (CDCl$_3$, 298K, 400 MHz, δ, ppm): 3.60 (t, J=6.5 Hz, 2H), 3.40 (t, J=6.6 Hz, 2H), 1.85 (q, J=7.6 Hz, 2H), 1.29 (m, 16H), 0.89 (s, 9H), 0.05 (s, 6H).

^{13}C-NMR (CDCl$_3$, 298K, 100 MHz, δ, ppm): 62.80, 33.74, 33.25, 30.61, 29.60, 29.54, 29.50, 28.61, 26.01, 25.85, -4.31.

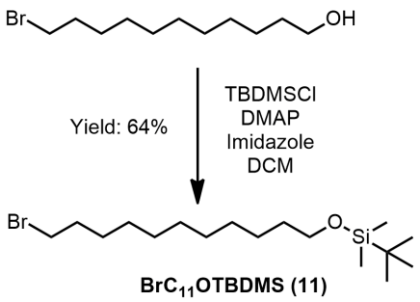

***Scheme 5.2.** Synthesis of **BrC$_{11}$OTBDMS**.*

***5.5.2.2** Synthesis of **dMetAzoCN (9)** (Scheme 5.1 in section 5.3.1)*

Synthesis of **MedOHAzoCN (3):** In a two-neck flask were dissolved methyl gallate (8.37 g, 45.4 mmol), potassium hydrogen carbonate (4.54 g, 45.40 mmol) and potassium iodide (spatula tip) under argon atmosphere in a mix of DMF/Acetone (40/10 ml). Then, the mixture was heated at 80ºC and vigorously stirred. Finally, **AzoCN (1)** (1.50 g, 4.54 mmol) was added to the mixture and let react overnight. The crude was poured into 100 ml of water and was extracted with ethyl acetate (3x100 ml). The organic phases were collected and washed with water 5x100 ml, dried with $MgSO_4$, filtered and evaporated in the rotavapor. The product was purified by recrystallization in ethanol with a yield of 70%.

^{1}H-NMR (DMSO-d_6, 298K, 400 MHz, δ, ppm): 9.49 (s, 2H), 8.05 (m, 2H), 7.96 (m, 4H), 7.17 (m, 2H), 6.97 (s, 2H), 4.39 (m, 4H), 3.78 (s, 3H).

^{13}C-NMR (DMSO-d_6, 298K, 100 MHz, δ, ppm): 166.01, 162.24, 154.19, 150.66, 146.18, 138.59, 133.77, 125.29, 122.90, 115.34, 108.50, 70.18, 67.94, 51.93.

Synthesis of **MedSilAzoCN (5):** In a two-neck flask were dissolved in DMF (50 ml) **MedOHAzoCN (3)** (1.20 g, 2.77 mmol), potassium carbonate (1.14 g, 8.31 mmol) and a spatula tip of potassium iodide under argon atmosphere. The mixture was stirred and heated at 80ºC, and then, **BrC_{11}OTBDMS (11)** (2.52 g, 6.92 mmol) was added and let react overnight at 80ºC. The crude was poured into 100 ml of water and was extracted with ethyl acetate (3x50 ml). The organic phases were collected and washed with water 5x100 ml, dried with $MgSO_4$, filtered and evaporated in the rotavapor. The crude was purified by flash column chromatography in a mix of DCM 5:1 hexane with a yield of 62%.

^{1}H-NMR (CD_2Cl_2, 298K, 400 MHz, δ, ppm): 7.95 (m, 4H), 7.81 (m, 2H), 7.26 (s, 2H), 7.02 (m, 2H), 4.42 (m, 2H), 4.36 (m, 2H), 3.99 (t, J=6.6 Hz, 4H), 3.87 (s, 3H), 3.57 (t, J=6.6 Hz, 4H), 1.75 (q, J=Hz, 4H), 1.48-1.25 (m, 32H), 0.88 (s, 18H), 0.03 (s, 12H)

^{13}C-NMR (CD_2Cl_2, 298K, 100 MHz, δ, ppm): 167.15, 163.01, 155.37, 153.26, 147.53, 142.03, 133.81, 126.07, 125.95, 123.60, 119.13, 115.54, 113.88, 108.10, 71.69, 69.79, 68.83, 63.76, 52.57, 33.49, 30.23, 30.18, 30.04, 29.99, 29.87, 26.63, 26.41, 26.30, 18.78, -5.02.

Synthesis of **dOHAzoCN (7):** Over a solution of **MedSilAzoCN (5)** (1.60 g, 1.59 mmol) in THF (20 ml), was added a solution of LiOH (192 mg, 7.97 mmol) in water (10 ml), and then the mixture was stirred for 6 hours. After that time the crude was poured in HCl/H_2O 4M obtaining an orange solid that was purified by recrystallization in ethanol, obtaining the product with a yield of 70%.

^{1}H-NMR ($CDCl_3$, 298K, 400 MHz, δ, ppm): 7.94 (m, 4H), 7.79 (m, 2H), 7.33 (s, 2H), 7.01 (m, 2H), 4.41 (m, 4H), 4.00 (t, J=6.5 Hz, 4H), 3.63 (t, J=6.6 Hz, 4H), 3.33 (s, 2H), 1.75 (q, J=7.6 Hz, 4H), 1.54 (q, J=7.8 Hz, 4H), 1.29 (m, 36H).

^{13}C-NMR ($CDCl_3$, 298K, 100 MHz, δ, ppm): 169.41, 162.54, 154.93, 152.73, 147.07, 142.12, 133.33, 125.57, 123.25, 115.16, 113.40, 108.57, 71.17, 69.37, 68.18, 63.19, 32.82, 29.65, 29.60, 29.54, 29.50, 29.35, 29.27, 26.01, 25.85.

Synthesis of **dMetAzoCN (9):** in a flask was dissolved **dOHAzoCN (7)** (0.30 g, 0.40 mmol) in 20 ml of THF at 0^{o}C under argon atmosphere; then triethylamine (0.13 ml, 0.90 mmol) was added and let react for 30 minutes. Finally, methacryloyl chloride (0.10 ml, 0.90 mmol) was added dropwise and let react for 3 hours. The crude was dissolved in ethyl acetate (50 ml) and extracted with water (3x50 ml), dried with $MgSO_4$, filtered and evaporated. The product was purified by flash column chromatography in a mixture of hexane 6:4 ethyl acetate, obtaining the product with a yield of 56%.

^{1}H-NMR (CD_2Cl_2, 298K, 400 MHz, δ, ppm): 7.95 (m, 4H), 7.80 (m, 2H), 7.32 (s, 2H), 7.02 (m, 2H), 6.05 (m, 2H), 5.53 (m, 2H), 4.44 (m, 4H), 4.35(m, 4H), 4.09 (t, J=6.5 Hz, 4H), 4.00 (t, J=6.6Hz, 4H), 1.91 (m, 6H), 1.76 (q, J=7.8 Hz, 4H), 1.65 (q, J=6.9 Hz, 4H), 1.40-1.20 (m, 24H).

^{13}C-NMR (CD_2Cl_2, 298K, 100 MHz, δ, ppm): 170.64, 167.89, 162.95, 155.32, 153.29, 147.49, 142.77, 137.33, 133.81, 125.93, 125.26, 124.74, 123.57, 119.12, 115.50, 113.86, 108.62, 71.72, 69.78, 68.82, 65.31, 30.10, 30.06, 29.92, 29.80, 29.15, 26.56, 26.52, 18.63.

FT-IR (KBr, ν: cm^{-1}): 3425 (OH), 3030 (C=CH), 2925 (C=C-H), 2850 (C-C-H), 2227 (C≡N), 1715 (C=O), 1678 (C=O), 1585 (C=C), 1500 (C=C), 1235 (C-O), 1113 (C-O).

MS (MALDI$^+$, dithranol, m/z): found 918.4 [M+Na^+] calculated with sodium 916.08 (896.10+22.98).

5.5.2.3 *Synthesis of* ***dMetAzoC$_8$ (10)*** *(Scheme 5.1 in section 5.3.1)*

Synthesis of **MedOHAzoC$_8$ (4):** In a two-neck flask were dissolved methyl gallate (0.51 g, 2.77 mmol), potassium hydrogen carbonate (0.27 g, 2.77 mmol) and potassium iodide (spatula tip) under argon atmosphere in a mix of DMF/Acetone (20/5 ml). Then, it was heated at 80ºC and vigorously stirred. Finally, **AzoC$_8$ (2)** (0.80 g, 1.85 mmol) was added to the mixture and let react overnight at 80ºC. The crude was let cool down and the salts were filtered over celite, washed with DCM and evaporated. The crude was dissolved in ethyl acetate/hexane (50 ml) and washed with water 5x100 ml, dried with $MgSO_4$, filtered and evaporated in the rotavapor. The product was purified by flash column chromatography in a mixture of DCM 8: 2 hexane with a yield of 70%.

^{1}H-NMR (CD_2Cl_2, 298K, 400 MHz, δ, ppm): 7.91 (m, 2H), 7.87 (m, 2H), 7.19 (s, 2H), 7.12 (m, 2H), 7.00 (m, 2H), 6.34 (s, 2H), 4.42 (m, 4H), 4.05 (t, J=6.6 Hz, 2H), 3.86 (s, 3H), 1.82 (q, J=7.8 Hz 2H), 1.48 ppm (q, J=8 Hz, 2H), 1.32 (m, 8H), 0.90 (t, J=6.9 Hz, 3H).

^{13}C-NMR (CD_2Cl_2, 298K, 100 MHz, δ, ppm): 166.01, 162.24, 154.19, 150.66, 146.18, 138.59, 133.77, 125.29, 122.90, 115.34, 108.50, 70.18, 67.94, 51.93.

Synthesis of **MedSilAzoC$_8$ (6):** In a two-neck flask were dissolved in DMF (30 ml) **MedOHAzoC$_8$ (4)** (1.30 g, 2.42 mmol), potassium carbonate (1.00 g, 7.26mmol) and a spatula tip of potassium iodide under argon atmosphere. The mixture was stirred and heated at 80ºC, and then,

BrC_{11}OTBDMS (11) (2.65 g, 7.26 mmol) was added and let react overnight at 80ºC. The crude was poured into 150 ml of water and was extracted with ethyl acetate (5x100 ml). The organic phases were collected and washed with water 5x100 ml, dried with $MgSO_4$, filtered and evaporated in the rotavapor. The crude was purified by flash column chromatography in a mix of DCM 6:1 hexane with a yield of 67%.

^{1}H-NMR ($CDCl_3$, 298K, 400 MHz, δ, ppm): 7.85 (m, 4H), 7.26 (s, 2H), 6.97 (m, 4H), 4.40 (m, 4H), 4.01 (m, 6H), 3.90 (s, 3H), 3.58 (t, J=6.6Hz, 4H), 1.76 (m, 8H), 1.50-1.20 (m, 28H), 0.89 (s, 18H), 0.04 (s, 12H).

^{13}C-NMR ($CDCl_3$, 298K, 100 MHz, δ, ppm): 166.99, 161.36, 160.90, 152.80, 147.31, 147.08, 141.88, 125.40, 124.46, 124.39, 114.87, 114.80, 107.98, 71.25, 69.39, 68.49, 67.98, 63.48, 52.31, 33.04, 31.96, 29.79, 29.73, 29.60, 29.54, 29.51, 29.41, 29.38, 26.18, 26.14, 25.96, 22.80, 18.52, 14.24, -5.10.

Synthesis of **dOHAzoC$_8$ (8):** Over a solution of **MedSilAzoC$_8$ (6)** (0.90 g, 0.81 mmol) in THF (10 ml) was added a solution of LiOH (88 mg, 3.26 mmol) in water (10 ml), and then it was stirred overnight. After that time, the crude was poured in HCl/H_2O 4M, diluted in ethyl acetate (50 ml), washed with water (3x50 ml), dried with $MgSO_4$, filtered and evaporated. The solid obtained was dissolved in 5 ml of ethyl acetate and poured into cold hexane, obtaining the product with a yield of 78%.

^{1}H-NMR (CD_2Cl_2, 298K, 400 MHz, δ, ppm): 7.81 (m, 4H), 7.19 (s, 2H), 7.05 (m, 4H), 4.31 (m, 4H), 4.04 (t, J=6.4 Hz, 2H), 3.90 (m, 8H), 1.73 (q, J=7.7 Hz, 2H), 1.61 (m, 4H), 1.50-1.10 (m, 38H), 0.86 (t, J=6.8 Hz, 3H)

^{13}C-NMR (CD_2Cl_2, 298K, 100 MHz, δ, ppm): 169.31, 161.38, 160.89, 152.79, 147.28, 147.03, 142.48, 124.47, 124.41, 114.87, 114.81, 108.57, 71.28, 69.37, 68.50, 67.95, 63.19, 32.82, 31.96, 29.65, 29.60, 29.55, 29.50, 29.38, 29.36, 29.25, 26.18, 26.02, 25.83, 22.81, 14.25.

Synthesis of **dMetAzoC$_8$ (10):** in a flask was dissolved **dOHAzoC$_8$ (8)** (0.40 g, 0.46 mmol) in 20 ml of THF at 0ºC under argon atmosphere. Then triethylamine (0.11 ml, 1.15 mmol) was added and let react for 30 minutes. Finally, methacryloyl chloride (0.12 ml, 1.15 mmol) was added

dropwise and let react for 3 hours. The crude was dissolved in ethyl acetate (50 ml) and extracted with water (3x50 ml), dried with $MgSO_4$, filtered and evaporated. The product was purified by flash column chromatography in a mixture of DCM 12:1 ethyl acetate, obtaining the product with a yield of 41%.

^{1}H-NMR (CD_2Cl_2, 298K, 400 MHz, δ, ppm): 7.85 (m, 4H), 7.33 (s, 2H), 7.00 (m, 4H), 6.05 (m, 2H), 5.53 (m, 2H), 4.42 (m, 2H), 4.35 (m, 2H), 4.06 (m, 6H), 3.58 (t, J=6.7 Hz, 4H), 1.91 (m, 6H), 1.73 (m, 2H), 1.50 (m, 6H), 1.37-1.12 (m, 40H), 0.86 (t, J=7.0 Hz, 3H).

^{13}C-NMR (CD_2Cl_2, 298K, 100 MHz, δ, ppm): 169.95, 166.50, 163.14, 162.06, 160.92, 160.57, 152.46, 152.11, 146.24, 146.06, 142.76, 135.97, 135.01, 130.72, 125.23, 124.07, 124.01, 122.84, 114.86, 108.25, 68.70, 68.11, 67.90, 64.24, 63.76, 32.41, 30.13, 29.94, 29.83, 29.19, 26.50, 26.31, 23.25, 20.68, 18.44, 14.44.

FT-IR (KBr, ν: cm^{-1}): 3373 (OH), 2922 (C=C-H), 2851 (C-C-H), 1716 (C=O), 1582 (C=C), 1499 (C=C), 1243 (C-O).

MS (MALDI$^+$, dithranol, m/z): found 999.8 [M+H$^+$] calculated 999.3.

5.5.2.4 *Preparation of supramolecular complexes*

All supramolecular complexes were prepared dissolving the corresponding acid and template in dichloromethane in a molar proportion of 3:1. Then, the solvent was slowly evaporated under agitation and the resulting solid was melted before using.

M-dMetAzoC$_8$

^{1}H-NMR (CD_2Cl_2, 298K, 400 MHz, δ, ppm): 7.85 (m, 12H), 7.31 (s, 6H), 6.99 (m, 12H), 6.11 (s, 1H), 6.05 (m, 6H), 5.87 (s, 3H), 5.57 (s, 1H), 5.52 (m, 6H), 4.38 (m, 12H), 4.03 (m, 30H), 3.05 (m, 2H), 1.91 (m, 18H), 1.79 (m, 18H), 1.64 (m, 16H), 1.51-1.28 (m, 132H), 0.88 (m, 12H).

^{13}C-NMR (CD_2Cl_2, 298K, 400 MHz, δ, ppm): 176.34, 170.15, 167.89, 161.95, 161.45, 153.23, 147.68, 147.41, 141.63, 137.37, 125.22, 124.82,

115.29, 110.60, 71.80, 69.78, 68.63, 65.34, 63.36, 41.44, 33.38, 32.41, 30.12, 29.97, 29.93, 29.80, 29.19, 26.58, 26.56, 26.32, 23.24, 18.64, 14.44.

FT-IR (KBr, ν: cm^{-1}): 3348 (OH), 2924 (C=C-H), 2850 (C-C-H), 1788 (C=O), 1720 (C=O), 1596 (C=C), 1585 (C=C), 1238 (C-O).

TTT-dMetAzoC$_8$

^{1}H-NMR (CD_2Cl_2, 298K, 400 MHz, δ, ppm): 9.06 (s, 3H), 7.85 (m, 6H), 7.78 (m, 12H), 7.32 (s, 6H), 7.09 (m, 12H), 6.99 (m, 6H), 6.05 (m, 6H), 5.53 (m, 6H), 4.40 (m, 12H), 4.03 (m, 30H), 3.58 (t, J=6.6 Hz, 6H), 1.91 (m, 18H), 1.78 (m, 24H), 1.63 (m, 12H), 1.60-1.20 (m, 114H), 1.01 (m, 18H).

^{13}C-NMR (CD_2Cl_2, 298K, 400 MHz, δ, ppm): 169.55, 167.88, 167.39, 161.96, 161.43, 160.56, 160.08, 155.31, 147.69, 147.40, 146.38, 142.64, 137.37, 134.44, 131.11, 130.30, 126.25, 125.22, 1271.81, 69.80, 69.01, 68.87, 65.33, 63.37, 32.41, 31.79, 30.13, 30.10, 29.98, 29.93, 29.83, 29.80, 29.18, 26.55, 26.31, 23.24, 19.79, 18.64, 14.44, 14.18.

FT-IR (KBr, ν: cm^{-1}): 3418 (OH), 2924 (C=C-H), 2853 (C-C-H), 1721 (C=O), 1596 (C=O), 1567 (C=C), 1512 (C=C), 1224 (C-O).

Hpz-dMetAzoC$_8$

^{1}H-NMR (CD_2Cl_2, 298K, 400 MHz, δ, ppm): 8.92 (s, 1H), 8.77 (s, 1H), 8.55 (s, 1H), 7.85 (m, 12H), 7.45 (m, 6H), 7.35 (s, 6H), 6.99 (m, 12H), 6.90 (m, 6H), 6.05 (m, 6H), 5.53 (m, 6H), 4.40 (m, 6H), 4.35 (m, 6H), 4.09 (m, 36H), 1.91 (m, 18H), 1.76 (m, 24H), 1.61 (m, 12H), 1.50-1.18 (m, 144), 0.90 (m, 18H).

^{13}C-NMR (CD_2Cl_2, 298K, 400 MHz, δ, ppm): 171.52, 167.88, 161.97, 161.43, 157.45, 157.21, 153.34, 149.41, 147.71, 147.42, 147.23, 142.79, 137.38, 129.74, 125.22, 125.17, 124.82, 124.80, 122.68, 115.40, 115.30, 115.22, 110.61, 108.71, 71.84, 69.88, 69.02, 68.94, 68.67, 65.34, 32.42, 30.15, 30.13, 29.99, 29.94, 29.85, 29.21, 26.63, 26.59, 26.49, 23.25, 21.32, 18.64, 14.45.

FT-IR (KBr, ν: cm^{-1}): 3363 (OH), 2921 (C=C-H), 2851 (C-C-H), 1785 (C=O), 1717 (C=O), 1598 (C=C), 1500 (C=C), 1234 (C-O).

M-dMetAzoCN

^{1}H-NMR (CD_2Cl_2, 298K, 400 MHz, δ, ppm): 8.95 (m, 12H), 7.81 (m, 6H), 7.32 (s, 6H), 7.01 (m, 6H), 6.05 (m, 6H), 5.80 (s, 1H), 5.60 (m, 3H), 5.53 (m, 6H), 4.41 (m, 6H), 4.38 (m, 6H), 4.26 (s, 1H), 4.09 (t, J=6.7 Hz, 12H), 4.00 (t, J=6.7 Hz, 12H), 3.36 (m, 2H), 1.91 (m, 18H), 1.76 (m, 12H), 1.61 (m, 14H), 1.47-1.17 (m, 102H), 0.88 (t, J=7.1 Hz, 3H).

^{13}C-NMR (CD_2Cl_2, 298K, 400 MHz, δ, ppm): 170.29, 167.89, 162.96, 155.32, 153.27, 147.49, 142.60, 137.33, 133.81, 125.93, 125.26, 125.11, 123.57, 119.12, 115.50, 113.86, 108.57, 71.71, 69.77, 68.82, 65.31, 41.65, 32.49, 30.21, 30.07, 29.93, 29.86, 29.80, 29.15, 26.57, 26.52, 23.26, 18.63, 14.45.

FT-IR (KBr, ν: cm^{-1}): 3393 (OH), 2925 (C=C-H), 2851 (C-C-H), 2223 (C≡N), 1721 (C=O), 1714 (C=O), 1597 (C=C), 1582 (C=C), 1320 (C-O).

TTT-dMetAzoCN

^{1}H-NMR (CD_2Cl_2, 298K, 400 MHz, δ, ppm): 9.05 (s, 3H), 7.95 (m, 12H), 7.80 (m ,12H), 7.32 (s, 6H), 7.06 (m, 12H), 6.05 (m, 6H), 5.53 (m, 6H), 4.41 (m, 12H), 4.03 (m, 24H), 1.91 (m, 18H),1.78 (m, 30H), 1.68-1.20 (m, 90H), 1.01 (t, J=7.4 Hz, 9H).

^{13}C-NMR (CD_2Cl_2, 298K, 400 MHz, δ, ppm): 170.19, 167.91, 165.29, 162.97, 160.62, 155.34, 153.31, 147.52, 145.89, 142.77, 137.36, 133.82, 130.26, 126.33, 125.94, 125.25, 124.81, 123.58, 122.81, 122.04, 119.12, 116.01, 115.53, 113.88, 108.67, 71.73, 69.81, 68.89, 68.84, 65.32, 31.79, 30.11, 30.08, 29.93, 29.81, 29.17. 26.57, 26.53, 19.78, 18.63, 14.18.

FT-IR (KBr, ν: cm^{-1}): 3416 (OH), 2924 (C=C-H), 2852 (C-C-H), 2227 (C≡N), 1711 (C=O), 1638 (C=O), 1595 (C=C), 1513 (C=C), 1251 (C-O).

Hpz-dMetAzoCN

^{1}H-NMR (CD_2Cl_2, 298K, 400 MHz, δ, ppm): 10.09 (s, 3H), 7.95 (m, 12H), 7.81 (m, 6H), 7.55 (m, 6H), 7.32 (s, 6H), 7.03 (m, 6H), 6.65 (m, 6H), 6.05 (m, 6H), 5.53 (m, 6H), 4.44 (m, 6H), 4.37 (m, 6H), 4.09 (t, J=6.6 Hz, 12H), 4.00 (t, J=6.6 Hz, 12H), 3.83 (m, 6H), 1.92 (m, 12H), 1.76 (m, 20H), 1.65 (m, 12H), 1.43-1.20 (m, 114H), 0.91 (t, J=7.0 Hz, 9H).

^{13}C-NMR (CD_2Cl_2, 298K, 400 MHz, δ, ppm): 170.40, 167.89, 162.96, 156.61, 155.96, 155.32, 153.29, 147.50, 142.69, 137.34, 133.82, 131.05, 125.94, 125.25, 124.86, 123.57, 122.04, 119.12, 115.51, 114.69, 113.87, 108.63, 74.85, 71.72, 69.80, 68.82, 65.31, 32.47, 30.12, 30.09, 30.08, 29.95, 29.91, 29.89, 29.81, 29.16, 26.63, 26.59, 26.53, 26.33, 23.28, 18.63, 14.47.

FT-IR (KBr, ν: cm^{-1}): 3301 (OH), 3091 (C=CH), 2921 (C=C-H), 2852 (C-C-H), 2223 (C≡N), 1716 (C=O), 1681 (C=O), 1609 (C=C), 1528 (C=C), 1504 (C=C), 1233 (C-O).

5.5.3 Experimental procedures

5.5.3.1 Preparation of the chiral nanoporous membranes

Liquid crystal polymers were prepared by sandwiching 2 mg of product and photoinitiator(bis(cyclopenta-1,3-diene)bis(1-(2,4-difluorophenyl)-3H-pyrrol-3-yl)titanium 2% weight) between two glasses that were previously spin-coated (1500 rpm, 30s) with a solution of poly(vinyl alcohol) (1% in water) with spacers of 10 µm. The sandwich was heated above isotropization temperature and let slowly cool down until room temperature. After that, it was irradiated with a 700 nm LED for 30 min and introduced in hot water until PVA was dissolved obtaining the corresponding self-standing polymeric material.

To remove the template molecules the polymeric material was immersed in a solution of HCl/Ethanol 3M for 24 hours in the case of melamine and TTT. For heptazine stronger conditions were necessary, using DMSO (1%) HCl/EtOH (3M). Finally, the nanoporous materials were washed with water and dried under vacuum before using.

5.5.3.2 *Adsorption experiments*

A piece of 2 mg of the nanoporous material was immersed in a solution (0.6 ml) of the corresponding molecule that was previously study by UV with a maximum absorbance of 1. Then the adsorption process was followed by UV monitoring the changes. In the case of the chiral selective experiments the vial with the membrane and the solution was protected from the light.

5.6 Appendix

5.6.1 NMR spectra

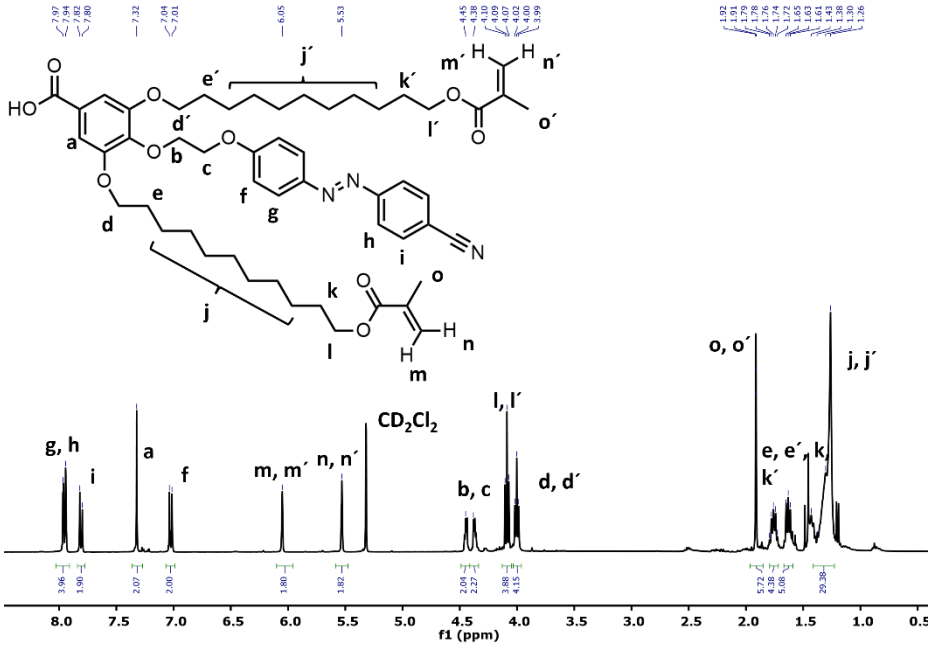

Figure 5.31. [1]*H-NMR spectrum of* ***dMetAzoCN****,* CD_2Cl_2*, 298K, 400 MHz.*

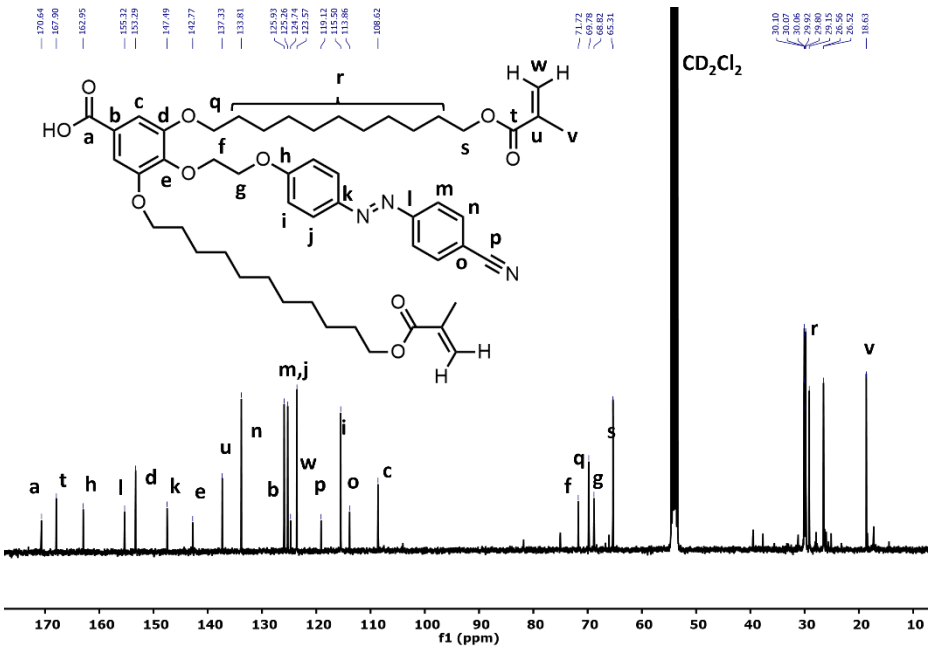

Figure 5.32. [13]*C-NMR spectrum of* ***dMetAzoCN****,* CD_2Cl_2*, 298K, 100 MHz.*

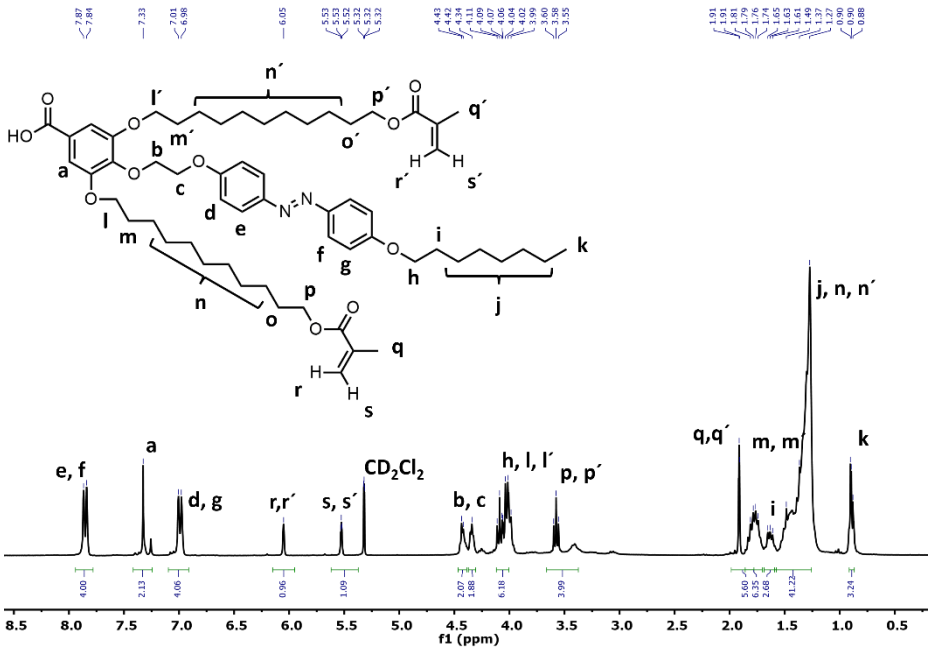

Figure 5.33. *^{1}H-NMR spectrum of **dMetAzoC$_8$**, CD_2Cl_2, 298K, 400 MHz.*

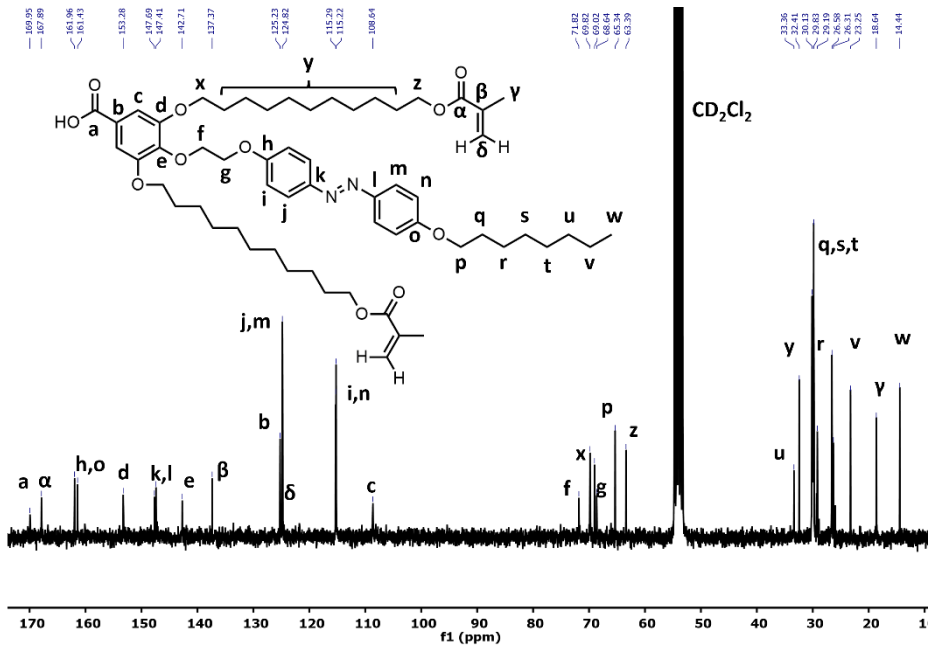

Figure 5.34. *^{13}C-NMR spectrum of **dMetAzoC$_8$**, CD_2Cl_2, 298K, 100 MHz.*

5.6.2 Mass spectrometry spectra

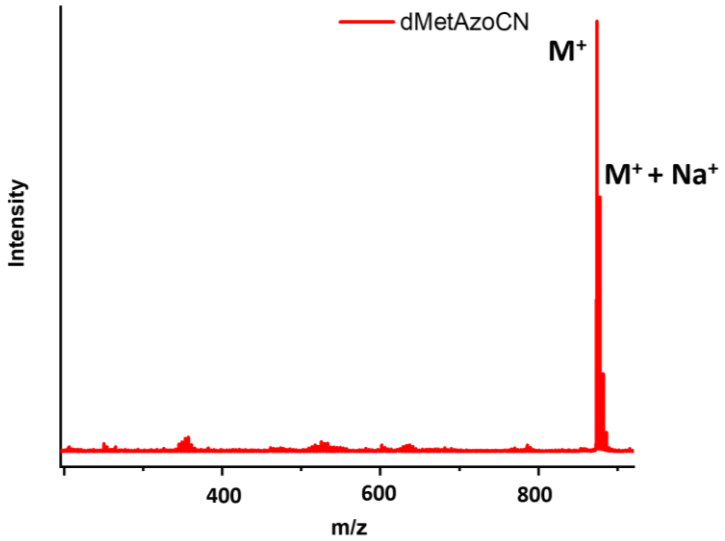

*Figure 5.35. ESI spectrum of **dMetAzoCN**.*

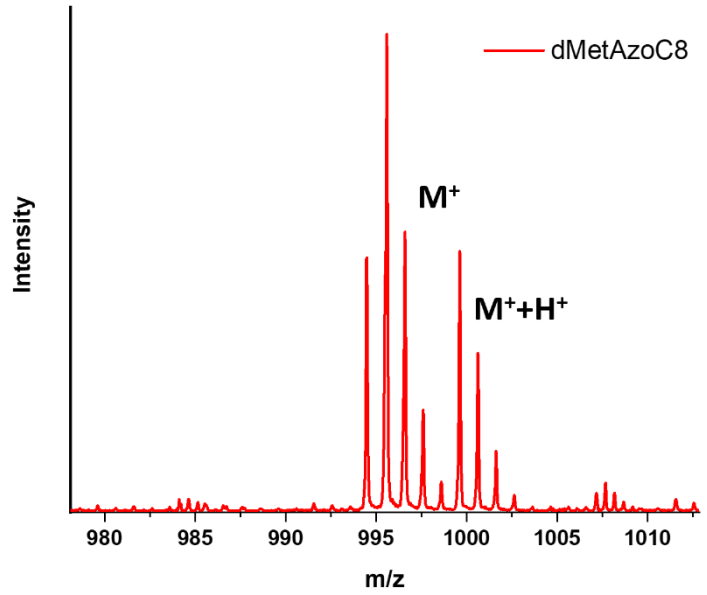

*Figure 5.36. ESI spectrum of **dMetAzoC$_8$**.*

5.6.3 DSC thermograms

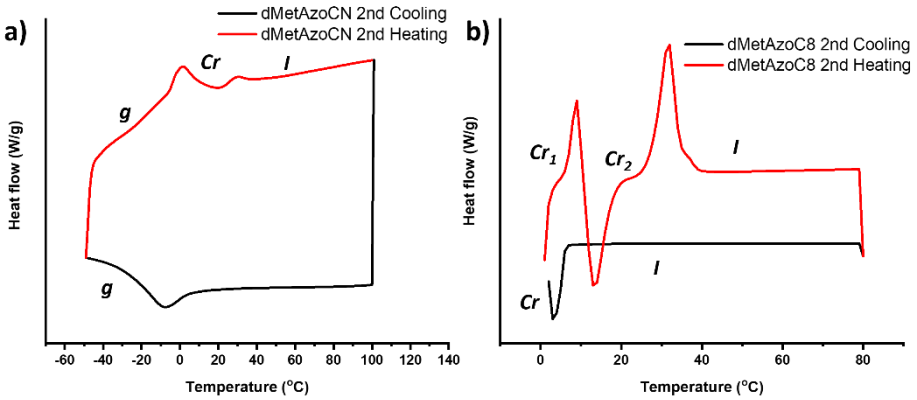

Figure 5.37. 2nd DSC cycle (10°C/min) of a) ***dMetAzoCN*** and b) ***dMetAzoC8***.

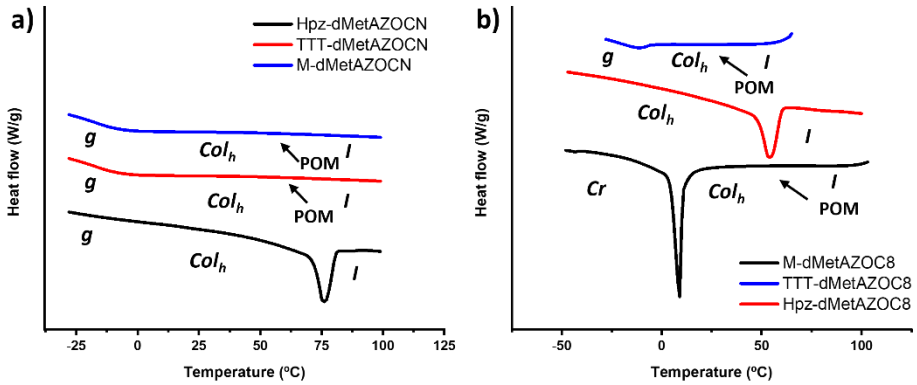

Figure 5.38. DSC traces of the second cooling (10°C/min) of the supramolecular complexes.

5.7 References

[1] Y. Zhan, D. J. Broer and D. Liu, Perspiring Soft Robotics Skin Constituted by Dynamic Polarity-Switching Porous Liquid Crystal Membrane, *Adv. Mater.*, 2023, **35**, 2211143-2211151.

[2] N. Marets, D. Kuo, J. R. Torrey, T. Sakamoto, M. Henmi, H. Katayama and T. Kato, Highly Efficient Virus Rejection with Self-Organized Membranes Based on a Crosslinked Bicontinuous Cubic Liquid Crystal, *Adv. Healthcare Mater*., 2017, **6**, 1700252-1700258.

[3] I. Bala, S. P. Gupta, S. Kumar, H. Singh, J. De, N. Sharma, K. Kailasam and S.K. Pal, Hydrogen-bond mediated columnar liquid crystalline assemblies of C3-symmetric heptazine derivatives at ambient temperature, *Soft Matter*, 2018, **14**, 6342-6352.

[4] F. Rabie, Z. Sedlakova, S. Sheth, E. Marand, S. M. Martin and L. Polakova, (Meth)acrylate liquid crystalline polymers for membrane applications, *Appl. Polym. Sci.,* 2015, **132**, 42694-42702.

[5] A. Karausta and E. Bukusoglu, Liquid Crystal-Templated Synthesis of Mesoporous Membranes with Predetermined Pore Alignment , *ACS Appl. Mater. Interfaces*, 2018, **10**, 33484−33492.

[6] J. Lugger, D. J. Mulder, R. Sijbesma and A. P. H. J. Schenning, Nanoporous Polymers Based on Liquid Crystals, *Materials*, 2018, **11**, 104-122.

[7] Z-Z. Nie, B. Zuo, L. Liu, M. Wang, S. Huang, X-M. Chen and H. Yang, Nanoporous Supramolecular Liquid Crystal Polymeric Material for Specific and Selective Uptake of Melamine, *Macromolecules,* 2020, **53**, 4204−4213.

Chapter 6

Resumen y conclusiones

En esta Tesis doctoral se ha investigado la preparación de **materiales orgánicos** funcionales basados en **cristales líquidos** con aplicación en diferentes campos como: nanotransportadores de fármacos, materiales conductores de protones o materiales nanoporosos para la separación de moléculas. El hilo conductor que ha guiado la investigación en la Tesis doctoral es el uso de la **química supramolecular** como aproximación para la obtención de nuevos cristales líquidos no convencionales. De entre sus múltiples vertientes las empleadas en el desarrollo de esta Tesis han sido el **enlace iónico** y el **enlace de hidrógeno**. Estas interacciones han permitido dirigir la formación de cristales líquidos a partir de unidades no mesogénicas, promoviendo la ordenación de dichas unidades dando lugar a materiales anisótropos con potenciales aplicaciones.

Las conclusiones obtenidas en cada uno de los capítulos de investigación se detallan a continuación:

Capítulo 2 Ionic self-assembly of pillar[5]arenes: proton-conductive liquid crystals and aqueous nanoobjects with encapsulation properties.

En este capítulo se estudió la funcionalización de un macrociclo pilar[5]areno que contenía 10 grupos amina mediante interacciones iónicas (COO^-/NH_3^+) con diferentes ácidos (benzoicos y alifáticos con y sin coumarinas). Estos materiales iónicos se autoorganizaron en cristales líquidos de tipo nemático en estado sólido, dando lugar a materiales conductores de protones con valores similares a los reportados en la bibliografía previamente. La formación de dichos enlaces iónicos dotó a los materiales de un carácter anfífilo, el cual sirvió para obtener una serie de nanoestructuras (micelas, vesículas, nanoesferas, nanotubos…) en disolución acuosa. La morfología de los nanoagregados se pudo relacionar con el tipo de ácido utilizado en la preparación de los macrociclos iónicos. Dando lugar a estructuras huecas en aquellos materiales que contenían ácidos con coumarinas y estructuras compactas sin coumarinas. Estas nanoestructuras huecas fueron utilizadas como nanotransportadoras de fármacos, usando

como modelo Rojo Nilo y mostrando su liberación controlada al ser irradiadas con luz de 325 nm, provocando la dimerización de las coumarinas. La dimerización de coumarinas permitió obtener nanotransportadores de fármacos con respuesta a la luz para su la liberación controlad; así como, materiales cristal líquido mecánicamente estables con aplicación como conductores de protón.

Capítulo 3 Preparation of Ionic Bent-Core Pillar[5]arenes for Proton Conduction and Self-Assembly Nanostructures.

Tras haber demostrado en el **Capítulo 2** la capacidad de los pilar[n]arenos para organizar ácidos mediante enlaces iónicos y dar lugar a cristales líquidos, en este capítulo se decidió explorar su funcionalización con ácidos bent-core. Las moléculas tipo bent-core poseen propiedades muy interesantes (moléculas polares que se apilan en capas con cierta inclinación) y dan lugar a mesofases únicas (SmCP, HNFs, DC…). Por tanto, se llevó a cabo la síntesis de seis ácidos, divididos en tres grupos funcionales: azobenzenos, bifenilos y ester con espaciadores cortos (4 carbonos) y largos (10 carbonos) entre el ácido y la estructura bent-core. Los seis materiales iónicos dieron lugar a mesofases de tipo columnar (oblicua y rectangular) con valores de movilidad de protón similares a los del capítulo 2. El estudio de estructura química en relación con los valores de movilidad reveló mejores resultados para los espaciadores cortos y en cuanto a los grupos funcionales, los azobencenos fueron los más destacados.

La preparación de agregados en disolución acuosa dio ligar a una gran variedad de morfologías de tipo fibrilar. Tras ello, se realizó un estudio para establecer la relación entre el tipo de espaciador con la morfología obtenida: espaciadores cortos se autoensamblaron en HNFs y los espaciadores largos dieron lugar a fibras helicoidales. En el caso específico de los esteres, las morfologías obtenidas fueron nanotubos huecos.

Capítulo 4 Size and chiral selective nanoporous membranes based on coumarins.

En el **Capítulo 4** se llevó a cabo la síntesis de moléculas con forma discótica para la preparación de materiales nanoporosos mediante enlace de hidrógeno. Estos materiales son de alto interés y valor hoy en día en múltiples aplicaciones como la captación de gases, separación de moléculas o purificación de aguas.

Para dicha aproximación se sintetizaron diversos complejos supramoleculares entre dendrones (derivados de ácido benzoico) y moléculas plantilla que contienen grupos amina. El enlace de hidrogeno formado entre ácidos y aminas, se puede romper fácilmente una vez formado el material polimérico obteniendo nanoporos. Por ello se utilizaron diversas moléculas plantilla dando lugar a materiales nanoporosos de diferente tamaño de poro. Los dendrones sintetizados contenían coumarinas como unidades fotopolimerizables y azobenzenos como unidad capaz de inducir quiralidad mediante irradiación con luz circularmente polarizada.

Aquellos materiales que exhibieron mesofases de tipo columnar fueron empleados en la preparación de materiales nanoporosos, irradiando primero con CPL y más tarde con luz de 325 nm fijando la estructura columnar. Los estudios de adsorción revelaron una separación efectiva por tamaño, dependiendo de la molécula plantilla empleada en la formación del complejo supramolecular. Y una separación en función de la quiralidad, al irradiar con luz circularmente polarizada de un signo u otro, así como el reconocimiento en mezclas racémicas especificas (en función de tamaño y quiralidad).

Capítulo 5 Preparation of discotic shaped molecules through H-bond for chiral nanoporous membranes based on methacrylates.

Continuando con la temática iniciada en el **Capítulo 4** sobre materiales nanoporosos, algunos de los aspectos claves en estos materiales son la reutilizabilidad y su estabilidad mecánica. Por ello, en este capítulo se exploró la sustitución de las coumarinas por metacrilatos como unidad fotopolimerizable, al ser materiales más resistentes mecánicamente.

La aproximación utilizada fue la misma, formación de complejos supramoleculares por enlace de hidrogeno entre moléculas plantilla y ácidos benzoicos que contenían grupos metacrilato y azobenzenos. En este caso, todos los materiales sintetizados se organizaron en mesofases columnares y su irradiación con luz circularmente polarizada indujo una señal quiral de alta intensidad. Los materiales nanoporos obtenidos conservaron el orden columnar y la señal quiral, sin embargo, tras el tratamiento ácido el tamaño del poro disminuyó, tal y como se ha descrito previamente en otros artículos de la misma temática. Las membranas quirales se emplearon como materiales con reconocimiento de moléculas por tamaño, en función de la plantilla empleada y por quiralidad al ser irradiadas con *r* o *l*-CPL.

Functional nanoarchitectures based on liquid crystal phases: ionic pillararenes and chiral columnar organizations. Materials for ionic conductivity and molecular segregation

Iván Marín Miana

Memoria presentada en la Universidad de Zaragoza para optar al Grado de Doctor

Departamento de Química Orgánica

Facultad de Ciencias-INMA

Universidad de Zaragoza-CSIC

Zaragoza, Abril 2024